

**NUMERICAL AND PHYSICAL MODELS  
FOR MICROWAVE BREAST IMAGING**

NUMERICAL AND PHYSICAL MODELS FOR  
MICROWAVE BREAST IMAGING

By

AASTHA TREHAN, B.ENG.

A Thesis

Submitted to the School of Graduate Studies

in Partial Fulfillment of the Requirements

for the Degree

Master of Applied Science

McMaster University

© Copyright by Aastha Trehan, September 2009

MASTER OF APPLIED SCIENCE (2009)  
(Electrical and Computer Engineering)

McMaster University  
Hamilton, Ontario

**TITLE:**           **Numerical and Physical Models for Microwave Breast  
Imaging**

**AUTHOR:**       Aastha Trehan  
B.Eng. (Electrical and Biomedical Engineering,  
                          McMaster University, Hamilton, Canada)

**SUPERVISORS:** Natalia K. Nikolova, Professor,  
Department of Electrical and Computer Engineering,  
McMaster University  
Dipl.Eng. (Technical University of Varna)  
Ph.D. (University of Electro-Communication)  
P.Eng. (Province of Ontario)  
Senior Member, IEEE

Michael D. Noseworthy, Ph.D.  
MRI Physicist & Assistant Professor  
Department of Electrical and Computer Engineering, School  
of Biomedical Engineering, and Department of Medical  
Physics, McMaster University  
B.Sc., M.Sc., Ph.D. (University of Guelph)

**NUMBER OF PAGES:** XXXIV, 282

# ABSTRACT

Breast cancer is a serious health problem that severely affects the society. Science and engineering communities are looking to find more advanced and new cures to contain this deadly disease. There has been considerable success in increasing the efficacy of conventional imaging techniques for breast cancer detection such as mammography. However, the use of ionizing radiation, the incidence of patient discomfort and the low specificity are some of the negative aspects of mammography. Also, the chances to successfully cure breast cancer can increase manifold with early detection of the malignant tumors. Magnetic Resonance Imaging (MRI) is successful with its highly clear and detailed images, but it is considered too expensive for wide screening. Its low specificity is another disadvantage.

Microwave imaging of the breast, which uses non-ionizing radiation, is a very active research area of recent times. It is hoped that once developed, it can override the negative aspects of the existing imaging modalities. The idea is to detect malignant lesions in the breast based on their electrical-property contrast

with healthy breast tissues.

The electrical properties of biological tissues in the microwave region are described by their complex permittivity. Previous studies claimed that malignant tumors have very high permittivity and high loss compared to the surrounding healthy tissue. It was assumed that the modality exploiting this contrast can easily detect sub-centimeter tumors. Hence, very simple models with high permittivity and loss tumor models embedded in low permittivity homogenous models were employed to show the detection capabilities of microwave imaging techniques. The examples were fairly amateurish and claimed unrealistic performance of the rather simplistic microwave imaging techniques.

Recent studies have shown that the breast is not as simple an electromagnetic medium as was thought previously. It is a complex heterogeneous environment with high permittivity and high loss healthy tissues (such as glandular tissue) and low permittivity and low loss healthy tissues (such as fat). The internal tissue distribution and volume varies significantly from woman to woman. Thus, simple models made with hemispheres, cylinders, etc., filled with water or oil cannot mimic the reality of the breast in imaging experiments and simulations.

This is why there is a considerable demand of representing breasts as realistic physical and numerical models. Physical models are required to experimentally verify the imaging scanning systems with antennas. The numerical models are required for electromagnetic (EM) simulations that are indispensable

in designing and testing image reconstruction algorithms.

The work in this thesis mainly deals with the construction and representation of breast models both in experiments and in simulations. This is important work toward making microwave imaging a practical stand-alone detection system.

## ACKNOWLEDGEMENTS

The thesis has been a cumulative work of two years and there are many to be grateful to, for this splendid journey. I would like to start by expressing my sincere appreciation to my senior supervisor, Dr. Natalia K. Nikolova, without whose help this thesis would have been impossible. I am indebted to Prof. Nikolova for giving me an opportunity in an upcoming research area. She has always been available to support, helping me to seek simple and practical solutions to complex problems, constantly providing me fruitful comments, and for never ceasing to train me to improve my technical and other weaknesses. She is a very tolerant and patient person, letting the student learn from his/her mistakes, thus, facilitating effective learning with personal growth. She is an excellent teacher and her graduate course made very intimidating material relating to antennas a lot more realizable. It was also a good learning experience to be a TA in her undergraduate courses.

I would also want to express my sincere gratitude and appreciation to my co-supervisor, Dr. Mike Noseworthy. During the past year, Dr. Noseworthy and

Dr. Colm Boylan, from Imaging Research Centre, St. Joseph Hamilton Hospital, have made available many MRI sets for my project. Thanks to the staff at SJHH and Arv (Dr. Noseworthy's student) to help me access the many images from their busy servers. They have also given me solutions and guidance on determining some key aspects for my study. Prof. Noseworthy's graduate course relating to medical imaging exposed me to real-world problems in the biomedical imaging field and helped me immensely with my research project.

I am also grateful to Prof. Mohamed Bakr and Prof. Jim Reily for being outstanding mentors of my undergraduate courses and for their brilliant lectures in graduate courses. Their graduate courses helped me with getting the grasp of numerical techniques as well as become efficient with MATLAB. This proved invaluable in my research project. Prof. Bakr has been extremely kind with his flexibility in teaching me the course on numerical techniques in Electromagnetics. It is a pleasure to have him as a member on my committee as well.

I would also like to thank my senior colleagues Reza K. Amineh, Yunpeng Song, and Li Liu from the Computational Electromagnetics Laboratory, with whom I did my major project work both in experiments and in simulations. I learned a great deal from them and they have been amazing friends during my stay here. Also, thanks to Mihail Georgiev and Robert Zimmerman, to build the much required hardware in my work.

Thanks to my fellow colleagues and friends, Xiaying Zhu and Shefali Kulkarni, for their many helpful suggestions and for being my good friends for



the past two years at McMaster University.

Many thanks are also due to the technical staff members in the Department of Electrical and Computer Engineering at McMaster University, Terry Greenlay, Cosmin Coroiu and Steve Spencer. Special thanks to Cosmin Coroiu for helping me through countless software trials in my projects.

Last but not least, I want to express my heartfelt gratitude to my wonderful family, grandmother, and late grandparents, for continuously being there for me and, for their unconditional support and love. My mother has helped me with countless recipes in my research with physical phantoms, during which time I made her kitchen a chemical lab for long stretches of days. Thanks to my brother Vivek, whose multiple co-op experiences at Autodesk indirectly gave me an insight into the 3-D modeling field. Special thanks to my dad, for keeping me motivated and creating a supportive environment at home. And of course thanks to God for such a wonderful life and opportunities.

# CONTENTS

<b>ABSTRACT</b>	III
<b>ACKNOWLEDGMENTS</b>	VI
<b>LIST OF FIGURES</b>	XV
<b>LIST OF TABLES</b>	XXVIII
<b>LIST OF SYMOLS AND ACRONYMS</b>	XXXI

## **CHAPTER 1 INTRODUCTION**

1	MOTIVATION	1
2	OUTLINE OF THESIS	13
3	CONTRIBUTIONS	16
	REFERENCES	17

## **CHAPTER 2 ELECTROMAGNETIC (EM) PROPERTIES OF HUMAN BREAST TISSUES – A LITERATURE REVIEW**

	INTRODUCTION	22
1	DIELECTRIC PARAMETERS AND MODELS	24
2	EXPERIMENTAL STUDIES	29
2.1	Previous Studies	30

2.2	Recent Studies	33
2.2.1	<i>Sample and measurement protocol</i>	34
2.2.2	<i>Data fitting and reduction</i>	37
2.2.3	<i>Data analysis</i>	38
2.2.4	<i>Results for dielectric parameters of various breast tissues</i>	42
2.2.5	<i>Sources of Variability within each study</i>	50
2.2.6	<i>Variability in dielectric parameters within the two studies and within tissue groups</i>	51
2.2.7	<i>Comparison with previous studies</i>	59
2.2.8	<i>Conclusions from these studies</i>	63
3	DIELECTRIC PARAMETERS FOR NUMERICAL BREAST PHANTOM	65
3.1	Dielectric Parameters for Skin	65
3.2	Dielectric Parameters for Muscle	68
3.3	Dielectric Parameters for Breast Interior	70
4	MECHANISMS OF MALIGNANCY	77
4.1	Electrical and Mechanical Mechanisms	77
4.2	Physical Mechanisms	79
	REFERENCES	82

**CHAPTER 3 SUMMARY OF PHYSICAL BREAST PHANTOMS AND THEIR RECIPES**

---

INTRODUCTION	85
1 PHANTOM REQUIREMENTS	87
2 METHODS AND MATERIALS	89
2.1 Apparatus for Measurements	89
2.2 Promising Recipes and Ideas	91
2.3 Materials for Phantom Fabrication	95
2.4 Tissue-specific Recipes	99
2.5 Generic Fabrication Procedures	105
2.5.1 <i>Procedure for glycerine phantom recipes (Table 3.2, Table 3.3, Table 3.4, Table 3.5)</i>	105
2.5.2 <i>Procedure for other recipes (Table 3.6, Table 3.7 and Table 3.8)</i>	107
2.6 Measurement Related Theory and Protocol	108
3 RESULTS – TARGETS AND ACHIEVED PARAMETERS	111
4 PROMISING EXAMPLES AND FUTURE WORK	122
REFERENCES	129
<b>CHAPTER 4 THREE-DIMENSIONAL (3-D) SURFACE AND SHAPE ACQUISITION WITH PHOTOGRAMMETRY</b>	
INTRODUCTION	132
1 SURFACE RECONSTRUCTION WITH PHOTOGRAMMETRY	136

1.1	Software Requirements	136
1.2	Assistive Hardware and Software Components	144
1.3	Generic Procedure	148
2	EXAMPLES AND APPLICATIONS OF PHOTOGRAMMETRY APPROACH	154
2.1	Reconstructed Shapes and Accuracy Assessment	154
2.2	File Compatibility for EM Simulators	157
3	VERIFICATION WITH FORWARD EM MODELS	159
3.1	Hardware and Measurements	160
3.2	Results	163
4	RECENT DEVELOPMENTS	165
4.1	Published Work	165
4.2	Laser Scanner	166
	REFERENCES	167

## **CHAPTER 5 PATIENT SPECIFIC NUMERICAL BREAST PHANTOMS**

	INTRODUCTION	171
1	PHANTOM REQUIREMENTS	173
1.1	Patient Specificity	173
1.2	3-D Model Specificity	178
1.2.1	<i>3-D modeling norms</i>	179
1.2.2	<i>Compatibility issues</i>	183
1.2.3	<i>Level of affordable complexity</i>	185
2	USING PATIENT SPECIFIC MAGNETIC	186

---

	RESONANCE IMAGES (MRI)	
	2.1 Image Formats	187
	2.2 Patient Database	190
	2.3 Image Processing	190
3	3-D MODELING WITH HFSS	197
	3.1 Contour Construction in MATLAB	197
	3.2 Polygon Formation in HFSS	207
	3.3 Simple GUI	209
	3.4 Slice-by-Slice Solid Construction in HFSS	211
	3.5 SAT Models and Compatibility with Other EM Simulators	217
4	SCOPE FOR MODEL SIMPLIFICATION	219
	REFERENCES	221

## CHAPTER 6 CONTRIBUTIONS TO NUMERICAL MODELING

	INTRODUCTION	224
1	FIDELITY OF THE ANTENNA	226
	1.1 Antenna Structure and Impedance Results	226
	1.2 Fidelity Evaluation	231
	1.2.1 <i>Theory and formulas</i>	231
	1.2.2 <i>Simulations and results</i>	232
2	3-D JACOBIAN MAPS FROM SELF ADJOINT SENSITIVITY ANALYSIS	242
	2.1 Objective Functions for Jacobian Maps	242

---

2.1.1	<i>Objective functions based on magnitudes of responses</i>	244
2.1.2	<i>Objective functions based on phases of responses</i>	244
2.1.3	<i>The sign of the Jacobian maps</i>	245
2.2	Simple Numerical Models and Results	246
	REFERENCES	257
<b>CHAPTER 7</b>	<b>CONCLUSIONS AND SUGGESTIONS</b>	260
1	RESULTS CONCLUDED	260
2	SUGESSTIONS FOR FUTURE WORK	262
2.1	Future Enhancements of The Work Presented in Thesis	262
2.2	Future Directions for AMWI	264
	REFERENCES	266
	<b>APPENDIX A</b>	267
	<b>BIBLIOGRAPHY</b>	270

## LIST OF FIGURES

Figure 1.1	The inside of the breast.	6
Figure 1.2	Schematic representation of ductal (top) and lobular (bottom) carcinoma of the breast.	6
Figure 2.1	Typical frequency dependence of the dielectric permittivity of biological tissues over a wide range of frequencies; where $\epsilon'$ and $\epsilon''$ denote the real and the imaginary part of the complex permittivity, respectively. Various processes are labeled on the image as ionic, dipolar relaxation, atomic and electronic resonances.	25
Figure 2.2	Dielectric spectroscopy of freshly excised breast tissue using a precision probe: (a) photograph of individual tissue samples (two adipose and two non-adipose) in the experimental setup at UC; (b) photograph of a UW tissue specimen illustrating the heterogeneous mixture of adipose (yellow) and fibro connective/glandular (white) tissue. The black ink spots mark the measurement sites.	35
Figure 2.3	Photograph of a UW tissue specimen showing malignant tissue (white region, upper right) and normal adipose tissue (yellow region, lower left). The black ink spots mark the measurement sites. The black ink around the perimeter of the specimen denotes the margins of the	36



	excised tissue.	
Figure 2.4	One-pole Cole–Cole fits to 354 dielectric properties data sets of reduction surgery study: (a) dielectric constant; (b) effective conductivity. The dashed (lower) black curve corresponds to the dielectric properties of lipid, and the dash-dot (upper) black curve corresponds to the dielectric properties of physiological saline.	44
Figure 2.5	One-pole Cole–Cole fits to the 85 normal data sets from cancer surgery study: (a) dielectric constant; (b) effective conductivity. The curves are color coded based on the amount of adipose tissue present in each sample. The solid black (upper) curve represents the dielectric properties of saline, the dashed black (lower) curve represents the dielectric properties of lipids, and the dash-dot black (middle) curve represents the dielectric properties of blood.	46
Figure 2.6	One-pole Cole–Cole fits to the five UW benign data sets (four cystic cases, solid lines, and one ductal hyperplasia case, dotted line): (a) dielectric constant; (b) effective conductivity. The black curves are as in Figure 2.5.	47
Figure 2.7	One-pole Cole–Cole fits to the five UC benign data sets (all fibro adenomas): (a) dielectric constant; (b) effective conductivity. The black curves are in Figure 2.5.	47
Figure 2.8	One-pole Cole–Cole fits to the 60 cancer data sets: (a) dielectric constant; (b) effective conductivity. The black curves are as in Figure 2.5.	48
Figure 2.9	Comparison for group 1 normal samples from the cancer surgery study and reduction surgery study. The red continuous line is for data from the cancer surgery study	54

	and the green dashed line is for data from the reduction surgery study. The top graph is for dielectric constant and the bottom graph is for effective conductivity.	
Figure 2.10	Comparison for group 2 normal samples from the cancer surgery study and reduction surgery study. The red continuous line is for data from cancer surgery study and the green dashed line is for data from the reduction surgery study. The top graph is for dielectric constant and the bottom graph is for effective conductivity.	55
Figure 2.11	Comparison for group 3 normal samples from the cancer surgery study and reduction surgery study. The red continuous line is for data from cancer surgery study and the green dashed line is for data from the reduction surgery study. The top graph is for dielectric constant and the bottom graph is for effective conductivity.	56
Figure 2.12	Median dielectric properties curves for malignant samples from the cancer surgery study. The top graph is for dielectric constant and the bottom graph is for effective conductivity.	58
Figure 2.13	Comparison of data from reduction surgery study with previous studies. Lines are median dielectric properties of the three adipose-defined tissue groups from the recent study (dash-dot line: group 1, dashed line: group 2, solid line: group 3). Symbols are for normal breast tissue dielectric properties published previously (◦: Chaudhary <i>et al.</i> , ×: Surowiec <i>et al.</i> , *: Joines <i>et al.</i> ). Vertical arrows: range of data reported by Campbell <i>et al.</i> at 3.2 GHz for adipose (solid lines) and normal (dashed lines) breast tissues.	61

Figure 2.14	Comparison of data from cancer surgery study with previous studies. Lines are median dielectric properties of the cancer samples from the recent study with 30% or greater malignant tissue content. Symbols are malignant breast tissue dielectric properties published previously (◦: Chaudhary <i>et al.</i> , ×: Surowiec <i>et al.</i> , *: Joines <i>et al.</i> ). Vertical arrows: range of data reported by Campbell <i>et al.</i> at 3.2 GHz for malignant tissues.	62
Figure 2.15	Comparison between four-pole Cole-Cole model of dry skin and wet skin from Gabriel <i>et al.</i> The dashed line is for dry skin model and the continuous line is for the wet skin model.	66
Figure 2.16	Comparison of the Cole-Cole model with the simple Debye model fitted to the dielectric properties for group 1 in the UWB.	73
Figure 2.17	Comparison of the Cole-Cole model with the simple Debye model fitted to the dielectric properties for group 2 in the UWB.	74
Figure 2.18	Comparison of the Cole-Cole model with the simple Debye model fitted to the dielectric properties for group 3 in the UWB.	75
Figure 2.19	Comparison of the Cole-Cole model with the simple Debye model fitted to the dielectric properties for the malignant group in the UWB.	76
Figure 2.20	The various shapes of breast masses. The last two are strongly associated with malignancy.	80
Figure 2.21	The various margins of lesions found in breast. The last three are strongly associated with malignancy.	80
Figure 2.22	Location and probability of carcinomas in breast.	81

Figure 3.1	Agilent 85070E dielectric Performance Probe Kit connected to an Agilent E8363B PNA.	91
Figure 3.2	Dielectric constants ( $\epsilon'$ ) from chapter 2 of all major breast tissues.	102
Figure 3.3	Conductivities ( $\sigma$ ) from chapter 2 of all major breast tissues.	102
Figure 3.4	The structure of LWCT (left) is more firm and solid in comparison to Fat-gel	105
Figure 3.5	Comparison between dielectric property model for muscle and phantom measurement for HWCT-1. The top graph is for dielectric constant and the bottom graph is for conductivity.	114
Figure 3.6	Comparison between dielectric property model for FG and phantom measurement for HWCT-2. The top graph is for dielectric constant and the bottom graph is for conductivity.	115
Figure 3.7	Comparison between dielectric property model for skin, transitional tissue and phantom measurement for IWCT. The top graph is for dielectric constant and the bottom graph is for conductivity.	116
Figure 3.8	Comparison between dielectric property model for adipose fat and phantom measurement for LWCT. The top graph is for dielectric constant and the bottom graph is for conductivity.	117
Figure 3.9	Comparison between dielectric property model for adipose fat and measurement for fat-gel phantom. The top graph is for dielectric constant and the bottom graph is for conductivity.	118
Figure 3.10	Comparison between dielectric property model for malignant tissue and phantom measurement for gelatine-	119

	saline recipe. The top graph is for dielectric constant and the bottom graph is for conductivity.	
Figure 3.11	Comparison between dielectric property model for malignant tissue and phantom measurement for alginate powder-saline recipe. The top graph is for dielectric constant and the bottom graph is for conductivity.	120
Figure 3.12	Dielectric constants ( $\epsilon'$ ) for all phantom recipes of breast tissues.	121
Figure 3.13	Conductivities ( $\sigma$ ) for all phantom recipes of breast tissues.	121
Figure 3.14	Phantoms mimicking malignant tumors, healthy homogenous breast and homogenous breast with a scatterer.	122
Figure 3.15	Phantoms with and without food color: (a) green and (b) yellow.	123
Figure 3.16	Comparison between dielectric parameters measurement on HWCT-2 phantoms – with and without food color. The top graph is for dielectric constant and the bottom graph is for conductivity.	124
Figure 3.17	Simple layered phantom in contact with a recently designed antenna.	127
Figure 3.18	Imaging array designs in literature: (a) symmetrical curved (bowl-shaped) antenna array; and (b) tapered imaging chamber integrated with an Alderson Treatment Brassiere cup.	127
Figure 3.19	The top two images show the snapshots of the process for fabricating more detailed breast physical phantom. The bottom two images show the views of the phantom created. The yellow phantom layer is IWCT for skin; white interior	128

	phantom is LWCT for fat and the green-fill phantom is HWCT-2 for FG	
Figure 4.1	An illustration of geometric estimation algorithm for breast surface.	135
Figure 4.2	Calibration-grid sheet with positions marked for taking 2-D photos.	138
Figure 4.3	(a) Horizontally held camera. (b) Vertically held camera. (c) Position of camera with respect to Calibration Grid.	139
Figure 4.4	A photograph showing stick-on on a balloon.	140
Figure 4.5	Photograph showing the designing of peripheral control points.	141
Figure 4.6	One of the 8-bit coded targets.	142
Figure 4.7	Photograph showing the final set up with a balloon when the 2-D images for modeling can be taken.	143
Figure 4.8	A phantom ready for 2-D image acquisition.	143
Figure 4.9	Components of the photogrammetry imaging set up: (a) PGR Flea 2 camera, (b) Cosmical TV Zoom Lens, (c) dot matrix grid, (d) stand design (dimensions in mm), and (e) stand with projector in use.	147
Figure 4.10	Auto-referenced target points are marked with crosses in PhotoModeler.	150
Figure 4.11	The view of object marked points in the 3-D Viewer window in PhotoModeler.	151
Figure 4.12	The model in the 3-D Viewer window in PhotoModeler by connecting the targets with triangular surface elements.	151
Figure 4.13	A screen capture from PhotoModeler with the reconstructed phantom surface.	152
Figure 4.14	A screen capture from PhotoModeler showing the adding of scale to the 3-D model using a pair of control points.	152

Figure 4.15	A screen capture from PhotoModeler showing axes definition for the 3-D model.	153
Figure 4.16	The Export Options dialog in PhotoModeler.	153
Figure 4.17	Actual (top) vs. reconstructed (bottom) for random shapes: (a) round bowl-like shape with marked targets; and (b) surface of cone with curved tip formed by joining marked targets with triangular surface elements.	156
Figure 4.18	Actual (top) vs. reconstructed (bottom) for canonical shapes: (a) cone with pointed tip; and (b) long cylinder. Both are formed with NURBS based surfaces.	157
Figure 4.19	The two-media simple breast model in XFDTD.	158
Figure 4.20	The two-media simple breast model in HFSS.	159
Figure 4.21	The UWB antenna element and its dimensions.	162
Figure 4.22	Components of the experimental set-up: (a) the two UWB antennas and the physical phantom immersed in the isopropyl alcohol; and (b) the Advantest R3770 VNA performing 2-port measurement.	162
Figure 4.23	Complete EM forward model using HFSS containing the two antenna elements, their feed-lines, coupling medium and the 3-D shape obtained via photogrammetry for: (a) random physical phantom, and (b) canonical physical phantom.	163
Figure 4.24	Comparison between measured and simulated results for the 2-antenna set up for random shaped phantom: (a) return loss, and (b) insertion loss.	164
Figure 4.25	Comparison between measured and simulated insertion loss (in dB) for the two UWB antennas with a cone-shaped phantom.	165
Figure 4.26	A handheld 3-D laser scanner from Creaform Inc.	167

Figure 5.1	Mammograms showing age related variability.	176
Figure 5.2	Examples of non-manifold topology: (a) a non-manifold vertex, (b) a non-manifold edge, and (c) a non-manifold vertex in a face.	181
Figure 5.3	Common examples of non-manifold edge creation in solid modeling: (a) two solid regions touching along a non-manifold edge; (b) a single solid region with a non-manifold edge; (c) a solid region touches a sheet region along a non-manifold edge; and (d) two solid cubes united at a non-manifold edge.	182
Figure 5.4	An excerpt from an ACIS SAT file for a cube.	184
Figure 5.5	A voxel of tomographic slice through brain mapped to a pixel in MRI.	189
Figure 5.6	Flow chart showing the first three steps in the image processing of the MR images.	183
Figure 5.7	The segmentation process in <i>assign_material_numbers.m</i> .	194
Figure 5.8	Flowchart showing the results of MATLAB codes in deriving a material map.	195
Figure 5.9	Material map conversion to dielectric property maps at 8 GHz.	196
Figure 5.10	The boundary traced for polygons from material map in coordinate space.	199
Figure 5.11	Example of two polygons of materials numbered 40 and 80. They are traced with connectivity nodes as shown on the left. A gap $\Delta$ as coming from MRI, is left between the polygons due to no transition between 3 <sup>rd</sup> and 4 <sup>th</sup> row. One possible solution is to give higher priority to material polygon numbered 40 (top) and extend it towards the	200



	material polygon numbered 80 (bottom), as shown on the right.	
Figure 5.12	The top example shows the wrong path that can be formed if proper criteria are not taken in tracing the boundary (usually happens in connectivity-based algorithms). The bottom example shows the correct path that must be traced for a valid polygon formation.	203
Figure 5.13	Minimum-difference algorithm to trace Hamiltonian-contour between nodes of a tissue polygon (CW: counterclockwise; CCW: counterclockwise; P#: priority to select node based on direction). The above plot is for a sum-of-differences (SD) of 1 and the plot below is for SD 2	204
Figure 5.14	Examples showing the results of <i>edging.m</i> and <i>boundary_trace.m</i> after the lists of nodes making a Hamiltonian Contour are obtained.	205
Figure 5.15	Examples showing various detected holes that are basically a small polygon within a bigger polygon (the bigger polygon's material is different from that of the smaller). These holes do not have shared boundaries with polygons of different tissues	206
Figure 5.16	The screen shots showing the polygon formation in HFSS interface using a Visual Basic script. The first and second images in the flow show the muscle and fat polygon constructed while the polygon for fibro-glandular tissue is being traced. The third image shows the transitional-tissue polygon being traced next. The fourth image shows all contiguous tissue polygons constructed.	208
Figure 5.17	The muscle polygon in HFSS.	209
Figure 5.18	The simple GUI layout for PSNBPM.	210

Figure 5.19	Screen shot showing HFSS slice for the MR image and the 3D validation check.	213
Figure 5.20	The voxel-by-voxel construction process in HFSS.	214
Figure 5.21	The screen shot showing the slice in the time-domain solver QWED with information on file sizes. The slice is made by the voxel-by-voxel method.	215
Figure 5.22	The screen shot showing the slice in the time-domain solver QWED with information on file sizes. The slice is made by the CCW Hamiltonian-contour construction method as required in QWED.	216
Figure 5.23	Screen shots showing the SAT file made by unifying 80 slices in HFSS. Muscle and fat for all the slices are unified without modeling error as shown in the bottom screen shot.	218
Figure 5.24	The diagram shows illustrates how fewer segments and nodes (see solid-line contour) can approximate a complex region-of-interest (see red shaded area).	220
Figure 6.1	Antenna structure: (a) the TEM horn with a coaxial feed and the balun; (b) top view of the TEM horn; (c) bottom view of the TEM horn.	226
Figure 6.2	Antenna structure: (a) the TEM horn placed in a dielectric medium with relative permittivity of 10 with copper sheets on all outer surfaces except the front aperture and a microwave absorbing sheet on the top surface; (b) the copper sheet pattern on the top surface; (c) the copper sheet pattern on the bottom surface.	228
Figure 6.3	Simulated and measured insertion loss.	230
Figure 6.4	Measuring the breast phantom when grabbing the antenna directly.	230

Figure 6.5	Antenna structure with meshed coaxial cable with a PEC stub at end.	234
Figure 6.6	Resistive voltage source connected at the end of the inner cylinder. The source is at the centre of the white oval between the inner wire and the coax termination.	234
Figure 6.7	Time waveform ( $E_z$ field) recorded between the horn plates inside the antenna.	238
Figure 6.8	Fidelity along the boresight direction of the antenna as a function of the distance from the aperture.	238
Figure 6.9	The top graph shows the time waveform recorded at probe SP1 and the bottom graph shows the same waveform shifted to coincide with the incident waveform to obtain maximum fidelity.	237
Figure 6.10	Antenna structure in CST which is imported from HFSS.	238
Figure 6.11	Coaxial cable excited with automatic waveguide port template in CST.	239
Figure 6.12	$ S_{11} $ simulated in CST compared to that simulated in HFSS and the measured one.	240
Figure 6.13	Probe set up in CST to record the $E_z$ field time waveforms in the skin and tissue layers.	240
Figure 6.14	Time waveform ( $E_z$ field) recorded between the horn plates inside the antenna.	241
Figure 6.15	Fidelity in the boresight direction of the antenna as a function of the distance from the aperture.	241
Figure 6.16	Four types of scenarios for the derivatives of the objective function $F = 0.5(R - \bar{R})^2$ with respect to a parameter $p$ , which can be expressed as $\partial F / \partial p = (R - \bar{R})\partial R / \partial p$ , where $R$ and $\bar{R}$ are the responses from the forward model and the	246

	measured (target) model.	
Figure 6.17	Cross-section in the $xy$ plane of the: (a) target model and, (b) the corresponding forward model where the red-dash rectangle is the Jacobian computational domain.	248
Figure 6.18	Jacobian maps in the plane $z = 20$ mm at 10 GHz: (a) $\partial F /\partial\epsilon_r$ ; (b) $\partial F /\partial\sigma$ ; (c) $\partial\angle F/\partial\epsilon_r$ ; (d) $\partial\angle F/\partial\sigma$ .	249
Figure 6.19	3-D Jacobian maps: (a) Center Case with the scatterer's center at (20, 20, 20) mm; (b) Right Case with the scatterer's center at (23.5, 20, 20) mm	256

## LIST OF TABLES

TABLE 1.1	PROBABILITY OF BREAST CANCER WITH AGE.	11
TABLE 2.1	CHRONOLOGICAL SUMMARY OF STUDIES PUBLISHED FOR HUMAN BREAST TISSUE BEFORE LAZEBNIK <i>ET AL.</i>	32
TABLE 2.2	COLE-COLE PARAMETERS FOR GROUP 1 FROM REDUCTION SURGERY STUDY.	45
TABLE 2.3	COLE-COLE PARAMETERS FOR GROUP 2 FROM REDUCTION SURGERY STUDY.	45
TABLE 2.4	COLE-COLE PARAMETERS FOR GROUP 3 FROM REDUCTION SURGERY STUDY.	45
TABLE 2.5	COLE-COLE PARAMETERS FOR TISSUE GROUP 1 FROM CANCER SURGERY STUDY.	48
TABLE 2.6	COLE-COLE PARAMETERS FOR TISSUE GROUP 2 FROM CANCER SURGERY STUDY.	49
TABLE 2.7	COLE-COLE PARAMETERS FOR TISSUE GROUP 3 FROM CANCER SURGERY STUDY.	49
TABLE 2.8	COLE-COLE PARAMETERS FOR 49 CANCER SAMPLES THAT CONTAIN 30% OR GREATER MALIGNANT TISSUE CONTENT.	49
TABLE 2.9	FOUR-POLE COLE-COLE MODEL FOR SKIN FROM GABRIEL <i>ET AL.</i>	67
TABLE 2.10	ONE-POLE DEBYE MODEL FOR SKIN FROM WINTERS <i>ET AL.</i>	67

TABLE 2.11	FOUR-POLE COLE-COLE MODEL FOR MUSCLE FROM GABRIEL <i>ET AL.</i>	69
TABLE 2.12	TWO-POLE DEBYE MODEL FOR MUSCLE FROM WUNER <i>ET AL.</i>	70
TABLE 2.13	ONE-POLE DEBYE MODELS FOR THREE ADIPOSE DEFINED NORMAL TISSUE GROUPS AND MALIGNANT TISSUE.	71
TABLE 3.1	A LOOK-UP FOR ALL THE MATERIALS TO BE USED IN RECIPE RATIOS.	98
TABLE 3.2	RECIPE RATIO FOR HWCT-1.	103
TABLE 3.3	RECIPE RATIO FOR HWCT-2.	103
TABLE 3.4	RECIPE RATIO FOR IWCT.	103
TABLE 3.5	RECIPE RATIO FOR LWCT.	103
TABLE 3.6	RECIPE FOR FAT-GEL.	104
TABLE 3.7	RECIPE RATIO FOR MALIGNANT-1	104
TABLE 3.8	RECIPE RATIO FOR MALIGNANT-2	104
TABLE 4.1	COMPARISON OF THE ACTUAL DIMENSIONS WITH THE RECONSTRUCTED DIMENSIONS OF THE 3-D MODELS FOR VARIOUS SHAPES USING PHOTOMODELER.	155
TABLE 5.1	SOME OF THE VARIOUS ATTRIBUTES STORED IN DICOM METADATA.	189
TABLE 6.1	DESIGN PARAMETERS OF ANTENNA.	229
TABLE 6.2	TRUE MINIMA FOR TWO OBJECTIVE FUNCTIONS W.R.T. $\epsilon_r$ OR $\sigma$ IN THE FREQUENCY RANGE FROM 3 GHz TO 10 GHz.	251
TABLE 6.3	AVERAGE TRUE MINIMUM FOR TWO OBJECTIVE FUNCTIONS W.R.T. $\epsilon_r$ OR $\sigma$ .	252
TABLE 6.4	TRUE MINIMA FOR TWO OBJECTIVE FUNCTIONS W.R.T. $\epsilon_r$ OR $\sigma$ IN THE FREQUENCY RANGE FROM 3 GHz TO 10 GHz	254

---

	FOR THE RIGHT CASE.	
TABLE 6.5	AVERAGE TRUE MINIMUM FOR TWO OBJECTIVE FUNCTIONS W.R.T. $\varepsilon_r$ OR $\sigma$ .	255
TABLE 6.6	TRUE MINIMUM IN THE COMBINATION MAPS.	256

# LIST OF SYMBOLS AND ACRONYMS

## Symbols

$\omega$	Frequency in radians
$\epsilon_r$ or $\epsilon'$	Relative permittivity
$\epsilon''$	Dielectric Loss
$\tilde{\epsilon}$	Complex permittivity
$\epsilon_0$	Permittivity of free space
$\epsilon_\infty$	High frequency permittivity
$\epsilon_s$	Low frequency permittivity
$\epsilon_b$	Permittivity of background
$\mu$	Permeability
$\sigma$	Conductivity
$\sigma_s$ or $\sigma_i$	Ionic conductivity



$\theta$	Loss angle
$\delta$	Penetration depth
$F$	Fidelity
$\tau$	Time shift
$d$	Distortion parameter
$F(\varepsilon)$	Objective function based on complex response
$F_M$	Objective function based on magnitude of responses
$F_p$	Objective function based on phase of responses
$S_{ij} (i \neq j)$	Transmission coefficients

### Acronyms

ACR	American College of Radiology
ACS	American Cancer Society
ASTM	American Society of Testing and Materials
BIRADS	Breast Imaging Reporting and Database System
CADD	Computer-Aided Detection and Diagnosis
CAD	Computer-Aided Design
CEM	Computational Electromagnetics
CW	Clockwise
CCW	Counter-clockwise

DICOM	Digital Imaging and Communications in Medicine
DIW	De-ionized Water
EM	Electromagnetic
FEM	Finite Element Method
FDTD	Finite Difference Time Domain
HFSS	High Frequency Structure Simulator
HWCT	High Water Content Tissue
HC	Hamiltonian-contour
IEEE	Institute of Electrical and Electronics Engineers
IWCT	Intermediate Water Content Tissue
LWCT	Low Water Content Tissue
MRI	Magnetic Resonance Imaging
NCI	National Cancer Institute
NEMA	National Electrical Manufacturers Association
PML	Perfectly Matched Layer
PEP	Polyethylene powder
RF	Radio Frequency
S-parameters	Scattering Parameters
SASA	Self-Adjoint Sensitivity Analysis
T1	Relaxation Time Constant in MRI
TEM	Transverse Electromagnetic

TM	Transverse Magnetic
TR	Time of Repetition
UWB	Ultra-Wideband
VSWR	Voltage Standing Wave Ratio
VV	Voxel-by-voxel

# CHAPTER 1

## INTRODUCTION

### 1) MOTIVATION

Breast cancer is the most common cancer among Canadian women, excluding non-melanoma skin cancer. In 2009, an estimated 22,700 women will be diagnosed with breast cancer and 5400 will die of it in Canada [1]. For women in the U.S., breast cancer death rates are higher than those for any other cancer except lung cancer [2].

X-ray mammography remains the primary screening method for detecting early-stage breast tumors. The mammographic technique involves X-ray imaging of a compressed breast. Most cancer societies and studies indicate the presence of a considerable high false positive rate in mammography, such that 10% of the patients screened are recalled for further testing, of which only 2% actually have

cancer. Significant technical advances such as digital mammography, driven in part by the Mammography Quality Standards Act (MQSA), have greatly improved the overall quality and interpretation of mammographic images [4]. Also computer-aided detection and diagnosis (CADD) systems have been incorporated, to aid the radiologists in finding suspicious regions in mammograms. Yet further studies are needed to evaluate their efficacy. Recently, a new three-dimensional (3-D) method called stereoscopic digital mammography has been introduced [6], which, compared with conventional mammography, gives a 3-D view of the inner structures of the breast and reduces the false-positive rate by 49 percent. These developments have had positive effect in increasing the specificity of mammography and bring down the false positive rate. Mammography is the gold standard for wide screening of women over 40 years old, for breast cancer, [3], [8].

The most prevalent invasive breast cancer, invasive ductal carcinoma (IDC), and the non-invasive breast cancer, ductal carcinoma in situ (DCIS), occur in milk ducts, and is associated with random specks of calcium deposits, called micro-calcifications, in the breast. These are best seen in the mammograms compared to any other imaging modality.

Despite the progress and benefits, the drawbacks of mammography include the need for improved sensitivity (*measures the proportion of true positives, e.g., sick patients, which are correctly identified*) and specificity (*measures the proportion of true negatives, e.g., normal patients, which are*

*correctly identified*), as mammography also has a high false negative rate, of up to 20%. A false negative case is where a mammogram appears normal even though a breast cancer is present. Though false positive rate has the drawbacks of creating anxiety and increasing diagnostic costs, but it is still considered an acceptable price paid to prevent this deadly disease. Besides, patients can be educated about the possibility of false alarm. On the other hand, a false negative rate is more detrimental for the loss of lives. Mammograms are particularly difficult to interpret in women with dense breast tissue, which is especially common in young women. The dense tissue interferes with identification of abnormalities associated with tumors in lobular regions or those near to the chest, leading to a higher rate of false test results (both positive and negative) in these women. A negative mammogram does not exclude cancer. For instance, lobular cancer such as the very aggressive, though less occurring, invasive lobular carcinoma (ILC), is very hard to detect from mammograms. It occurs in milk sacs or lobes (a very dense tissue). This cancer has a high incidence of bilateral (*term pertaining to the left and right breasts in a woman*) existence, which mammograms have difficulty to detect. For better understanding, a general structure of the inside of the breast is given in Figure 1.1. The two major kinds of breast cancers with their locations are shown in Figure 1.2. The difficulties associated with dense tissue are especially problematic for women who wish to begin screening at a younger age for being in the high-risk category. The high risk category implies 20% or greater lifetime risk and includes women with: (i) a strong family history of breast and/or ovarian

cancer; (ii) those who are likely or known carriers of the BRCA1 or BRCA2 mutation (a breast and ovarian cancer gene mutation); (iii) women who have lobular carcinoma; (iv) women with very dense breasts; and (v) those who have already had breast cancer [3]-[11].

Most cancer societies recommend less usage of mammography for screening such high-risk patients, especially young women, in order to limit their lifetime radiation dose. The same recommendation holds for the surviving breast cancer patients, who have undergone radiation therapy [3], [7]. This is where another modality known as magnetic resonance imaging (MRI) is a valuable tool. The studies by the American Society of Clinical Oncology (ASCO) [11], concluded that MRI is a more sensitive screening tool in finding cancers than mammography, ultrasound, or clinical breast exams (CBEs). MRI is sensitive to both invasive and non-invasive types of cancers, but is not able to show the micro-calcifications. MRI has a high negative predictive value, implying if nothing is found in an examination, there really is no cancer. However, results also showed that MRI gives a higher number of false positives. The imaging technique is so sensitive that it finds many breast changes taking place in the patients continuously with age and natural menstrual cycles. Often such suspicious growths turn out not to be breast cancer (false positive). This results in many additional tests, biopsies, and increased patient anxiety. Availability and cost are also two other important obstacles to a broader use of breast MRI [7]. A breast MRI can cost \$1,000 to \$1,500, which is ten times the typical cost of

mammography. Also, there are currently not enough radiologists trained in the procedure. The dedicated breast MRI machines are also insufficient in order to provide screening to a larger population of women. Overall, the false positive results remain the biggest impediment to the use of breast MRI in the screening of average-risk women. Hence, for the average-risk women, the harms of MRI outweigh the risks [7]. Yearly MRI screening is not recommended for women whose lifetime risk of breast cancer is less than 15% by the American Cancer Society (ACS) [3]. The ACS does recommend that women at average risk for breast cancer should get an annual mammogram starting at age 40, whereas women at high risk should get an MRI and a mammogram every year beginning at age 30 [3]. Though it is very routine and safe for most patients, it is important to mention that MRI requires a contrast agent called gadolinium, which is not recommended to be used by patients who have kidney disease. This is, however, debatable and studies are required to confirm these safety concerns.

Another popular imaging modality is ultrasound. It can only be used as an adjunct to mammography as it is effective for evaluating cysts vs. solid tumors. It is not very specific as a standalone modality. Also, ultrasound is highly operator dependent, leading to false negatives. It is usually used during biopsies.



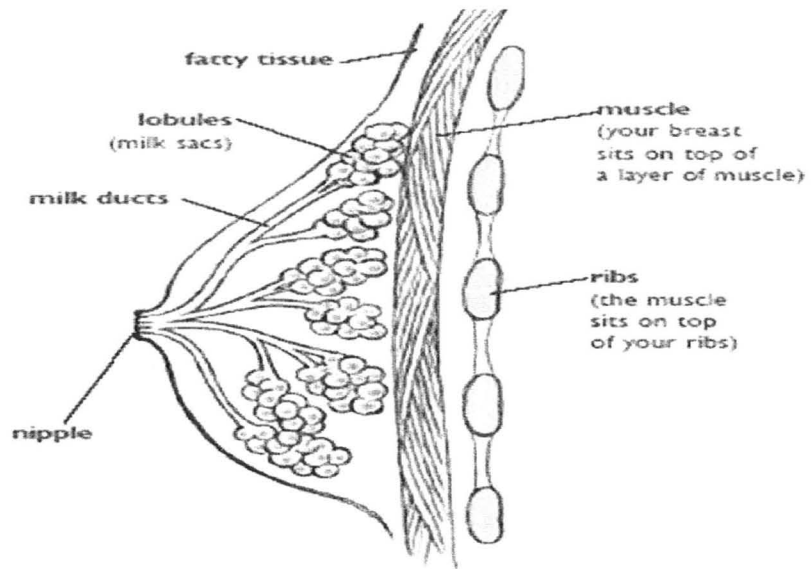


Figure 1.1: The inside of the breast (from [5]).

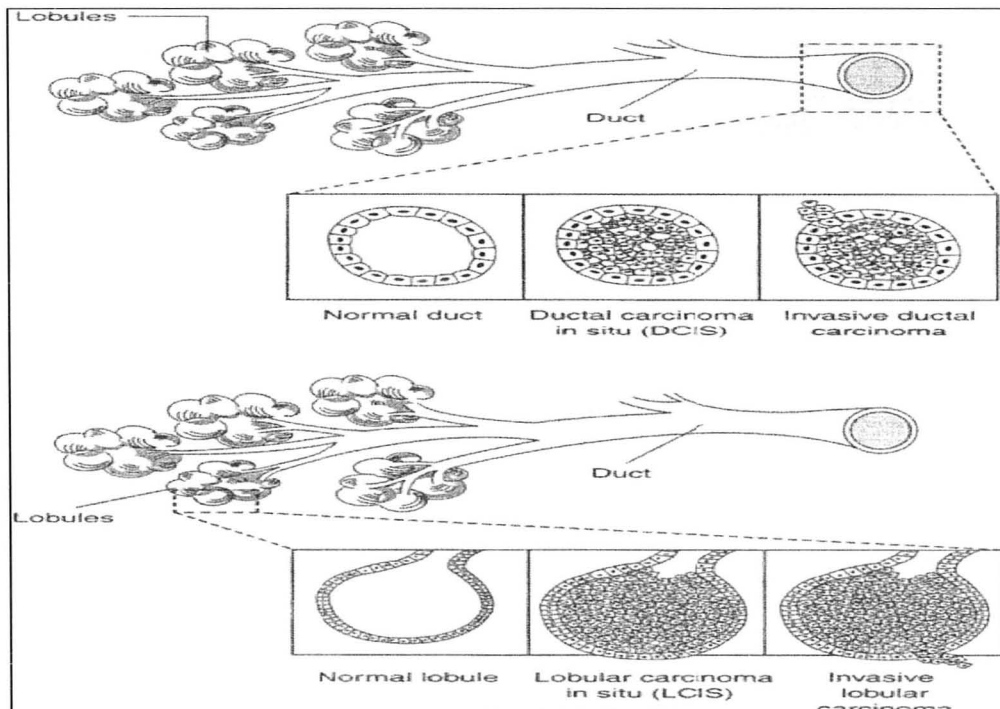


Figure 1.2: Schematic representation of ductal (top) and lobular (bottom) carcinoma of the breast (from [4]).

Microwave imaging is a promising new technique under research for early breast cancer detection [20]. It relies on a sufficient contrast between the dielectric properties of normal and malignant breast tissues at microwave frequencies [12]-[19]. Though earlier studies indicated a high contrast in the relative permittivity of a malignant tumor compared to the healthy tissue (due to high water content), it proved to be mostly in comparison with fat. The recent studies have shown that malignant regions are hypo-conductive compared to the surrounding breast tissue. This is to be expected as malignant breast cells gather calcium ions from breast milk and have other unique features associated with malignancy and metastasis such as vascularization or angiogenesis. Through these features malignant cells develop their own blood supply system to provide nutrients to growing cancer cells. This in turn implies that there is a lot of ionic flow in the malignant region. Thus, a detection technique exploiting this contrast can achieve sufficient specificity to diagnose malignancy. Following are some key points that exemplify the motivation to develop microwave imaging as malignancy imaging modality in breast:

- The technique will have high resolution because it is based on microwaves with frequency above 3 GHz and it aims at detecting sub-centimeter tumors.
- The imaging should be able to discriminate a healthy breast from the one with malignancy. Once robust, this will be highly specific modality to aid existing imaging modalities and cut back false rates.
- The modality should work with all kinds of malignancy as cancer cells

either in ducts or in lobules portray similar dielectric contrast.

- It uses non-ionizing radiation, and the detection modality once developed can be used to screen high-risk younger patients, aiding early detection of malignancy. Early detection implies higher survival rates.
- Patient imaging can be done as frequently as needed.
- The modality depends on natural contrast in dielectric properties and requires no external agents.
- The technique should be cost effective and cheaper compared to MRI and mammography.
- Microwave imaging requires microwave equipment and computer algorithms for detection. This puts less pressure on the operators and users and hence there are fewer propensities of operator dependent mistakes.
- The imaging procedure requires a slight compression just to prevent motion of the breast during microwave measurements, which is not as uncomfortable as in mammography.

All these positive aspects that microwave imaging brings to the table are promising. With more research and improvement of the technique accompanying successful clinical trials, it can progress to become a wide screening method that is safe, specific and reasonably inexpensive. However, to create this modality, it requires novel solutions in terms of both hardware and algorithms.

Current research in active microwave breast imaging can be divided into two main categories: microwave tomography [21]-[25], and ultra-wideband

(UWB) radar [26]-[31].

In tomographic breast imaging, the scattered microwave signals are usually measured in a phase-coherent way (complex  $S$ -parameters) using a vector network analyzer (VNA). The image reconstruction involves the solution of a nonlinear optimization problem whereby the permittivity profile of the imaged domain is reconstructed.

In radar-based imaging, the breast is illuminated with an ultra wide-band (UWB) pulse, and the backscattered signal is recorded for a number of antenna positions, followed by post-processing algorithms to get the tumor signature.

Both approaches are complicated mostly due to the unknown and patient-specific breast shape and tissue distribution. Most reported results with these techniques are in simulations and measurements with very simple and canonical structures. The phantoms in the experiments and the simulations are mostly homogenous whereas it is known that human breast is an extremely heterogeneous environment. Hence, when a patient's breast is examined with the optimized imaging set-up, obtained from simulations, it cannot perform well due to unknown clutter sources from the breast itself. Also, as seen before, most cancers occur in fibro-glandular or connective tissue (ducts and lobules). There, the range of contrast in the dielectric properties of malignant vs. the surrounding healthy tissue becomes very low [17]. If the optimization and detection algorithms are burdened with reconstruction of shape, volume and dielectric properties of the imaged breast, the convergence can easily fail. This makes the hardware

complicated, as seen in current scanning systems for both radar and tomographic approaches. However, if a good initial model of the patient's breast is used in electromagnetic (EM) simulations, the reconstruction algorithms become reliable. The work represented in this thesis is an attempt to provide the best possible initial patient-specific breast model for microwave imaging through simulations and experiments.

The first step in this work was to have a novel and simple approach to acquire breast shape and size at the time of the microwave measurements. This was done with a photogrammetry-based in-house system, designed by our group. It converts 2-D images from a camera to a 3-D structure. This method can also provide the exact mutual location and orientation of the imaged breast with respect to the antenna elements. The knowledge of the surface shape of the imaged object can bring great benefits to both radar-based and tomographic microwave imaging approaches. In the former case, it provides the exact shape and location of the skin interface with respect to the imaging array thus making the identification of skin-clutter signal components much easier in comparison with all currently existing approaches. In the latter case, it clearly identifies the surface of the volume where permittivity reconstruction must take place. This will be discussed further in chapter 4 of the thesis. Also, phantoms to mimic the average breast tissue were made both for the experiments for shape acquisition as well as for the forward electromagnetic (EM) models, which must be tuned to match the measurements.

The second step towards a patient-specific breast model is the modeling of the interior tissue composition. The main tissues that are important in the model are fat, skin, muscle or chest wall, fibro-glandular tissue that includes ducts and lobules, and transitional tissue that surrounds the fibro-glandular tissue and connects with fat. Blood supply forms 2% to 3% of the breast and its effect is accounted for by the water content of these tissues.

The tissue identification is required to make reliable and high-fidelity numerical phantoms in the EM simulations, which play a central role in the reconstruction algorithms. The patient-specific breast model must include age as a criterion as there are changes in the composition of the breast as a woman gets older. Also the chance of acquiring breast cancer becomes higher with age. A woman's chance of being diagnosed with breast cancer depending on age is given by the National Cancer Institute (NCI) as shown in Table 1.1 [9].

TABLE 1.1: PROBABILITY OF BREAST CANCER WITH AGE.

Age (in years)	Probability (as %)	Probability (as occurrence)
30-39	0.43	1 in 233
40-49	1.44	1 in 69
50-59	2.63	1 in 38
60-69	3.65	1 in 27

Two categories are prominent with age as a factor: (a) pre-menopausal or women of age less than 50 years; and (b) post-menopausal or women of age more than 50 years. It is observed that a patient undergoes many changes during post-menopause that increase the risk for acquiring cancer.

Another classification is based on the breast composition with regard to density. Breast Imaging Reporting and Database System (BI-RADS®) is a quality assurance guide issued by the American College of Radiology (ACR) [10] to standardize breast imaging and classification for mammography, ultrasound and magnetic resonance imaging (MRI). According to BI-RADS®, the consistent classification of the breast composition for all patients, should use the following pattern [10]:

- The breast is almost entirely fat (< 25 % glandular).
- There are scattered fibro-glandular densities (approximately 25%-50% glandular).
- The breast tissue is heterogeneously dense, which could obscure detection of small masses (approximately 51%-75% glandular).
- The breast tissue is extremely dense. This may lower the sensitivity of mammography (>75% glandular).

Based on these classifications, eight patient specific categories are used to set up a data base, two for age and four for composition. The source of these numeric models are T1 weighted MR images. They will be discussed in detail in chapter 5. This work is essential to test novel detection algorithms and to optimize

them for a real-case situation in the microwave imaging of the breast.

## 2) **OUTLINE OF THESIS**

We aim to probe into various issues related to representing as accurate as possible breast models both in simulations and experiments. These issues and their suggested solutions with some contributions will be discussed within the following chapters.

Chapter 2 starts by reviewing the various research studies on the dielectric properties of the major tissues of the breast from 10 Hz to 35 GHz, for instance by Gabriel *et al.* [14] and Joines *et al.*[15]. A major most recent study on breast-tissue electrical properties is reported by Lazebnik *et al.* [16]-[17] from 0.5 GHz to 20 GHz. This study is based on excised human breast tissue obtained from breast reduction surgeries and cancer surgeries at the University of Wisconsin and the University of Calgary hospitals. Using methodical experimentation and protocol techniques, the inconsistencies of the previous works (compiled both by Sha *et al.* [18] and Lazebnik *et al.* [16]) are overcome. Also, efficient statistical tools for data fitting (such as Cole-Cole model), were used to establish a database for the dielectric properties of normal breast tissue as compared with dielectric properties of the diseased and malignant breast tissue. It has been concluded that the main tissues important to model heterogeneous interior of a healthy human breast tissue in a microwave simulation are: adipose fat, glandular tissue and transitional tissue, besides chest wall and skin. This chapter is



concluded with the latest first-order simple Debye model applicable in the frequency band from 3.1 GHz to 10.6 GHz, which is obtained by fitting to the experimental data by the Wisconsin group [19].

Chapter 3 discusses the main recipes that we are using currently in experiments to simulate a single tissue such as skin, fat and tumor, with electrical properties close to those discussed in chapter 2. These recipes have been prepared with non-biological materials, as biological material (mostly from animals), though similar to human tissue, have much shorter shelf life and may contain air sacs, which leads to problems during microwave experiments. The phantoms prepared from our recipes are solid. There is an intention to increase the complexity of these phantoms by incorporating various tissues in one solid phantom. The chapter shows some images of the phantoms and the electrical properties measured with the Agilent Dielectric Performance Probe [41].

Chapter 4 shows the development related to the novel approach of surface shape acquisition for any randomly shaped object. It is to be expected that the shape and size of the breast varies drastically among patients. Here, we propose a photogrammetry method for the accurate reconstruction of the surface shape of an imaged object, i.e., breast, at the time of the microwave measurement. The approach can also provide the exact mutual location and orientation of the imaged breast with respect to the antenna elements. The knowledge of the surface shape of the imaged object can bring great benefits to both radar-based and tomographic microwave imaging approaches. In radar-based imaging, knowing the shape and

size of the breast as well as its relative position with respect to the imaging array will lead to more accurate skin-artefact removal. In tomographic imaging, this knowledge will reduce drastically the dimensionality of the inverse problem, thus leading to faster convergence and reduction of the number of local minima. This greatly simplifies the complexity of the inversion procedure. The accuracy of the surface reconstruction of the object through photogrammetry is better than  $\pm 1$  mm. The approach is simple to implement and is automated. It requires conventional cameras and the related software is commercially available. Accuracy assessment of our system is described in this chapter. It also illustrates the method with results of the reconstructed models and frequency-domain experiments in the forward model.

Chapter 5 starts by discussing the need to represent as accurately as possible the interior of the patient's breast for better convergence of the algorithms in both direct and tomographic approaches. This is a challenging job and is essential to make microwave imaging a standalone cancer detection system. The realistic solution has been given in this chapter. The source of numerical breast models is a set of T1 weighted magnetic resonance images (MRI). These 2-D images are converted into dielectric maps by segmentation using the tissue composition and the dielectric properties given by the latest study on breast tissues, discussed in chapter 2. The patient categorization comprises eight categories based on the patient age and on the BI-RADS<sup>®</sup> (Breast Imaging Reporting and Data System) classification. The software to produce such patient-specific breast models is

designed in MATLAB [39] and includes a simple graphical user interface (GUI). This is a first attempt at making this sort of software. It can be enhanced with more interface tools, MRI sets and probability studies in the future. The software has been named “Patient Specific Numerical Breast Phantom Modeller” (PSNBPM).

Chapter 6 discusses some contributions made to the numerical modeling by the author. The chapter reports the results for fidelity characteristics evaluated for the newly designed sensor by our group. Also, suitable way has been found to compose an objective function for sensitivity based algorithm and produce images of a scatterer in simple structures with Jacobian maps. The simulations have been done with time domain solvers.

The thesis concludes with results achieved and suggestions for future research in chapter 7. For convenience, a summary of all bibliography is given at the end of the thesis.

### **3) CONTRIBUTIONS**

The author contributed substantially to the following original developments presented in this thesis:

- I. Established a novel method to shape acquisition with photogrammetry and contributed to make an in-house built system. This method received successful acceptance at two major international conferences [34]-[35].
- II. Phantoms were prepared for forward analysis and experiments. These

- phantoms were also used for antenna testing [36]. The main recipe and many other relevant research topics are discussed in a technical report [33].
- III. Developed a procedure to convert T1 weighted MR images to segmented dielectric maps, which are further converted to CAD models for EM simulators such as Ansoft HFSS ver. 11 [40]. This is done with a generic program written in MATLAB.
  - IV. In a process to create a database of 3-D CAD models from MR images for eight categories of patients based on age and density classification.
  - V. Components contributed to numerical models such fidelity calculation of the newly designed UWB antenna to be used in the imaging set-up by the group [38].
  - VI. Contributed to the development of an objective functions for the SASA tool for detection of scatterers in a known background medium. This has been presented in [37].

## REFERENCES

- [1] (April 2009). Breast Cancer Statistics 2009. Canadian Cancer Society, Toronto, ON. [Online]. Available: [http://www.cancer.ca/canada-wide/about%20cancer/cancer%20statistics/stats%20at%20a%20glance/breast%20cancer.aspx?sc\\_lang=en](http://www.cancer.ca/canada-wide/about%20cancer/cancer%20statistics/stats%20at%20a%20glance/breast%20cancer.aspx?sc_lang=en)
- [2] (November 2008). Breast Cancer Statistics. Breastcancer.org (BCO). [Online]. Available: [http://www.breastcancer.org/symptoms/understand\\_bc/statistics.jsp](http://www.breastcancer.org/symptoms/understand_bc/statistics.jsp).
- [3] (September 2008). Mammograms and other Breast Imaging Procedures. American Cancer Society (ACS). [Online]. Available:

- [http://www.cancer.org/docroot/PED/content/PED\\_2\\_3X\\_Mammography\\_and\\_Other\\_Breast\\_Imaging\\_Procedures.asp](http://www.cancer.org/docroot/PED/content/PED_2_3X_Mammography_and_Other_Breast_Imaging_Procedures.asp).
- [4] National Academy Press. (2001). *Mammography and Beyond: Developing Techniques for the Early Detection of Breast Cancer*. Institutes of Medicine, Washington, DC. [Online]. Available: [http://books.nap.edu/openbook.php?record\\_id=10107&page=9](http://books.nap.edu/openbook.php?record_id=10107&page=9).
- [5] (February 2008). National Breast and Ovary Cancer Center, Australia. [Online]. Available: <http://www.breasthealth.com.au/types/preinvasive.html>.
- [6] M. Kerr. (November 2007). 3-D mammography cuts false-positive rates by half. Reuter Health, Chicago. [Online]. Available: <http://www.reuters.com/article/healthNews/idUSCOL97439820071129>.
- [7] S. Boyles. (August 2007). MRI detects early breast cancer cells. WebMD Health News. [Online]. Available: <http://www.medicinenet.com/script/main/art.asp?articlekey=83133>.
- [8] (April 2007). Screening Mammograms: Questions and Answers. National Cancer Institute (NCI). [Online]. Available: <http://www.cancer.gov/cancertopics/factsheet/Detection/screening-mammograms>.
- [9] (May 2006). Probability of Breast Cancer in American Women. National Cancer Institute (NCI). [Online]. Available: <http://www.cancer.gov/cancertopics/factsheet/Detection/probability-breast-cancer>.
- [10] (November 2008). The American College of Radiology BI-RADS® ATLAS and MQSA: Frequently Asked Questions. American College of Radiology (ACR). [Online]. Available: [http://www.acr.org/SecondaryMainMenuCategories/quality\\_safety/BIRAD\\_SAtlas/BIRADSFAQs.aspx](http://www.acr.org/SecondaryMainMenuCategories/quality_safety/BIRAD_SAtlas/BIRADSFAQs.aspx).
- [11] (October 2003). MRI vs. Mammography: Which is better for screening women at high risk of breast cancer? National Cancer Institute (NCI). [Online]. Available: <http://www.cancer.gov/clinicaltrials/results/mri-vs-mammography0603>.
- [12] S. S. Chaudhary, R. K. Mishra, A. Swarup, and J. M. Thomas, “Dielectric properties of normal and malignant human breast tissues at radiowave and microwave frequencies,” *Indian J. Biochem. Biophys.*, vol. 21, pp. 76 – 79,

February 1984.

- [13] J. Surowiec, S. S. Stuchly, J. R. Barr, and A. Swarup, “Dielectric properties of breast carcinoma and the surrounding tissues,” *IEEE Trans. Biomed. Eng.*, vol. 35, pp. 257 – 263, April 1988.
- [14] S. Gabriel, R. W. Lau, and C. Gabriel, “The dielectric properties of biological tissues: II. Measurements on the frequency range 10 Hz to 20 GHz,” *Phys. Med. Biol.*, vol. 41, no. 11, pp. 2251 – 2269, November 1996.
- [15] W. T. Joines, Y. Zhang, C. Li, and R. L. Jirtle, “The measured electrical properties of normal and malignant human tissues from 50 to 900 MHz,” *Med. Phys.*, vol. 21, pp. 547 – 550, April 1994.
- [16] M. Lazebnik, L. McCartney, D. Popovic, C. B. Watkins, M. J. Lindstorm, J. Harter, S. Sewall, A. Magliocco, J. H. Brooske, M. Okoniewski and S. C. Hagness, “A large – scale study of the ultra wideband microwave dielectric properties of normal breast tissue obtained from reduction surgeries,” *Phys. Med. Biol.*, vol. 52, pp. 2637 – 2656, April 2007.
- [17] M. Lazebnik, L. McCartney, D. Popovic, C. B. Watkins, M. J. Lindstorm, J. Harter, S. Sewall, A. Magliocco, J. H. Brooske, M. Okoniewski and S. C. Hagness, “A large-scale study of the ultrawideband microwave dielectric properties of normal, benign and malignant breast tissues obtained from cancer surgeries,” *Phys. Med. Biol.*, vol. 52, pp. 6093 – 6115, October 2007.
- [18] L. Sha, E. R. Ward, B. Story, “A review of dielectric properties of normal and malignant breast tissue,” *Proc. IEEE Southeast Conf.*, pp. 457 – 462, 2002.
- [19] M. Lazebnik, M. Okoniewski, J. H. Brooske, S. C. Hagness, “Highly accurate Debye models for normal and malignant breast tissue dielectric properties at microwave frequencies,” *IEEE Microwave and Wireless Components Letters*, vol. 17, no. 12, pp. 822 – 824, December 2007.
- [20] E. C. Fear and M. A. Stuchly, “Microwave detection of breast cancer,” *IEEE Trans. Microwave Theory Tech.*, vol. 48, no. 11, pp. 1854 – 1863, 2000.
- [21] P. M. Meaney, M. W. Fanning, D. Li, S. P. Poplack, and K. D. Paulsen, “A clinical prototype for active microwave imaging for the breast,” *IEEE Trans. Microwave Theory Tech.*, vol. 48, no. 11, pp. 1841 – 1853, November 2000.

- 
- [22] A. E. Bulyshev, S. Y. Semenov, A. E. Souvorov, R. H. Svenson, A. G. Nazarov, Y.E. Sizov and G. P. Tatsis, “Computational modeling of three-dimensional microwave tomography of breast cancer,” *IEEE Trans. Biomed. Eng.*, vol. 48, no. 9, pp. 1053 – 1056, September 2001.
- [23] Q. H. Liu, Z. Q. Zhang, T. T. Wang, J. A. Bryan, G. A. Ybarra, L. W. Nolte, and W. T. Joines, “Active microwave imaging I — 2-D forward and inverse scattering methods,” *IEEE Trans. Microwave Theory Tech.*, vol. 50, no. 1, pp. 123 – 133, January 2002.
- [24] Z. Q. Zhang, Q. H. Liu, C. Xiao, E. Ward, G. Ybarra, and W. T. Joines, “Microwave breast imaging: 3-D forward scattering simulation,” *IEEE Trans. Biomed. Eng.*, vol. 50, no. 10, pp. 1180 – 1189, 2003.
- [25] T. Rubæk, P. M. Meaney, P. Meincke, and K. D. Paulsen, “Nonlinear microwave imaging for breast-cancer screening using gauss–newton’s method and the CGLS inversion algorithm,” *IEEE Trans. Antennas Propagat.*, vol. 55, no. 8, pp. 2320 – 2331, 2007.
- [26] X. Li, E. J. Bond, B. D. Van Veen and S. C. Hagness, “An overview of ultra-wideband microwave imaging via space-time beamforming for early-stage breast-cancer detection,” *IEEE Antennas Propagat. Mag.*, vol. 47, pp. 19 – 34, February 2005.
- [27] X. Li, S. K. Davis, S. C. Hagness, D. W. Weide and B. D. Van Veen, “Microwave imaging via space–time beamforming: experimental investigation of tumor detection in multilayer breast phantoms,” *IEEE Trans. Microwave Theory Tech.*, vol. 52, pp. 1856 – 1865, August 2004.
- [28] X. Li and S. C. Hagness, “A confocal microwave imaging algorithm for breast cancer detection,” *IEEE Microwave Wireless Compon. Lett.*, vol. 11, no. 3, pp. 130 – 132, 2001.
- [29] E. J. Bond, S. C. Hagness, and B. D. Van Veen, “Microwave imaging via space-time beamforming for early detection of breast cancer,” *IEEE Trans. Antennas Propagat.*, vol. 51, no. 8, pp. 1690 – 1705, 2003.
- [30] J. M. Sill and E. C. Fear, “Tissue sensing adaptive radar for breast cancer detection—experimental investigation of simple tumor models,” *IEEE Trans. Microwave Theory Tech.*, vol. 53, pp. 3312 – 3319, November 2005.
- [31] X. Li, S. K. Davis, S. C. Hagness, D. W. V. Weide, and B. D. Van Veen, “Microwave imaging via space-time beamforming: experimental investigation of tumor detection in multilayer breast phantoms,” *IEEE*

---

*Trans. Microwave Theory Tech.*, vol. 52 no. 8, pp. 1856 – 1865, 2004.

- [32] A. Trehan, “3-D reconstruction of curved objects from 2-D images: recovery of breast shape,” Computational Electromagnetics Res. Lab., McMaster University, CEM-R-33, August 2006.
- [33] A. Trehan, “Summary of materials and recipes available in the literature to fabricate biological phantoms for RF and microwave experiments,” Computational Electromagnetics Res. Lab., McMaster University, CEM-R-45, August 2008.
- [34] A. Trehan, R. K. Amineh, M. S. Georgiev, and N. K. Nikolova, “Photogrammetry-based surface reconstruction for improving microwave breast tumor detection,” *Proc. of 24th Int. Review of Progress in Applied Computational Electromagnetics (ACES)*, March 2008.
- [35] A. Trehan, R. K. Amineh, M. S. Georgiev, and N. K. Nikolova, “Accuracy assessment of photogrammetry surface reconstruction for improving microwave imaging,” *IEEE International Symposium on Antennas and Propagation (APS)*, July 2008.
- [36] R. Khalaj Amineh, A. Trehan, and N. K. Nikolova, “TEM horn antenna for ultra-wide band microwave breast imaging,” *Progress In Electromagnetics Research B*, vol. 13, 59 – 74, 2009.
- [37] N.K. Nikolova, L. Liu, and A. Trehan, “Adjoint sensitivities in microwave imaging and design tuning,” Workshop on EM-Based Microwave Optimization Technology: State of the Art and Applications, *IEEE MTT-S Int. Symposium* (Boston, MA), June 2009.
- [38] A. Trehan, “Fidelity evaluation of a novel UWB TEM horn antenna,” Computational Electromagnetics Res. Lab., McMaster University, May, 2009.
- [39] MATLAB™ 7.1, The MathWorks Inc., 3 Apple Hill Drive, Natick, MA, 2005. [Online]. Available: <http://www.mathworks.com/>.
- [40] Ansoft HFSS ver. 11, Ansoft Corporation, 225 West Station Square Drive, Suite 200, Pittsburgh, PA 15219 USA, 2008. [Online]. Available: <http://www.ansoft.com>.
- [41] Agilent ADS, Agilent Technologies, 1400 Fountaingrove Parkway, Santa Rosa, CA 95403-1799, USA. [Online]. Available: <http://www.home.agilent.com/agilent/home.jsp?cc=US&lc=eng>.



## **CHAPTER 2**

# **ELECTROMAGNETIC (EM) PROPERTIES OF HUMAN BREAST TISSUES – A LITERATURE REVIEW**

### **INTRODUCTION**

As breast cancer is on the rise, the science and engineering communities are looking to find more advanced methods for early detection of the malignant breast tumors. A budding technology in this area is the use of the non-ionizing microwave radiation. The high-frequency range of interest is from 0.9 GHz to 10 GHz. The band allocated from 3.1 GHz to 10.6 GHz for ultra-wideband (UWB) medical imaging applications by the Federal Communications Commission (FCC)

is considered promising due to a compromise between penetration depth and resolution.

The diagnostic efficacy of the microwave breast cancer detection depends on the contrast in the dielectric properties of normal and malignant breast tissues. To make the detection of the small malignant tumors reliable, a dependable database of the dielectric properties of the healthy breast tissue is essential. Studies have been carried out to establish the normal breast morphology, the electromagnetic properties of various breast tissues, the factors that affect the breast composition, and the electromagnetic properties and shapes of the malignant tumors.

The early studies claim that the contrast in the dielectric properties of healthy breast tissues as compared to the malignant tissues is significant, especially for the mammary gland. This motivated the development of techniques that use non-ionizing radio waves in detecting malignant tumors, collectively called active microwave imaging (AMWI). However, these early studies were small-scale and amateurish.

This chapter aims at summarizing these early studies and discussing in more detail the recent studies. These studies also suggest simple models for use in the ultra-wideband (UWB) frequency range from 3.1 GHz to 10.6 GHz. Such models are important in the development of numerical and physical breast phantoms for use in experimental and algorithmic evaluation of pre-clinical AMWI techniques.

The chapter is divided as follows. Section 1 presents the theory of dielectric

properties and the models used in experiments to fit the measured data. Section 2 reviews briefly the old studies along with related methods and discrepancies. It then presents a compilation of the latest data on the dielectric properties of various human breast tissues by a recent large-scale study. It also outlines the methodology and the assumptions the new study made. Section 3 gives simple models for all major tissue groups that can be used for numerical and physical breast phantoms. Section 4 gives a brief summary of the mechanisms that explain possible differences between malignant and normal breast tissues.

## 1) DIELECTRIC PARAMETERS AND MODELS

From an electromagnetic point of view, the biological tissues can be described as lossy dielectrics. The biological medium is also characterized by strong frequency dispersion. Figure 2.1 represents a typical variation of the real and imaginary parts of the relative permittivity as a function of frequency in a wide range. It also indicates the various processes that influence a particular segment of the frequency range.

According to Kramer and Kronig's formula, when the permittivity varies as a function of frequency, it must be a complex function of frequency. Furthermore, its real part can be calculated from the variation of the imaginary and vice versa. These relationships are [2]:

$$\begin{aligned}\varepsilon'(\omega) &= \varepsilon_s + \frac{2}{\pi} \int_0^{\infty} \frac{x\varepsilon''(x)}{x^2 - \omega^2} dx \\ \varepsilon''(\omega) &= -\frac{2\omega}{\pi} \int_0^{\infty} \frac{\varepsilon'(x) - \varepsilon_{\infty}}{x^2 - \omega^2} dx\end{aligned}\quad (1)$$

where  $\varepsilon_s$  and  $\varepsilon_{\infty}$  are the values of the relative permittivity at frequencies zero and infinity, respectively, and  $\omega$  is the angular frequency.

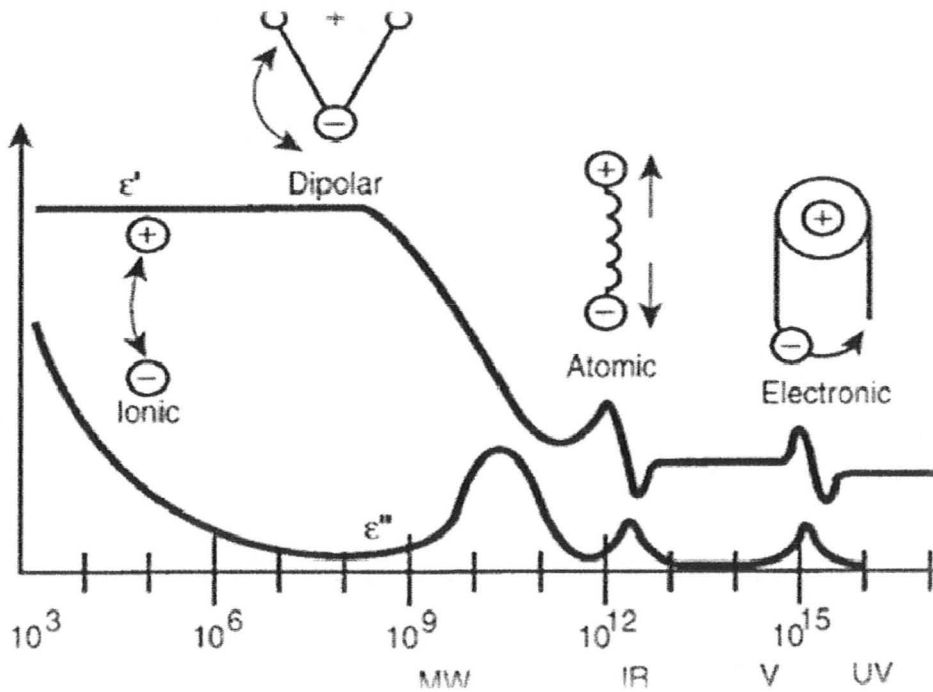


Figure 2.1: Typical frequency dependence of the dielectric permittivity of biological tissues over a wide range of frequencies; where  $\varepsilon'$  and  $\varepsilon''$  denote the real and the imaginary part of the complex permittivity, respectively. Various processes are labeled on the image as ionic, dipolar relaxation, atomic and electronic resonances (from [1]).

The complex function for the relative permittivity is therefore written as [3]:

$$\hat{\epsilon} = \epsilon_r' - j\epsilon_r'' \quad (2)$$

The real part is called the dielectric constant and the imaginary part is a measure of the dielectric losses. These are often expressed as the tangent of the loss angle  $\theta$ :

$$\tan \theta = \frac{\epsilon_r''}{\epsilon_r'} = \frac{\sigma}{\omega \epsilon_r' \epsilon_0} \quad (3)$$

where  $\sigma$  is the electrical conductivity in S/m. From (3), the effective conductivity at any frequency is evaluated as:

$$\sigma_{eff} = \omega \epsilon_0 \epsilon_r'' \quad (4)$$

where  $\epsilon_0$  is the permittivity of free space. Hence it can also be said that the Kramer-Kronig equations [see (1)] relate the conductivity of the biological tissues to their permittivity.

Another related parameter is the skin or penetration depth  $\delta$ :

$$\delta = \left( \frac{1}{\omega} \right) \left\{ \left( \frac{\mu \epsilon}{2} \right) \left[ \left( 1 + \left( \frac{\sigma}{\omega \epsilon} \right)^2 \right)^{1/2} - 1 \right] \right\}^{1/2} \quad (5)$$

From (5), it is clear that higher frequencies imply smaller penetration. Hence, for medical applications with microwaves, the frequency range has to be chosen carefully.

The phenomenon of permittivity, conductivity, and/or permeability varying as a function of frequency is called dispersion. Biological materials are very dispersive. On the other hand, if a material has non-zero imaginary part of the

permittivity (or the permeability), it exhibits losses and is said to be dissipative (or lossy). It is said that dissipation induces dispersion and vice versa [2]. Water is the major constituent in most tissues, such that it accounts for 80% of the volume of most soft tissues (surrounding tissues as fat, muscle etc.). It is called biological water. It is the dipolar relaxation (shown as a process in the microwave range in Figure 2.1) associated with this biological water that determines the dielectric properties of tissues. Dielectric relaxation is the result of the movement of dipoles or electric charges due to a changing electric field in the frequency range from few megahertz (MHz) to a few gigahertz (GHz) [1]. It is a slow process and takes time to reach equilibrium called relaxation time. The relaxation time of water in tissues is generally longer than that of the pure liquid [2].

There are three major dispersion regions where the value of the permittivity is varying strongly with frequency called alpha, beta, and gamma, at relaxation frequencies in the ranges of kilohertz (KHz), hundreds of KHz, and gigahertz (GHz), respectively. The permittivity undergoes almost monotonous decrease over the entire frequency range. As also seen in Figure 2.1, the astonishingly high value of permittivity at very low frequencies (ELF), due to alpha dispersion, is largely attributed to counter ion diffusion effects [2]. For engineering applications, the alpha dispersion has little significance [4]. Beta dispersion occurs at radio-frequencies (RF) and arises principally from the charging of cellular membranes, with smaller contributions from the protein constituents and ionic diffusion along surfaces in the tissue. The delta dispersion or “UHF (ultra

high frequency) relaxation”, located half way between the beta and gamma regions (roughly a range between 0.1 GHz and 3 GHz), has also been identified [2], [4]. A combination of mechanisms is suggested for this region such as: (i) dipolar relaxation of the water of hydration “bound” to proteins; (ii) a Maxwell-Wager effect (*an effect related to introduction of dispersion due to capacitive charging of the cellular membranes often owing to tissue heterogeneity*) due to ions in the cytoplasm collection against relative nonconductive protein surface; and (iii) rotation of polar side-chains on the protein surface. The relaxation frequency is dominant mostly by bound water (100 MHz - 1000 MHz), protein molecules (40 MHz - 300 MHz) and free water (25 GHz). The gamma dispersion occurs with a center frequency near 25 GHz at body temperature. It is due to the dipolar relaxation of the free and bound water, and to ionic conductivity.

In its simplest form, each of these relaxation regions is the manifestation of a polarization mechanism characterized by a single time constant. To a first-order approximation, this time constant gives the following expression for the complex relative permittivity, also known as the first-order Debye expression [5]:

$$\hat{\epsilon} = \epsilon_{\infty} + \frac{\epsilon_s - \epsilon_{\infty}}{1 + j\omega\tau} \quad (6)$$

Here,  $\epsilon_{\infty}$  is the permittivity at infinite frequencies where  $\omega\tau \gg 1$ ,  $\epsilon_s$  is the permittivity at  $\omega\tau \ll 1$ , and  $\tau$  is the relaxation time constant. The magnitude of the dispersion is described as  $\Delta\epsilon = \epsilon_s - \epsilon_{\infty}$ . For more complicated data fitting, the general multi-pole Debye expression is used:

$$\hat{\epsilon}(\omega) = \epsilon_{\infty} + \sum_n \frac{\Delta\epsilon_n}{1 + j\omega\tau_n} + \frac{\sigma_i}{j\omega\epsilon_0} \quad (7)$$

where  $\sigma_i$  is the static ionic conductivity.

To broaden the multiple contributions to the dispersion model, an alternative to the Debye model is often used in experimental studies and it is called the Cole-Cole equation:

$$\hat{\epsilon} = \epsilon_{\infty} + \frac{\Delta\epsilon}{1 + (j\omega\tau)^{(1-\alpha)}} \quad (8)$$

where the distribution parameter  $\alpha$  is a measure of the broadening of the dispersion. Hence, in the Cole-Cole model the relaxation time constant is distributed. A general multi-pole Cole-Cole model is given as [5]:

$$\hat{\epsilon}(\omega) = \epsilon_{\infty} + \sum_n \frac{\Delta\epsilon_n}{1 + (j\omega\tau_n)^{(1-\alpha_n)}} + \frac{\sigma_i}{j\omega\epsilon_0} \quad (9)$$

These models, with a proper choice of parameters, can be used to predict the dielectric behavior over the desired frequency range for various tissues and are encountered in most experimental studies.

## 2) EXPERIMENTAL STUDIES

The contrast in the dielectric properties between normal and malignant tissues is the basis for diagnostic applications using microwaves [4]. The study of biological tissues has been widely reviewed for electromagnetic dosimetry and cancer detection. Previous reports of substantial contrast in the dielectric



properties of normal and malignant breast tissues across portions of the EM spectrum have invoked interest in non-ionizing microwave techniques for cancer detection. However, the earlier studies [8]-[13] were mostly small-scale and are not all in agreement. The most extensive and recent study has been done in collaboration by the University of Wisconsin-Madison (UW) and the University of Calgary (UC). This study has endeavored to build an extensive database of the dielectric properties for a variety of healthy and diseased breast tissues [6]-[7]. This section refers to all earlier studies, excluding the recent UW-UC study as the ‘Previous Studies’. The UW-UC study is referred to as the ‘Recent Study’.

### 2.1. *Previous Studies*

Sha *et al.* [4] have compiled the dielectric property data on healthy and malignant breast tissues from a number of researchers and presented them in a graphical form, both for high and low frequency regions. For active microwave imaging, the region of interest is the data in the high-frequency range. A comprehensive table, with the major studies done on breast tissues of humans in chronological order, is displayed in Table 2.1. The data is taken from both [4] and [6]. Sha *et al.* [4] reports various data inconsistencies and discrepancies among studies in mean dielectric values of normal and malignant breast tissues. The possible two reasons are given as:

- (a) Limitation in experiments such as collection of samples in physiological saline by Chaudhary *et al.* [9] and frosting/defrosting of malignant samples before measurements by Campbell *et al.* [11]. Also, there is difference among

experiments with *in vivo* as compared to *ex vivo* samples, where Meaney *et al.* [13] reported much higher dielectric properties from clinical trials with dielectric properties reconstruction of patient's breast with microwave tomography. Temperature of the sample was another variant in these studies.

(b) The second problem arises from the inherent challenges of characterizing breast tissue, which is quite heterogeneous. Normal breast tissues are composed of breast fat, connective tissue, glandular tissue, etc. This poses difficulties in determining the true range of tissue-specific properties with probes and techniques limited to larger sensing volumes. For instance, dielectric spectroscopy techniques unavoidably average the dielectric properties throughout the volume traversed by the EM fields [6]. Also, different stages of tumor development will change the tumor's dielectric properties and introduce variability [4].

This inconsistency indicates the importance of using proper sample storage method before experiments and suggests a standardization of the experiment conditions like the sample and environment temperatures, as well as the need to record patients' information for later analysis. Although there were so many conditions out of control in early studies, Sha *et al.* [4] record the following trends as conclusive: (i) malignant tissues have higher mean permittivity and conductivity values than those of normal breast tissues; and (ii) fatty tissues have the lowest mean permittivity and conductivity values.

TABLE 2.1: CHRONOLOGICAL SUMMARY OF STUDIES PUBLISHED FOR HUMAN BREAST TISSUE BEFORE LAZEBNIK *ET AL.* [6] COMPILED FROM [4] AND [6].

Tissue type	Frequency range	No. of patients	Measurement details (temperature)	Reference
<i>Ex vivo</i> normal (adipose) malignant	3-24 GHz	Not available (NA)	Samples inserted into waveguide (37°C)	England <i>et al.</i> (1949) [8]
<i>Ex vivo</i> normal (NA) malignant	3 MHz-3GHz	15	Samples collected in physiological saline; inserted into RX-meter chamber or pressed against probe (25°C)	Chaudhary <i>et al.</i> (1984) [9]
<i>Ex vivo</i> normal (various) malignant	20 KHz-100 MHz	7	Measured input reflection coefficient of samples with coaxial line sensor connected to HP3577 network analyzer (37°C)	Surowiec <i>et al.</i> (1988) [10]
<i>Ex vivo</i> normal (various) malignant	3.2 GHz	37	Resonant cavity perturbation method (24°C)	Campbell <i>et al.</i> (1992) [11]
<i>Ex vivo</i> normal (adipose) malignant	50 MHz-900MHz	12	Samples pressed against open-ended coaxial probe connected to HP8754A network analyzer (24°C)	Joines <i>et al.</i> (1994) [12]
<i>In vivo</i>	900 MHz	5	Clinical microwave breast imaging prototype (37°C)	Meaney <i>et al.</i> (2000) [13]
<i>Ex Vivo</i> malignant, lymph nodes	0.5-30 GHz	12	Samples pressed against open-ended coaxial probe connected to HP8510C (37°C)	Choi <i>et al.</i> (2004) [14]
<i>In vivo</i>	10-900 KHz, 300-900 MHz, near-infrared	23	EM breast imaging using 3 non-invasive modalities (37°C)	Poplack <i>et al.</i> (2004) [15]

## 2.2. *Recent Studies* [6]-[7]

The most recent study on the dielectric properties of the human breast tissues has been done by Lazebnik *et al.* [6]-[7]. The group has published two studies:

(a) The first study is based on the excised human breast tissue obtained from breast reduction surgeries at UW and UC hospitals [6]. The group conducted 488 measurements on normal breast tissue obtained from 93 patients. The breast reduction surgery specimens were quite large and typically included all of the normal tissue types present in the breast. This helped to establish the baseline dielectric properties and the variability degrees for the normal within-patient and between-patient tissues. This study will be referred to as ‘reduction surgery study’ in rest of the chapter.

(b) The second study is based on the excised human breast tissue obtained from breast cancer surgeries such as lumpectomies, mastectomies, and biopsies [7]. The group conducted 319 measurements on tissue specimens from 196 patients. This study will be referred to as ‘cancer surgery study’ in rest of the chapter. In contrast to reduction surgeries, the amount of normal tissue present in the cancer specimens was small and confined to the margins of the specimen. As a validation check, comparison between the dielectric properties of the normal samples obtained from cancer surgeries with the dielectric properties of normal samples obtained from the reduction surgeries was done, and will be discussed later.

Thus, using methodical experimentation and protocol techniques to

overcome the inconsistencies of previous studies, Lazebnik *et al.* [6]-[7] have established a database for the electrical properties of the normal breast tissues that can be compared with the dielectric properties of the malignant breast tissues.

### 2.2.1. Sample and measurement protocol

The term ‘sample’ means the portion of tissue specimen that was selected for dielectric characterization. The tissue handling protocols at UW and UC differed slightly, but the differences were noted and analyzed statistically during data analysis. Care was taken to minimize the desiccation of samples till measurement. The dielectric properties of samples were done over a frequency range of 0.5 GHz to 20 GHz using a precision open-ended coaxial probe technique, where the diameter of the aperture of the probe was 3 mm. This probe was placed in direct contact with the unperturbed sample. As a result, it overcomes some of the challenges of other dielectric spectroscopy techniques (e.g. loaded resonators and loaded waveguides), which require extensive sample preparation and are generally narrowband. The probes were used with Agilent 8720ES and Agilent 8722D vector network analyzer (VNA) at UW and UC, respectively. The tissue composition within the probe’s small sensing region was also quantified in terms of dominant tissue type. This was done by first marking with blank ink the exact site on the tissue surface where the probe was placed. Then the analysis was carried out under a microscope. The samples with black ink mark are shown in Figure 2.2 for the reduction surgery study and in Figure 2.3 for the cancer surgery study.

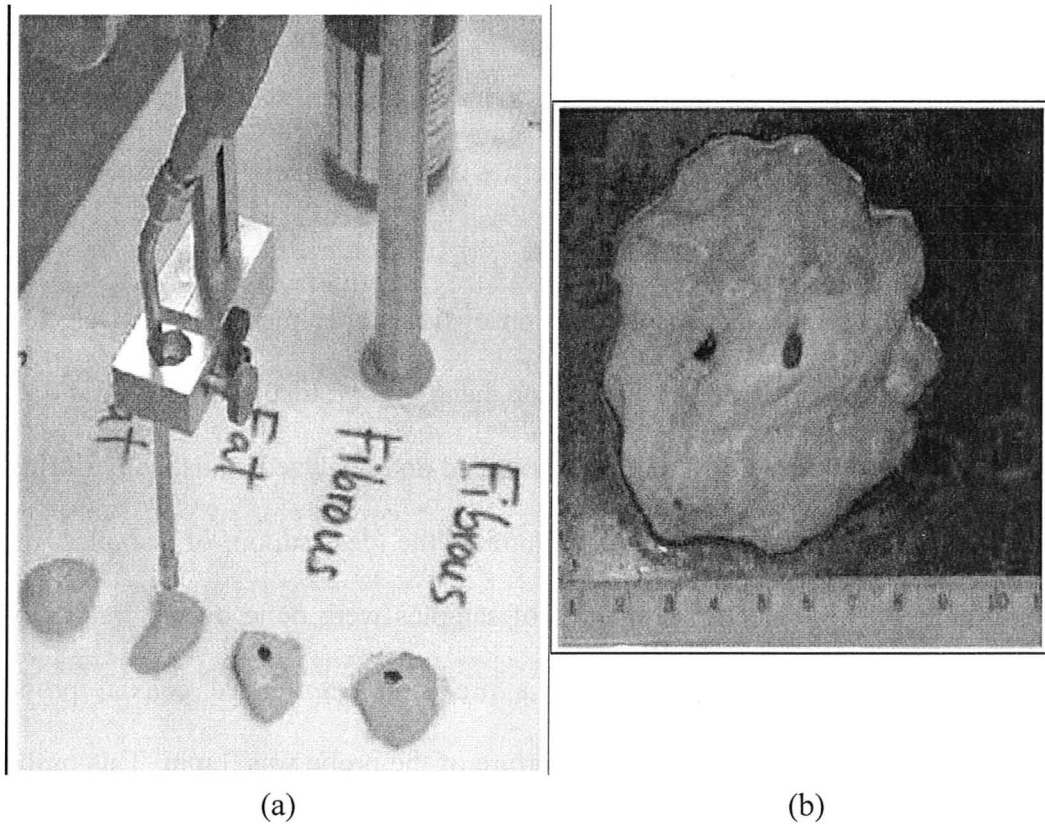


Figure 2.2: Dielectric spectroscopy of freshly excised breast tissue using a precision probe: (a) photograph of individual tissue samples (two adipose and two non-adipose) in the experimental setup at UC; (b) photograph of a UW tissue specimen illustrating the heterogeneous mixture of adipose (yellow) and fibro connective/glandular (white) tissue. The black ink spots mark the measurement sites (from [6]).

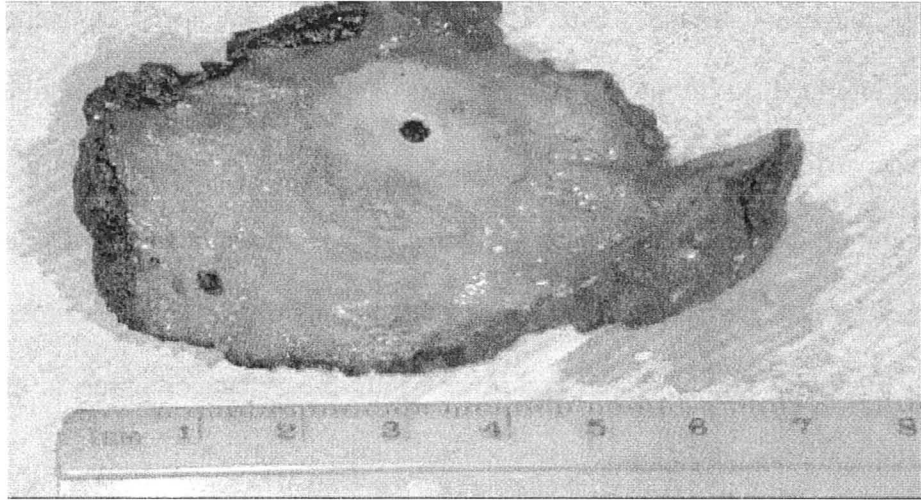


Figure 2.3: Photograph of a UW tissue specimen showing malignant tissue (white region, upper right) and normal adipose tissue (yellow region, lower left). The black ink spots mark the measurement sites. The black ink around the perimeter of the specimen denotes the margins of the excised tissue (from [7]).

Histological analysis (microscopic analysis) of the two-dimensional cross-section containing the ink spot was used as an estimate of the tissue composition in the three-dimensional volume sensed by the probe, and the pathologists determined and recorded the dominant tissue type directly beneath the black ink.

For the reduction surgery study, the tissue was simply quantified in terms of percentages of adipose, glandular and fibro-connective tissue.

On the other hand, for cancer surgery study, the samples were diagnosed as either normal, benign or cancer. Then the tissue samples diagnosed as ‘normal’ were characterized in the same manner as the samples in the reduction surgery study. The tissue samples diagnosed as ‘benign’ were characterized in terms of

percentages of benign tissue. The tissue samples diagnosed as ‘cancer’ were characterized in terms of percentages of invasive ductal carcinoma (IDC), invasive lobular carcinoma (ILC), ductal carcinoma in situ (DCIS) and lobular carcinoma in situ (LCIS). Also the percentage of necrotic tissue, if present, was noted in each sample. It is to be noted that the majority of breast cancers arise in the glandular region of the breast, and thus breast cancer tissue is effectively malignant glandular tissue.

### 2.2.2. Data fitting and reduction

Lazebnik *et al.* [6] chose the following one-pole Cole-Cole model to fit all the experimental complex permittivity ( $\varepsilon^*$ ) data sets:

$$\varepsilon^*(\omega) = \varepsilon'(\omega) - j\varepsilon''(\omega) = \varepsilon_\infty + \frac{\Delta\varepsilon}{1 + (j\omega\tau)^{(1-\alpha)}} + \frac{\sigma_s}{j\omega\varepsilon_0} \quad (10)$$

where  $\omega$  is the angular frequency and  $\varepsilon_\infty$ ,  $\Delta\varepsilon$ ,  $\alpha$  and  $\sigma_s$  are the model parameters as discussed in (8). Parameter values for each complex-permittivity data set corresponding to each characterized tissue sample were obtained by minimizing the following criterion:

$$e = \frac{\sum_{i=1}^N \left( \frac{\varepsilon'(\omega)_i - \hat{\varepsilon}'(\omega)}{\text{median}[\varepsilon'(\bar{\omega})]} \right)^2 + \sum_{i=1}^N \left( \frac{\varepsilon''(\omega)_i - \hat{\varepsilon}''(\omega)}{\text{median}[\varepsilon''(\bar{\omega})]} \right)^2}{N} \quad (11)$$

where  $N$  is the number of frequency points in the 0.5 GHz to 20 GHz range. It was chosen as approximately  $N = 50$  equally spaced frequency points. All fitting and data analysis was accomplished using a statistical software package.

As the scale of the study is large and experimental errors are inevitable,



there were some statistical tools and exclusionary criteria set up by Lazebnik *et al.* [6] such as:

(a) Histology-based exclusionary criterion: Some of the histology slides were considered of poor quality if: (a) black ink spot was missing; (b) black ink spot was smeared on the tissue surface; and (c) the cross-sectional slice of sample was somehow deformed during histological processing. This became the basis for slide-based exclusionary criteria. 118 samples were excluded from reduction surgery study leaving 370 samples for further analysis. In the cancer surgery study, 159 samples were excluded based on this and this left 160 samples for further analysis.

(b) Physics-based exclusionary criterion: A constraint was imposed that each data set had to be reasonably consistent with Kramers-Kronig [see (1)] relation between the real and imaginary parts of the complex permittivity. A total of 16 samples were excluded in reduction surgery study, based on this, leaving 354 samples for final analysis. For cancer surgery study, only 5 samples were excluded based on this criterion leaving 155 samples from 119 patients for final analysis. These 155 samples were distributed as: 85 normal samples, 60 cancer samples and 10 benign samples.

### 2.2.3. Data analysis

Several processes were employed to analyze the data. The first step the group conducted was an inter-rater analysis to verify that the UW and UC pathologists used similar methodology to evaluate the histology slides. This

verification was a critical step towards ensuring that the data collected at UW and UC could be consistently combined. Kappa statistic (*a statistical measure used in assessing the degree to which two or more raters, examining the same data, agree when it comes to assigning the data to categories*) was used to quantitatively evaluate the agreement between pathologists. A kappa value of less than 0 indicates no agreement, while a kappa value of 1 indicates perfect agreement. The kappa statistic computed for inter-rater analysis of reduction surgery study was 0.81, indicating very good agreement in the methodology utilized by the pathologists at UW and UC. The kappa statistic calculated for the inter-rater analysis of cancer surgery study was 0.75, indicating substantial agreement in the methodology utilized by the pathologists at the two universities. Therefore, it was concluded that the data from UW and UC could be combined into a single data set.

To summarize the data in reduction surgery study, three groups of tissue samples were formed. The three divisions were based only on the percent adipose tissue content in each sample and were chosen to maximize the difference between the groups and minimize the variability within the groups: (i) group 1 contained all samples with 0% to 30% adipose tissue (the high-water-content group), (ii) group 2 contained all samples with 31% to 84% adipose tissue, and (iii) group 3 contained all samples with 85% to 100% adipose tissue (the low-water-content group). The samples had the following distribution: 99 samples in group 1, 84 samples in group 2 and 171 samples in group 3. Group 3

(predominantly adipose tissue) was approximately half of the total number of samples, with the combination of groups 1 and 2 (heterogeneous mixture of fibro-connective, glandular and some adipose tissue) making up the other half. There are two primary reasons for this skewed distribution: (a) the samples in this study were obtained from breast reduction specimens that are inherently dominated by the presence of adipose tissue, and (b) the protocol was designed to take measurements at an adipose sample site and a fibro-connective/glandular sample site for each excised specimen.

In the reduction surgery study, the median dielectric constant and the effective conductivity dispersion curves were obtained for each of the three groups by first calculating the fitted values for each sample in the group at  $N$  equally spaced frequency points. Then the median value at each frequency point was calculated across samples within the group. Finally, the Cole–Cole model [see (10)] was used to fit these median values. The upper and lower quartiles (25th and 75th percentiles) of the fitted curves in each group were also calculated at 5 GHz, 10 GHz and 15 GHz to summarize the spread of the curves in each group. To evaluate the sources of variability in the dielectric properties at 5 GHz, 10 GHz and 15 GHz, a nested analysis of variance (ANOVA) was used to compare patient-to-patient variability, breast-to-breast variability within patient and sample-to-sample variability within breast. The analysis was performed on the tissue group 2 as it offered distributional assumptions required for the analysis. A preliminary ANOVA was conducted to test whether the variability

between breasts (within patient) was significantly larger than the variability between samples (within breast). A second ANOVA was conducted to test whether the variability between patients was larger than the variability between samples within patients. For each of the three groups of varying adipose tissue content, the effect of patient age, temperature and time from excision (the predictors) on the dielectric properties was also analyzed.

In the cancer surgery study, for the normal tissue samples, three groups of tissue samples were formed similar to the reduction surgery study. Whereas, in cancer samples, the adipose and glandular tissue content was very low such that 83% of them contained 0% to 20% adipose tissue, and all 60 cancer samples contained 10% or less glandular tissue. This is because the vast majority of cancer tissues analyzed in this study originated within the glandular region of the breast, so it is to be expected that these tumors contain very little adipose and normal (non-malignant) glandular tissues. The term ‘malignant’ tissue referred to all cancer types found in this study (IDC, ILC, DCIS and LCIS). Very few cancer samples contained appreciable amounts of cancer types other than IDC. This is due to the fact that IDC is the most prevalent type of breast cancer in women. The next most prevalent cancer type was DCIS, where six samples contained 30% or more malignancy and fifty-one samples had 0% to 10% malignancy. The compositions of the other two cancer types in this study were very low: (i) LCIS content ranged from 2% to 10% (two samples); and (ii) ILC content ranged from 1% to 10% (five samples).

The Cole-Cole model was fitted to median values in the cancer surgery study in the same manner as in reduction surgery study. Multivariate analysis of variance (MANOVA) was used to compare the dielectric properties of normal and malignant tissues at 5 GHz, 10 GHz and 15 GHz. For the malignant samples, the samples that contained equal to or more than 30% malignancy were considered. Three separate techniques were conducted during results comparison between normal and malignant tissues and will be discussed later.

#### 2.2.4. Results for dielectric parameters of various breast tissues

Figure 2.4 shows the Cole–Cole fits for the 354 tissue samples characterized and analyzed in the reduction surgery study. This figure vividly illustrates the important finding that the normal breast tissue dielectric properties span a large range. At the low end, tissue dielectric properties are bounded by the properties of lipids. At the high end, tissue dielectric properties are bounded by the properties of physiological saline. This is to be expected since the water content of different tissues in the breast varies from extremely low (pure adipose) to high (glandular and fibro-connective). The tissue dielectric properties are not expected to reach those of saline because even the highest-water-content biological tissue contains less than about 80% water. The dielectric property curves are color-coded by their tissue composition. In order of highest to lowest adipose content, the colors are red, purple, blue, cyan and green. The dielectric parameters of Cole-Cole model for the three adipose-defined groups from reduction surgery study are given in Table 2.2, Table 2.3 and Table 2.4. Variability about the median values is given

by 25<sup>th</sup> and 75<sup>th</sup> percentile parameters. The group with intermediate dielectric properties (group 2) displays the greatest variability in the dielectric properties due to the large degree of tissue heterogeneity in this group.

Figure 2.5 shows the one-pole Cole–Cole curves for the 85 normal data sets from cancer surgery study. Here also the dielectric properties of normal samples span a very large range. Figure 2.6 and Figure 2.7 show the one-pole Cole–Cole curves for the five UW benign samples and five UC benign samples, respectively. The UW and UC benign cases were not combined into a single set because the types of benign tissues differed at the two locations. There were four cystic cases and one ductal hyperplasia case at UW, while all the benign cases at UC were fibro-adenomas. Further statistical analysis on the dielectric properties of benign tissues was not performed.

Figure 2.8 shows the one-pole Cole–Cole curves for the 60 cancer data sets. The majority of the Cole–Cole curves for the cancer samples are green (low adipose content), and are found towards the higher end of the dielectric-property range. In all these figures, the curves for dielectric properties of blood are also shown, which lie in the high range cluster. Table 2.5, Table 2.6 and Table 2.7 give the Cole-Cole parameters for three groups of normal samples in the cancer surgery study. Table 2.8 gives the Cole-Cole parameters of malignant tissue (49 samples with 30% or more malignancy).

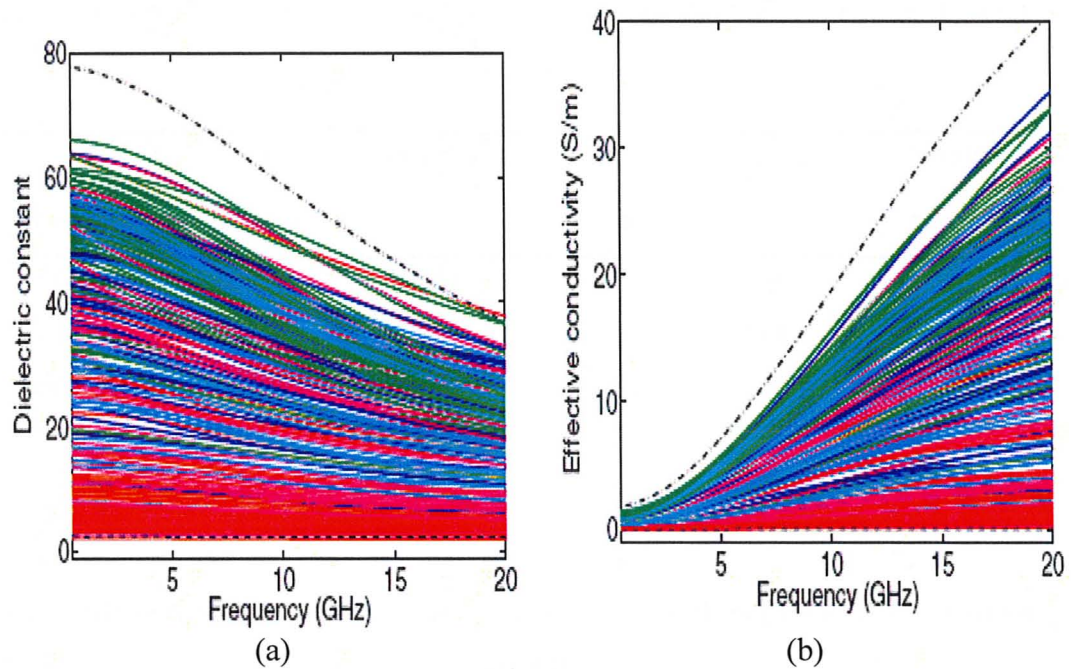


Figure 2.4: One-pole Cole–Cole fits to 354 dielectric properties data sets of reduction surgery study: (a) dielectric constant; (b) effective conductivity. The dashed (lower) black curve corresponds to the dielectric properties of lipid, and the dash-dot (upper) black curve corresponds to the dielectric properties of physiological saline (from [6]).

TABLE 2.2: COLE-COLE PARAMETERS FOR GROUP 1 FROM REDUCTION SURGERY STUDY.

Percentile	$\epsilon_{\infty}$	$\Delta\epsilon$	$\tau$ (ps)	$\alpha$	$\sigma_s$ (S/m)
25th	9.941	26.60	10.90	0.003	0.462
50th	7.821	41.48	10.66	0.047	0.713
75th	6.151	48.26	10.26	0.049	0.809

TABLE 2.3: COLE-COLE PARAMETERS FOR GROUP 2 FROM REDUCTION SURGERY STUDY.

Percentile	$\epsilon_{\infty}$	$\Delta\epsilon$	$\tau$ (ps)	$\alpha$	$\sigma_s$ (S/m)
25th	8.718	17.51	13.17	0.077	0.293
50th	5.573	34.57	9.149	0.095	0.524
75th	5.157	45.81	8.731	0.091	0.766

TABLE 2.4: COLE-COLE PARAMETERS FOR GROUP 3 FROM REDUCTION SURGERY STUDY.

Percentile	$\epsilon_{\infty}$	$\Delta\epsilon$	$\tau$ (ps)	$\alpha$	$\sigma_s$ (S/m)
25th	2.908	1.2	16.88	0.069	0.020
50th	3.140	1.708	14.65	0.061	0.036
75th	4.031	3.654	14.12	0.055	0.083



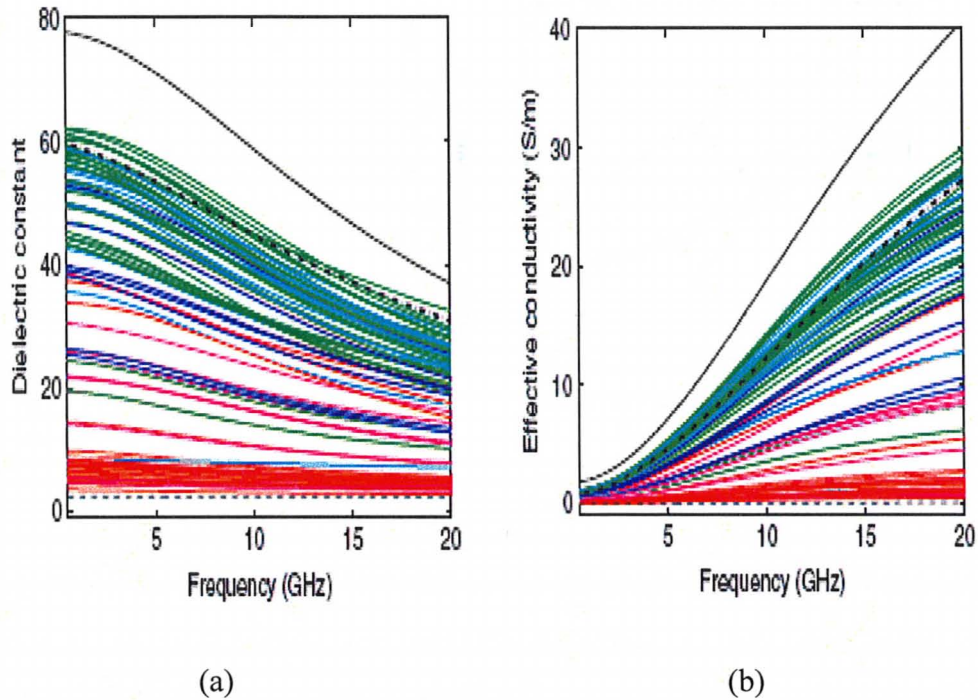


Figure 2.5: One-pole Cole–Cole fits to the 85 normal data sets from cancer surgery study: (a) dielectric constant; (b) effective conductivity. The curves are color coded based on the amount of adipose tissue present in each sample. The solid black (upper) curve represents the dielectric properties of saline, the dashed black (lower) curve represents the dielectric properties of lipids, and the dash-dot black (middle) curve represents the dielectric properties of blood (from [7]).

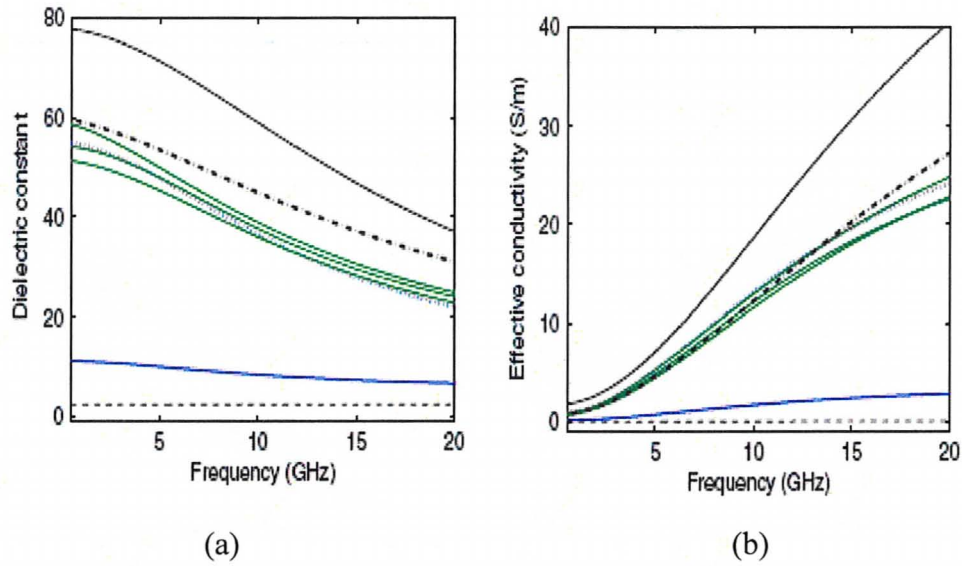


Figure 2.6: One-pole Cole–Cole fits to the five UW benign data sets (four cystic cases, solid lines, and one ductal hyperplasia case, dotted line): (a) dielectric constant; (b) effective conductivity. The black curves are as in Figure 2.5 (from [7]).

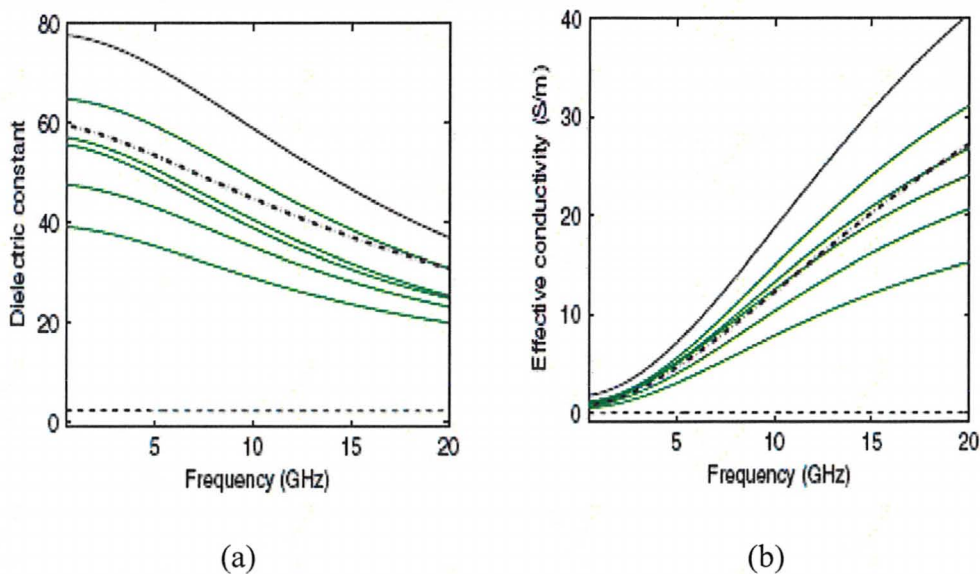


Figure 2.7: One-pole Cole–Cole fits to the five UC benign data sets (all fibro adenomas): (a) dielectric constant; (b) effective conductivity. The black curves are in Figure 2.5 (from [7]).

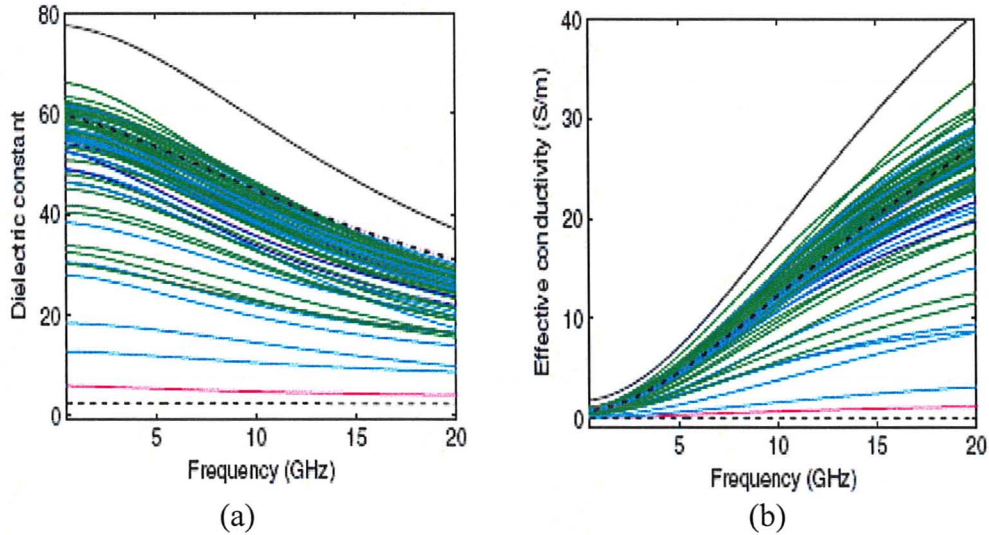


Figure 2.8: One-pole Cole–Cole fits to the 60 cancer data sets: (a) dielectric constant; (b) effective conductivity. The black curves are as in Figure 2.5 (from [7]).

TABLE 2.5: COLE-COLE PARAMETERS FOR GROUP 1 FROM CANCER SURGERY STUDY.

Percentile	$\epsilon_{\infty}$	$\Delta\epsilon$	$\tau$ (ps)	$\alpha$	$\sigma_s$ (S/m)
25th	5.013	40.6	10.16	0.091	0.607
50th	7.237	46.0	10.3	0.049	0.808
75th	7.816	50.21	10.47	0.055	0.889

TABLE 2.6: COLE-COLE PARAMETERS FOR GROUP 2 FROM CANCER SURGERY STUDY.

Percentile	$\epsilon_{\infty}$	$\Delta\epsilon$	$\tau$ (ps)	$\alpha$	$\sigma_s$ (S/m)
25th	3.891	4.113	13.83	0.038	0.082
50th	6.080	19.26	11.47	0.057	0.297
75th	6.381	32.30	10.41	0.081	0.561

TABLE 2.7: COLE-COLE PARAMETERS FOR GROUP 3 FROM CANCER SURGERY STUDY.

Percentile	$\epsilon_{\infty}$	$\Delta\epsilon$	$\tau$ (ps)	$\alpha$	$\sigma_s$ (S/m)
25th	3.122	2.133	14.27	0.099	0.034
50th	3.581	3.337	15.21	0.052	0.053
75th	3.882	5.020	12.92	0.059	0.103

TABLE 2.8: COLE-COLE PARAMETERS FOR 49 CANCER SAMPLES THAT CONTAIN 30% OR GREATER MALIGNANT TISSUE CONTENT.

Percentile	$\epsilon_{\infty}$	$\Delta\epsilon$	$\tau$ (ps)	$\alpha$	$\sigma_s$ (S/m)
25th	7.670	43.92	10.70	0.028	0.748
50th	6.749	50.09	10.5	0.051	0.794
75th	9.058	51.31	10.84	0.022	0.899

### 2.2.5. *Sources of variability within each study*

(a) Patient variability: Breast-to-breast and sample-to-sample variability specific to a patient was not statistically significant. Patient-to-patient and sample-to-sample variability among patients also showed no significant variability. There were small differences in standard deviations in the dielectric properties; however, these differences were judged not to have engineering importance in the light of the overall span of dielectric property values and no further analysis was done on the same.

(b) Age, temperature and time variability: When considering the effects of patient age, temperature and time between excision and measurement on the dielectric spectroscopy data, the effect of adipose content was first adjusted as this was always statistically significant even though the samples being analyzed were restricted to one of the three adipose-defined groups for normal samples in both studies. Patient age and sample temperature did not show any identifiable pattern. However, a statistically significant trend between the dielectric properties and the time post excision was observed for the 85%–100% adipose group. Both the dielectric constant and the effective conductivity decrease as the time between tissue excision and measurement increases. For example, at 5 GHz, the median dielectric constant for the samples that were characterized 0 to 50 min post-excision was about 6, while the median dielectric constant for the samples where 250 min to 300 min elapsed post excision, was about 4. Similarly, the effective conductivity decreased from about 0.4 S/m to about 0.1 S/m in this time range.

While this trend was statistically significant, the magnitude of the change is negligible compared to the much larger (by more than an order-of-magnitude) range of properties spanned by all tissue groups (0%–100% adipose) in the breast. Consequently, it was concluded that this trend is not important from an engineering point of view. The conclusions drawn from such studies are not expected to depend on a specific value of the dielectric constant and effective conductivity of the adipose tissue region (whether 6 or 4 for dielectric constant) but rather on the contrast of those values with the dielectric properties of breast regions that have little adipose content (associated with higher dielectric constant and effective conductivity). This trend was not observed for the other two adipose-defined tissue groups with higher water contents. It is suggested that the extracellular water is more dominant than the intracellular water in adipose tissue, whereas the opposite is true of non-adipose tissue. Hence, it can be hypothesized that the extracellular water was lost due to desiccation faster in adipose tissue samples than the intracellular water that is contained within cellular membranes in non-adipose tissues.

Thus, no trend was considered of engineering importance based on sample variability, patient's age, sample temperature, and time between excision and measurement, for both studies.

#### 2.2.6. Variability in dielectric parameters within the two studies and within tissue groups

(a) Variability in normal samples within the two studies: The normal samples

obtained from cancer surgery study were distributed across the three adipose defined tissue groups as follows: (i) group 1 contained 39 samples, (ii) group 2 had 16 samples, and (iii) group 3 contained 30 samples. In comparison, the distribution of normal samples obtained from reduction surgeries was as follows: (i) group 1 had 99 samples, (ii) group 2 contained 84 samples and (iii) group 3 had 171 samples. Statistically significant differences were observed in the dielectric properties of the normal samples obtained from reduction and cancer surgeries for all the three adipose-defined tissue groups. The differences in the dielectric properties for groups 1 and 3 are small in light of the variability of the dielectric properties of individual curves, and thus do not signify the presence of any important bias. The plot of the median dielectric properties in the UWB for group 1 is shown in Figure 2.9 and for group 3 is shown in Figure 2.11. The values of the parameters for the Cole-Cole model is particularly close for the median (or 50th percentile) values (compare Table 2.2 with Table 2.5 and Table 2.4 with Table 2.7). In contrast, the differences in the dielectric properties for group 2 for breast tissues obtained from reduction and cancer surgeries are larger. The Cole–Cole curves for the median dielectric properties of group 2 for samples obtained from cancer surgeries are substantially lower than the Cole–Cole curves for the median dielectric properties of this group for samples obtained from reduction surgeries. The plot of the median dielectric properties in the UWB for group 2 is shown in Figure 2.10. This difference is attributed to two factors. First, the number of samples contributing to the medians is very different - 84 samples

for the breast reduction surgery study database and 16 samples for the cancer surgery study database. The median estimated from a smaller number of samples is likely to be less accurate than the median estimated from a larger number of samples. Secondly, the distribution of tissue compositions for the samples obtained from reduction and cancer surgeries are skewed. Samples containing 51%–84% adipose tissue make up three-fourths of all normal samples obtained from cancer surgeries, while they make up only half of all normal samples obtained from reduction surgeries. Specifically, since measurements collected on normal samples in cancer surgery study was away from the site of the tumor, and since all of the breast cancers considered in the study arise in the glandular tissue, it follows that the normal tissue samples characterized in cancer surgery study had higher adipose contents than the normal tissue samples characterized in the reduction surgery study. Since more of the samples in the intermediate group obtained from cancer surgeries have higher adipose contents than the samples obtained from reduction surgeries, it is expected that the median dielectric properties of these samples is lower.



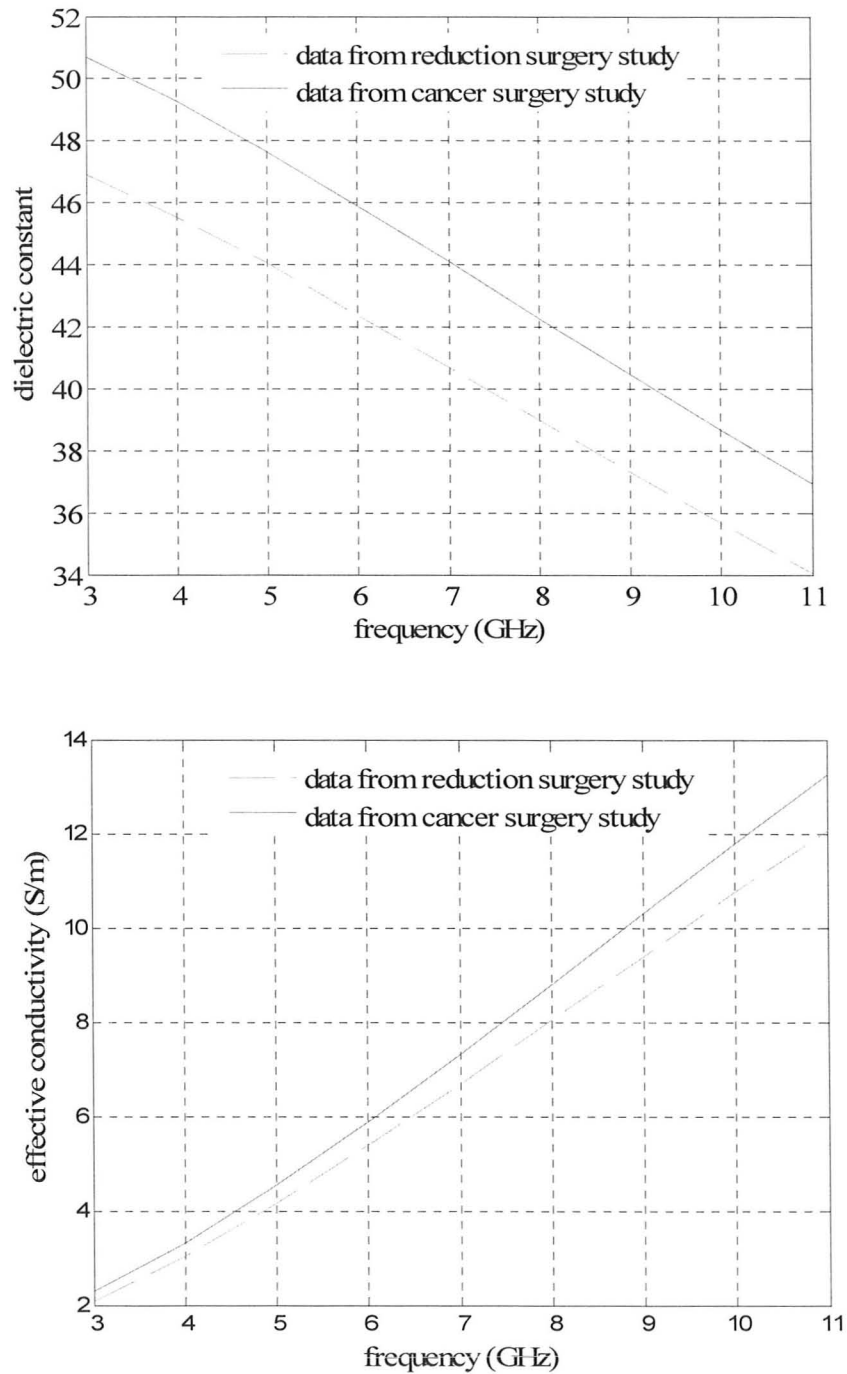


Figure 2.9: Comparison for group 1 normal samples from cancer surgery study and reduction surgery study. The solid line is for data from the cancer surgery study and dashed line is for data from the reduction surgery study. The top graph is for dielectric constant and the bottom graph is for effective conductivity.

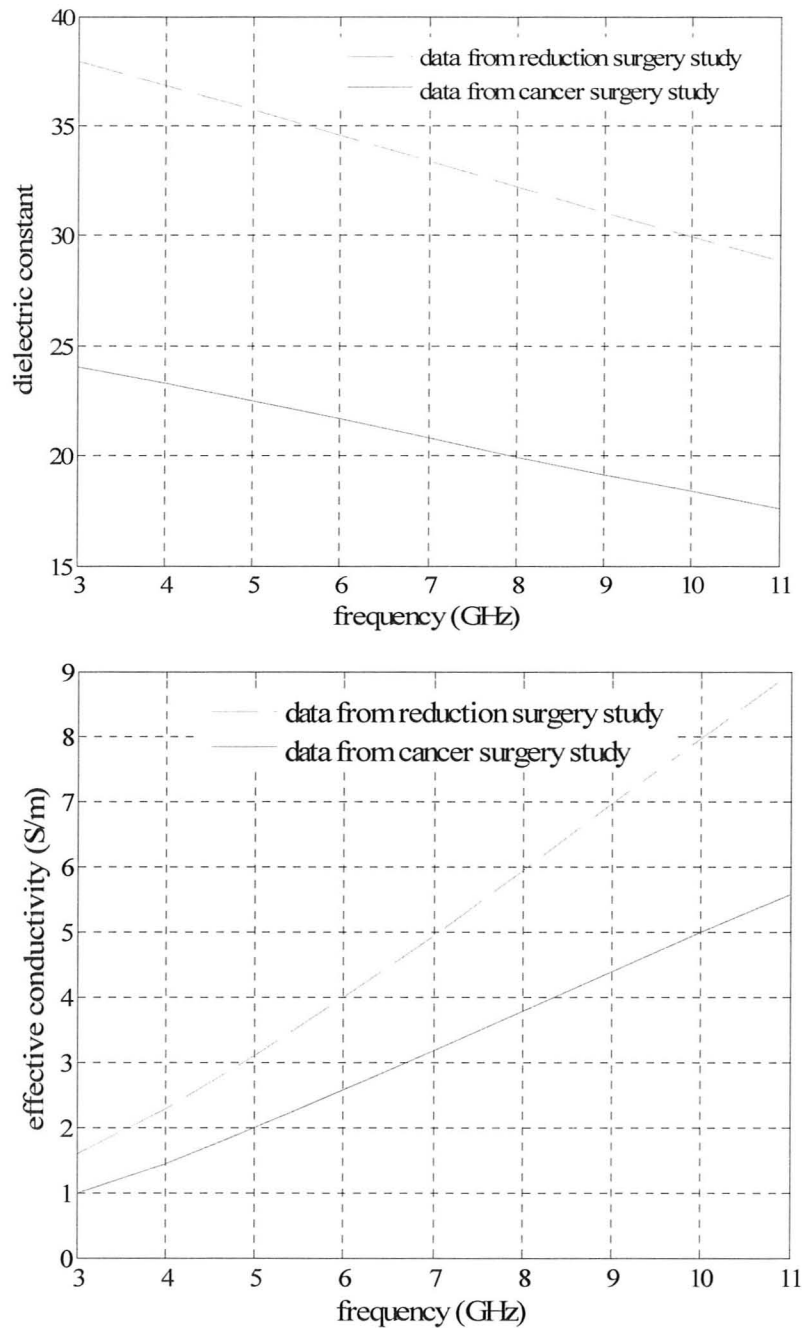


Figure 2.10: Comparison for group 2 normal samples from the cancer surgery study and reduction surgery study. The solid line is for data from the cancer surgery study and the dashed line is for data from the reduction surgery study. The top graph is for dielectric constant and the bottom graph is for effective conductivity.

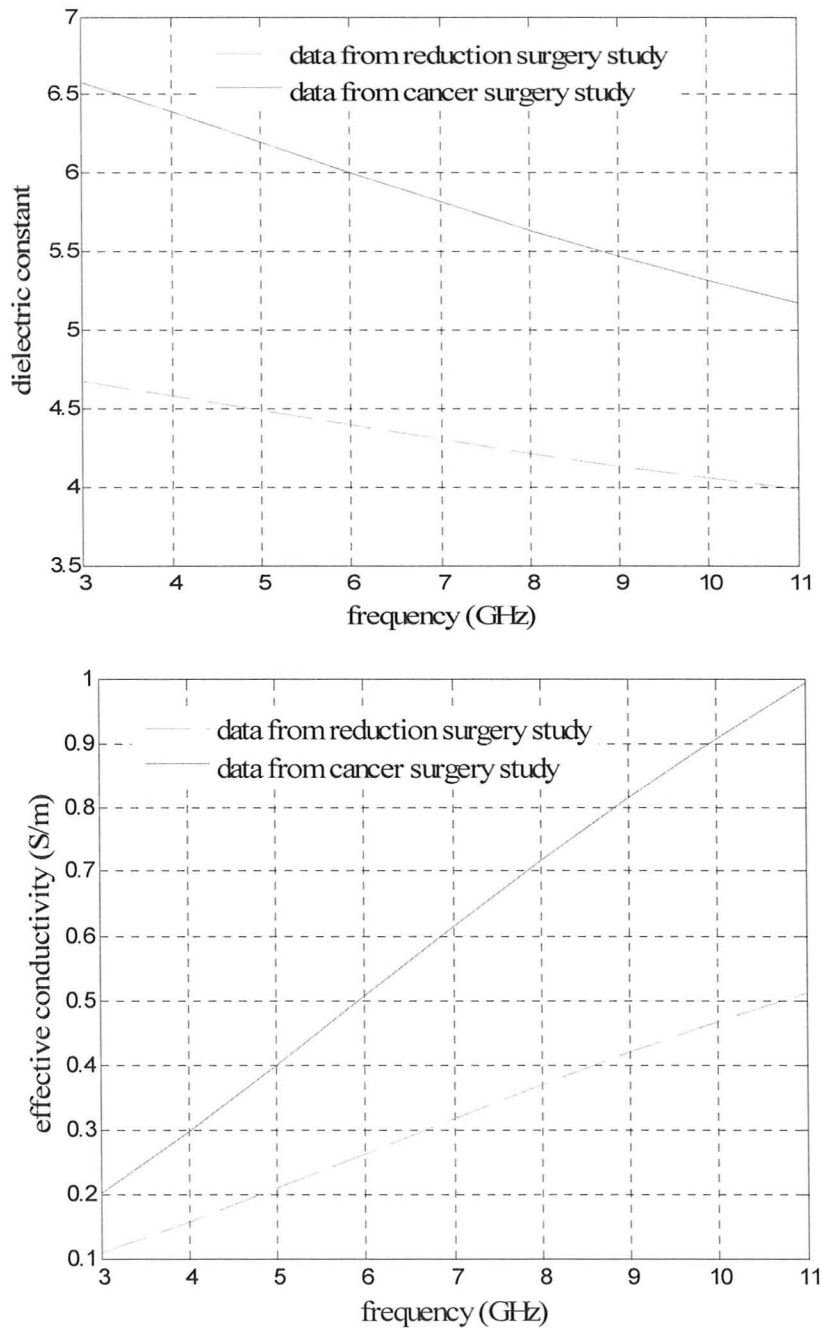


Figure 2.11: Comparison for group 3 normal samples from the cancer surgery study and reduction surgery study. The solid line is for data from the cancer surgery study and the dashed line is for data from the reduction surgery study. The top graph is for dielectric constant and the bottom graph is for effective conductivity.

(b) Contrast between malignant and normal samples: The plot of the dielectric properties of malignant samples is given in Figure 2.12. To conduct comparison between the dielectric properties of malignant and normal samples, three techniques were utilized.

(i) *Technique 1* – Adjusting for adipose content. In this way, the considered normal samples had a maximum adipose content of 10%. 28 normal samples (primarily glandular or fibro-connective tissues) were compared with 37 cancer samples. The mean contrast was found to be about 7.9% for the dielectric constant and about 10% for the effective conductivity with the highest of 11.7% obtained for the effective conductivity at 15 GHz. Even if perfusion of blood is considered *in vivo* for malignancy, owing to angiogenesis, it cannot affect too much the dielectric contrast. This is because the dielectric-property curves for the cancer surgery study shows blood among a cluster of curves for malignant samples in Figure 2.5.

(ii) *Technique 2* - Adjusting for adipose and fibro-connective tissue contents. No statistically significant differences between the dielectric properties of normal and cancer samples was found when the samples with maximum adipose content of 10% were considered, which were also adjusted for fibro-connective tissue content. By adjusting for fibro-connective tissue content, a direct comparison of the dielectric properties of normal glandular and malignant glandular tissues is conducted in the breast.

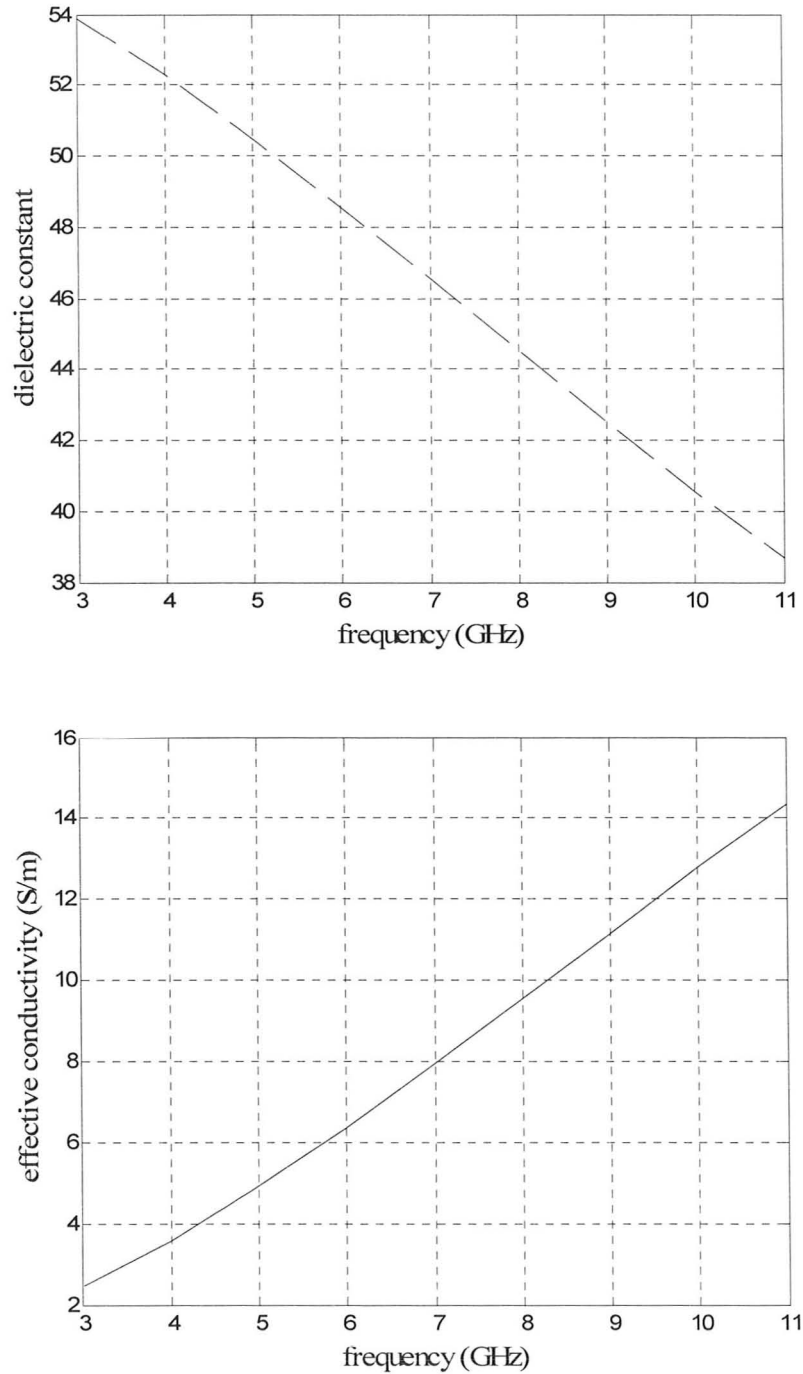


Figure 2.12: Median dielectric properties curves for malignant samples from the cancer surgery study. The top graph is for dielectric constant and the bottom graph is for effective conductivity.

(iii) *Technique 3* – Not adjusting for adipose or fibro-connective tissues contents. This analysis included 49 cancer samples and all 85 normal samples. Both mean dielectric constant and effective conductivity of the cancer samples were consistently 40% to 50% larger than those of the normal samples. However, it needs to be noted that 30% of the normal samples analyzed in this technique have adipose contents of 90% to 100% while none of cancer samples have high adipose content. This reveals that there is a large dielectric contrast between normal adipose-dominated tissues and malignant glandular tissues in the breast. This contrast is about 10:1 which is huge compared to the contrast obtained from the first two techniques.

### 2.2.7. Comparison with previous studies

Figure 2.13 shows the median curves (lines) for the three tissue groups from reduction surgery study in comparison with the data points (symbols) reported in three earlier studies (Chaudhary *et al.* [9], Surowiec *et al.* [10], Joines *et al.* [12]). The earlier data are bounded from below by the median curve for high-adipose-content breast tissue in this recent study, and from above by the median curve for low-adipose content breast tissue. The dielectric constant and effective conductivity values for the normal breast tissue reported in the recent study span a much larger range than those reported in the previous smaller-scale studies, with the exception of Campbell *et al.* [11]. The vertical arrows in Figure 2.13 represent

the data range reported in Campbell *et al.* [11] at 3.2 GHz for adipose tissue (solid lines) and normal tissue (dashed lines), defined as a mixture of glandular and connective tissues. The substantial heterogeneity observed in the wideband data from this large-scale study (reduction surgery study) as well as the single-frequency data from the smaller study in [11] had not been noted in other previous studies because the tissue source for earlier studies was primarily cancer surgeries. In order to characterize the dielectric properties of normal tissue in such specimens, it would have been necessary to characterize a region of tissue away from the tumor. Since breast cancer arises in glandular tissues, a site distinct from the tumor would likely have higher adipose content, leading to the lower and more homogeneous dielectric properties values reported in several of the earlier studies.

Figure 2.14 shows the median curves (lines) of the cancer samples characterized in cancer surgery study with samples that had 30% or more malignant tissue content in comparison with the data points (symbols) that represent results published in three earlier studies (Chaudhary *et al.* [9], Surowiec *et al.* [10], Joines *et al.* [12]) for malignant breast tissues. The median dielectric properties for breast cancer samples reported in this recent study fall near the top of the range given in Campbell *et al.* [11] and agree well with the other studies.

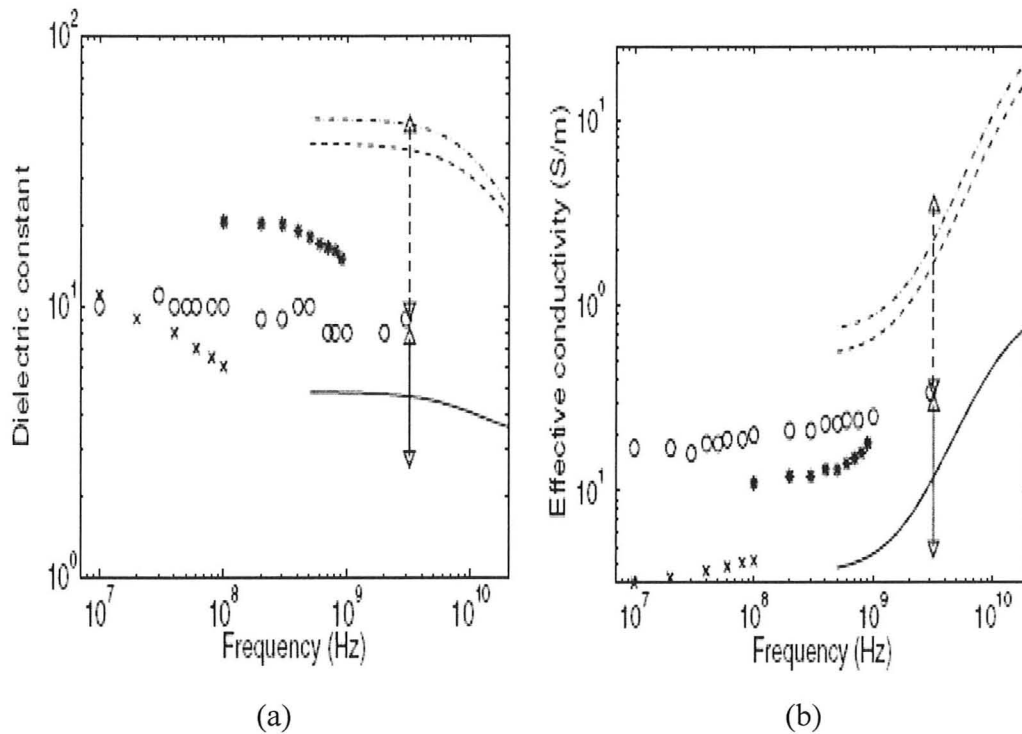


Figure 2.13: Comparison of data from reduction surgery study with previous studies. Lines are median dielectric properties of the three adipose-defined tissue groups from the recent study (dash-dot line: group 1, dashed line: group 2, solid line: group 3). Symbols are for normal breast tissue dielectric properties published previously ( $\circ$ : Chaudhary *et al.*,  $\times$ : Surowiec *et al.*,  $*$ : Joines *et al.*). Vertical arrows: range of data reported by Campbell *et al.* at 3.2 GHz for adipose (solid lines) and normal (dashed lines) breast tissues (from [7]).



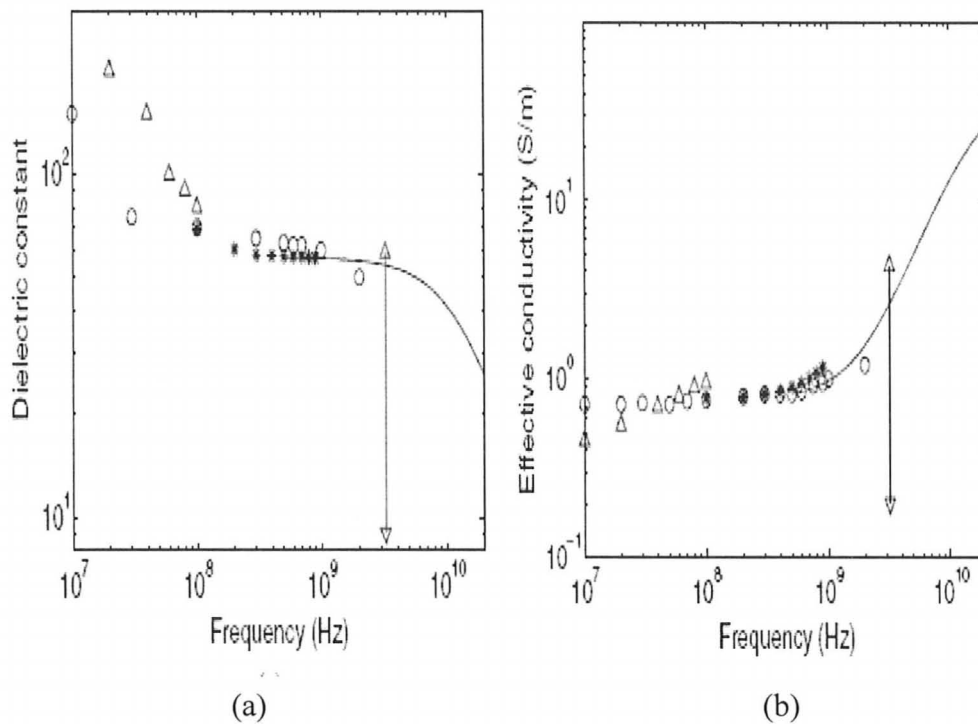


Figure 2.14: Comparison of data from cancer surgery study with previous studies. Lines are median dielectric properties of the cancer samples from the recent study with 30% or greater malignant tissue content. Symbols are malignant breast tissue dielectric properties published previously ( $\circ$ : Chaudhary *et al.*,  $\times$ : Surowiec *et al.*,  $*$ : Joines *et al.*). Vertical arrows: range of data reported by Campbell *et al.* at 3.2 GHz for malignant tissues (from [7]).

Some of the previously published small-scale studies reported considerable dielectric-property contrast between normal and malignant breast tissues at microwave frequencies. For example, Joines *et al.* [12], who analyzed 12 measurements on normal breast tissue and 12 measurements on malignant breast tissue, found that the dielectric properties of malignant tissues were approximately 200%-500% greater than the dielectric properties of normal tissues

at 900 MHz. From current results (technique 3 in cancer surgery study) it can be speculated that the normal tissues in these small-scale studies may have had significant adipose content. As a result, the contrasts reported in these studies were likely dielectric-property contrasts between normal adipose tissue and malignant glandular tissue. In contrast, Campbell *et al.* [11], who analyzed 22 normal and 41 diseased (malignant or benign) tissue samples at 3.2 GHz and distinguished between normal high-water-content tissue and adipose tissue in the breast, concluded that there was very little contrast between the dielectric properties of normal and diseased breast tissue. This conclusion is consistent with the results of the statistical analysis done by using two of the three techniques in the cancer surgery study (technique 1 and technique 2).

#### 2.2.8. Conclusions from these studies

To conclude, these two studies have been very instrumental in establishing the database of the dielectric properties of various breast tissues in the range from 0.5 GHz and 20 GHz. One of the important findings is that breast tissue heterogeneity must be accounted for not only at the macroscopic (centimeter) scale but also at the microscopic (sub-millimeter) scale. The compact Cole–Cole representation for the wideband dielectric property makes it possible to readily incorporate accurate dielectric-properties values into numerical and experimental breast phantoms to be used in the development of microwave breast imaging and breast cancer detection, monitoring, and treatment applications.

While this thesis had been written, results regarding differences between *in*

*vivo* and *ex vivo* measurements emerged in a new study [16]. The group at Dartmouth College conducted electrical impedance spectroscopy (from 100 Hz to 100 MHz) and microwave impedance spectroscopy (from 0.1 GHz to 8.5 GHz) on six patients undergoing cancer surgery where microwave imaging was done a week prior to the surgery, and both *in vivo* and *ex vivo* spectroscopy studies were done before and after the surgery. The tissue samples were mainly the excised malignant and fibro-cystic tissues. For further details on the protocols and methods refer to [16]. As mentioned with earlier studies (in sub-section 2.1), this group has again concluded with the latest correlation study [16] that there is a difference in both conductivity and permittivity by 20% and higher of excised tissues compared with *in vivo* tissues. This arises mainly from temperature changes, tissue dehydration and ischemic effects. In fact the predominant property changes occur immediately (within seconds) following tissue removal. Whereas, in the studies by Lazebnik *et al.* [6]-[7], the measurements were done between 5 minutes to 5 hours post-excision of tissues. On the other hand, it can be argued that all the samples undergo changes after excision and the respective dielectric-property contrast remains more or less the same. But knowing the heterogeneity of human breast, these changes can also be heterogeneous in nature depending on the tissue type. There is more room for work in this area, but for now there are no models fitted to *in vivo* tissue dielectric parameters and the models available to be used in breast phantoms for simulations and experiments are from the *ex vivo* measurements.

### 3) DIELECTRIC PARAMETERS FOR NUMERICAL BREAST PHANTOMS

#### 3.1. *Dielectric Parameters for Skin*

The effect of breast skin on the electromagnetic scattering in the microwave region is important. Thus, it must be properly included in the numerical breast phantoms. Ignoring the presence of skin in the numerical models can introduce errors according to [17]. The thickness of the skin is not constant at all locations on the human breast and nominally ranges from 0.5 mm to 2.7 mm [18]. However, skin is very hard to detect even in magnetic resonance images (MRI). Hence, an assumption has to be made about a uniform skin thickness in numerical phantoms. Winters *et al.* [19] carried out simulations with various skin thicknesses and proved that assuming a uniform thickness of 2 mm is the most appropriate in image reconstruction algorithms and gives least errors. The dielectric properties of the skin depend on the moisture content [5]. The 4-pole Cole-Cole model [ $n = 4$  in (9)] for dry skin and wet skin is given in [5] for the frequency range from 10 Hz to 100 GHz. It is shown in Table 2.9. Wet skin has higher permittivity compared with dry skin. The plot in Figure 2.15 shows this comparison.

For dry skin model, a one-pole Debye model [ $n = 1$  in (7)] is given in [19] for the frequency range from 1.67 GHz to 11.1 GHz. Also, one-pole Debye model is given for the wet skin model but it is in the frequency range from 0.5 GHz to 2.5 GHz. Hence, it has to be extrapolated for a higher frequency range. An

average between the dry and wet skin models, called damp skin model, has also been given in [19]. It is suggested by Winters *et al.* [19] that damp skin model is effective when no *a priori* information regarding skin moisture content is available. However, this model is also fitted to a frequency range below 3 GHz. These Debye models with one pole are given in Table 2.10.

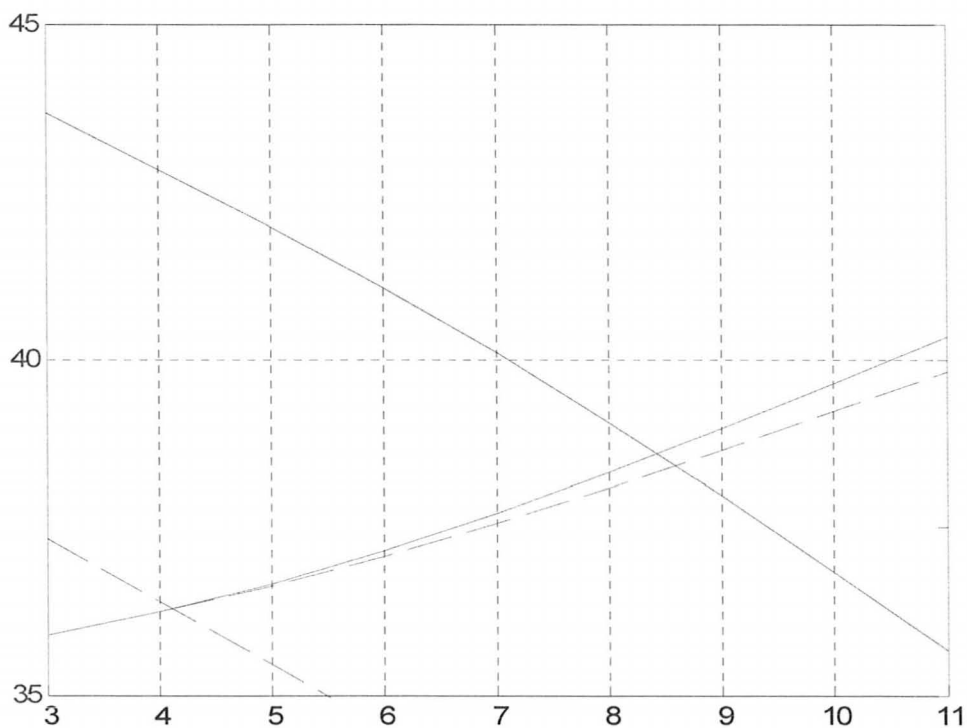


Figure 2.15: Comparison between four-pole Cole-Cole model of dry skin and wet skin from Gabriel *et al.* [5]. The dashed lines are for dry skin model and the solid lines are for the wet skin model.

TABLE 2.9: FOUR-POLE COLE-COLE MODEL FOR SKIN FROM GABRIEL *ET AL.* [5].

Tissue type Parameters	Dry skin	Wet skin
$\epsilon_\infty$	4	4
$\Delta\epsilon_1$	32	39
$\tau_1$ (PS)	7.96	7.23
$\alpha_1$	0.0	0.10
$\Delta\epsilon_2$	1100	280
$\tau_2$ (NS)	32.48	79.58
$\alpha_2$	0.2	0.0
$\Delta\epsilon_3$	0.0	3E4
$\tau_3$ ( $\mu$ S)	NA	1.59
$\alpha_3$	NA	0.16
$\Delta\epsilon_4$	0.0	3E4
$\tau_4$ (MS)	NA	1.592
$\alpha_4$	NA	0.2
$\sigma_i$ (S/M)	0.0002	0.0004

TABLE 2.10: ONE-POLE DEBYE MODEL FOR SKIN FROM WINTERS *ET AL.* [19].

Tissue type Parameters	Dry skin	Wet skin	Damp skin
$\epsilon_\infty$	4	33.9	33.4
$\Delta\epsilon$	33	13.5	12.1
$\tau$ (PS)	7.23	51.0	64.2
$\sigma_i$ (S/M)	1.10	0.658	0.663

### 3.2. *Dielectric Parameters for Muscle*

Muscle is a widely studied tissue for its electrical properties but mostly at lower frequencies for hyperthermia applications. In the low frequency range, muscle tissue even exhibits anisotropy. At high frequencies, it behaves as a high-water content tissue with high permittivity and conductivity. In fact, muscle and malignant tissues are considered very close in dielectric properties. Muscle tissue is often a component in numerical and physical breast phantoms representing the muscle layer at the rib cage called pectoralis major. A four-pole Cole-Cole model is given for muscle in [5] for the frequency range from 10 Hz to 100 GHz. The parameters are listed in Table 2.11 for the same. Also, a two-pole Debye model [ $n = 2$  in (7)] for average muscle tissue is given in [20] for the frequency range from 100 MHz to 6 GHz. It is given in Table 2.12.

TABLE 2.11: FOUR-POLE COLE-COLE MODEL FOR MUSCLE FROM GABRIEL *ET AL.*  
[5].

Parameters	Muscle
$\varepsilon_{\infty}$	4
$\Delta\varepsilon_1$	50
$\tau_1$ (PS)	7.23
$\alpha_1$	0.1
$\Delta\varepsilon_2$	7000
$\tau_2$ (NS)	353.68
$\alpha_2$	0.1
$\Delta\varepsilon_3$	1.2E6
$\tau_3$ ( $\mu$ S)	318.12
$\alpha_3$	0.1
$\Delta\varepsilon_4$	2.5E7
$\tau_4$ (MS)	2.274
$\alpha_4$	0.0
$\sigma_i$ (S/M)	0.2



TABLE 2.12: TWO-POLE DEBYE MODEL FOR MUSCLE FROM WUNER *ET AL.* [19].

Tissue type	Muscle
Parameters	
$\epsilon_{\infty}$	21.0151
$\Delta\epsilon_1$	34.2007
$\Delta\epsilon_2$	12.0813
$\tau_1$ (PS)	13.56
$\tau_2$ (NS)	0.74791
$\sigma_i$ (S/M)	0.69874

### 3.3. Dielectric Parameters for Breast Interior

It has been concluded that the main tissues important to model the heterogeneous human breast in a microwave simulation are: fibro-connective-glandular tissue, transitional tissue, and adipose fatty tissue corresponding to group 1, group 2 and group 3, respectively, from the studies by Lazebnik *et al.* [6]-[7]. These three tissues were distinguished by examining the percentage of adipose fat content as discussed before. The model that was fitted in the large-scale experimental study was one-pole Cole-Cole model. However, a simpler one-pole Debye model [ $n = 1$  in (7)] valid from 3.1 GHz to 10.6 GHz has been proposed by Lazebnik *et al.* in [21]. The proposed Debye models provide a means for creating computationally efficient FDTD breast models with realistic wideband dielectric properties. The parameters for the model for the three groups are given in Table 2.13.

TABLE 2.13: ONE-POLE DEBYE MODELS FOR THREE ADIPOSE DEFINED NORMAL TISSUE GROUPS AND MALIGNANT TISSUE [21].

Tissue type Parameters	Group 1	Group 2	Group 3	Malignant
$\varepsilon_\infty$	7.82	5.57	3.14	6.75
$\Delta\varepsilon$	40.14	32.56	1.61	48.35
$\tau$ (ps)	10.62	9.24	14.11	10.47
$\sigma_s$ (S/m)	0.71	0.52	0.036	0.79

The Debye model has been fitted to the median curves (50<sup>th</sup> percentile) shown in Tables 2.2, 2.3, 2.4, (reduction surgery study) and Table 2.8 (cancer surgery study). This implies that the normal tissue dielectric properties from the reduction surgery study form the baseline for healthy normal tissues in human breast and their differences from normal tissue groups in cancer surgery study (which was especially high for group 2) is ignored. Figure 2.16 shows the curves for one-pole Cole-Cole model from Table 2.2 and one-pole Debye model for group 1 from Table 2.13, plotted together. Figure 2.17 shows the curves for one-pole Cole-Cole model from Table 2.3 and one-pole Debye model for group 2 from Table 2.13, plotted together. Figure 2.18 shows the curves for one-pole Cole-Cole model from Table 2.4 and one-pole Debye model for group 3 from Table 2.13, plotted together. Figure 2.19 shows the curves for one-pole Cole-Cole model from Table 2.8 and one-pole Debye model for malignant tissue from Table 2.13 plotted together. All the plots show good match in the FCC allocated UWB.

The one-pole Debye models listed in Table 2.13 are therefore good to be used in simulations to assign dielectric properties to the interior of the breast in numerical phantoms.

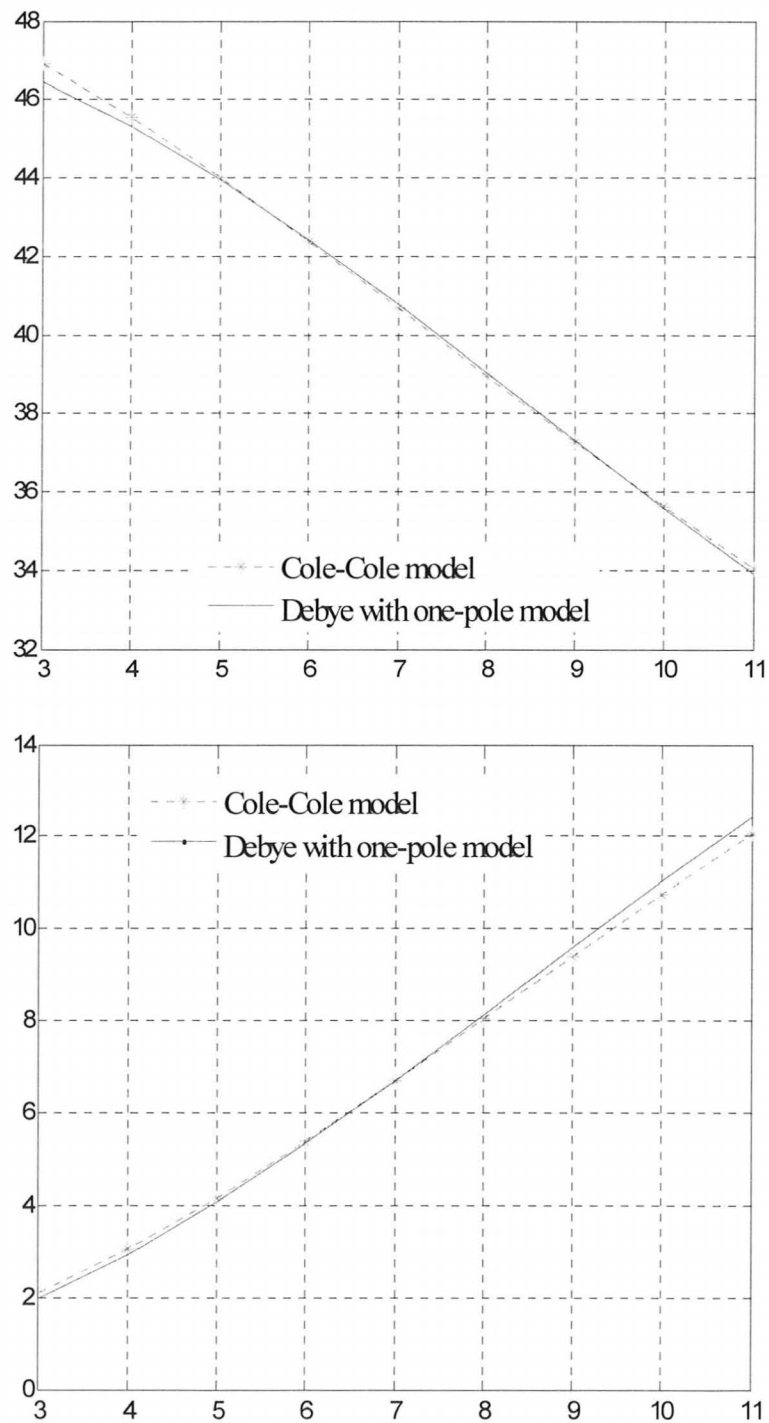


Figure 2.16: Comparison of the Cole-Cole model from [6] with the simple Debye model from [21] fitted to the dielectric properties for group 1 in the UWB.

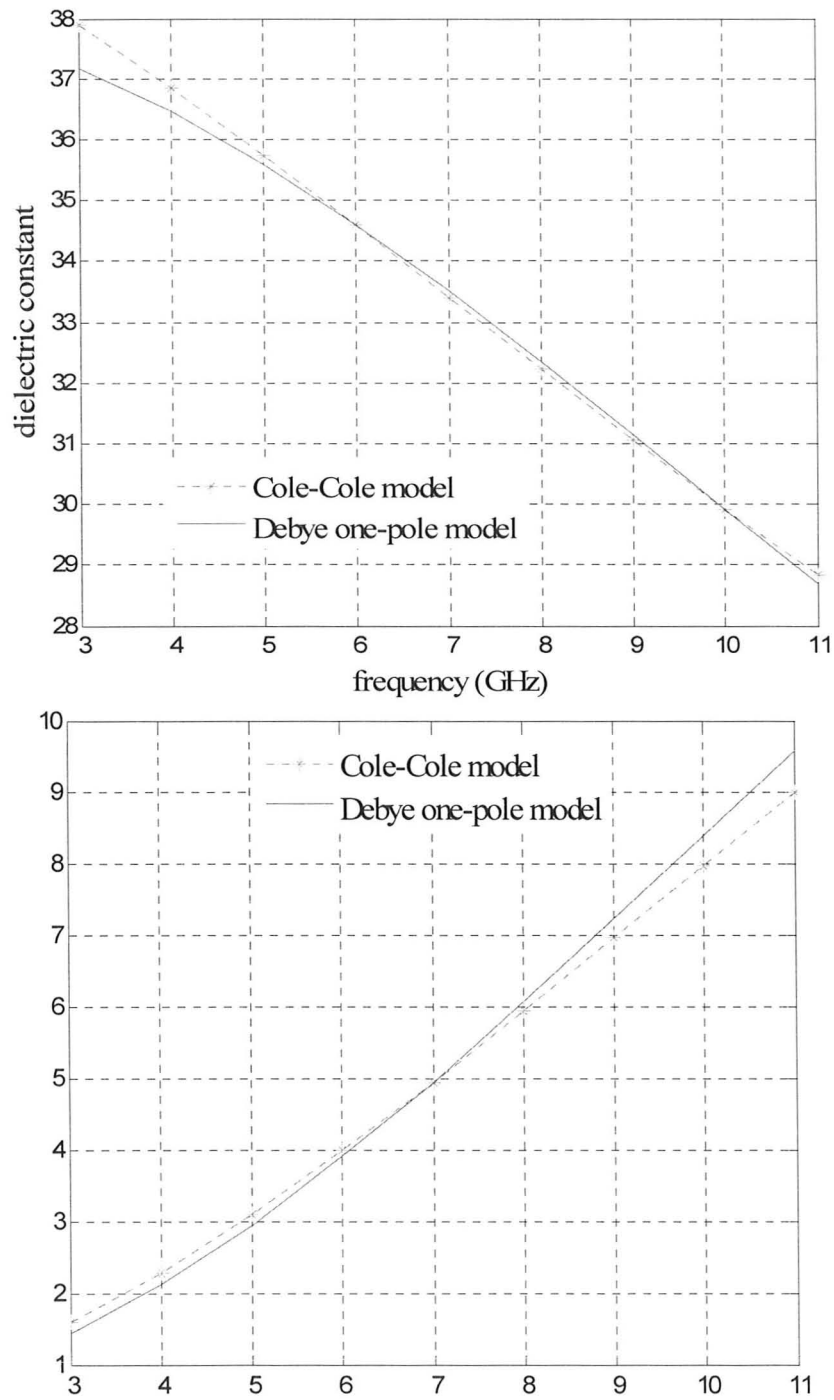


Figure 2.17: Comparison of the Cole-Cole model from [6] with the simple Debye model from [21] fitted to the dielectric properties for group 2 in the UWB.

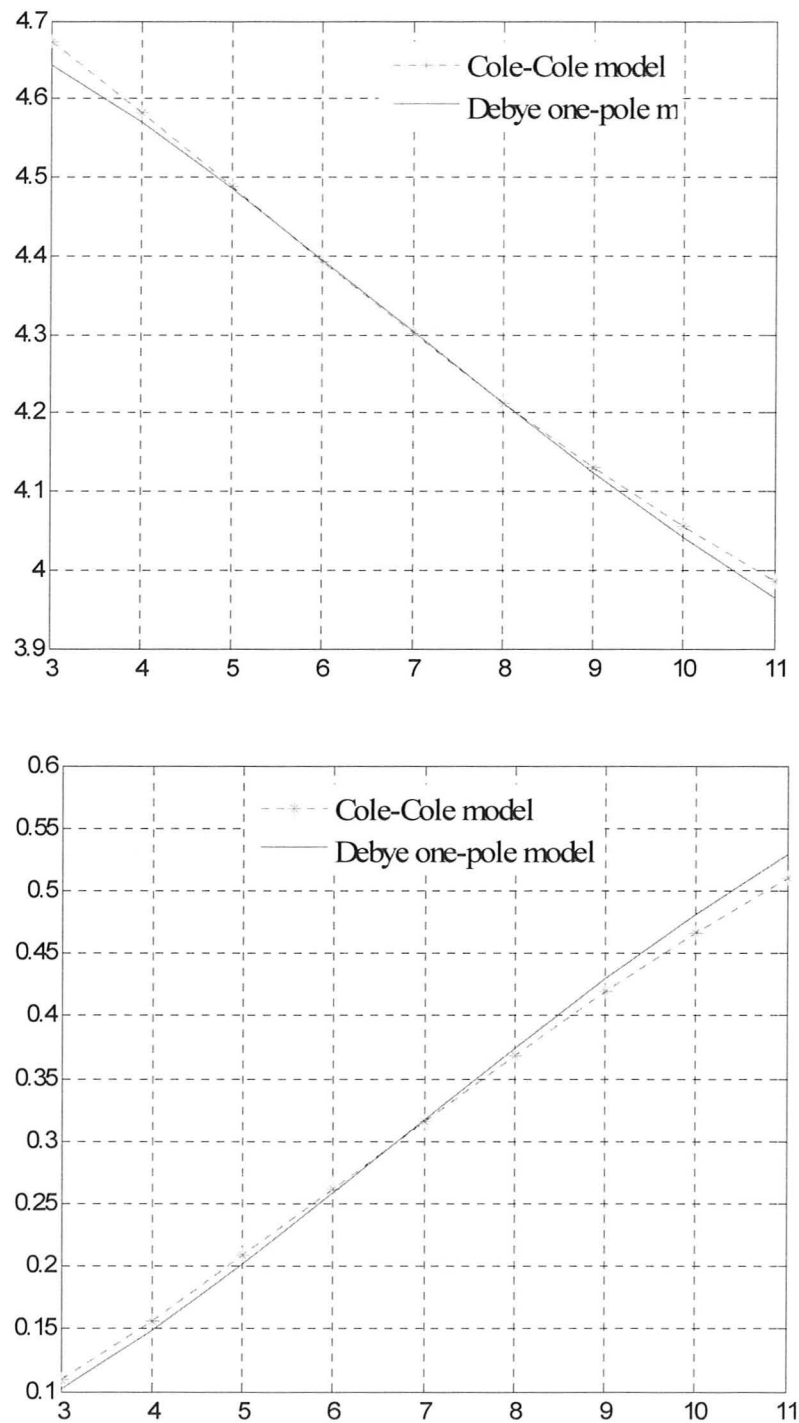


Figure 2.18: Comparison of the Cole-Cole model from [6] with the simple Debye model from [21] fitted to the dielectric properties for group 3 in the UWB.

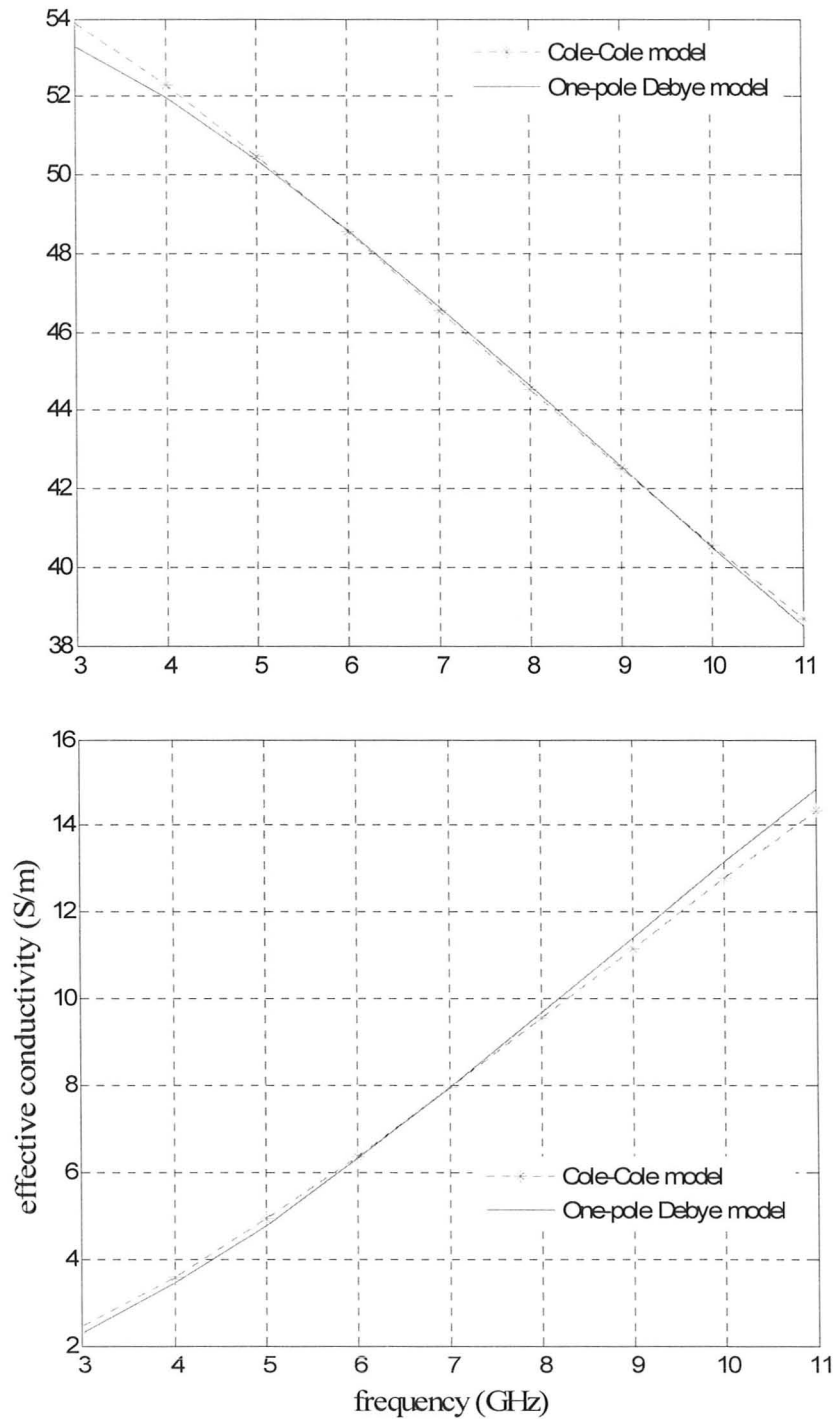


Figure 2.19: Comparison of the Cole-Cole model from [7] with the simple Debye model from [21] fitted to the dielectric properties for the malignant group in the UWB.

#### 4) MECHANISMS OF MALIGNANCY

Malignancy has some unique features. For microwave measurements, the foremost is its dielectric contrast with healthy tissues. However, as it has been discussed, this contrast is not significant when malignant tissue is compared to the healthy glandular tissue, where it usually develops. The maximum difference is of the order of 10% and it is in effective conductivity. Hence, it would be beneficial to enlist some of the mechanisms related to malignancy in theory that can explain the reason for malignant tissue's hyper-conductivity. This can also give us some idea about how to exploit the differences between malignant and healthy tissues to in hybrid modalities for detection.

##### 4.1. *Electrical and Mechanical Mechanisms*

A variety of factors have been listed in [2] and [4] to explain the differences in the dielectric properties of normal tissues compared with malignant tissues such as:

- (a) Necrosis: Inflammation and injured cells found in malignant breast tissues lead to breakdown of cell membranes, such that a larger fraction of the tissues can carry current at low frequency. At these frequencies, experimental studies show that necrosis yields 5 to 10-fold higher conductivity while permittivity is generally smaller than that of the normal tissue [2].
- (b) Charging of the cell membrane: In breast carcinoma, there is a progressive replacement of fat lobules with fibroblastic proliferation and epithelial cells. This is accompanied by a variety of alterations at the transformed cell surface. Cancer



cells have reduced membrane potentials and tend to have altered ability to absorb positive ions (such as micro-calcifications) developing a higher negative surface charge on their membranes. Accordingly, conductivity of the malignant tissues is increased with this mobile charge being displaced and rotated by the microwave field [4].

(c) Relaxation times: The relaxation times in malignant tissues are larger than those in normal tissue, indicating that a significant increase in the motional freedom of water has occurred [4].

(d) Sodium concentration and water content: The sodium concentration in tumor cells is higher than in normal cells. The excessive sodium concentration not only affects the cell membrane potentials, but also causes malignant tissue to retain more fluid. The fluid is retained in the form of bound water, which has larger values of dielectric constant and conductivity than free water [4].

Another mechanism related with malignant tissues is that corresponding mechanical properties such as elasticity and stiffness. Samani *et al.* [22] have developed specialized techniques to measure the elasticity of tissue samples and applied them to measure 169 fresh *ex vivo* breast tissue samples including fat and fibro-glandular tissue as well as a range of benign and malignant breast tumor types. Results show that, under small deformation conditions, the elastic modulus of normal breast fat and fibro-glandular tissues are similar while fibro-adenomas are approximately twice the stiffness. Fibrocystic disease and malignant tumors exhibit a 3–6-fold increased stiffness, with high grade invasive ductal carcinoma

(IDC) exhibiting up to a 13-fold increase in stiffness compared to fibro- glandular tissue. Their work is related to an imaging technique called elastography, which has been developed over the last two decades to measure elastic modulus of soft tissues. It is a more quantitative alternative to manual palpation that is commonly used as a means to detect breast cancer (as in breast self-examination techniques). For more details on elastography refer to [22]. The reason for higher stiffness in the malignant region is contemplated to be the high interstitial pressure in the malignant tissues owing to rapid multiplication of cells and angiogenesis that creates blood and ionic flow in the region. However, malignant cells do not have their own lymphatic system (available to all normal healthy tissues) to get rid of extra fluids and metabolic waste materials cumulated during cellular processes. This creates pressure and stiffness in the malignant region. This information was acquired in the Medical Imaging course at McMaster University. Interestingly, elastography is being followed upon by researchers in breast microwave imaging very recently for a hybrid elasticity-dielectric detection modality.

#### **4.2. *Physical Mechanisms***

This section aims to help with determining the type, shape and location of malignant-tumor simulants in numerical breast phantoms. The first major distinction to be noted is that between benign and malignant tumors. Benign tumors are more regularly shaped solid lumps that do not metastasize but can cause discomfort such as pain. Malignant tumors have irregular shapes and they cause fatal cancers. The differences in shapes and interfaces of these tumors are

shown in Figure 2.20 and Figure 2.21, taken from [23]. A general trend is that tumors with ill-defined boundaries and irregular shape are strongly associated with malignancy.

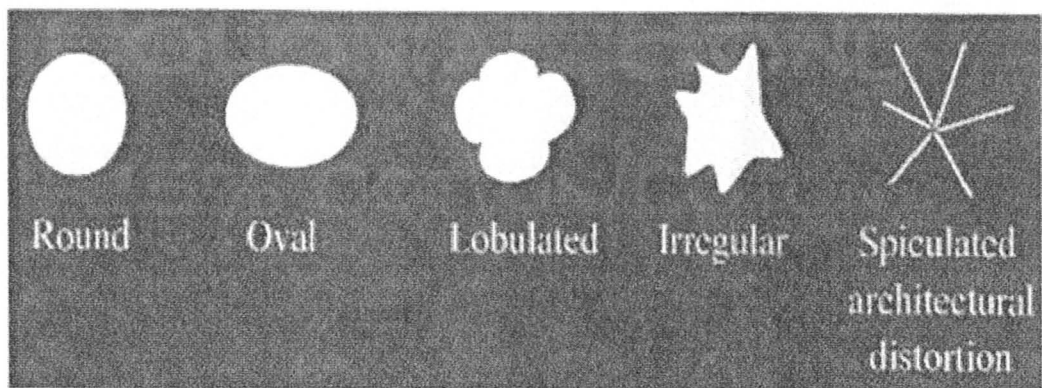


Figure 2.20: The various shapes of breast masses. The last two are strongly associated with malignancy (from [23]).

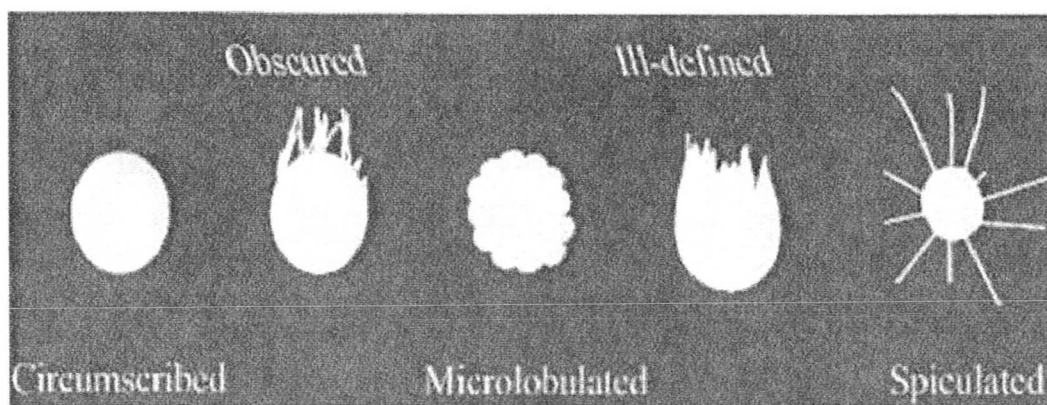


Figure 2.21: The various margins of lesions found in breast. The last three are strongly associated with malignancy (from [23]).

The following diagram in Figure 2.22, taken from [24], shows the incidence and probability of malignant tumors in the breast. This can be helpful in trying various locations in simulation models.

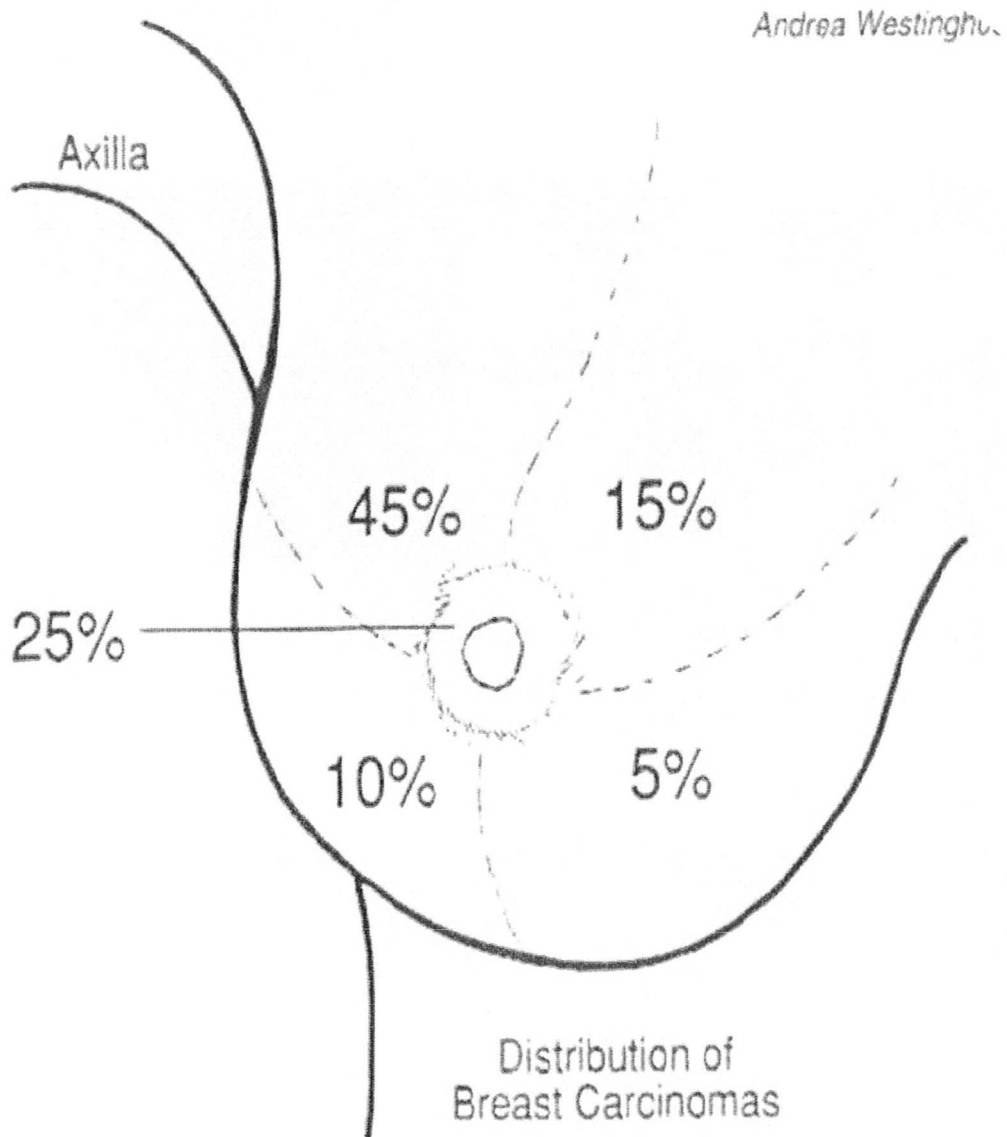


Figure 2.22: Location and probability of carcinomas in the breast (from [24]).

---

**REFERENCES**

- [1] Beau Lambert. (April 2008). Dr. K. A. Mauritz Research Group - Dielectric spectroscopy. [Online]. Available: <http://www.psrc.usm.edu/mauritz/dilect.html>.
- [2] A. V. Vorst, A. Rosen, Y. Kotsuka, *RF/Microwave Interaction with Biological Tissues*. John Wiley & Sons Inc., 2006, pp. 14 – 78.
- [3] M. N. O. Sadiku, *Elements of Electromagnetics*, 4<sup>th</sup> ed. Oxford University Press: New York, 2007, pp. 435 – 445.
- [4] L. Sha, E. R. Ward, B. Story, “A review of dielectric properties of normal and malignant breast tissue,” *Proc. IEEE Southeast Conf.*, pp.457 – 462, 2002.
- [5] S. Gabriel, R. W. Lau, and C. Gabriel, “The dielectric properties of biological tissues: III. Parametric models for the dielectric spectrum of tissues,” *Phys. Med. Biol.*, vol. 41, pp. 2271 – 2293, April 1996.
- [6] M. Lazebnik, L. McCartney, D. Popovic, C. B. Watkins, M. J. Lindstorm, J. Harter, S. Sewall, A. Magliocco, J. H. Brooske, M. Okoniewski and S. C. Hagness, “A large – scale study of the ultra wideband microwave dielectric properties of normal breast tissue obtained from reduction surgeries,” *Phys. Med. Biol.*, vol. 52, pp. 2637 – 2656, April 2007.
- [7] M. Lazebnik, L. McCartney, D. Popovic, C. B. Watkins, M. J. Lindstorm, J. Harter, S. Sewall, A. Magliocco, J. H. Brooske, M. Okoniewski and S. C. Hagness, “A large-scale study of the ultrawideband microwave dielectric properties of normal, benign and malignant breast tissues obtained from cancer surgeries,” *Phys. Med. Biol.*, vol. 52, pp. 6093 – 6115, October 2007.
- [8] T. S. England and N. A. Sharples, “Dielectric properties of the human body in the microwave region of the spectrum,” *Nature*, vol. 163, pp. 487 – 488, 1949.
- [9] S. S. Chaudhary, R. K. Mishra, A. Swarup, and J. M. Thomas, “Dielectric properties of normal and malignant human breast tissues at radiowave and microwave frequencies,” *Indian J. Biochem. Biophys.*, vol. 21, pp. 76 – 79, February 1984.
- [10] A. J. Surowiec, S. S. Stuchly, J. R. Barr and A. Swarup, “Dielectric properties of breast carcinoma and the surrounding tissues,” *IEEE Trans.*

---

*Biomed. Eng.*, vol. 35, pp. 257 – 63, 1988.

- [11] A. M. Campbell, and D. V. Land, “Dielectric properties of female human breast tissue measured in vitro at 3.2 GHz,” *Phys. Med. Biol.*, vol. 37, pp. 193 – 210, 1992.
- [12] W. T. Joines, Y. Zhang, C. Li, and R. L. Jirtle , “The measured electrical properties of normal and malignant human tissues from 50 to 900 MHz,” *Med. Phys.*, vol. 21, pp. 547 – 550, January 1994.
- [13] P. M. Meaney, M. W. Fanning, D. Li, S.P. Poplack, and K. D. Paulsen, “A clinical prototype for active microwave imaging of the breast,” *IEEE Trans. Microw. Theory Tech.*, vol. 48, pp. 1841 – 1853, 2000.
- [14] J. W. Choi *et al.*, “Microwave detection of metastasized breast cancer cells in the lymph node; potential applications or sentinel lymphadenectomy,” *Breast Cancer Res. Treat.*, vol. 86, pp. 107 – 115, 2004.
- [15] Poplack *et al.*, “Electromagnetic breast imaging: average tissue property values in women with negative clinical findings,” *Radiology*, vol. 231, pp. 571 – 580, 2004.
- [16] R. J. Halter *et al.*, “The correlation of in vivo and ex vivo tissue dielectric properties to validate electromagnetic breast imaging: initial clinical experience,” *Phys. Med. Biol.*, vol. 30, pp. 121 – 136, June 2009.
- [17] D. A. Woten, S. Pandalaraju, and M. El-Shenawee, “ Breast skin effect on scattered electromagnetic fields,” *Proc. of 24th Int. Review of Progress in Applied Computational Electromagnetics (ACES)*, March 2008.
- [18] T. L. Pope, M. E. Read, T. Medsker, A. J. Buschi, and A. N. Brenbridge, “Breast skin thickness: normal range and causes of thickening shown on film-screen mammography,” *J. The Canadian Assoc. Radiologists*, vol. 35, pp. 365 – 368, 1984.
- [19] D. W. Winters, E. J. Bond, B. D. Van Veen, S. C. Hagness, “Estimation of the frequency-dependent average dielectric properties of breast tissue using a time-domain inverse scattering technique,” *IEEE Trans. Antennas Propag.*, vol. 54, pp. 3517 – 3528, November 2006.
- [20] T. Wuren, T. Takai, M. Fujii, and I. Sakagami, “Effective 2-Debye-pole FDTD model of electromagnetic interaction between whole human body and UWB radiation,” *IEEE Microw. Wireless Comp. Lett.*, vol. 17, no. 7, pp. 483 – 485, July 2007.

- [21] M. Lazebnik, M. Okoniewski, J. H. Brooske, S. C. Hagness, “Highly accurate Debye models for normal and malignant breast tissue dielectric properties at microwave frequencies,” *IEEE Microw. Wireless Comp. Lett.*, vol. 17, no. 12, pp. 822 – 824, December 2007.
- [22] A. Samani, J. Zubovits, D. Plewes, “Elastic moduli of normal and pathological human breast tissues: an inversion-technique-based investigation of 169 samples,” *Phys. Med. Biol.*, vol. 52, pp. 1565 – 1576, February 2007.
- [23] Jay R. Harris, Marc E. Lippman, Monica Morrow, C. Kent Osborne, *Diseases of the Breast*, 2nd edition. Lippincott Williams and Wilkins, pp. 130, pp. 400 – 455, 1999.
- [24] Wende Logan Young M.D., Nancy Yanes Hoffman, *Breast Cancer: A Practical Guide to Diagnosis Volume 1 – Procedures*, 1<sup>st</sup> edition. Mt. Hope Publishing Co., pp. 23, 1994.

## CHAPTER 3

# SUMMARY OF PHYSICAL BREAST PHANTOMS AND THEIR RECIPES

### INTRODUCTION

Biological tissues have electrical properties, characterized by their dielectric parameters such as relative permittivity  $\epsilon_r$ , conductivity  $\sigma$ , and the dielectric loss tangent  $\tan \theta$ . These have been discussed in detail in chapter 2. The dielectric properties of biological tissues are dispersive being primarily influenced by their constituent water content and ion concentration. Among healthy tissues, high-water content tissues (HWCT) such as muscle exhibit highest dielectric constant and losses. Whereas low-water content tissues (LWCT) such as adipose fat display the lowest values for dielectric constant and losses. Various studies have been published on the electrical properties of major and specific tissue groups



both in the high and low frequency ranges [1]-[3].

The research related to radiation effects of RF/microwave applications and microwave imaging for medical diagnostics have invoked significant interest in recent times. Because of this, there is a major need to make physical phantoms for conducting experiments in such studies. At least three major bio-electromagnetic studies are active in research: (i) EM absorption and hyperthermia pattern studies for therapeutic microwave applicators; (ii) medical microwave imaging systems, and (iii) specific absorption rate (SAR) studies and dosimetry studies.

The physical phantoms should mimic the electric field distribution and relative heating patterns of the actual tissue in the presence of an electromagnetic source. Physical phantoms are fabricated according to specific recipes. The rest of the chapter refers to the physical phantoms as phantoms. A phantom recipe typically simulates a single tissue. It exhibits a homogenous distribution of electrical and thermal properties specific to the target tissue. The heterogeneity of human body tissues is very complicated to design and control with a single recipe. These recipes are prepared with non biological materials. This is because biological materials (mostly from animals) though similar to human tissues have much shorter shelf life and are prone to degradation. They may contain air sacs, which leads to problems during microwave experiments.

Phantoms can be classified into three main types based on phases – solid, liquid and gel. Different combinations and compositions of these phantoms are used to mimic biological systems such as brain, lung, torso and breast. The main

research of phantoms is mainly for three frequency ranges: (i) 10 MHz to 100 MHz (HF and VHF), (ii) 200 MHz to 3 GHz (UHF), and (iii) 3 GHz to 20 GHz (SHF). A technical report [4] compiles in a concise manner common recipes of preparing phantoms.

The aim of this chapter is to discuss the main recipes that were selected to model the breast tissues. The target dielectric properties are outlined in chapter 2. The phantoms have to simulate breast tissues in the ultra-wideband (UWB) frequency range (from 3 GHz to 10 GHz). Section 1 of this chapter enlists the desired requirements the phantoms must fulfill for the experiments in our lab. Section 2 discusses the select recipes that can be used by our group and the generic methodology of preparing the phantoms. Section 3 presents the results about the measured dielectric parameters of the phantoms and compares them to the target values. Section 4 shows some photos of the phantoms. It closes with a discussion on how they facilitate research in designing imaging arrays for active microwave imaging (AMWI).

## **1) PHANTOM REQUIREMENTS**

As mentioned in the Introduction, the phantoms are made according to recipes using non-biological materials. These materials are commonly available chemicals that are used widely in chemistry and life science experiments. From biological sources, pig is considered to have tissues with dielectric properties closest to human beings [5]. However the usage is impractical for repetitive

experiments, which is the case with most pre-clinical studies in AMWI research.

Some of the required features for the phantoms are:

(a) Mechanical stability of shape: We require phantoms to have good mechanical stability so that they can retain their shape. Very soft or jelly phantoms are not practical for system development as these phantoms cannot be used without support. Filling specifically shaped shells with gels is usually messy and the obtained phantoms tend to have air pockets. Liquid phantoms are good for their ease of fabrication. They can be poured in any desired shell easily and neatly. Their major drawback is the rapid evaporation of water, which changes the permittivity and conductivity in a short time. Restoring the liquid mixture ratios repeatedly within an experiment is a hassle. This also increases the chances of introducing errors due to tampering. Also, liquid phantoms are very narrow-band and a specific ratio is usually good for just one frequency.

We intend to make semi-solid/solid phantoms with good mechanical strength that can retain arbitrary shape of any human part by using specific moulds. Layered phantoms can also be easily realized with such solid phantoms.

(b) Non-toxicity: The phantom should be non-toxic such that touching or being in contact with it should not cause any detrimental health/safety concerns. The experimentalist should not require special gear and chambers to use the phantoms, as this will be too expensive and impractical for small scale studies. That being said, it is advised that even non-toxic chemicals are not to be ingested or inhaled as there can be always common allergy problems. Hence, normal care and

standard safety practices of washing hands after experiments or wearing gloves and a lab coat during experiments should be adopted. This alone will ensure enough safety when using phantoms repeatedly.

(c) Fabrication simplicity: The fabrication of a phantom should be easy and practical so that it can be fabricated from easily available materials in scientific stores. Fabrication should not require any special manufacturing apparatus.

(d) Wideband properties: The phantom should have as wideband dielectric characteristics as possible. This will be essential to obtain the  $\mathbf{E}$  field distribution similar to that in the biological tissue.

(e) Ease of maintenance: The phantom should preferably retain both physical and electrical properties for some time without degrading. It is essential to have a repetitive representation of the biological tissue in multiple experiments.

(f) Low costs: Overall the costs of fabricating and using phantoms should be as low as possible as the phantoms are usually to test pre-clinical set-ups that are generally very small scale. These studies have to be repeated, tested, and altered a number of times during research.

## 2) METHODS AND MATERIALS

### 2.1. *Apparatus for Measurements*

For phantom measurements, Agilent 85070E Dielectric Performance Probe Kit [6] is used. This kit comprises: (i) a slim probe with high-temperature and frequency rugged performance, (ii) easy to use software, and (iii) a calibration

short. This probe has a 9.5 mm wide flange and is optimum to measure liquid, semi-solid and flat solid phantoms. A high quality coaxial cable interfaces the probe with the network analyzer, which is an Agilent E8363B PNA (performance network analyzer) [6]. This analyzer has a PC interface and runs the kit software allowing measurement of materials from 10 MHz to 40 GHz. The software guides through the “three standard” calibration process of air/short/water for initializing the probe. Also, the probe calibration can be refreshed at any time using a single standard. In our lab, the calibration is usually refreshed with deionised water for every new measurement. The frequency range of the measurements for our phantoms is from 3 GHz to 10 GHz with 51 linearly spaced frequencies. Figure 3.1 shows the probe set-up with the PNA.

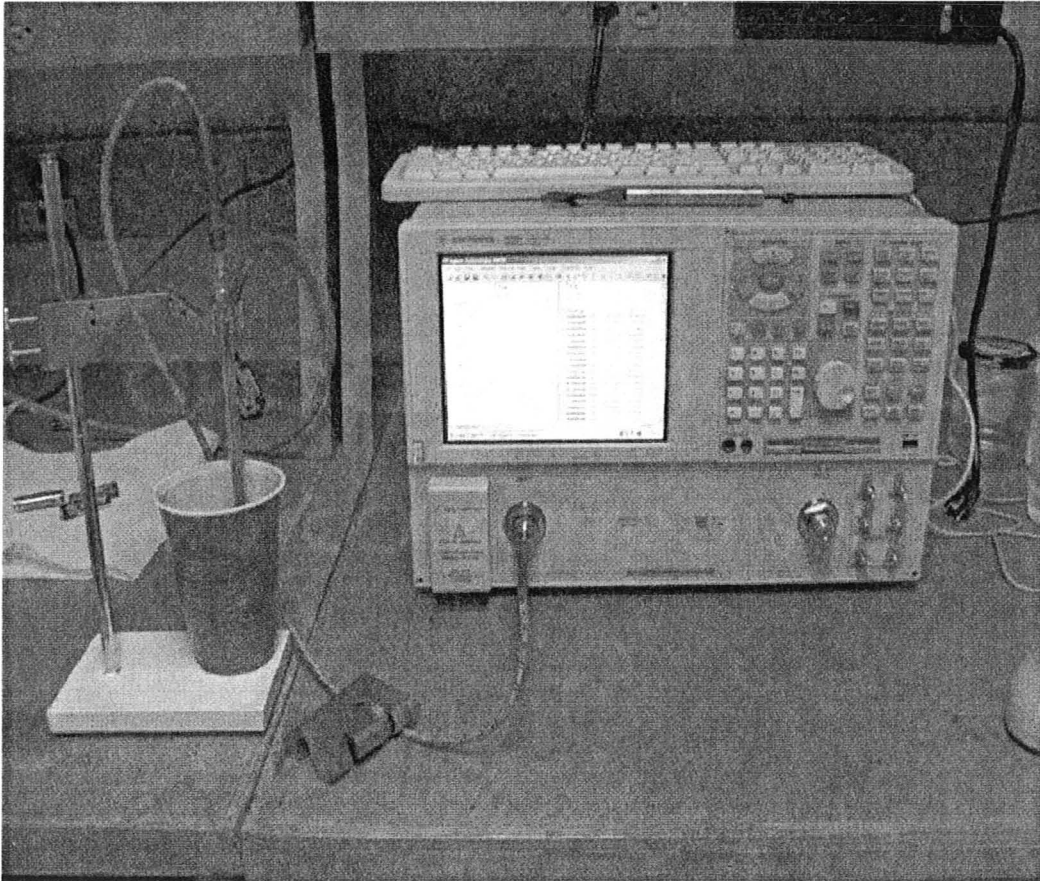


Figure 3.1: Agilent 85070E Dielectric Performance Probe Kit connected to an Agilent E8363B PNA.

## 2.2. *Promising Recipes and Ideas*

There are numerous recipes in the literature for phantom fabrication [4]. One of these recipes is selected to simulate the breast tissues. As discussed in chapter 2 the main tissues to consider in physical breast phantoms are: (i) high-water content tissues (HWCT) such as muscle (pectoralis major) and fibro-glandular tissue; (ii) intermediate-water content tissues (IWCT) such as skin (assumed dry model as sanitization will be with low-permittivity alcohols) and

transitional tissue (group 2 in chapter 2); and (iii) low-water content tissue (LWCT) which is the adipose fat in the breast.

There are two kinds of tissue-equivalent solid phantoms based on agar that are widely published and used in dosimetry studies. One of these phantoms is called glycerin phantom and the other is called TX-151 phantom (the name is derived from name of the constituent chemical as discussed later). The glycerin phantom has been designed by Yoshiki Okano [7] and the TX-151 phantom was proposed by the same group headed by Koichi Ito [7]. Variations of both recipes have also been used for SAR studies [9]. Each phantom has its own characteristics and benefits. Both phantoms can retain their shape. It is the agar which acts as a coagulant and gives mechanical strength to the polymer matrix of the phantom [10]. TX-151 (or sometimes the similar product TX-150) is also a solidifying agent. Glycerin phantoms can mimic both high- and low-water content tissues by varying the percentage of water and salt in glycerol. Water controls the permittivity and salt (NaCl) controls the conductivity. Polyethylene powder (PEP) is used for fine tuning of both dielectric parameters. The glycerin phantom is superior to the TX-151 phantom in terms of preservation as glycerin provides a moisturizing action leading to less evaporation of water. This also retains the dielectric properties of the phantom for a longer time. It is claimed that the phantom can be preserved for six months by wrapping it in vinyl/plastic film and storing it in refrigeration [10]. However, the TX-151 phantom is known to simulate tissues over a broader range compared to the glycerine phantom below 3

GHz. This is of no interest to us as our frequency range is above 3 GHz. The recipe ratios have to be changed from the ones given in the papers in order to target specific breast tissues in the UWB. This is because the target tissues for phantoms in dosimetry studies are mostly the brain and the homogenized human torso. The experimentally measured dielectric properties for tissues to model these homogenous phantoms are taken from studies different than those to be used for our algorithms. Also, the TX-151 phantom recipe uses very toxic preservation agents such as sodium de-hydro-acetate [7] or sodium azide [9], where the latter is considered a neuro-toxicant. This is not practical with our small scale set-up and repeated use. From our experience with fabrication, it is also observed that the TX-151 phantoms are prone to lump formation and may need special blenders to control TX-151 solidification process. The glycerin phantom is hence preferred due to its simple fabrication with easily available materials, high preservation capabilities, and non-toxicity.

The glycerin phantom recipe can be modified by changing the water ratio, PEP ratio and salt ratio to mimic the range of HWCT, IWCT and LWCT tissues in the breast. However, these guidelines are from papers addressing phantoms for the frequency range below 3 GHz. From our experience with phantom measurements in the frequency range from 3 GHz to 10 GHz, the losses from phantom materials such as glycerin, agar, water etc., are high enough and the recipes for healthy tissues do not need salt. The loss can be controlled by water and PEP alone. The hint for this trend also comes from studying graphs and tables



given in [7], where the glycerin phantoms were introduced. The paper is in Japanese. It gives the recipe ratios of glycerin phantoms from 900 MHz and 1.8 GHz. The author has used 0 g salt in all recipe ratios for 1.8 GHz, whereas, at 900 MHz salt is used in amounts from 3.3 g to 2.1 g for simulating a range of conductivities. This shows that materials exhibit more loss at high frequencies and do not require additional salt ions in the UWB frequency range.

The percentages of agar and glycerin are fixed from experience to achieve balanced moisturizing effect and good mechanical strength. These ratios have been assessed both by trial-and-error as well as carefully studying graphs and tables given in [7]. Some good ideas from other recipes are also instilled in the recipe ratios. One of them is the use of a bactericide to prevent breakdown of the polymer by bacterial agents and is adapted from Hartsgrove *et al.* [10]. This is a more non-toxic way to preserve the phantoms. Another adapted idea addresses the modification of the glycerin phantom recipe for LWCT and is taken from Bini *et al.* [12]. The idea is that to lower the permittivity of any phantom recipe, non-polar or low-permittivity liquids can be partially or totally substituted for water. These liquids have to be: (i) non-ionic to avoid uncontrolled conductivity; (ii) be miscible with water in all proportions and preferably miscible with other reagents; (iii) have high boiling point to withstand heating; and (iv) be non-toxic in touch or inhalation as then special fume hoods and gear will be required to handle it. A liquid satisfying all these conditions and which is easily available is ethylene glycol. It is used as anti-freeze fluid in cars and common reagent in chemistry

labs.

Beside the modified glycerin phantom recipe for adipose fat, there are other promising recipes for fat in the literature. One is a dough-type phantom by Legendijkt *et al.* [14] which uses a mixture of water, oil and flour. This recipe is however prone to dryness even with slight exposure and suffers from air pockets due to the use of flour. Hence, it is not used here. The other phantom is called fat-gel phantom and is designed by Mechii *et al.* [13]. The recipe uses water, detergent, cooking oil, agar and TX-151 as ingredients. This recipe and associated results will be shown later.

Other tissues to be simulated in experiments are malignant tumors. This is generally done by a homogenous liquid or solid phantom with high permittivity and conductivity. Hence, water and salt (NaCl) are the main constituents of most tumor recipes. For our purposes, we need a solid tumor to insert in a solid glycerin phantom. PEP cannot be used as the base powder as it lowers the dielectric properties. Alginate powder is suggested [15] to make tumors. Also gelatin can be used as it is miscible in water and sets in hard with higher concentration of gelatin powder used.

The specific ratios for all these tissues are ready to use. They have been confirmed through many trials. They are enlisted as tables in sub-section 2.4 of this chapter. The summary of the materials and how to get them are given next.

### **2.3. *Materials for Phantom Fabrication***

The materials that have been finally selected for recipes are easy to obtain.

Except ethylene glycol and PEP, other the materials are very common in use as components in food and drugs. Hence, none of them is highly toxic by skin touch and inhalation. Common safety laboratory procedures must suffice for this phantom work. These recipes are also easy to make with standard lab (chemistry) equipment such as regular glass flasks, disposable cups/dishes, stirrers and weighing balance.

Another important item to discuss is water. In phantom work and in most recipes [4], it is recommended to use deionised or pure water. This generally means not to use tap water which can be very dissipative due to dissolved salts and ions. On the other hand, there is a huge variety of purified water available. It is important that the pure water utilized for phantom work should be deionised – its description should state high resistivity and low conductivity. The presence of ions such as sodium, chloride, calcium etc. should be negligible. For instance, the pure water available in the scientific stores at McMaster University is highly purified but it is for chromatography purposes and may contain buffer solutions and salts specific to the process. The American Society for Testing and Materials (ASTM) [16] has defined four grades of pure water [17]. Among these, type 1 and type 2 have very high resistivity with the lowest amounts of solutes (both ionic and organic). ASTM type 2 is easily available and has been used in this phantom work.

Below, Table 3.1 enlists all materials that will be required for the recipes in sub-section 2.4 of this chapter. All the materials and equipment were assembled

during the beginning months of this research period. There were mainly three sources to obtain the equipment and materials: (i) the scientific stores in McMaster University, (ii) outside vendors, and (iii) grocery or pharmacy stores. In Table 3.1, only material information is given as it needs frequent replacement. The equipment is already in the lab and the detailed description is not required. Common items such as detergent and cooking oil were brought from general grocery store. TX-151 was not in stock and hence a similar solidifying agent called TX-150 was sent by the company. As per the material data sheets there is no difference between TX-151 and TX-150. Also, glycerin is a common name for glycerol.

TABLE 3.1: A LOOK-UP FOR ALL THE MATERIALS TO BE USED IN RECIPE RATIOS.

Material Name	Source	<ul style="list-style-type: none"> <li>• Product Code (if any)</li> <li>• Company Details (if any)</li> <li>• Online Link (if any)</li> </ul>
Glycerol	Scientific store	<ul style="list-style-type: none"> <li>• 5350-1</li> <li>• Caledon Laboratories Ltd., Georgetown, Ontario</li> <li>• <a href="http://www.caledonlabs.com/en/">http://www.caledonlabs.com/en/</a></li> </ul>
De-ionized water	Vendor via calling	<ul style="list-style-type: none"> <li>• CABDH1168-4LP</li> <li>• VWR International LLC Ltd. Of Canada, Mississauga, Ontario</li> <li>• <a href="http://vwr.com/index.htm">http://vwr.com/index.htm</a></li> </ul>
Salt (NaCl)	Scientific store	<ul style="list-style-type: none"> <li>• 7560-1</li> <li>• Caledon Laboratories Ltd., Georgetown, Ontario</li> <li>• <a href="http://www.caledonlabs.com/en/">http://www.caledonlabs.com/en/</a></li> </ul>
Poly-ethylene powder (PEP)	Vendor via order form from scientific store	<ul style="list-style-type: none"> <li>• 434264</li> <li>• Sigma Aldrich Inc., Oakville, Ontario</li> <li>• <a href="http://www.sigmaaldrich.com/canada-english.html">http://www.sigmaaldrich.com/canada-english.html</a></li> </ul>
Agar	Scientific store	<ul style="list-style-type: none"> <li>• AGR003</li> <li>• BioShop Canada Inc., Burlington, Ontario</li> <li>• <a href="http://www.bioshopcanada.com/default.asp">http://www.bioshopcanada.com/default.asp</a></li> </ul>
Alginate powder	Vendor via phone	<ul style="list-style-type: none"> <li>• Accu-Cast, Oregon, USA</li> <li>• <a href="http://www.accu-cast.us/tempsite2/MainPages/BuyNowAlginates.html">http://www.accu-cast.us/tempsite2/MainPages/BuyNowAlginates.html</a></li> </ul>
Ethylene glycol	Scientific store	<ul style="list-style-type: none"> <li>• E178</li> <li>• Fisher Scientific Company, Ottawa, Ontario</li> <li>• <a href="https://www.fishersci.ca/Default.aspx">https://www.fishersci.ca/Default.aspx</a></li> </ul>
TX-150	Vendor via phone	<ul style="list-style-type: none"> <li>• Balmar Llc, Lafayette, Louisiana, USA</li> <li>• Tel: +0001 337-232-2496</li> </ul>
Bactine (bactericide)	Pharmacy store	<ul style="list-style-type: none"> <li>• Bayer Inc., Toronto, Ontario</li> </ul>

#### 2.4. *Tissue-specific Recipes*

All the recipes derived from the glycerin phantom recipe have glycerin as the percentage base value. All other materials are given as percentage weight calculated with respect to glycerin. This is because the percentages of deionised water (DIW) and PEP are changed to tune dielectric properties. Agar also changes with PEP to obtain optimum homogenous thick solution that can solidify into a phantom with definite shape. These ingredients are hence termed variants of the recipe. For other non-glycerine recipe ratios, the materials are given as quantities in a specific test batch.

The ratios for each tissue are given in easy look-up tables. Tissues important for physical breast phantom are considered. As stated before, NaCl is not added in all the phantom recipes mimicking healthy tissues to curb the loss as measured by the probe. Salt is included in malignant tissue recipe to generate a contrast. However, if these recipes are to be used at frequencies below 3 GHz or require more loss salt can be used as an additional variant to create large contrasts in conductivities.

As stated before, these recipe ratios have been changed to work in the UWB (3 GHz to 10 GHz for our purposes) and are different from that in [7]. It is also important to state before the results are viewed that phantoms usually are made for narrowband purposes. For example, a specific phantom recipe ratio at 900 MHz is used in cellular telephony. Whereas, for microwave imaging, we consider broadband experiments with frequency hopping from 3 GHz to 10 GHz.

The target models for the dielectric properties of breast tissues are discussed in chapter 2, i.e., the one-pole Debye models for the three tissue groups inside breast [2], and the four-pole model of skin and muscle from [1]. For skin, it is safe to consider the dry skin model. The wet-skin model has too high permittivity that can diminish the penetration of the signals. Secondly, it is to be expected clinically that some antiseptic (e.g. alcohol) will be used to sanitize the breast surface and equipment during microwave measurement. This dehydrates the skin. Also, the sensors developed by our team (discussed in chapter 6) work without the need of liquid coupling mediums.

At this stage, it would be beneficial to revisit the target dielectric properties of the major breast tissues given by the theoretical models. The dielectric constants of malignant tissue, muscle, fibro-glandular (FG), skin, transitional tissue and fat are shown in Figure 3.2. The conductivities of the same tissues are plotted together in Figure 3.3. It is noticed that the dielectric properties ( $\epsilon_r$  and  $\sigma$ ) of transitional tissue and skin (both under IWCT) almost overlap. It cannot be expected to have different phantoms for these two tissues. The recipes for healthy tissues are broadly divided according to water content as:

- (a) HWCT-1 is the recipe for highest water content healthy tissue phantom for breast phantom i.e., muscle. It is given in Table 3.2.
- (b) HWCT-2 is the highest water content healthy tissue inside breast phantom, which is group 1 in chapter 2 also termed as fibro-glandular (FG) tissue. It is given in Table 3.3.

(c) IWCT is the intermediate water content tissue phantom, same for both skin and transitional tissue. It is given in Table 3.4.

(d) LWCT is for lowest permittivity and loss tissue phantom i.e., adipose fat in breast. It is given in Table 3.5.

If skin is to be modeled with parameters of wet skin given in chapter 2, the HWCT-2 recipe can be used for skin instead of IWCT. In conclusion, HWCT recipes (HWCT-1 and HWCT-2) have water as the highest component, IWCT recipes have water and glycerine in equal parts, and LWCT uses none or very minimal water. A small amount of water is used in Table 3.5 as it seems that water reinforces the polymer matrix and speeds up the solidification. The LWCT phantom is still the softest of all phantoms and needs more time for solidification. But it is able to retain its shape. Table 3.6 gives the recipe for the fat-gel phantom material by [13]. However, this phantom was much weaker mechanically than the LWCT phantom, whereas in the paper it was claimed that the fat-gel phantom can retain its shape. It seems to require a shell. The visual comparison of the fat-gel phantom and the LWCT phantom is given in Figure 3.4.

Table 3.7 and Table 3.8 give the recipes for simulating malignant tumors. There are two similar recipes where one uses alginate powder (malignant-1) in saline and the other uses gelatin powder in saline (malignant-2).



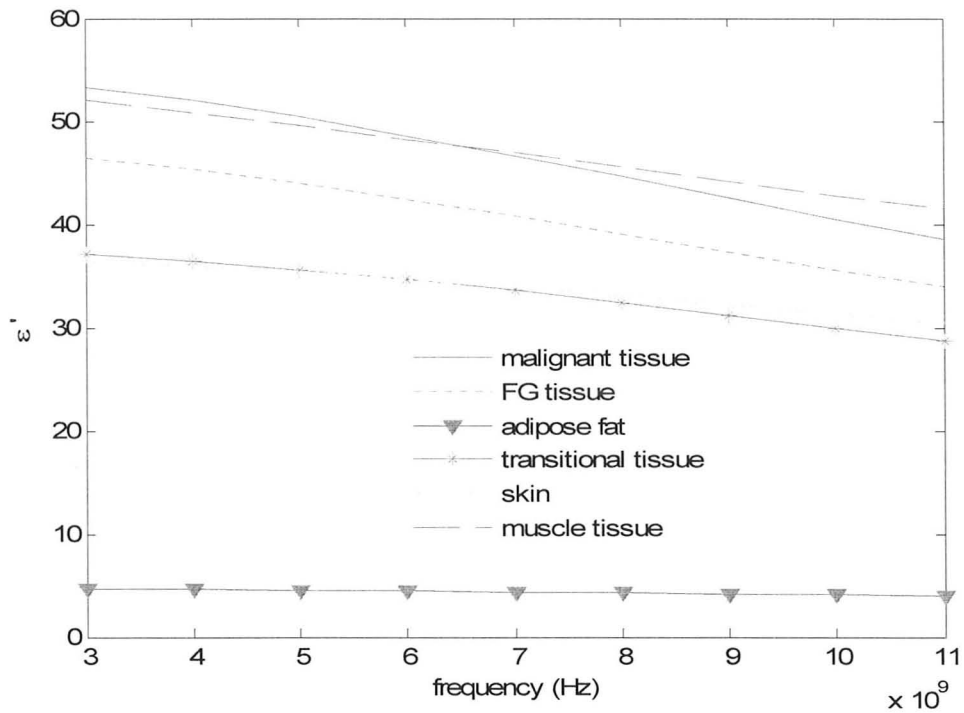


Figure 3.2: Dielectric constants ( $\epsilon'$ ) from chapter 2 of all major breast tissues.

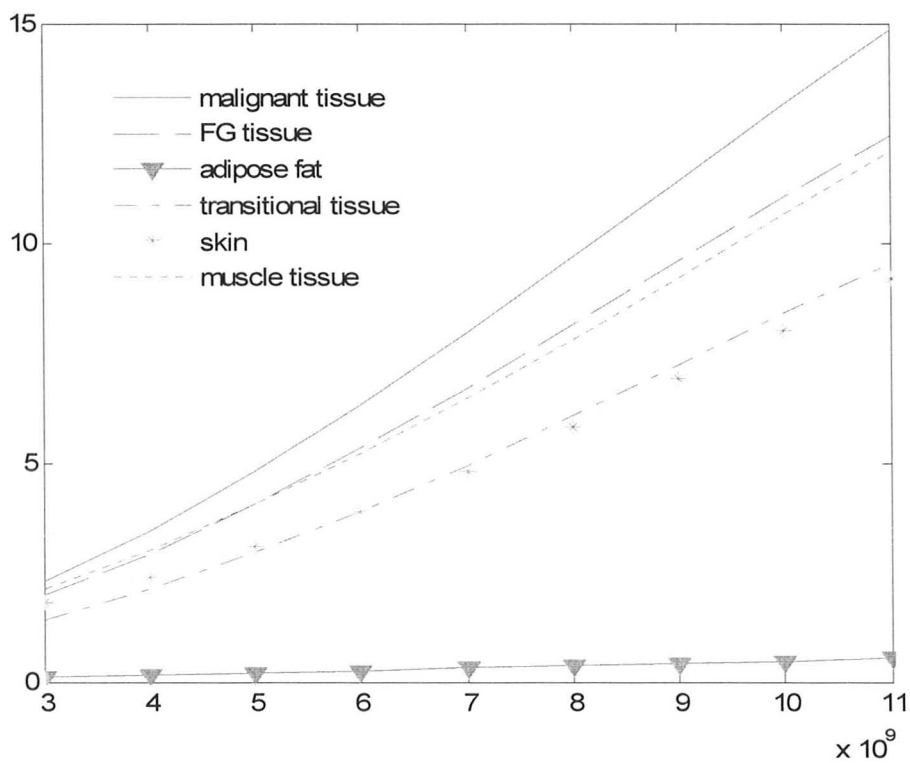


Figure 3.3: Conductivities ( $\sigma$ ) from chapter 2 of all major breast tissues.

TABLE 3.2: RECIPE RATIO FOR HWCT-1.

Materials	Weight % Based on Glycerine
Glycerine	100
DIW	180
PEP	15
Agar	12

TABLE 3.3: RECIPE RATIO FOR HWCT-2.

Materials	Weight % Based on Glycerine
Glycerine	100
DIW	140
PEP	14
Agar	11

TABLE 3.4: RECIPE RATIO FOR IWCT.

Materials	Weight % Based on Glycerine
Glycerine	100
DWI	100
PEP	8
Agar	8

TABLE 3.5: RECIPE RATIO FOR LWCT.

Materials	Weight % Based on Glycerine
Glycerine	100
DIW	8
Ethylene Glycol	52
PEP	10
Agar	11.5

TABLE 3.6: RECIPE FOR FAT-GEL FROM [13].

Materials	Quantity
Cooking Oil	100 ml
DIW	100 ml
Detergent	20 ml
TX-150	5 g
Agar	10 g

TABLE 3.7: RECIPE RATIO FOR MALIGNANT-1.

Materials	Quantity
Alginate Powder	18 g
DIW	100 g
NaCl	0.7 g

TABLE 3.8: RECIPE RATIO FOR MALIGNANT-2.

Materials	Quantity
Gelatine	7 g
DIW	100 g
NaCl	0.7 g

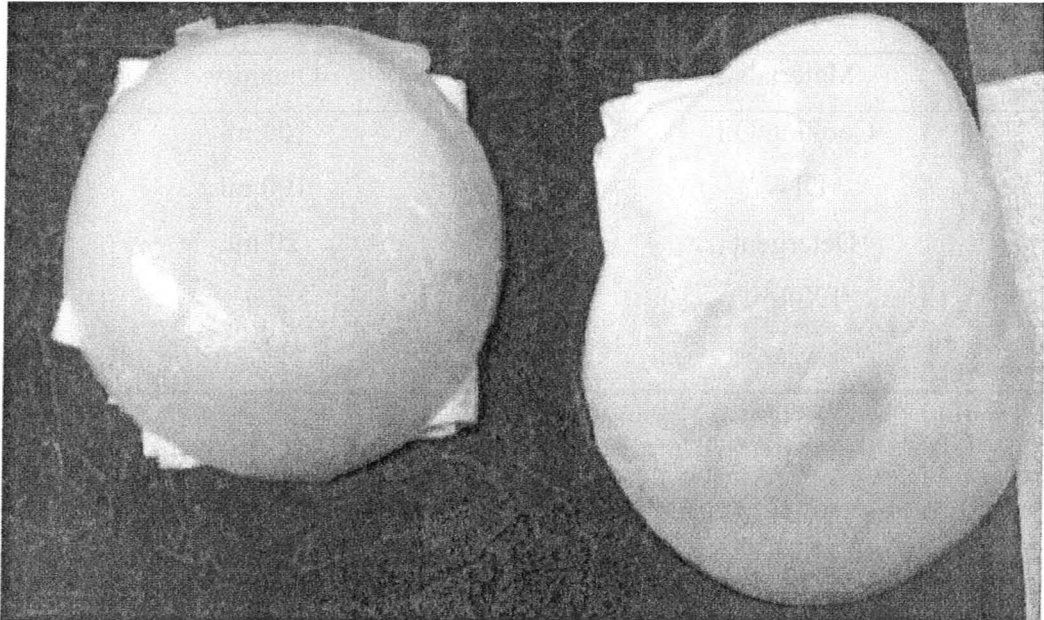


Figure 3.4: The structure of LWCT (left) is more firm and solid in comparison to Fat-gel from [13] (right).

## 2.5. Generic Fabrication Procedures

### 2.5.1. Procedure for glycerine phantom recipes (Table 3.2, Table 3.3, Table 3.4, Table 3.5):

There can be two methods of fabrication depending on the size of the phantom batch to be made. If the total volume of phantom mixture is below 800 ml, the following manual methodology of fabricating the phantom can be adopted (it was the only used method initially so as to set specific ratios of powders in the recipes):

- Wear gloves, lab goggles and a lab coat. Follow standard laboratory safety regulations.
- Pour DIW into a suitable glass flask (narrow opening of flask is preferred to a

cylindrical beaker so as to restrict air bubbles) and put it on a low flame on a burner. A mesh is recommended over a burner to avoid direct contact of the flask with flame. It is essential for better control of temperature.

- Pour all liquids relevant to recipe and stir to form a clear solution. Heat the solution to approximately 46°C.
- Add bactericide (a few drops) and stir it to a clear solution.
- Add the powder reagents, which are the mixture of PEP and agar for these recipes. The powder mixture is added in tiny amounts to the liquid mixture. The mixture is stirred continuously, gently and carefully to form a homogenous solution with as less bubbles as possible. Near the solidification point the bubbles escape. Do not stir very briskly or hard as this weakens polymerization reaction and phantoms are susceptible to easy breakdown post fabrication.
- Once the mixture is homogenous and thick, pour it in a suitable mould by holding the hot flask with a tong or cloth. Usually the temperature reached is in the range 68°C to 75°C. After initial cooling, keep the phantom in refrigerator for solidification via faster cooling. HWCT-1 and HWCT-2 take the shortest time while LWCT takes the longest time for solidification.
- Cover the mould with vinyl/plastic film once the phantom solidifies. Also use high quality plastic wraps (such as Para-film) to store the phantom post fabrication for longer use.

If a typical phantom batch is above 800 ml, it is recommended to use an

automatic kitchen food processor for blending the powder mixture of PEP and agar into the liquid mixture. The intermediately sharp kneading blade or chopping blade can be used as they not cause frothing and air bubbles. The procedure is as follows:

- Pour DIW into a suitable glass flask (bigger one in this case) and put it on a low flame on a burner. A mesh is recommended over a burner to avoid direct contact of the flask with flame. It is essential for better control of temperature.
- Pour all liquids relevant to recipe and stir to form a clear solution. Heat the solution to 88°C. High temperature is required as there cannot be any heat supply to the food processor.
- Add bactericide (a few drops) and stir it to a clear solution.
- Pour the liquid mixture into the food processor jar. Add the PEP/agar mixture and start churning the mixture at 5 RPM (on a scale from 2 RPM to 14 RPM). The food processor jar has a narrow opening for adding the powder mixture bit by bit. A weigh boat can be used for adding the mixture.
- As the ratios of powders are already set-up for achieving solidification, the phantom mixture is ready to be kept for cooling once all the mixture is added and mixed well by the non-frothing blade of the processor. After this follow the standard process for pouring the phantom into specific shaped moulds as discussed before.

#### 2.5.2. Procedure for other recipes (Table 3.6, Table 3.7 and Table 3.8)

The procedure for the fat-gel recipe in Table 3.6 is similar to the above mentioned procedure except that the powdery mixture is that of agar and TX-150. The procedure for malignant tissue phantoms is as follows:

- Pour water in a flask and heat it to a warm temperature.
- Dissolve salt in it and make a clear solution.
- Add a few drops of bactericide and put off the flame.
- For gelatine-based recipe, dissolve the gelatine powder directly in warm saline solution and set it to solidify. Whereas, for alginate powder, first let the saline cool down to room temperature and then dissolve the alginate powder quickly in saline to form a thick mixture. The alginate powder solidifies within 10 seconds. Hence immediately scoop out the alginate-saline mixture in specific mould. If this is not done in time, the only way to use the phantom is by cutting specific shapes from the solidified phantom chunk. This is not a big issue considering that irregular and random shapes are what malignant tumours have to model.

## 2.6. *Measurement Related Theory and Protocol*

The measured dielectric property is defined by the complex relative permittivity, which is written as:

$$\hat{\epsilon} = \epsilon'_r - j\epsilon''_r \quad (1)$$

The real part is called the dielectric constant and the imaginary part is a measure of the dielectric losses. These are often expressed as the tangent of the loss angle  $\theta$ :

$$\tan \theta = \frac{\epsilon_r''}{\epsilon_r'} = \frac{\sigma}{\omega \epsilon_r' \epsilon_0} \quad (2)$$

Here,  $\sigma$  is the equivalent electrical conductivity in S/m given as:

$$\sigma = \omega \epsilon_0 \epsilon_r'' \quad (3)$$

where  $\epsilon_0$  is the permittivity of free space and  $\omega$  is the angular frequency. The measurements with a dielectric probe give  $\epsilon_r'$  and  $\epsilon_r''$ .  $\epsilon_r''$  is converted to  $\sigma$  by (3). These measured values are directly compared with values from theoretical dielectric models.

The dielectric parameter models shown in Figure 3.2 and Figure 3.3 are approximated over multiple measurements where statistically assessed median values are fitted to either a Debye or a Cole-Cole model. Hence the values and trend of dielectric properties is a mathematical fit to measurement results. It cannot be expected that a single measurement of a phantom can exactly trace the dispersive properties. The controlling factor in phantom recipes is water (all water considered in this chapter is de-ionized water as discussed under sub-section 2.3. of this chapter). This is true macroscopically in tissue dielectric properties too as water is the key influence in microwave range. However, the exact cellular and metabolic processes of *in vivo* tissues cannot be exactly imitated with only water and other non-biological materials of the recipes. The idea is more to have a consistent contrast of dielectric properties among tissue groups. For instance, the malignant tissue should have some contrast in permittivity  $\epsilon_r$  and conductivity  $\sigma$  compared to the healthy HWCT inside the breast (which is fibro-glandular).



Similarly, the phantom mimicking adipose fat, must be lowest in permittivity and conductivity compared to other phantoms.

The phantoms were measured within 24 hours of fabrication. The measurement protocol is started with “three standard” calibration of the dielectric probe (probe) discussed in sub-section 2.1. of this chapter. The measurement is for 51 linear samples in the frequency range from 3 GHz to 10 GHz. The measurement is conducted by placing the solid phantom sample in complete contact with the probe’s aperture. There is always some variation and errors in the measurements due to cable motion artifacts, material adhesion to the probe’s aperture, local heterogeneity in phantom samples, calibration mistakes, instrument’s noise and so forth. To minimize these errors, a refresh calibration was conducted after every measurement and full calibration was conducted after a set of measurements on specific phantom recipe (HWCT-1, HWCT-2, etc.). For the results in the next section, the final measurement was recorded that appeared to occur consistently at multiple sites on the phantom sample placed below the probe’s aperture. The final recorded measurement curves showed least variation and ringing effects. The recorded dielectric properties of a phantom recipe hence came from a particular measurement from some arbitrarily selected site on the phantom. There is no averaging or data-fitting done over: (i) measurements for multiple samples, (ii) measurements for different sites on same phantom, and (iii) recurrent measurements at particular phantom site. These phantom measurement curves are plotted in comparison with theoretical dielectric models in the figures

in the next section.

### 3) RESULTS – TARGET AND ACHIEVED PARAMETERS

Figure 3.5 shows the comparison for both dielectric constant and conductivity between four-pole Cole-Cole model [1] for muscle and measurement on HWCT-1 phantom. Figure 3.6 shows the comparison between one-pole Debye model for FG [3] and a measurement on HWCT-2 phantom. Figure 3.7 shows the comparison between four-pole Cole-Cole model for dry skin, one-pole Debye model for transitional tissue [3] and measurement on IWCT phantom. It can be seen from these graphs that they do not exactly trace the model curves but trace them in proximity. The loss seems to be on higher side and hence the decision to not use the salt in recipes is justified. This loss is however supposed to go down as the phantom dries and loses some water. Figure 3.8 shows the comparison between one-pole Debye model for adipose fat and measurement on LWCT phantom. The trend traced by the phantom measurements is similar to model but the values are higher. However this can mimic the real case as it was discussed in chapter 2 that recent studies [2] seems to show that both dielectric parameters go down for fat post excision due to presence of extracellular water. Hence these properties might be closer to *in vivo* properties.

The properties of fat-gel phantom from [13] seem to be more different from the ideal case as shown in Figure 3.9. This can be due to the fact that the paper simulates this phantom in a lower frequency range. This makes the fat-gel

phantom recipe unusable for our purposes due to both weak mechanical strength and too high dielectric properties. However, water can be lowered in the recipe ratio or substituted for by glycerin etc., if an alternate jelly phantom is desired. This has not yet been tried in fabrication by us.

Figure 3.10 and Figure 3.11 compare the dielectric properties of malignant tissue [3] and the two recipes – gelatin-saline recipe and alginate powder-saline recipe. The measurements show that phantom measurements trace the model values well but are slightly higher. This is in fact beneficial considering:

- There is no glycerin to preserve the loss of moisture making these phantoms more susceptible to lower dielectric property values, as water dries out.
- The losses are higher for healthy tissue phantoms and hence to keep some contrast in measurements it is required to increase the values.

To introduce even more loss (conductivity), it is recommended to increase the amount of salt in the recipes. This increase in salt should be done in small increments and tested to see if the dielectric properties meet the requirement. The dependence of the dielectric parameters on the variants – water, salt and PEP is non-linear due to complexity of mixture of the recipe. The precise prediction of quantity of variants affecting the dielectric properties may require formulas fitted to multiple phantom measurements or special software to generate multi-dimensional gradient maps of quantities of variants versus dielectric properties at multiple frequencies generated based on several measurements. This has not been done presently, but may be done in future if these phantom recipes are chosen to

be used in clinical trials for the purpose of system calibration. However, as has been discussed in chapter 2, the *ex vivo* studies are not the final word on breast tissue properties and the target values might change with *in vivo* studies and associated dielectric models.

The overall comparison of the dielectric parameters of all phantoms is shown in Figure 3.12 and Figure 3.13. Compare these to Figure 3.2 and Figure 3.3. This shows that the current phantom work is able to mimic the theoretical contrast from *ex vivo* studies.

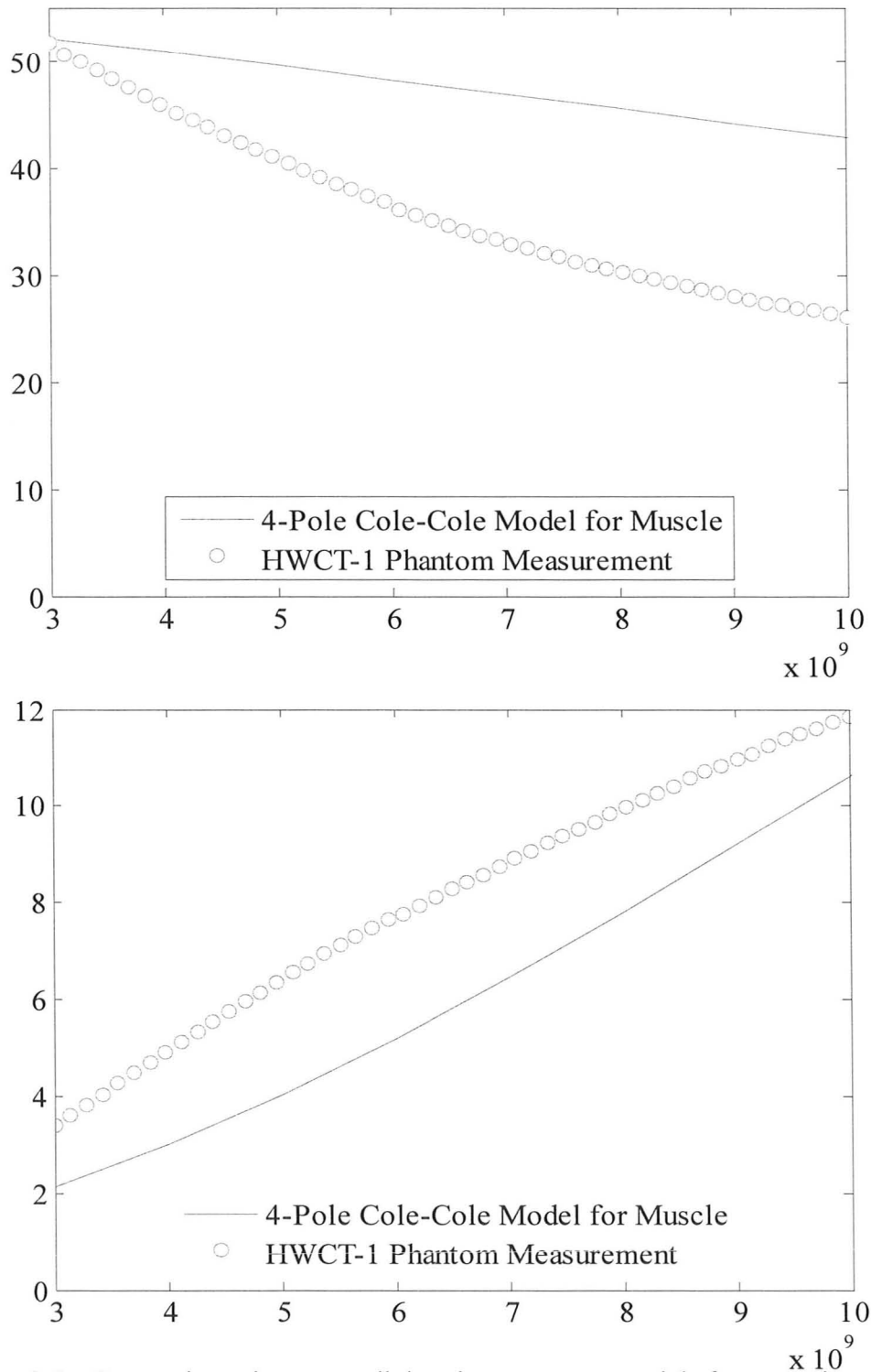


Figure 3.5: Comparison between dielectric property model for muscle and phantom measurement for HWCT-1. The top graph is for dielectric constant and the bottom graph is for conductivity.

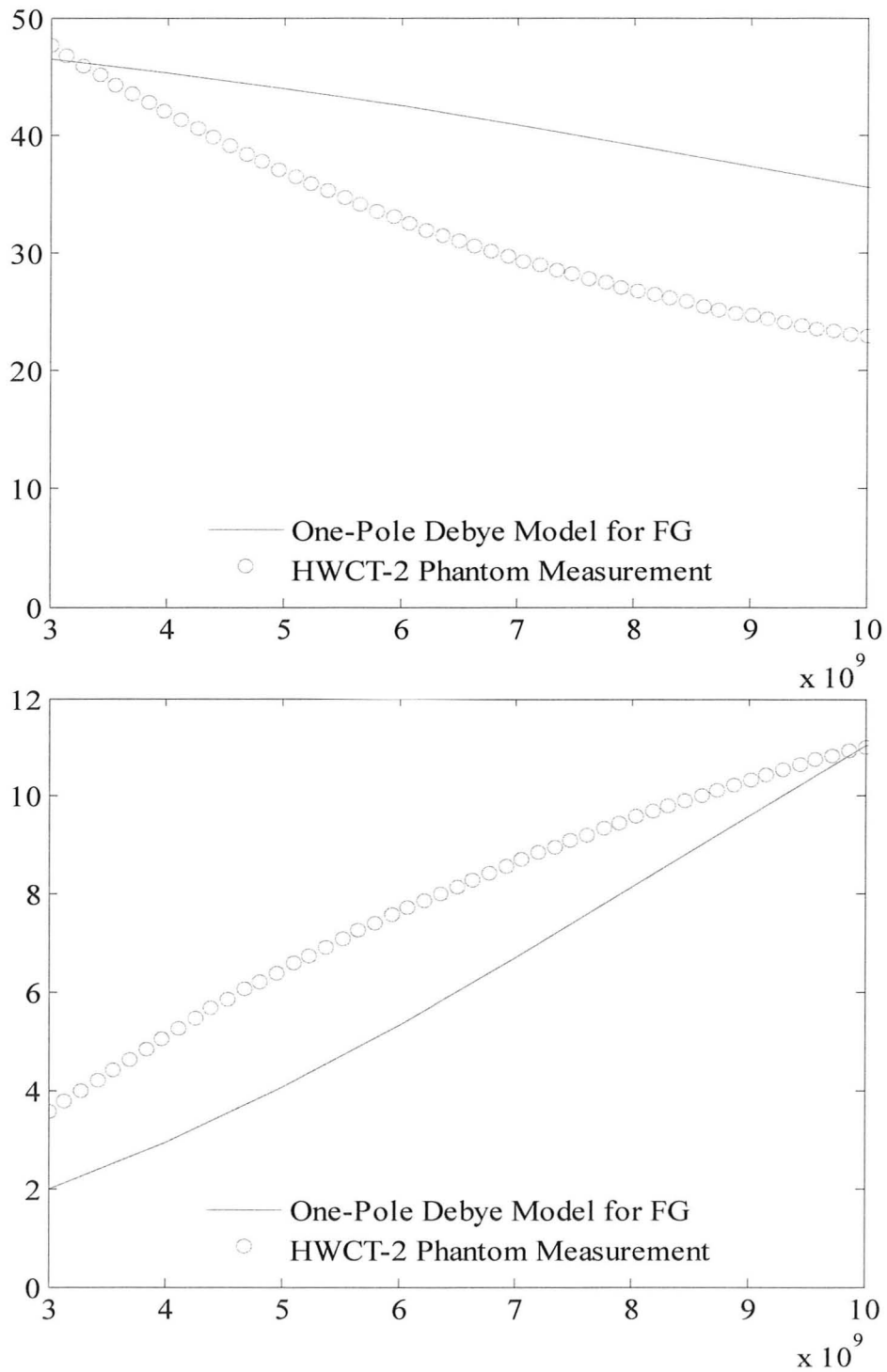


Figure 3.6: Comparison between dielectric property model for FG and phantom measurement for HWCT-2. The top graph is for dielectric constant and the bottom graph is for conductivity.

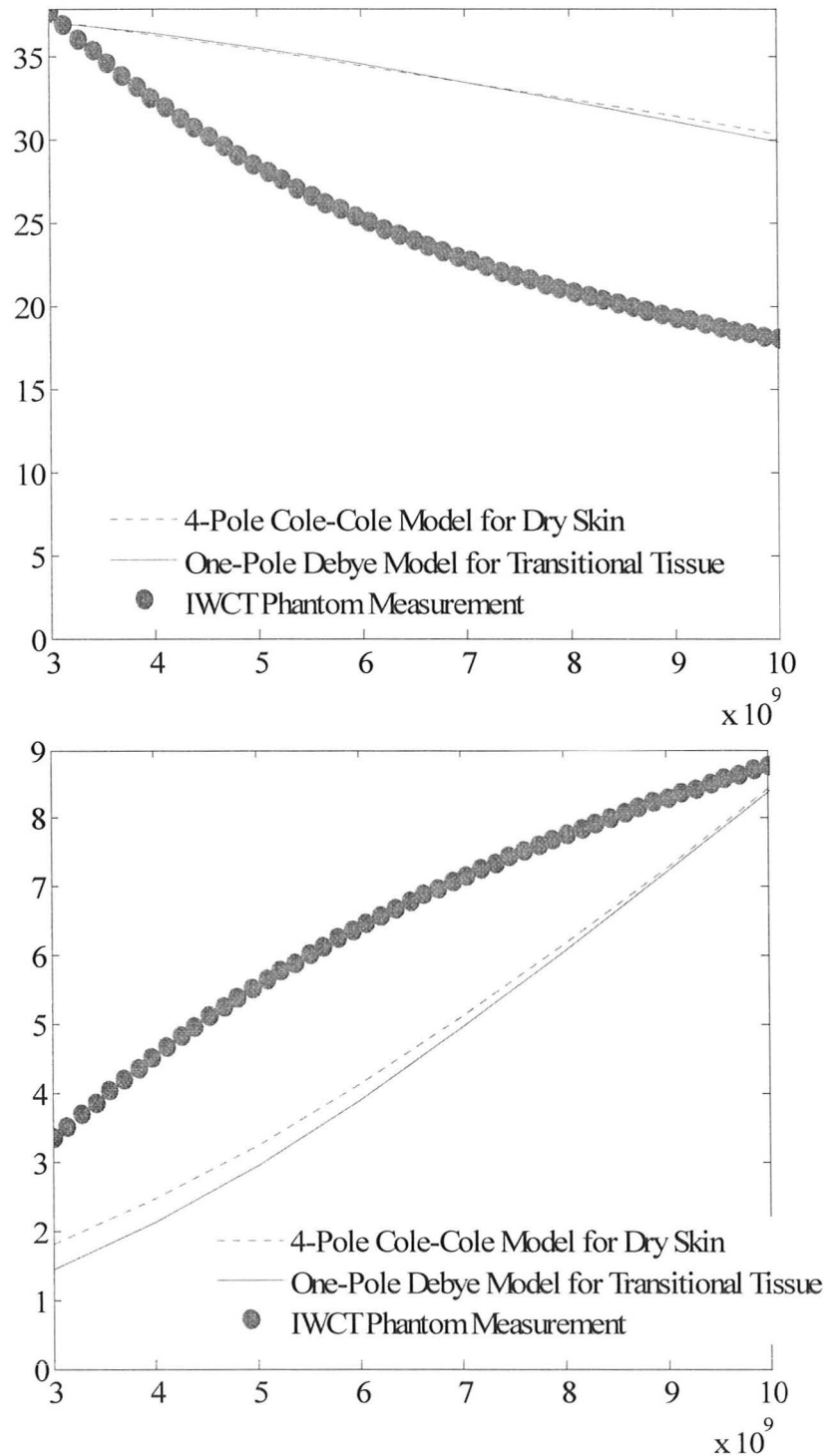


Figure 3.7: Comparison between dielectric property model for skin, transitional tissue and phantom measurement for IWCT. The top graph is for dielectric constant and the bottom graph is for conductivity.

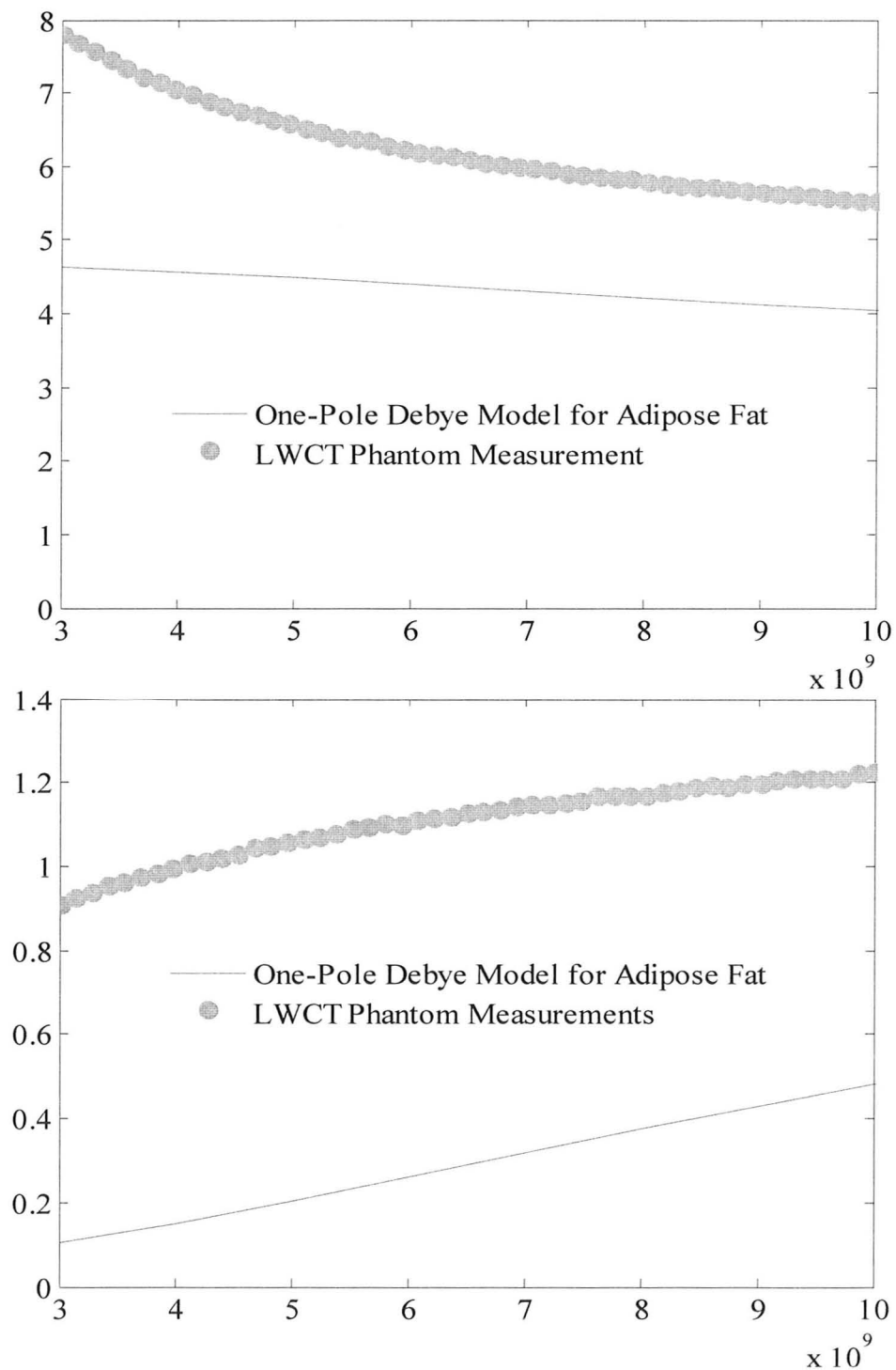


Figure 3.8: Comparison between dielectric property model for adipose fat and phantom measurement for LWCT. The top graph is for dielectric constant and the bottom graph is for conductivity.



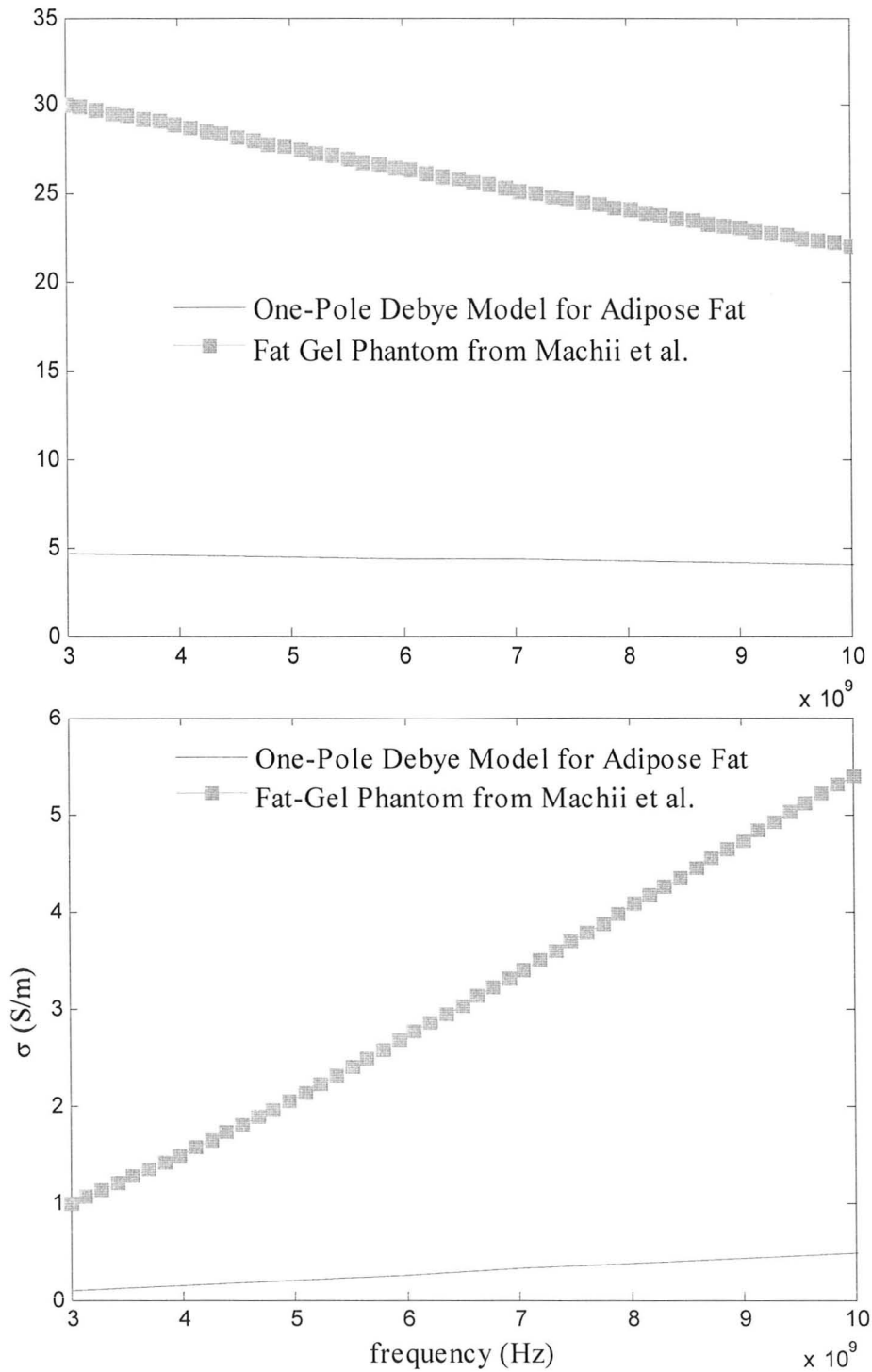


Figure 3.9: Comparison between dielectric property model for adipose fat and measurement for fat-gel phantom [13]. The top graph is for dielectric constant and the bottom graph is for conductivity.

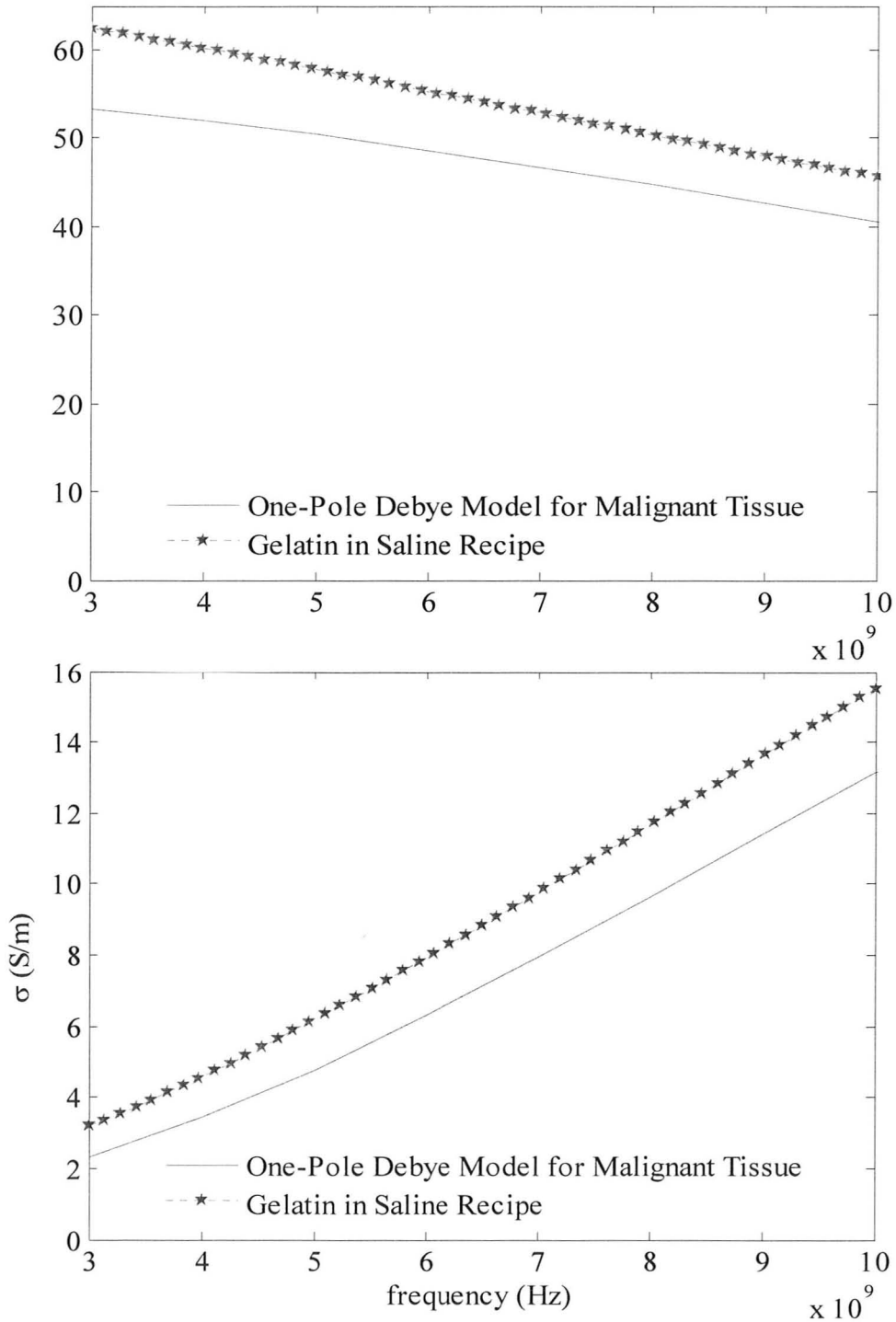


Figure 3.10: Comparison between dielectric property model for malignant tissue and phantom measurement for gelatin-saline recipe. The top graph is for dielectric constant and the bottom graph is for conductivity.

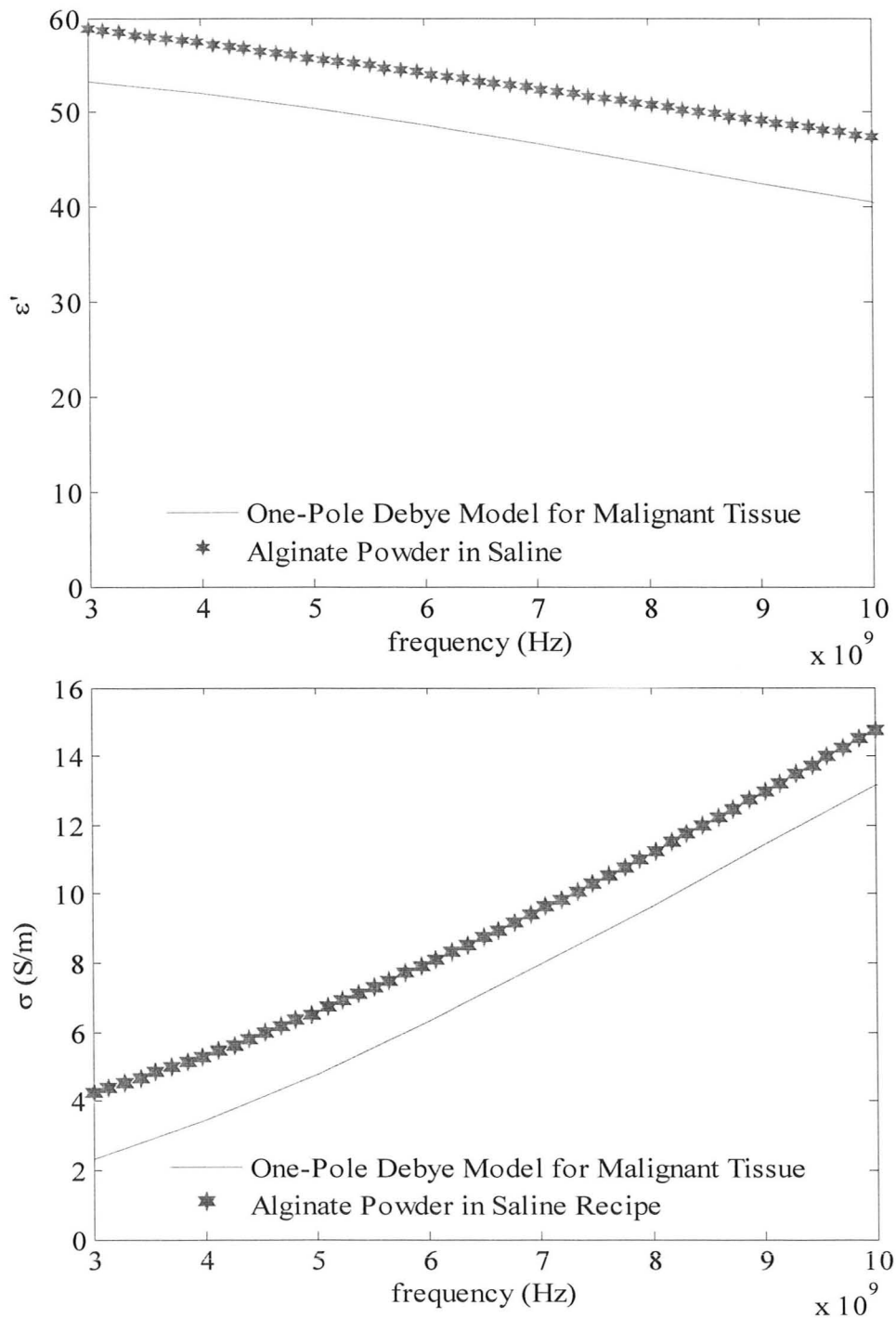


Figure 3.11: Comparison between dielectric property model for malignant tissue and phantom measurement for alginate powder-saline recipe. The top graph is for dielectric constant and the bottom graph is for conductivity.

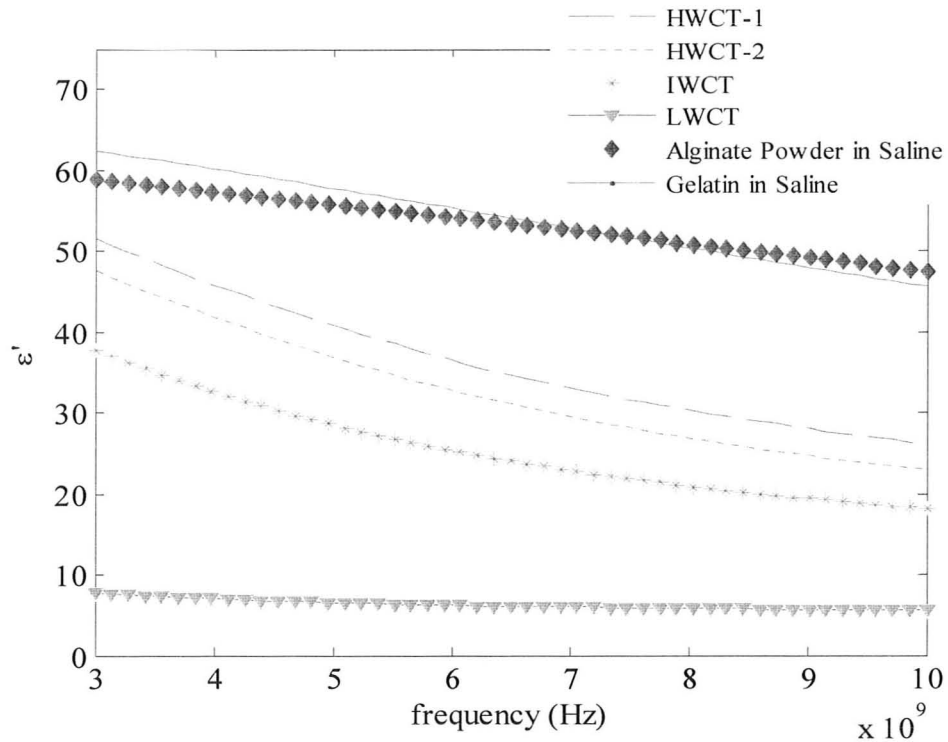


Figure 3.12: Dielectric constants ( $\epsilon'$ ) for all phantom recipes of breast tissues.

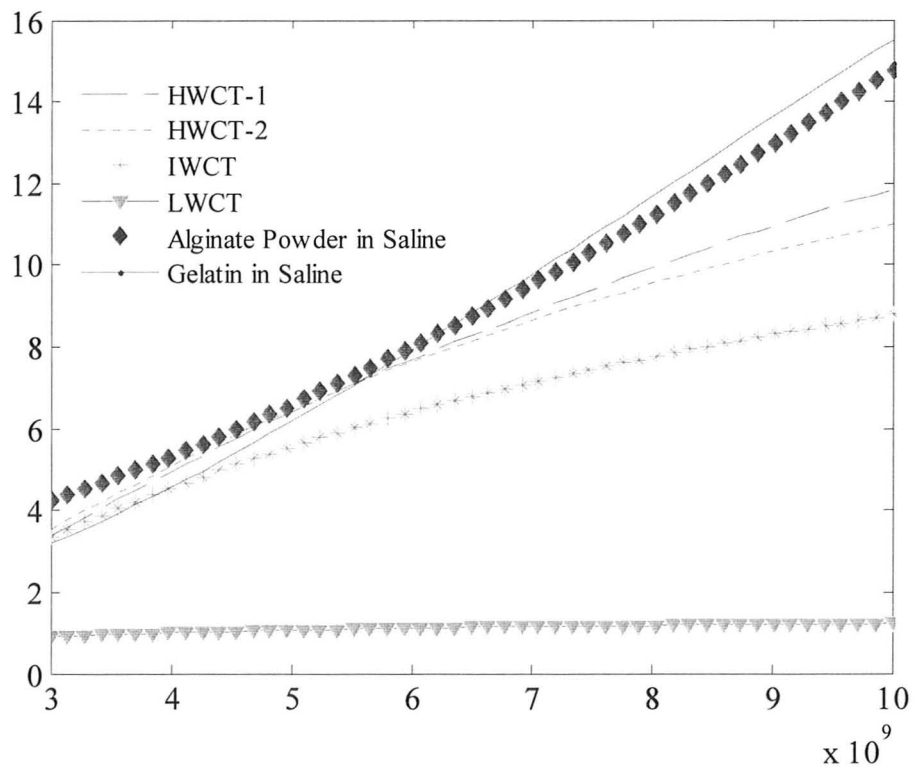


Figure 3.13: Conductivities ( $\sigma$ ) for all phantom recipes of breast tissues.

#### 4) PROMISING EXAMPLES AND FUTURE WORK

This section shows some examples of fabricated phantoms and their uses. Various phantom shapes will also be seen in chapter 4 where they are used to test the photogrammetry-based three-dimensional (3-D) surface acquisition system. Figure 3.14 shows malignant tissue phantoms with alginate powder (opaque pink) and gelatin (translucent) in small bowls. Also it shows two homogenous IWCT phantoms, where one of them has an alginate powder–saline based scatterer.

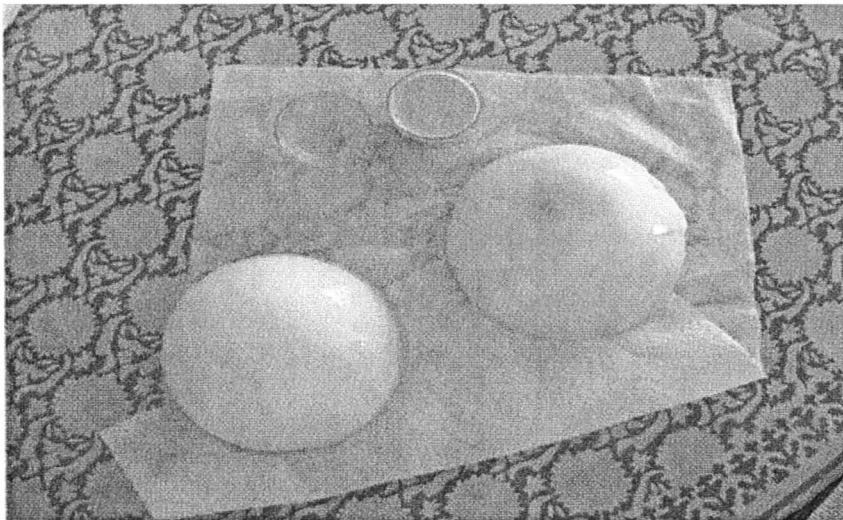


Figure 3.14: Phantoms mimicking malignant tumors, healthy homogenous breast and homogenous breast with a scatterer.

As can be seen in the figure above, the glycerin phantoms have a very shiny appearance and are mostly white/off-white in color. Artificial colors can be used to distinguish between different phantoms (HWCT, IWCT and LWCT). This also facilitates to make realistic variety of physical breast phantoms. The food colors

are good choices in this regard. These colors have water as base and chemicals such as sodium benzoate. A few drops should not affect the dielectric properties of phantoms in a significant manner. However, these colors can only be used for HWCT and IWCT recipes to avoid any tampering with LWCT. This is because LWCT requires having as low permittivity and loss as possible and these color drops can affect the delicate balance achieved. Hence colors can be added to all other phantoms, whereas, LWCT mimicking fat can stand different in its original color.

Figure 3.15 shows the appearance of phantoms before and after color addition (yellow and green). Figure 3.16 shows the comparison of properties of a pair of HWCT-2 phantoms where one of them has the food color added to it. It shows that the properties do not change and are within the nominal experimental variation.

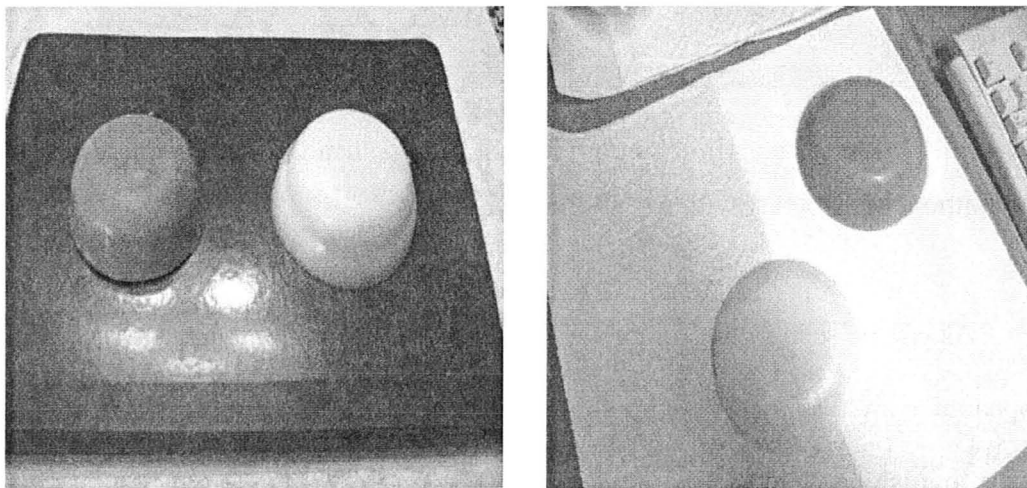


Figure 3.15: Phantoms with and without food color: (a) green and (b) yellow.

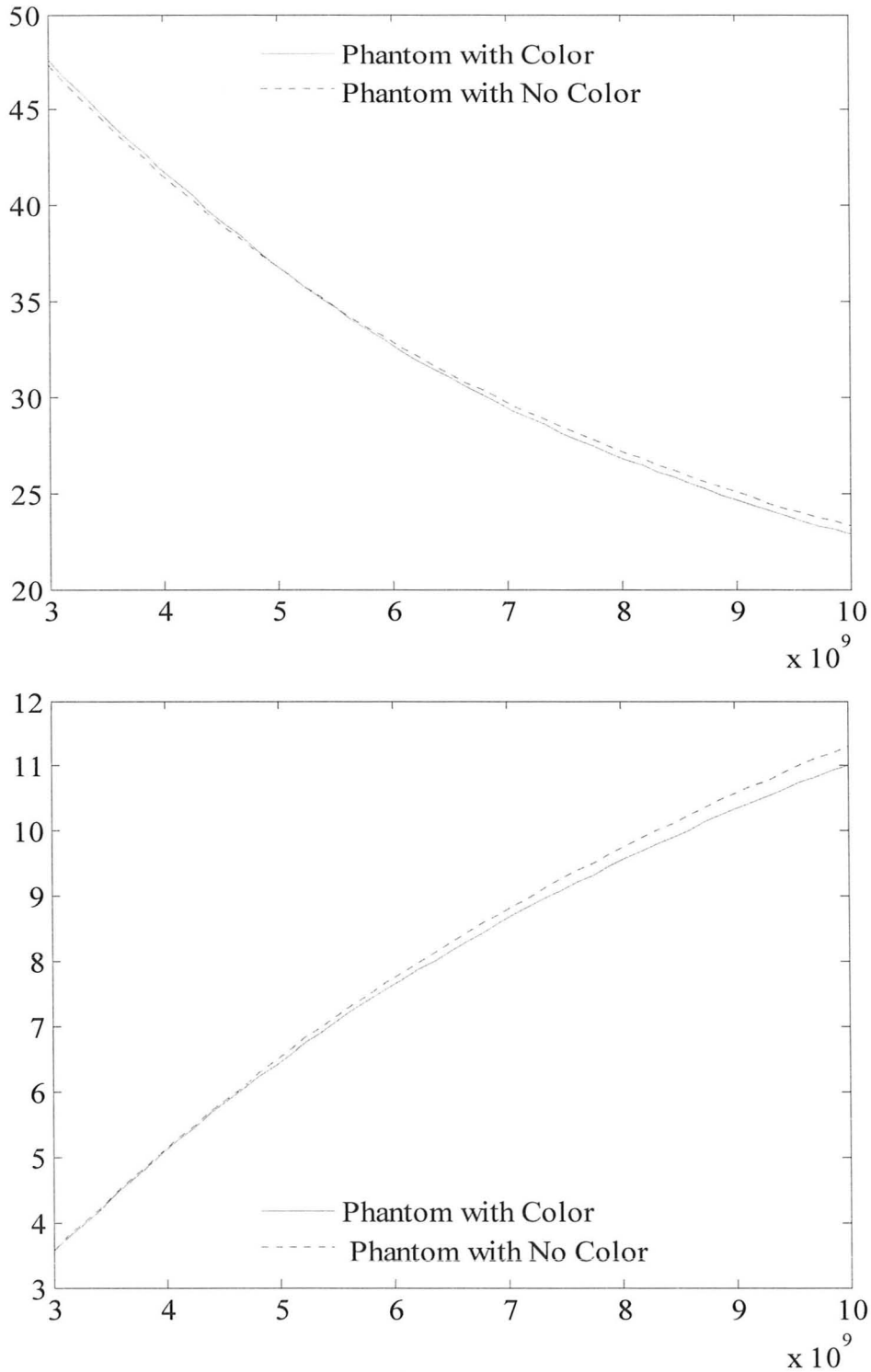


Figure 3.16: Comparison between dielectric parameters measurement on HWCT-2 phantoms – with and without food color. The top graph is for dielectric constant and the bottom graph is for conductivity.

Figure 3.17 shows the use of a two-layer phantom comprising a thin IWCT (skin) layer and a thick LWCT (fat) layer. This phantom was used to test the recently designed antenna 0 in our group that works without coupling medium. The lack of coupling medium makes the use of antennas more practical for clinical use, considering patient safety and sanitation. The sensor is placed in direct contact with the solid phantom layers as it has to be placed in direct contact with patient's breast in clinical scenario. We intend to design optimal imaging arrays for scanning arrangements with this antenna. Work is currently in progress toward real-aperture scanning procedures. For designing and optimizing the imaging array many different shapes and structures of test phantoms might be required to be placed in contact with the antennas. This is where our cheap and easy to make phantoms are helpful.

Physical phantoms can be as simple as two-media phantom or something intricate to resemble specific breast density. Also, shapes can be multiple depending on antenna scanning arrangements: (i) a flat layered phantom for parallel plate scanning arrangement; (ii) a cylindrical phantom for cylindrical scanning arrangement; (iii) bowl shaped or hemispherical phantoms for a symmetrical imaging arrangement [20], shown in Figure 3.18 (a) and, (iv) random convex shapes for tapered arrangement [21], shown in Figure 3.18 (b). This tapered imaging chamber has been integrated with an Alderson Treatment Brassiere cup [23] used in radiation therapies. This brassiere can be used to fit any random shape of solid phantoms and is quite select for mimicking real case



scenario.

The phantoms developed through this work are easy to make, replaceable, to some extent resemble the dielectric properties of breast tissues and reproduce well the contrast from HWCT to IWCT to LWCT. In fact, these phantoms are worse case scenarios than the real case. If the system designed for detection works with them, the clinical trials have a sure chance of success. Once an antenna arrangement and measurement procedure is finalized, a permanent phantom can be made with dry microwave materials from Emerson & Cuming [22]. This can be a standard phantom for microwave imaging along the same lines as the ones available for mammography [23], [24]. Also, exact knowledge of the complexity the phantom should exhibit is essential. A complex phantom from the demonstrated phantom recipes and methodology is shown in Figure 3.19.

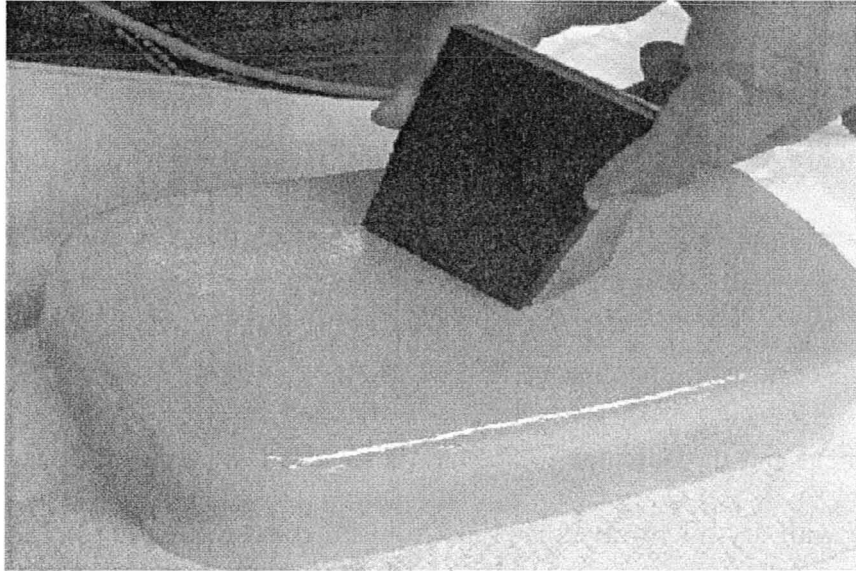
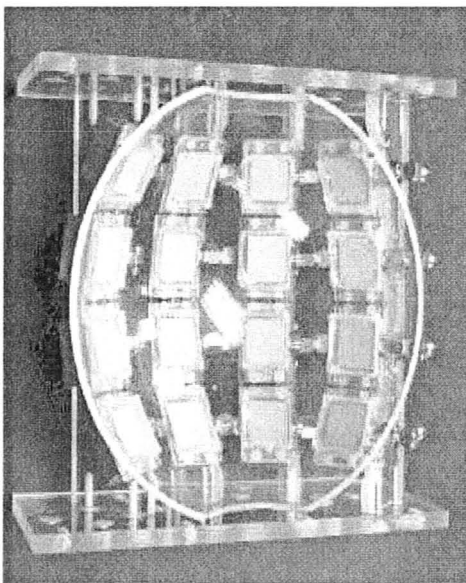
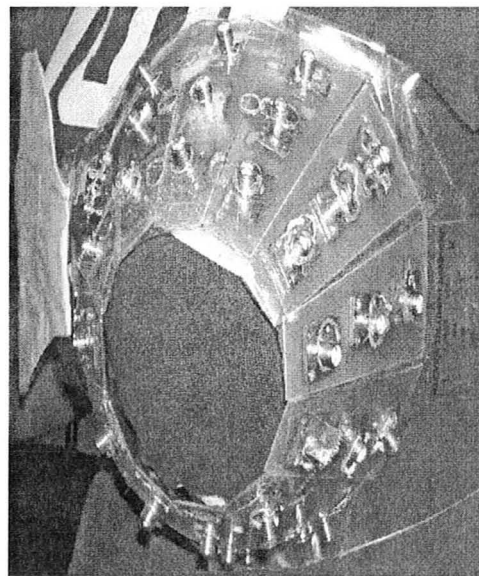


Figure 3.17: Simple layered phantom in contact with a recently designed antenna used in 0[19].



(a)



(b)

Figure 3.18: Imaging array designs in the literature: (a) symmetrical curved (bowl-shaped) antenna array (from [20]); and (b) tapered imaging chamber integrated with an Alderson Treatment Brassiere cup (from [21]).

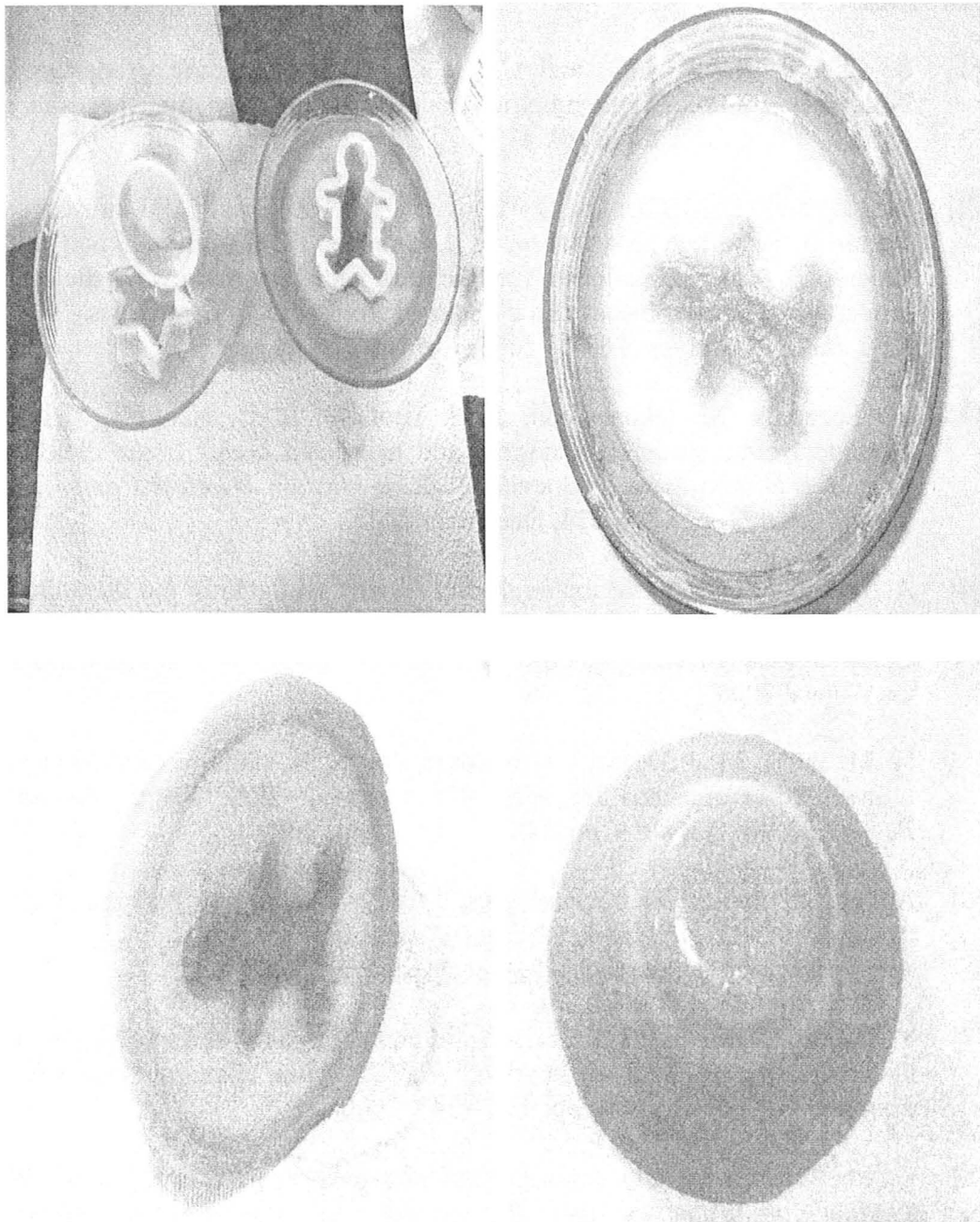


Figure 3.19: The top two images show the snapshots of the process of fabricating more detailed breast physical phantom. The bottom two images show the views of the phantom created. The yellow phantom layer is IWCT for skin; white interior phantom is LWCT for fat and the green-fill phantom is HWCT-2 for fibroglandular tissue.

---

**REFERENCES**

- [1] S. Gabriel, R. W. Lau, and C. Gabriel, “The dielectric properties of biological tissues: III. Parametric models for the dielectric spectrum of tissues,” *Phys. Med. Biol.*, vol. 41, pp. 2271 – 2293, April 1996.
- [2] M. Lazebnik, L. McCartney, D. Popovic, C. B. Watkins, M. J. Lindstorm, J. Harter, S. Sewall, A. Magliocco, J. H. Brooske, M. Okoniewski and S. C. Hagness, “A large – scale study of the ultra wideband microwave dielectric properties of normal breast tissue obtained from reduction surgeries,” *Phys. Med. Biol.*, vol. 52, pp. 2637 – 2656, April 2007.
- [3] M. Lazebnik, M. Okoniewski, J. H. Brooske, S. C. Hagness, “Highly accurate Debye models for normal and malignant breast tissue dielectric properties at microwave frequencies,” *IEEE Microw. Wireless Comp. Lett.*, vol. 17, no. 12, pp. 822 – 824, December 2007.
- [4] A. Trehan, “Summary of materials and recipes available in the literature to fabricate biological phantoms for RF and microwave experiments,” Computational Electromagnetics Res. Lab., McMaster University, CEM-R-45, August 2008.
- [5] H. M. Jafari, M. J. Deen, S. Hranilovic, and N. K. Nikolova, “A study of ultrawideband antennas for near-field imaging,” *IEEE Trans. Antennas Propagat.*, Vol. 55, no. 4, pp. 1184 – 1188, April 2007.
- [6] Agilent ADS, Agilent Technologies, 1400 Fountaingrove Parkway, Santa Rosa, CA 954031799, USA. [Online]. Available: <http://www.home.agilent.com/agilent/home.jsp?cc=US&lc=eng>.
- [7] Y. Okano, K. Ito, and H. Kawai, “Solid phantom composed of glycerin and its application to SAR estimation,” *IEICE Trans. Commun. (Japanese Edition)*, Vol. J83-B, no. 4, pp. 534 – 543, 2000.
- [8] K. Ito, “Numerical and experimental human body phantoms,” *2007 IET Seminar on Antennas and Propagation for Body-Centric Wireless Communications*, April 2007.
- [9] Y. Okano, K. Ito, I. Ida, M. Takahashi, “The SAR evaluation method by a combination of Thermographic Experiments and Biological Tissue-Equivalent Phantoms,” *IEEE Trans. Microwave Theory Tech.*, vol. 48, no. 11, pp. 2094 – 2103, November 2000.
- [10] T. Onishi, R. Ishido, T. Takimoto, K. Saito, S. Uebayashi, M. Takahashi and

- K. Ito, "Biological tissue-equivalent agar-based solid phantoms and SAR estimation using the thermo graphic method in the range of 3-6 GHz," *IEICE Trans Commun*, vol. E88-B, no. 9, pp. 3733 – 3741, September 2005.
- [11] G. Hartsgrove, A. Kraszewski, and A. Surowiec, "Simulated biological materials for electromagnetic radiation absorption studies," *Bioelectromagnetics*, vol. 8, pp. 29 – 36, 1987.
- [12] M. G. Bini, A. Ignesti, L. Millanta, Olmi R, N. Rubino, R. Vanni, "The polyacrylamide as a phantom material for electromagnetic hyperthermia studies," *IEEE Trans Biomed. Eng.*, vol. 31, no. 3, pp. 317 – 322, March 1984.
- [13] Y. Machii, H. Aoki, K. Koshiii, "Fat thickness estimation method using bio electrical property examination by gel phantom model test," *2006 International Symposium on Micro-NanoMechatronics and Human Science*, November 2006.
- [14] J. W. Lagendijkt, P. Nilssoni, "Hyperthermia dough: a fat and bone equivalent phantom to test microwave/radiofrequency hyperthermia heating systems," *Phys. Med. Biol.*, vol. 30, no. 7, pp. 709 – 712, February 1985.
- [15] J. M. Sill, E. C. Fear, "Tissue sensing adaptive radar for breast cancer detection - experimental investigation of simple tumor models," *IEEE Trans. Microw. Theory Tech.*, vol. 53, no. 11, pp. 3312 – 3319, November 2005.
- [16] ASTM International, 100 Barr Harbor Drive, West Conshohocken, PA, 19428-2959 USA. [Online]. Available: <http://www.astm.org/>.
- [17] Product Selector – Laboratory Water Types. Millipore Corporate Headquarters, Billerica, MA 01821, USA. [Online]. Available <http://www.millipore.com/labwater/lw3/productselector>.
- [18] MATLAB™ 7.1, The MathWorks Inc., 3 Apple Hill Drive, Natick, MA, 2005. [Online]. Available: <http://www.mathworks.com/>.
- [19] R. Khalaj Amineh, A. Trehan, and N. K. Nikolova, "TEM horn antenna for ultra-wide band microwave breast imaging," *Progress In Electromagnetics Research B*, vol. 13, 59 – 74, 2009.
- [20] M. Klemm, I. J. Craddock, J. Leendertz, A. W. Preece, R. Benjamin, "Breast cancer detection using symmetrical antenna array," *IEEE International Symposium on Antennas and Propagation (APS)*, July 2008.

- [21] J. P. Stang, W. T. Joines, Q. H. Liu, G. A. Ybarra, R. T. George, M. Yuan, and I. Leonhardt, "A tapered microstrip patch antenna array for use in breast," *IEEE International Symposium on Antennas and Propagation (APS)*, June 2009.
- [22] Emerson & Cuming Microwave Products, Inc., 28 York Avenue, Randolph, MA 02368 USA. [Online]. Available: <http://www.eccosorb.com/main/RegionalHome.html>.
- [23] Radiology Support Devices Inc., 1904 East Dominguez Street Long Beach, CA 90810 USA. [Online]. Available: <http://www.rsdphantoms.com/index.html>.
- [24] M. K. Hoevel, "Contoured mammography phantom with skin," U.S. Patent 4 655 716, April 7, 1987.

## **CHAPTER 4**

# **THREE-DIMENSIONAL (3-D) SURFACE AND SHAPE ACQUISITION WITH PHOTOGRAMMETRY**

### **INTRODUCTION**

Active microwave imaging (AMWI) techniques for early detection of breast cancer are promising [1]. They rely on sufficient contrast between the dielectric properties of normal and malignant breast tissues at microwave frequencies as discussed in chapter 2. AMWI can be divided into two major categories: (i) radar based approaches [2]-[5] and (ii) tomographic approaches [6]-[10].

In radar-based imaging, the breast is illuminated with an ultra wide-band

(UWB) pulse, and the backscattered signal is recorded. This is usually repeated for a number of antenna positions. A time-shift-and-add algorithm is applied to the set of recorded signals in order to enhance returns from high-contrast (contrast in dielectric parameters) objects and reduce clutter in signals [2]. Because of the relatively large permittivity of the skin, scattering from its surface is a major clutter or noise component and a disturbing factor in the image reconstruction. This is also termed ‘skin clutter’. Special algorithms have to be developed to extract the location of the skin interface relative to the imaging array from the total backscattered signal. They are discussed in [2], [3], [11] and [12]. Simulations show that in order to achieve acceptable accuracy, complex geometric algorithms and scanning arrangements are required. The geometric algorithm discussed in [2] is one such example. The figure corresponding to this idea is shown in Figure 4.1. In this algorithm, the backscattered signals from the skin interface are recorded to estimate the propagation time from the antenna to the skin-breast interface. This propagation time locates the skin-breast interface on the sphere with known radius, where the antenna elements form the centers of the spheres. The skin surface is assumed to be convex and tangent to the sphere. These tangents are found mathematically by assuming that the spheres centered at adjacent antennas share the same tangent. This methodology is claimed to become more accurate if the antennas are sufficiently closely spaced relative to the curvature of the breast surface. This calls upon the need for complex antenna scanning scenarios with multiple antenna positions around the breast. For



example, in [11], one arrangement consists of 90 antenna positions and another (for an outline in the sagittal plane only) consists of 37 antenna positions. Experimental verification of these algorithms with realistic arbitrarily shaped objects is not yet available.

In tomographic breast imaging, the scattered microwave signals are usually measured in a phase-coherent way (complex  $S$ -parameters) using a vector network analyzer (VNA). Image reconstruction involves the solution of a nonlinear optimization problem where the optimizable parameters are the complex permittivities of all voxels within the imaged domain. The forward solvers are typically two-dimensional (2-D) or three-dimensional (3-D) numerical engines for high-frequency electromagnetic simulation [7]-[10]. The inversion problem is often ill-posed and extremely time consuming [11]. The main reason for the ill-posedness is the large number of optimizable parameters. The permittivity distribution is usually estimated on a dense mesh where the number of voxels in a 3-D problem may exceed tens of thousands. Thus, knowledge of the surface can drastically reduce the dimensionality of the inverse problem by providing physical constraints. This is done by assessing the volume for the solver where image reconstruction has to be performed.

Our group introduced a much simpler and easy to employ approach for 3-D surface acquisition of the imaged object. This approach is based on a well known method to reconstruct 3-D surface of any object from 2-D digital photos. It is called photogrammetry. The photogrammetry-based surface acquisition is simple

to implement and to automate. It operates on images obtained through standard inexpensive cameras, and, most importantly, the reconstructed surface is accurate to less than a millimetre. It also provides the relative position and orientation of the object with respect to the imaging antenna array.

The photogrammetry approach can greatly benefit both tomographic and radar-based imaging technologies. In radar-based imaging, knowing the shape and size of the breast as well as its relative position with respect to the imaging array will lead to more accurate skin-artifact removal without complicated antenna arrays. In tomographic imaging, this knowledge will reduce drastically the dimensionality of the inverse problem, thus leading to faster convergence and reduction of the number of local minima.

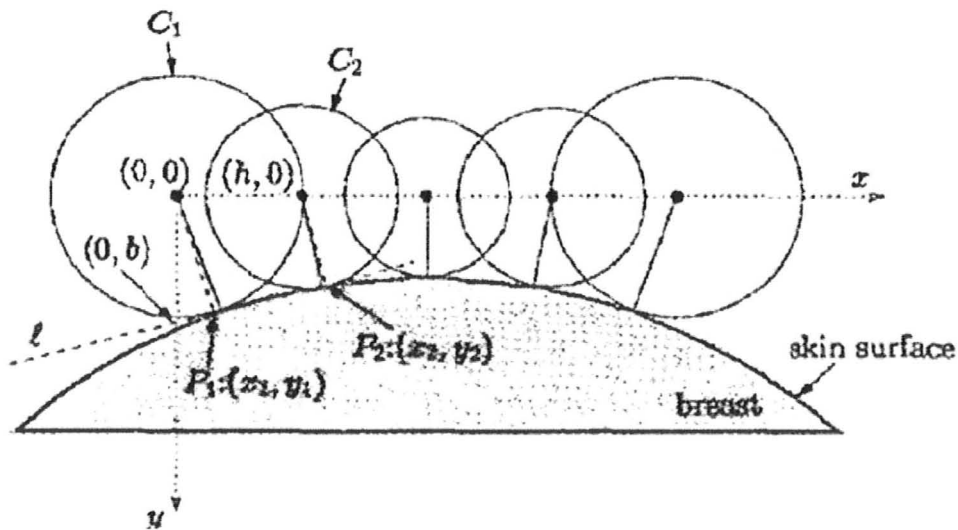


Figure 4.1: An illustration of geometric estimation algorithm for breast surface (taken from [2]).

This chapter discusses the photogrammetry approach implementation and the experimental results obtained and published with it. Section 1 discusses the software and hardware set up for this approach. Section 2 shows the reconstruction examples and accuracy assessment study. Section 3 illustrates the verification of the photogrammetry approach with forward electromagnetic (EM) models. Section 4 reports the work presented at two international conferences and the latest developments in this field.

## 1) SURFACE RECONSTRUCTION WITH PHOTOGRAMMETRY

The software used to recover the 3-D surface of a curved object from 2-D images taken with a digital camera is PhotoModeler Pro 5.2.3. [13]. This software, based on the photogrammetry technique, involves taking a few photos of the object at different viewing angles. The typical number of photos is from 12 to 16 for a mostly convex object. A detailed help manual specific to this software is given in a technical report [14]. Related aspects will be presented in a condensed form in the following sub-sections. The photogrammetry software is referred to as ‘PhotoModeler’ in the rest of the chapter.

### 1.1. *Software Requirements*

There are some key procedures when using the PhotoModeler. These are:

- (a) Camera calibration: This is the process of determining the characteristics of a camera so that it can be used as a measurement device. PhotoModeler can use photographs taken by different types of cameras. It needs the values for some

specific parameters of the camera, such as: (i) focal length of the lens, (ii) the digitizing scale (which is the CCD format size of a scanner or digital camera) and, (iii) the principal point (a point where the optical axis of the lens intersects the photograph). To get improved accuracy, parameters that describe the distortion characteristics of the lens are also used. Once a camera is calibrated, it provides accurate measurements. In a general scenario, if one camera is used with the same focal-lens setting under similar lighting conditions, then the calibration procedure needs to be conducted just once. The calibration settings can be saved and reused with the other 3-D modeling projects.

The calibration project uses a Calibration Grid which comes as ‘PhotoModelerCalibrationGrid.pdf’ in the install directory. Since our projects are within an area of one square meter, the grid can be printed on a standard Letter sheet (8.5”x11”). This grid is shown in Figure 4.2.

Approximately 8 landscape shaped photographs of the grid are taken with the camera held with horizontal orientation at the positions shown by the numbers in Figure 4.2. Also, 4 portrait shaped photographs are taken by flipping the camera by 90 degrees to hold it with vertical orientation at positions 1, 3, 5, and 7. The horizontally held camera stance is shown in Figure 4.3 (a) and vertically held camera stance is shown in Figure 4.3 (b). Figure 4.3 (c) shows the arrangement for taking each picture. The distance between the camera and the object is kept approximately between 35 cm and 45 cm, at an elevation angle of about 60 degrees [14].

After taking the pictures of the Calibration Grid, the calibration project is conducted. The details in [14] and the associated tutorial videos can facilitate the user to conduct, save, use and trouble-shoot the calibration project.

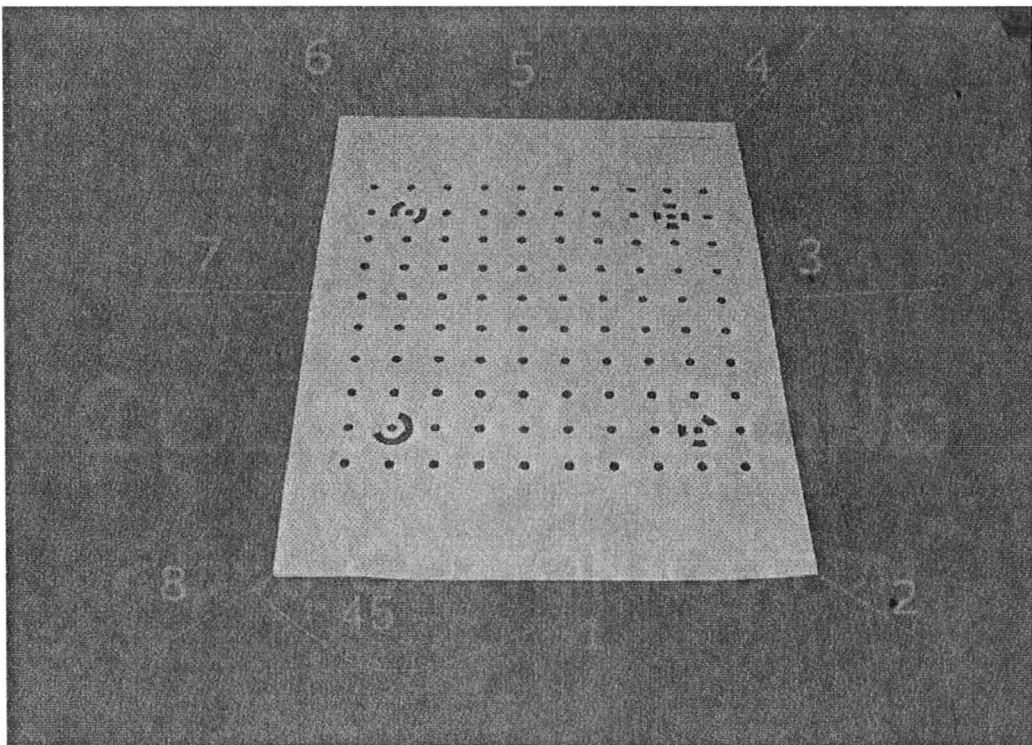
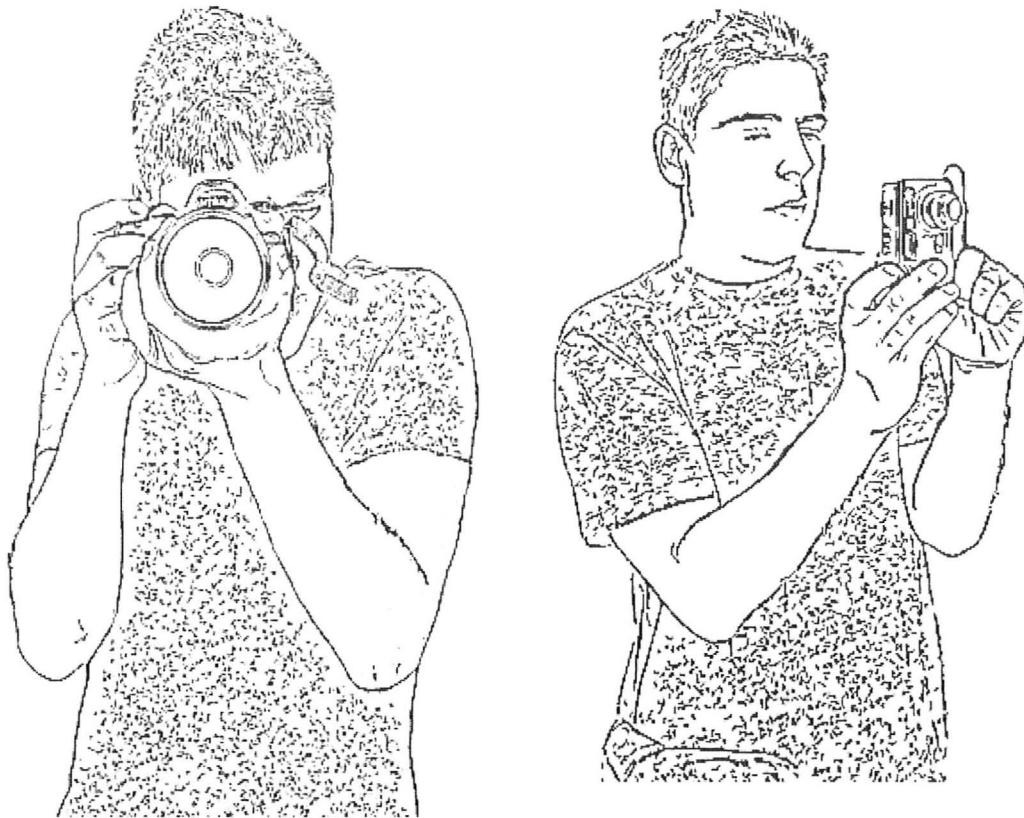
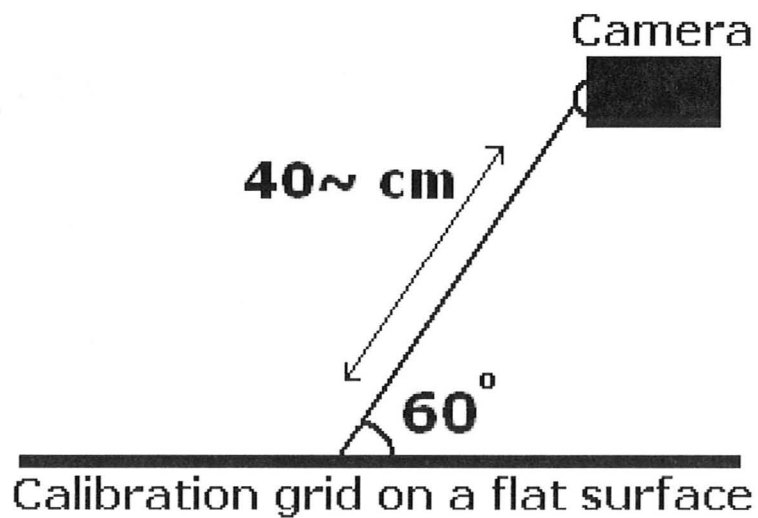


Figure 4.2: Calibration Grid sheet with positions marked for taking 2-D photos.



(a)

(b)



(c)

Figure 4.3: (a) Horizontally held camera (from [15]). (b) Vertically held camera (from [15]). (c) Position of camera with respect to Calibration Grid.

(b) Experimental set-up for 3-D modeling project: To acquire the shape of a random object, which would be the case with patient-specific breasts; the automatic tools of PhotoModeler are used. Examples for such randomly shaped objects were earlier taken as balloons and later as solid phantoms (discussed in chapter 3). The automatic tools in PhotoModeler require a particular set-up prior to taking 2-D photos from the digital camera. The object to be modeled requires a large number of circular targets positioned on it. These targets should have high contrast from the background. A dense grid of points facilitates in approximating the surface effectively. These targets can be something as simple as natural light stick-on as shown in Figure 4.4. In the next sub-section of this chapter, the use of a programmable grid is also discussed.

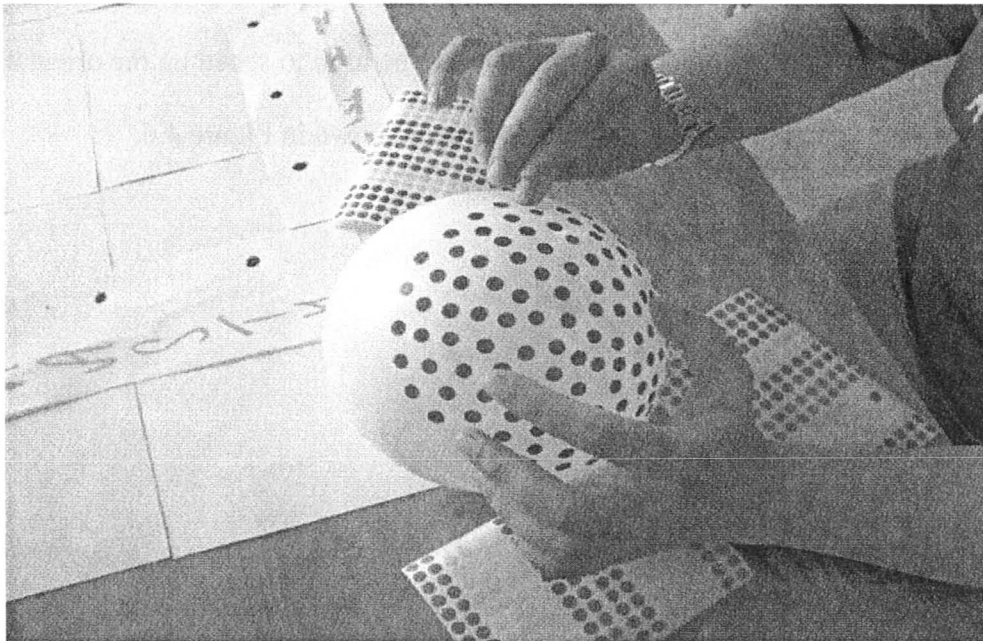


Figure 4.4: A photograph showing stick-on on a balloon.

The other key factor is the orientation process. A typical 3-D modeling project requires at least 15-16 photographs of the 3-D object from specific angles. The software requires knowing the position of the camera when each of these pictures is taken. This process is called orientation of photographs. To facilitate this, the user needs to design some points called control points along the periphery of the area where the object to be modeled is placed. In this design process, the user needs to assign some distinct tags to these points such as numbers or alphabets, so that they can be differentiated when the orientation process is carried out in the software. The process of designing these control points is shown in the photograph in Figure 4.5. These points also help in scaling and adding axes, when the final model is constructed in the software (explained later). A module available through PhotoModeler called coded targets is also a good option. These are circular targets with some additional bits that can be easily recognized by the PhotoModeler software. These targets can also be used to speed up the orientation process. An example of a typical coded target is shown in Figure 4.6.

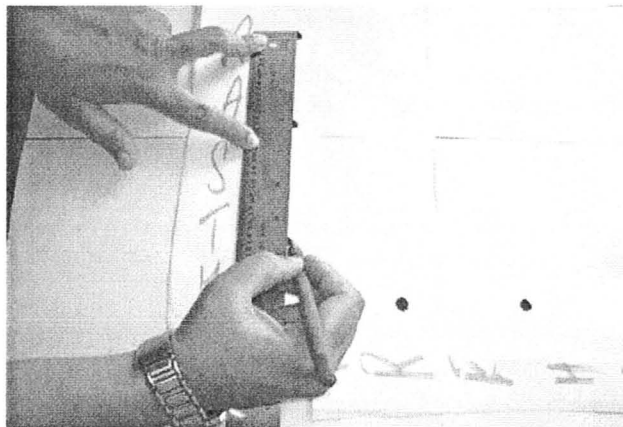


Figure 4.5: Photograph showing the designing of peripheral control points.



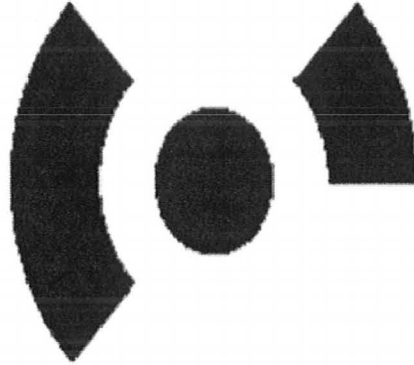


Figure 4.6: One of the 8-bit coded targets.

A final experimental set up for 2-D image acquisition is shown in Figure 4.7 with a balloon and in Figure 4.8 with a phantom. Approximately 12 photographs can be taken at positions 30 degrees apart. Additional 3 to 4 photographs for top views can be captured so that all control points are visible in some photographs for better orientation. The position of the camera should follow the guidelines shown in Figure 4.3. The focus, zoom settings, and sharpness settings are kept constant to what they were during the Calibration grid imaging. The purpose of following these procedures is standardizing a rule of thumb to get proper photographs, which can cover maximum number of circular targets on the object and the control points, with camera settings known to the software.

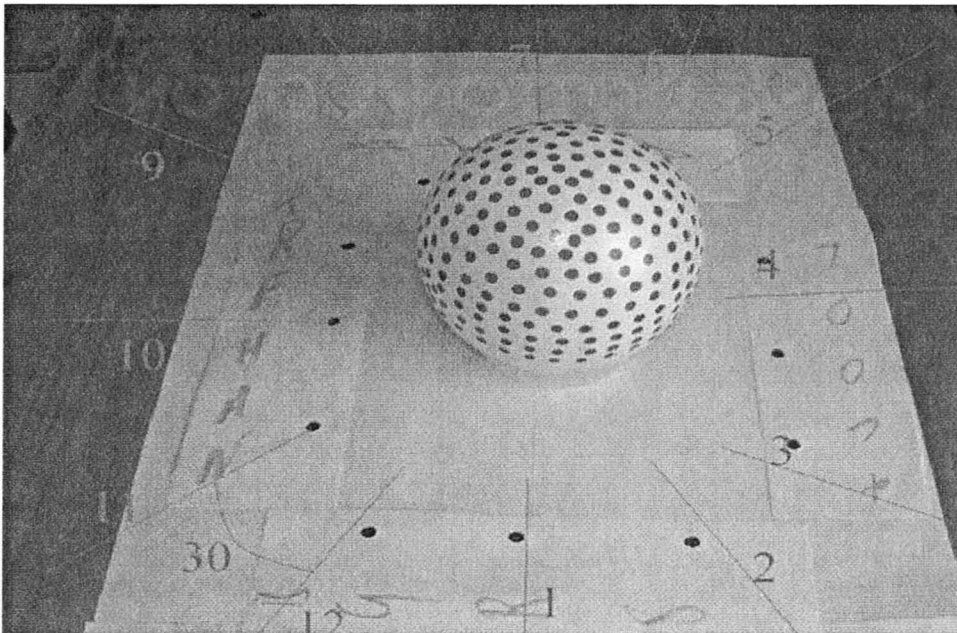


Figure 4.7: Photograph showing the final set-up with a balloon when the 2-D images for modeling can be taken.

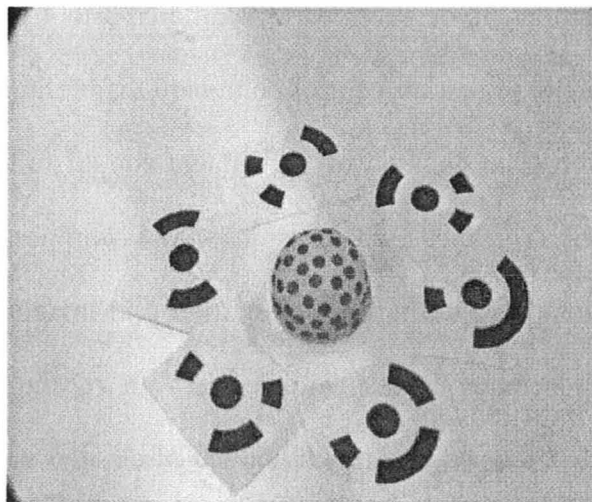


Figure 4.8: A phantom ready for 2-D image acquisition.

## 1.2. *Assistive Hardware and Software Components*

The photogrammetry procedure requires some hardware and software components to automate the 2-D image acquisition for accurate 3-D reconstruction. These components are given in detail in a technical report [16]. Here, their description is again mentioned in a condensed form:

(a) Camera: The camera is a Point Grey Research (PGR) Flea 2 [17]. Its maximum resolution is 1600x1200 pixels at 15 Hz (frames/second). However, the software with the camera allows no more than 1600x1200 pixels at 7.5 Hz. The lens is a Cosmocar TV Zoom lens. It has adjustable aperture, focus, and magnification. For our purposes, the camera is close to the photographed object, so it is left at the minimum magnification. The camera and the lens are shown in Figure 4.9 (a) and (b), respectively.

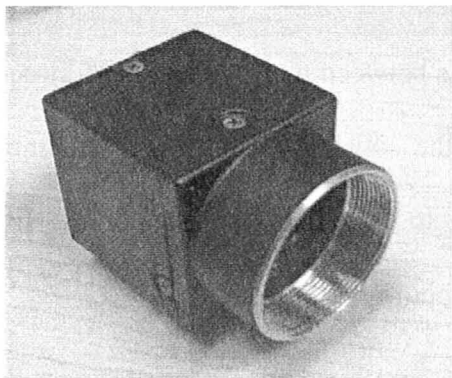
(b) Stand: To mount and rotate the camera, an ergonomic stand with a rotatable shoulder (turns around full 360 degrees) is designed. The views captured by the camera follow the guidelines discussed in the prior sub-section. The rotation of the shoulder mounting the camera is controlled by a stepper motor with labeled directional and power switches. The motor is powered by a 12 V lead-acid battery. The stand design in CAD software is shown in Figure 4.9 (d) and its view as in use is shown in Figure 4.9 (e).

(c) Dot Matrix and Take Pictures (TP) programs: A very easy to use program called Dot Matrix has been written in C#. It can make a re-sizable, flexible, and redraw-able grid of points that can be projected upon the object being

photographed. This is in reference to a more automatic way (compared to stick-on) to place the circular targets on random object being photographed as discussed in the previous sub-section. A typical example is shown in Figure 4.9 (c). The outer big dots are the control points and the inner smaller ones are the circular targets to be placed on the object. Coded targets can also be programmed and used as shown in Figure 4.9 (e). The grid in the same figure is projected by a mini-projector (Mitsubishi PK10) that does not come in the field of view of the camera. The grid can be made of any size and density by simple mouse controls and also dots can be changed to any color for better contrast. The details about the program are given in [16].

Another program that runs through command line is Take Pictures. It is abbreviated as TP. It takes pictures at regular intervals while the camera is rotating about the object. It is based on the code for PGRFlyCaptureTestCSharp. TP uses DLLs (Dynamic-link library) provided by PGR. When recompiling TP, it is to be ensured that all the necessary DLLs are made available in a directory where C# knows to look for them. For simplicity, if one is not familiar with DOS, TP can be directly invoked from Dot Matrix. The user has to just type the number of photographs desired to be taken in one of the options in the configuration box prompted upon compiling Dot Matrix. The command is executed by pressing the ‘Take Pictures’ button. The motor has to be started simultaneously so as to rotate the camera while TP acquires and stores the photos. It is recommended to select the number of pictures so as to complete one revolution about the imaged object

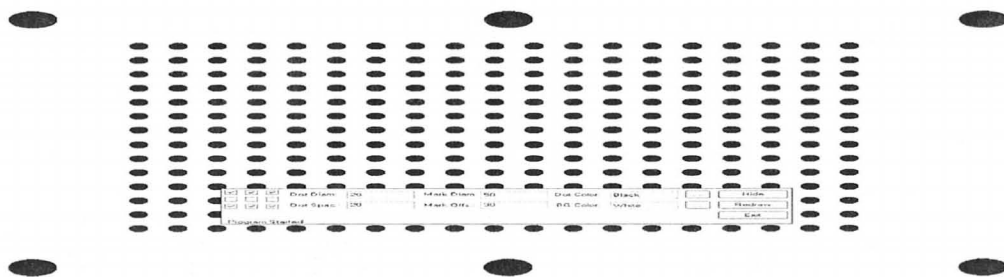
(for robust reconstruction). Also, one can use the option called ‘Timeout’, which is the amount of time the TP program waits between photographs in milliseconds. This can be calculated and modified in the source code as per the number of pictures required in one revolution. The photographs are saved in a bitmap format. The naming is according to the number of photos being taken.



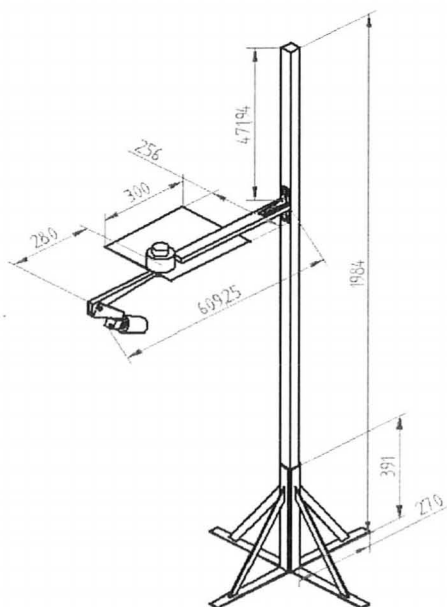
(a)



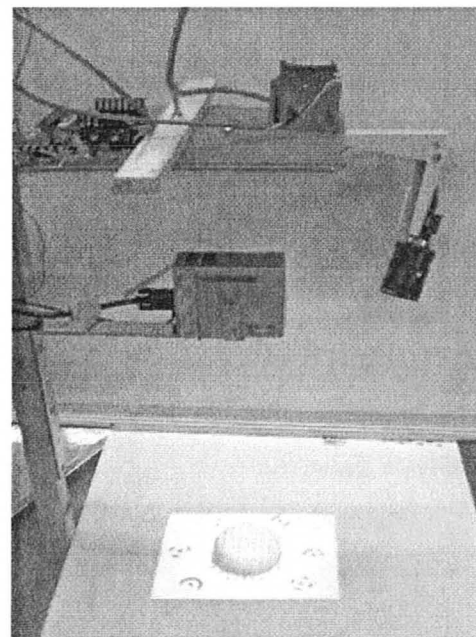
(b)



(c)



(d)



(e)

Figure 4.9: Components of the photogrammetry imaging set up: (a) PGR Flea 2 camera, (b) Cosmicar TV Zoom Lens, (c) dot matrix grid, (d) stand design (dimensions in mm), and (e) stand with projector in use.

The pictures are saved in a sub-folder of the main folder containing the TP and Dot Matrix programs. These pictures can then be immediately transferred to a suitable folder and renamed for later use.

### **1.3. *Generic Procedure***

So far, with the above sub-sections (1.1 and 1.2), the software for photogrammetry, PhotoModeler, has been described along with the components which make the 2-D image acquisition as automatic as possible. The 3-D modeling project in PhotoModeler is manual, but a skilled operator can obtain the 3-D surface from the 2-D images in about 20 minutes. For details on how to conduct the projects with PhotoModeler, please refer to the technical reports [14] and [16] as well as the tutorial videos associated with [14]. Here, a generic flow of steps is presented for converting the 2-D photos to a 3-D surface as a CAD model:

- Take pictures of the Calibration Grid and conduct the calibration project for the camera to be used in the 3-D modeling project. This can be a one-time step if the same camera is used for all the projects.
- Set up the object as per the requirements for 2-D image acquisition. All projects require orientation process and hence control points. The random object to be modeled also requires high-contrast circular targets. These targets can be either stick-on or dot-grid projected using the Dot Matrix program and a projector. The canonical shapes use specific shape tools and do not require circular targets.

- Run TP and start the motor to rotate the camera simultaneously. Take about 16 to 20 photographs as the camera completes one revolution about the object. Save these images (that are downloaded to the computer) in a suitable folder.
- Import these images in PhotoModeler and conduct the project to orient images and reconstruct the 3-D object. In a typical project with automatic tools, the targets picked up by PhotoModeler are marked with a cross as shown in Figure 4.10. The targets referenced and marked by the software can be seen as points in the 3-D viewer of PhotoModeler as in Figure 4.11. The points then can be converted into a surface by connecting them into triangular surface elements. The reconstructed shape looks as in Figure 4.12. Another example with the phantom is shown in Figure 4.13. This is however for random objects. For canonical objects (examples in next section) the specific shape tools reconstruct uniform 3-D surface models using NURBS (Non-Uniform Rational Bezier Spline) based surface elements.
- The reconstructed 3-D models have to be scaled and must be given a frame of reference so that suitable dimensions are allotted. The scaling can be done by simply registering the distance between any pair of control points. The screen capture showing the process is shown in Figure 4.14. The frame of reference for the model is defined by selecting suitable marked targets as origin and the three coordinate axes. An example of the process is shown in Figure 4.15.
- The final 3-D model can be exported in some standard CAD formats that are compatible with most of the popular electromagnetic (EM) simulators



(explained in next section of this chapter). These formats are shown in Figure 4.16. A preferred CAD file format is STL when exporting triangular surface elements. For NURBS-based surfaces, the preferred format is IGES.

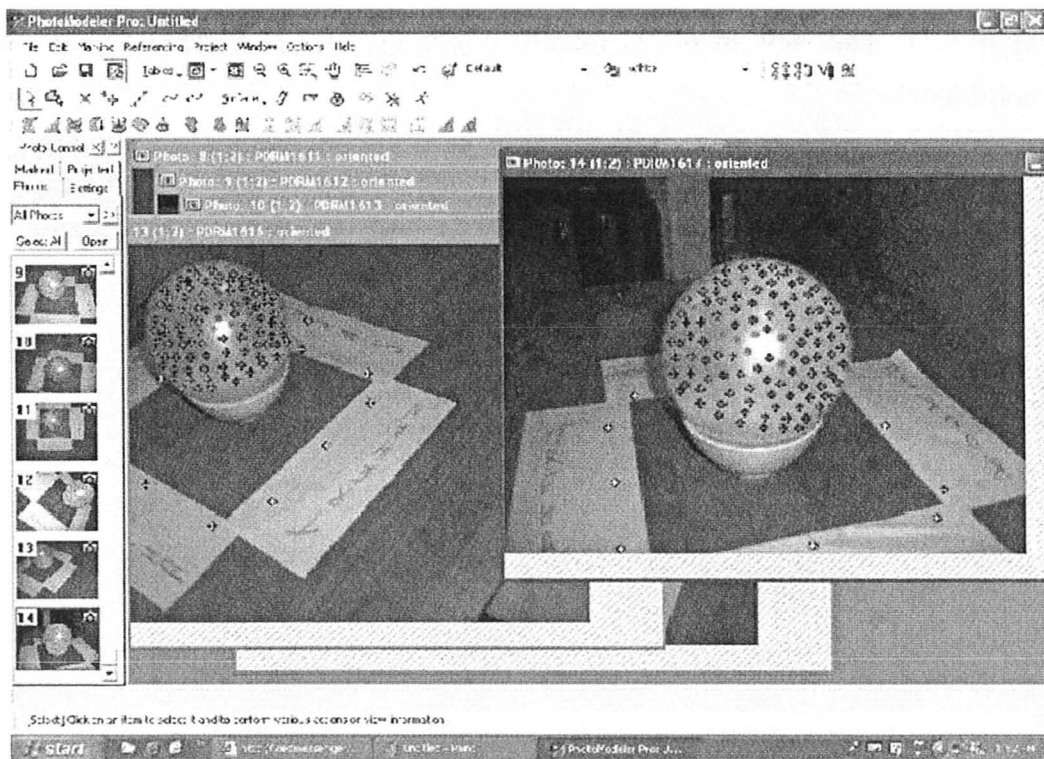


Figure 4.10: Auto-referenced target points are marked with crosses in PhotoModeler.

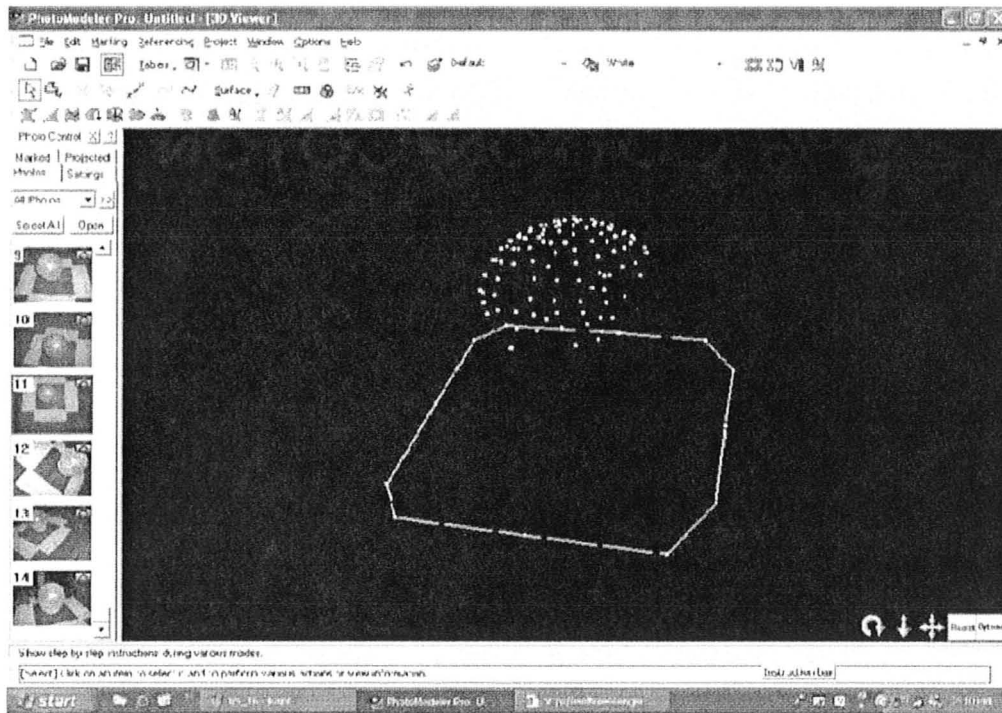


Figure 4.11: The view of object marked points in the 3-D Viewer window in PhotoModeler.

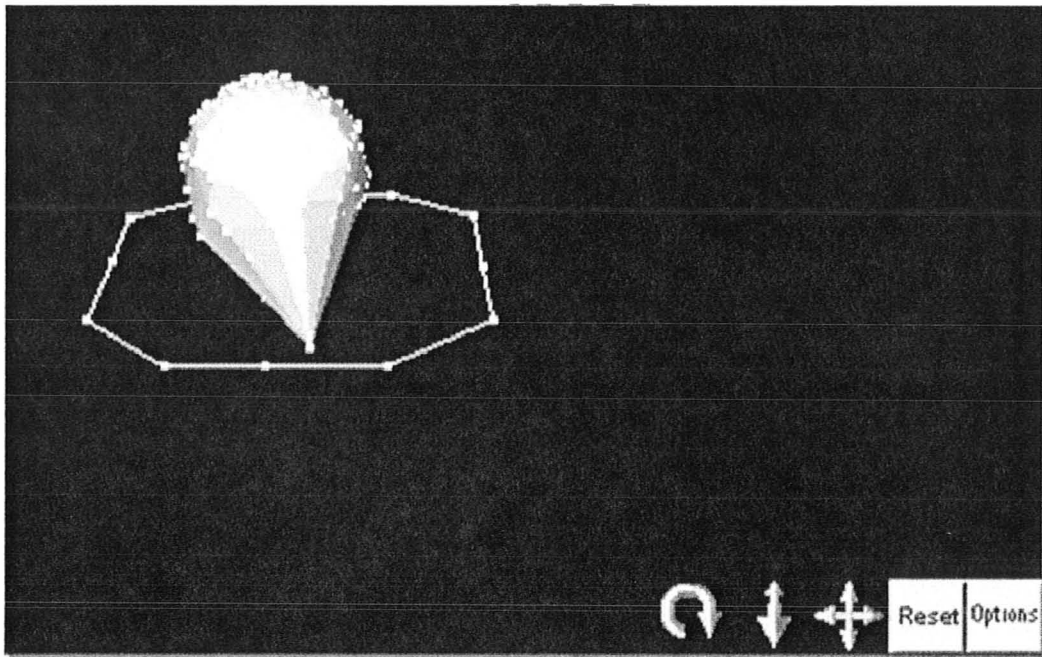


Figure 4.12: The model in the 3-D Viewer window in PhotoModeler by connecting the targets with triangular surface elements.

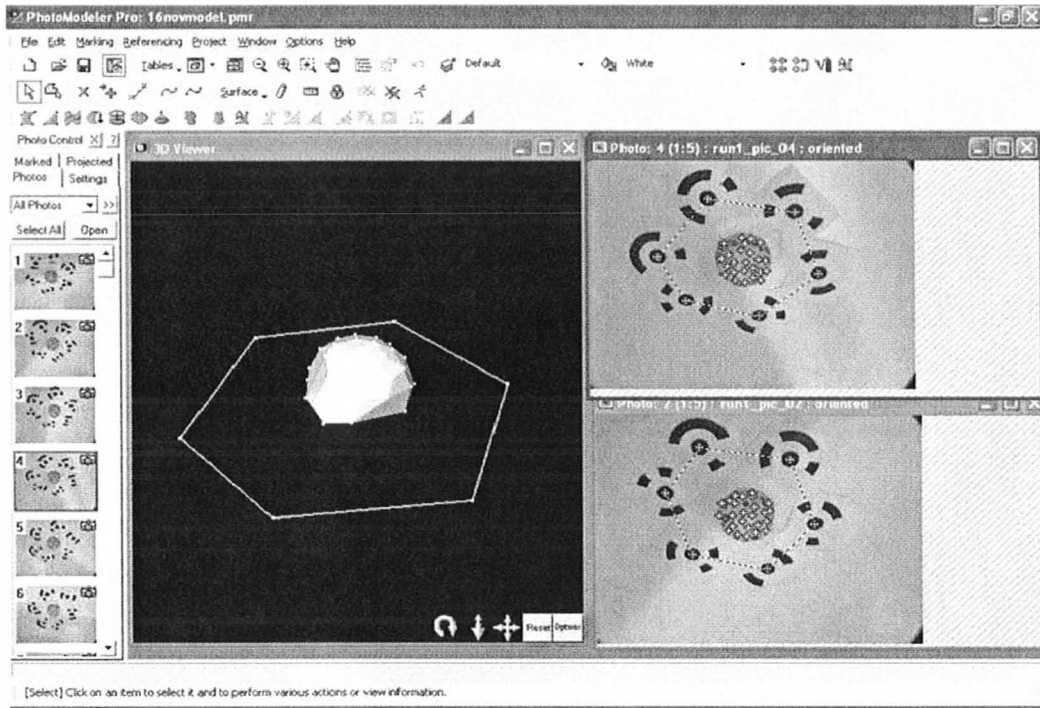


Figure 4.13: A screen capture from PhotoModeler with the reconstructed phantom surface.

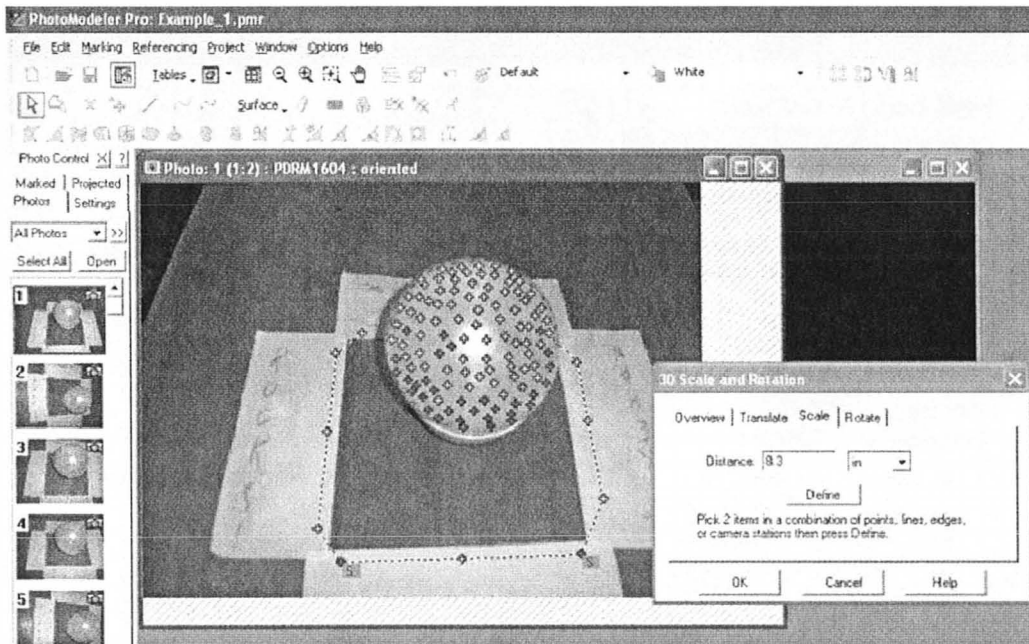


Figure 4.14: A screen capture from PhotoModeler showing the adding of scale to the 3-D model using a pair of control points.

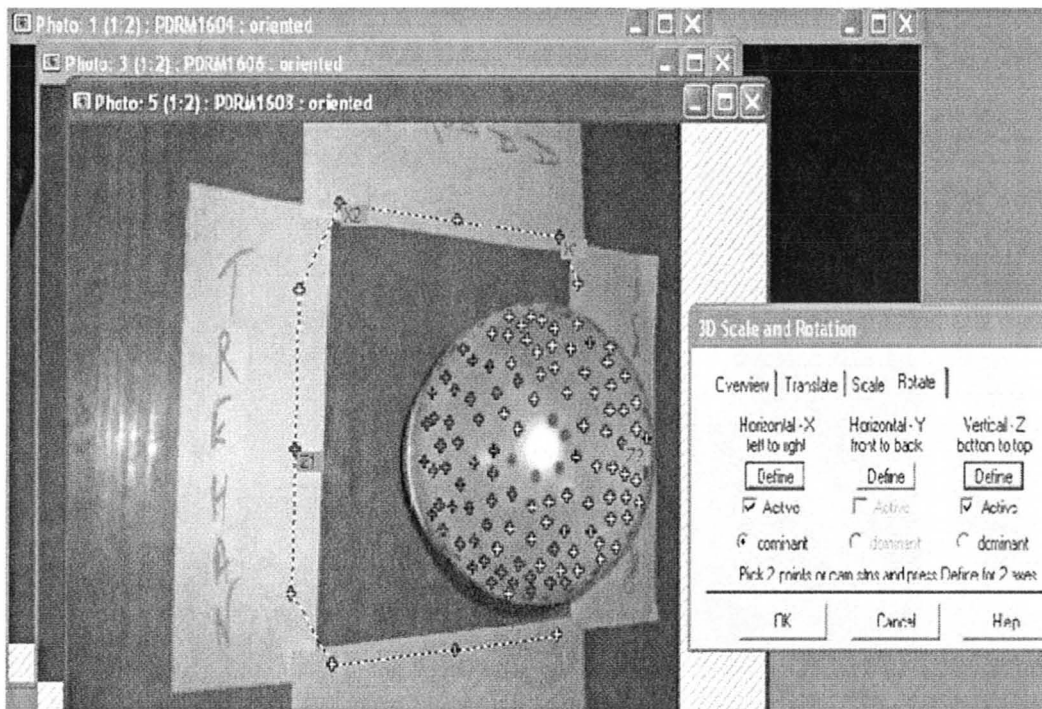


Figure 4.15: A screen capture from PhotoModeler showing axes definition for the 3-D model.

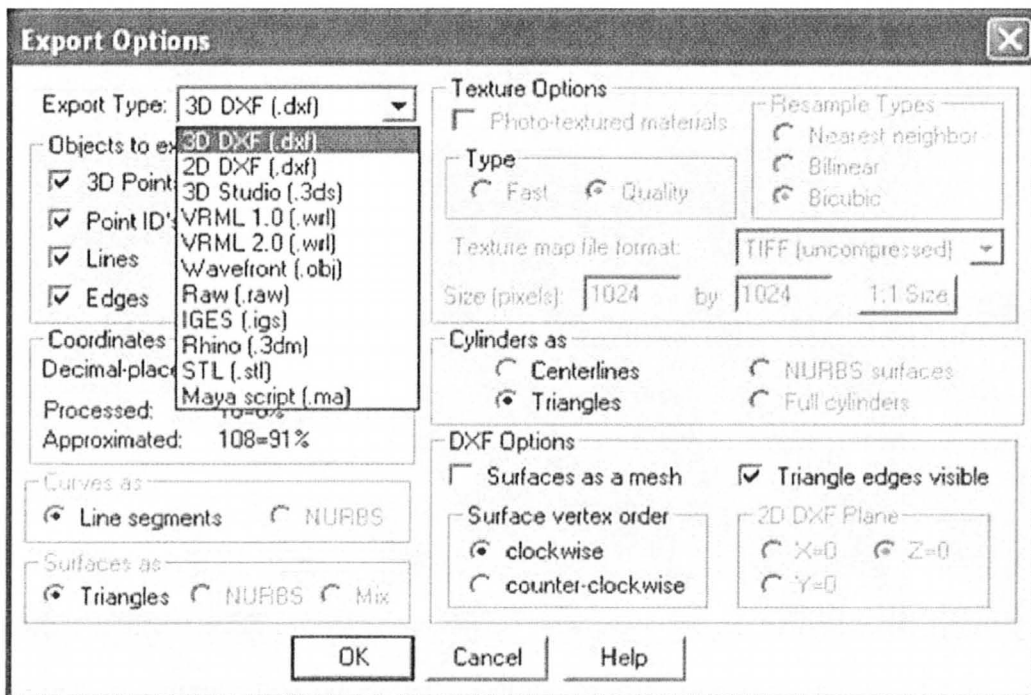


Figure 4.16: The Export Options dialog in PhotoModeler.

## 2) EXAMPLES AND APPLICATIONS OF PHOTOGRAMMETRY APPROACH

This section presents some of the examples for shape reconstruction using the apparatus and methodology detailed in the previous section of this chapter. These examples are also a part of published papers in conferences that will be discussed in last section. These examples along with an accuracy study prove beyond doubt that the photogrammetry approach is an easy-to-use and effective tool for acquiring the 3-D surface of a randomly shaped object. This technique is practical and can be easily adapted in clinical environment.

### 2.1. *Reconstructed Shapes and Accuracy Assessment*

To assess the precision of the photogrammetry apparatus, an experimental assessment with 3-D reconstruction was conducted. Two sets of solid glycerin phantoms were fabricated using the recipe for intermediate water content tissues (IWCT) [see chapter 3]. The 3-D models of the phantoms were reconstructed using PhotoModeler. To investigate the differences between the actual and the reconstructed model shapes and sizes, direct comparison was done between the dimensions of the CAD models from PhotoModeler and the actual measurements of the phantoms. There were two groups of shapes that were investigated: (i) canonical shapes such as cones with pointed tips and cylinders, and (ii) random shapes such as round or elongated phantoms and cones with curved tips. The difference in the modeling steps in PhotoModeler with these two shape types was mentioned in the sub-section 1.3 of this chapter.

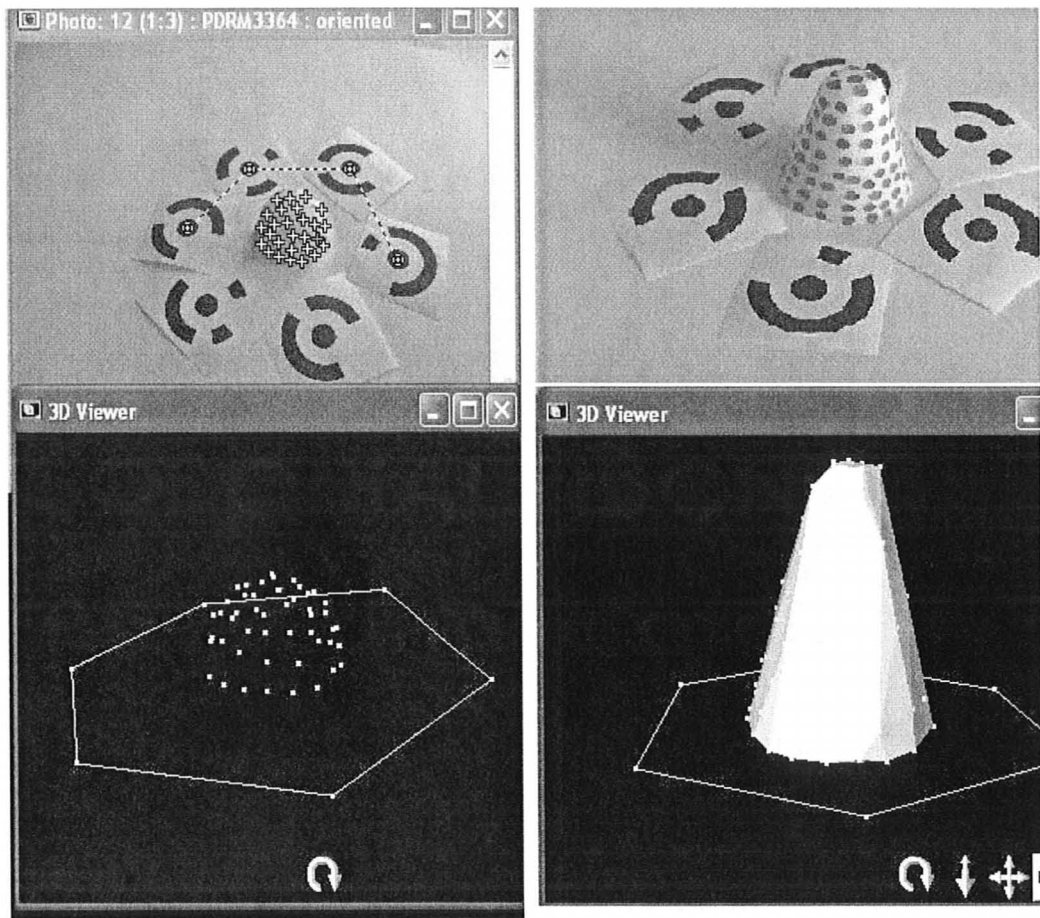
Table 4.1 shows the results of 3-D shape reconstructions for the imaged

phantoms. It demonstrates that the absolute maximum error for the dimensions of all 3-D models is 2 mm. This maximum error occurs for shapes that contain singular points, e.g., the tip of the cone. For regular smooth surfaces with mild curvatures, the reconstruction is more precise, with a maximum error below 1 mm. The reconstructed examples for random shapes are given in Figure 4.17 and that for canonical shapes are given in Figure 4.18.

TABLE 4.1: COMPARISON OF THE ACTUAL DIMENSIONS WITH THE RECONSTRUCTED DIMENSIONS OF THE 3-D MODELS FOR VARIOUS SHAPES USING PHOTOMODELER.

Shape of phantom	Size Parameter	Actual size (mm)	Reconstructed size (mm)	Absolute error (mm)	Average of errors (mm)	
Cylinder	Long	Height	95	94	1	1
		Radius	23	22	1	
	Medium	Height	70	70	0	0.5
		Radius	25	26	1	
	Short	Height	45	45	0	0
		Radius	25	25	0	
Cone	Pointed tip	S. height	94	96	2	1.5
		B. radius	35	36	1	
	Curved tip	S. height	92	91	1	2
		B. span	66	68	2	
		Top span	20	21	1	
Random	Round	Height	26	25	1	0.5
		B. span	53	53	0	
	Elongated	Height	45	45	0	1
		B. span	34	32	2	

'B.' - Base; 'S.' - Slant



(a)

(b)

Figure 4.17: Actual (top) vs. reconstructed (bottom) for random shapes: (a) round bowl-like shape with marked targets; and (b) surface of cone with curved tip formed by joining marked targets with triangular surface elements.

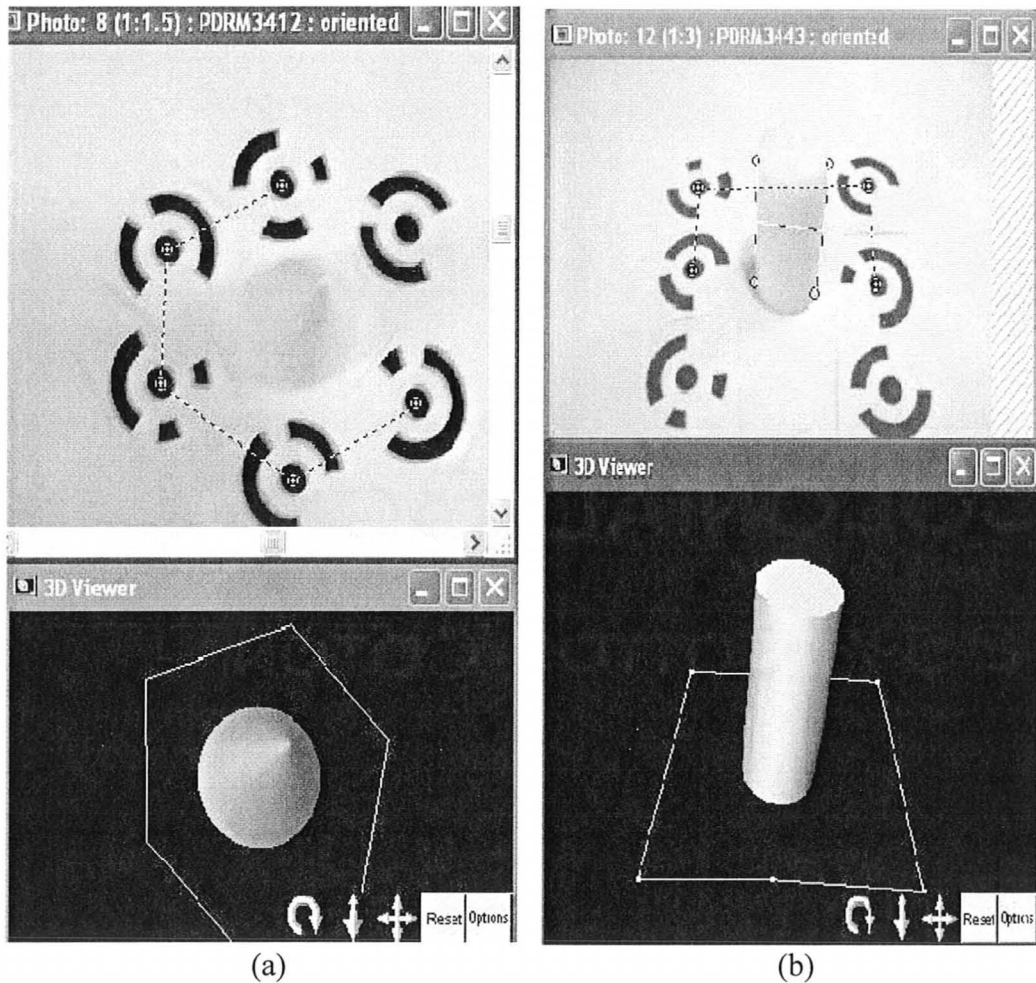


Figure 4.18: Actual (top) vs. reconstructed (bottom) for canonical shapes: (a) cone with pointed tip; and (b) long cylinder. Both are formed with NURBS based surfaces.

## 2.2. File Compatibility for EM Simulators

The most popular EM simulators such as HFSS [18], XFDTD [19] and CST [20] can import both STL and IGES formats easily. Also, STL CAD files imported in HFSS can be further exported into standard SAT format that is compatible with most simulators. An important point to make is that sometimes,



due to conversion, the models may have mistaken units. This may require proper model scaling.

Furthermore, CAD tools in these EM simulators can be used for making shelled or hollowed phantoms for simulations with two-media numerical phantoms comprising of skin layer and homogenized breast tissue. For example, various tools such as Copy and Paste; Scale; Boolean; Separate Lumps are used to construct the model in XFDTD (an FDTD solver) shown in Figure 4.19. Similarly, HFSS (a frequency domain FEM solver) has tools such as Scale, Boolean, Coordinate offset, Split, which can be used to create a similar simple breast model as shown in Figure 4.20.

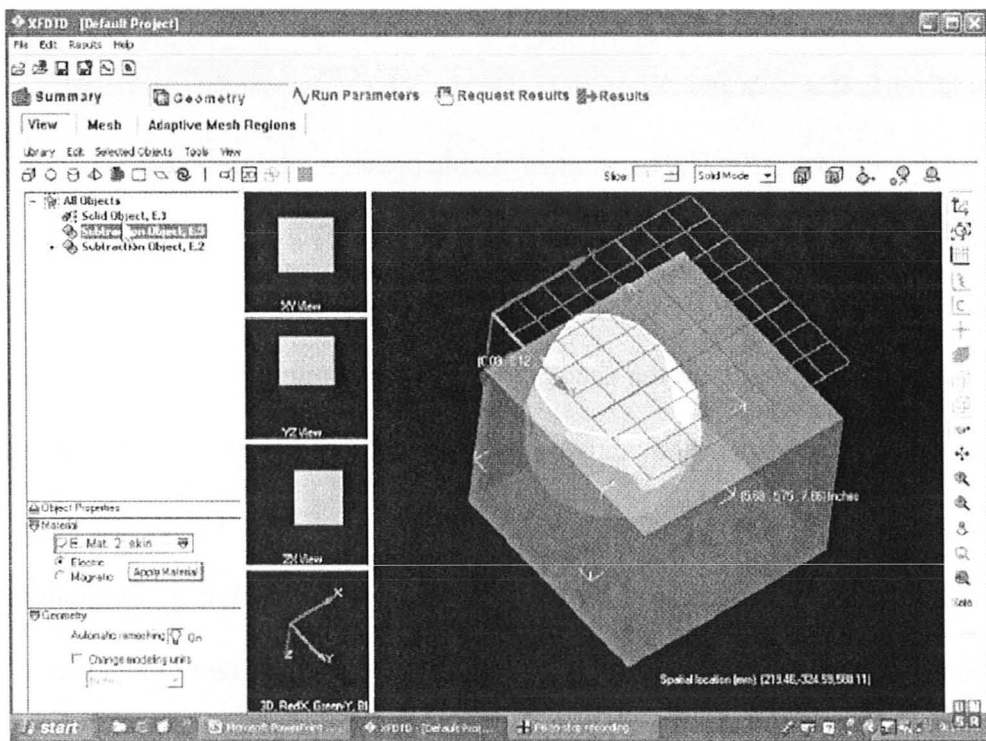


Figure 4.19: The two-media simple breast model in XFDTD.

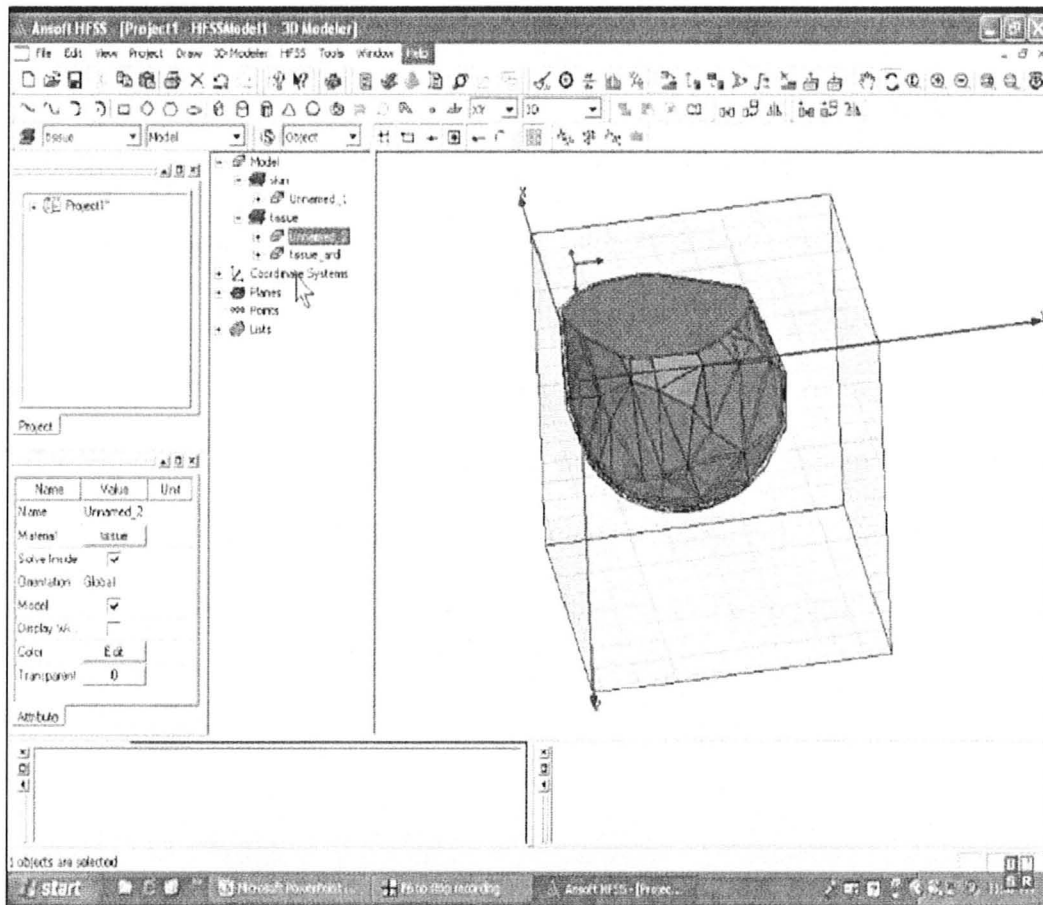


Figure 4.20: The two-media simple breast model in HFSS.

### 3) VERIFICATION WITH FORWARD EM MODELS

In order to investigate the accuracy of the photogrammetry-based approach, we conducted experiments to compare the measured and simulated S-parameters for a set-up. The experimental set-up comprised of two UWB antennas, a glycerine phantom emulating the breast, and isopropyl alcohol as the coupling medium. This investigation provides only the initial verification of the concept of using photogrammetry images to build accurate forward EM models in both

frequency- and time-domain techniques. The experimental procedure for a homogenous physical phantom is: (i) the surface of the imaged object is acquired; (ii) the dielectric parameters of the imaged object and coupling medium are measured and recorded; (iii) the imaged object and the antennas are immersed in the coupling medium; and, (iv) the S-parameter measurements are carried out. The mutual orientation of the antennas about the phantom is captured automatically in the photogrammetry images and facilitates accurate simulation.

### **3.1. *Hardware and Measurements***

The objective of this work was to achieve acceptable alignment between EM forward models and the microwave S-parameter measurements. Such alignment is a crucial requirement in tomographic image reconstruction. To validate the alignment, it is important to know the constitutive parameters of both the physical phantom emulating the breast and the host (coupling) medium. For that, Agilent 85070E Dielectric Performance Probe Kit [21] connected to a vector network analyzer was used. These instruments were already described in chapter 3. The frequency range of the measurements was between 2 GHz and 10 GHz. The physical phantom was the glycerine intermediate water content tissue (IWCT) recipe for the random shape and low water content tissue (LWCT) recipe for the canonical shape (see chapter 3).

The used UWB antennas were printed monopole antennas fed by a 50- $\Omega$  coplanar waveguide (CPW) [22]. Figure 4.21 shows the shape and dimensions of the UWB antenna which has been designed to operate in a lossy coupling

medium.

Our group used isopropyl alcohol as the coupling medium. Figure 4.22 (a) shows the complete measurement set-up including the antennas and the physical phantom immersed in isopropyl alcohol in a glass tank with dimensions 20"×10"×20". The phantom is placed on a thin Plexiglas stand, which is in the middle of the tank. This is to minimize the reflections from the sidewalls, the bottom and the alcohol bath surface. A vector network analyzer (Advantest R3770) is used to measure the S-parameters. This 4-port 20-GHz VNA has the added capability to perform up to 16-port S-parameter measurements with an additional test set (not shown). The VNA is shown in Figure 4.22 (b).

Figure 4.23 (a) and (b) show the simulated structures in HFSS. Both the structures contain the two UWB antenna elements. One of them is for a 3-D model of the randomly shaped physical phantom [Figure 4.23 (a)] and the other one is a 3-D model of the canonically shaped (conical) phantom [Figure 4.23 (b)]. Both are reconstructed by the photogrammetry approach. The computational domain is an 8 cm × 8 cm × 11 cm box terminated by absorbing boundaries. The constitutive parameters of the box are those of isopropyl alcohol. The measured permittivity and tangent loss of the alcohol and the phantom from the probe measurements are used in the simulation as frequency-dependent data sets.

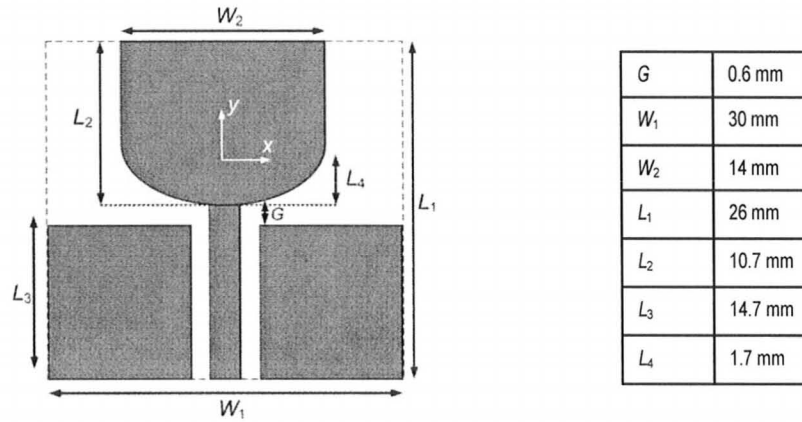
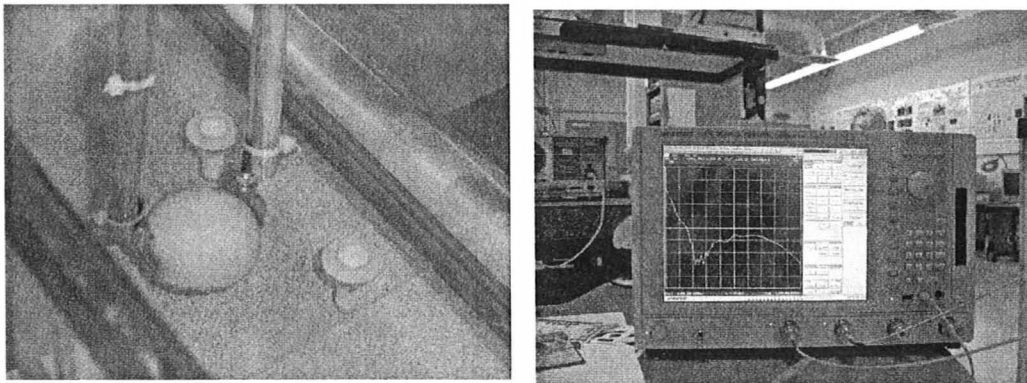


Figure 4.21: The UWB antenna element and its dimensions (from [22]).



(a)

(b)

Figure 4.22: Components of the experimental set-up: (a) the two UWB antennas and the physical phantom immersed in the isopropyl alcohol; and (b) the Advantest R3770 VNA performing 2-port measurement.

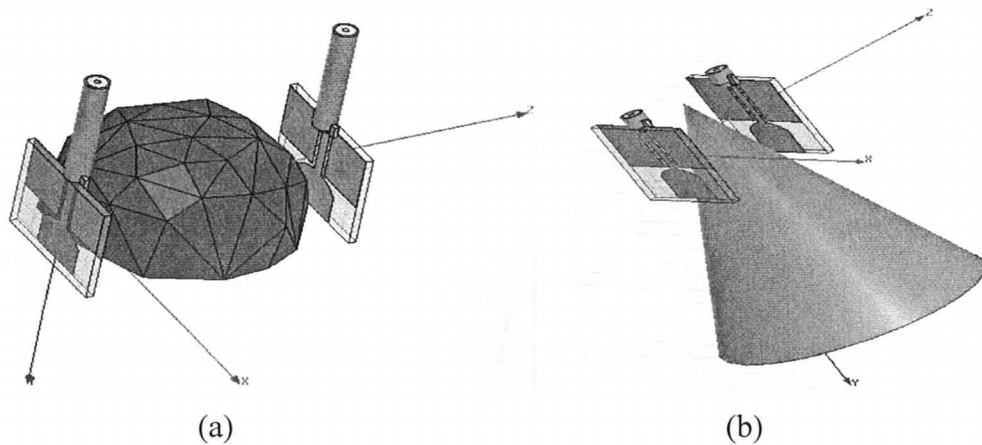


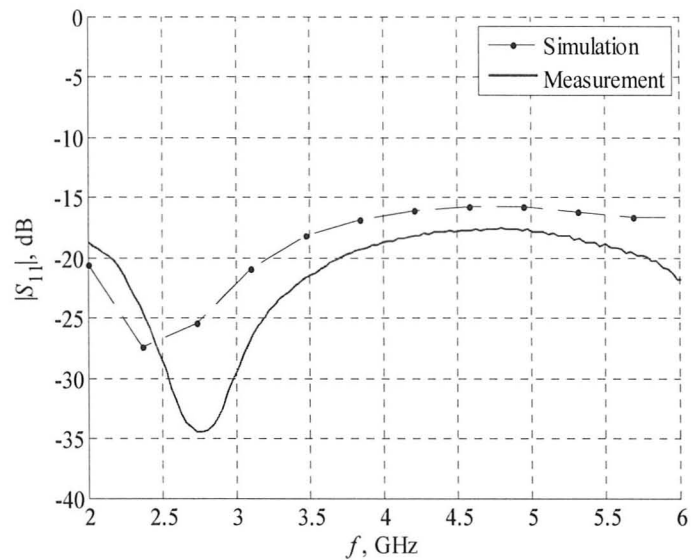
Figure 4.23: Complete EM forward model using HFSS containing the two antenna elements, their feed-lines, coupling medium and the 3-D shape obtained via photogrammetry for: (a) random physical phantom, and (b) canonical physical phantom.

### 3.2. Results

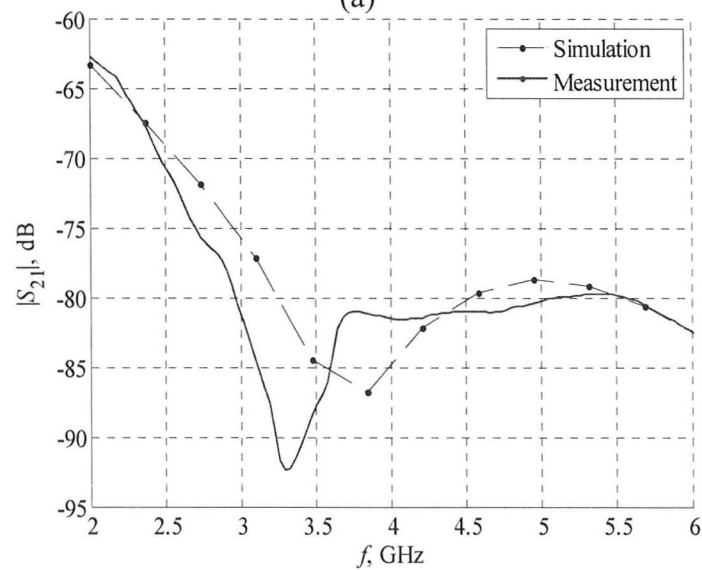
Figure 4.24 shows the measured and simulated S-parameters from 2 GHz to 6 GHz for the simulation set up in Figure 4.23 (a) (random shape phantom). In this frequency range, a good agreement is achieved between measured and simulated results, which demonstrate the accuracy of the photogrammetry surface model of the physical phantom. This is an encouraging result toward the development of our frequency-domain and time-domain EM forward models and their implementation in novel imaging algorithms. Due to the very dissipative coupling medium the signal at higher frequencies was too noisy to analyze.

Figure 4.25 compares the measured and the simulated S-parameters from 3 GHz to 11 GHz, which comprises the UWB frequency range. Good agreement was achieved between measured and simulated results that demonstrate the

accuracy of the constructed forward EM model using the photogrammetry surface reconstruction. The noise was less of a problem in this set up as the phantom was narrow near the tip where the antennas were placed. This made the separation between the antennas smaller, hence the smaller signal loss.



(a)



(b)

Figure 4.24: Comparison between measured and simulated results for the 2-antenna set up for random shaped phantom: (a) return loss, and (b) insertion loss.

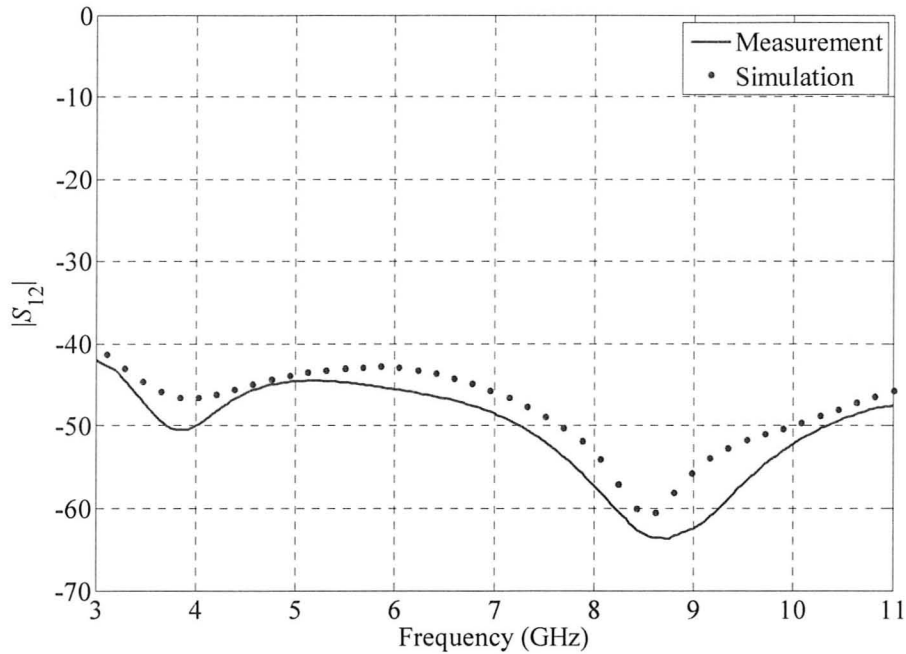


Figure 4.25: Comparison between measured and simulated insertion loss (in dB) for the two UWB antennas with a cone-shaped phantom.

## 4) RECENT DEVELOPMENTS

### 4.1. *Published work*

Our group has proposed a photogrammetry method for the accurate reconstruction of the 3-D surface of an imaged object, i.e., breast, at the time of the microwave measurement. The approach can also provide the exact mutual location and orientation of the imaged breast with respect to the antenna elements. The knowledge of the surface shape of the imaged object can bring great benefits to both radar-based and tomographic microwave imaging approaches. In the former case, it provides the exact shape and location of the skin interface with respect to the imaging array thus making the identification of skin-clutter signal components much easier in comparison with all currently existing approaches. In



the latter case, it clearly identifies the surface of the volume where permittivity reconstruction must take place. This greatly simplifies the complexity of the inversion procedure. The approach is simple to implement and automate as well as requires straightforward components. This is the gist of the work published in the first conference paper [23]. Section 1 and Section 3 describe the results published in this paper.

In the second conference paper [24], we conducted an accuracy assessment of the proposed 3-D photogrammetry-based surface reconstruction. It was established that the accuracy of the surface reconstruction of the object through photogrammetry is better than  $\pm 1$  mm. The results described in Section 2 and Section 3, were published in this paper. This paper received the ‘Honourable Mention Student Paper Award’ by IEEE Antenna and Propagation Society (APS).

#### **4.2. *Laser Scanner***

As a result of the validation of the photogrammetry application in microwave imaging, our group acquired in the summer of 2009 (while this thesis was being written), an automatic 3-D laser scanner REVscan [25]. This is one of the first auto-positioned handheld scanners in the market. The scanner is shown in Figure 4.26. The surface rendering is done in real time and the surface can be verified during the scanning process. It can build the models within minutes and this is highly advantageous in clinical environment where patient motion is usually a hassle. The surface and shape is reconstructed within a micrometer resolution.



Figure 4.26: A handheld 3-D laser scanner from Creaform Inc. [25].

However, laser scanning system costs around 45,000 dollars (with academic discounts). Thus, the photogrammetry-based system remains a good candidate for small scale studies and experiments with the AMWI techniques. A photogrammetry system can be assembled with less than 1500 dollars. As surface acquisition can benefit AMWI techniques greatly, such optical systems are indispensable. These systems are definitely easier to implement and utilize for clinical practice in comparison with the microwave radar measurements of the skin surface position, which were proposed previously (and proven only in simulations).

## REFERENCES

- [1] E. C. Fear, P. Meaney, and M. Stuchly, “Microwaves for breast cancer detection?,” *IEEE Potentials*, vol. 22, no. 1, pp. 12 – 18, 2003.
- [2] X. Li, E. Bond, B. Van Veen, and S. Hagness, “An overview of ultrawideband microwave imaging via space-time beamforming for early stage breast-cancer detection,” *IEEE Antennas Propag. Mag.*, vol. 47, no. 1, pp. 19 – 34, 2005.

- 
- [3] J. M. Sill and E. C. Fear, “Tissue sensing adaptive radar for breast cancer detection-experimental investigation of simple tumor models,” *IEEE Trans. Microw. Theory Tech.*, vol. 53, no. 11, pp. 3312 – 3319, 2005.
- [4] R. Nilavalan, J. Leendertz, I. Craddock, A. Preece, and R. Benjamin, “Numerical analysis of microwave detection of breast tumours using synthetic focussing techniques,” *In Proc. IEEE Antennas and Propagation Society Symp.*, pp. 2440–2443, vol. 3, 2004.
- [5] E. J. Bond, Li Xu, S. C. Hagness, and B. D. Van Veen, “Microwave imaging via space-time beamforming for early detection of breast cancer,” *IEEE Trans. Antennas Propagat.*, vol. 51, no. 8, pp. 1690 – 1705, 2003.
- [6] P. Meaney, M. Fanning, D. Li, S. Poplack, and K. Paulsen, “A clinical prototype for active microwave imaging of the breast,” *IEEE Trans. Microw. Theory Tech.*, vol. 48, no. 11, pp. 1841 – 1853, 2000.
- [7] A. E. Bulyshev, S. Y. Semenov, A. E. Souvorov, R. H. Svenson, A. G. Nazarov, Y. E. Sizov, and G. P. Tatsis, “Computational modeling of three-dimensional microwave tomography of breast cancer,” *IEEE Trans Biomed. Eng.*, vol. 48, no. 9, pp. 1053 – 1056, 2001.
- [8] Q. H. Liu, Z. Q. Zhang, T. T. Wang, J. A. Bryan, G. A. Ybarra, L. W. Nolte, and W. T. Joines, “Active microwave imaging 1—2-D forward and inverse scattering methods,” *IEEE Trans. Microwave Theory Tech.*, vol. 50, no. 1, pp. 123 – 133, 2002.
- [9] Z. Q. Zhang, Q. H. Liu, C. Xiao, E. Ward, G. Ybarra, and W. T. Joines, “Microwave breast imaging: 3-D forward scattering simulation,” *IEEE Trans. Biomed. Eng.*, vol. 50, no. 10, pp. 1180 – 1189, 2003.
- [10] T. Rubæk, P. M. Meaney, P. Meincke, and K. D. Paulsen, “Nonlinear microwave imaging for breast-cancer screening using gauss–newton’s method and the CGLS inversion algorithm,” *IEEE Trans. Antennas Propagat.*, vol. 55, no. 8, pp. 2320 – 2331, 2007.
- [11] T. C. Williams, E.C. Fear, David T. Westwick, “Tissue sensing adaptive radar for breast cancer detection: investigations of an improved skin sensing method,” *IEEE Trans. Microwave Theory Tech.*, vol. 54, no. 4, pp. 1308 – 1314, 2006.
- [12] D. W. Winters, B. D. V. Veen, and S. C. Hagness, “Dimensionality reduction in inverse scattering: applications to microwave imaging for breast cancer detection,” *1<sup>st</sup> Int. Conf. on Applied Inverse Problems 2007: Theoretical and Computational Aspects (AIP 2007)*, 2007.

- 
- [13] PhotoModeler Pro 5.2.3., Eos Systems Inc., 210 - 1847 West Broadway, Vancouver, BC, Canada, 2007. [Online]. Available: <http://www.photodeler.com/index.htm>.
- [14] A. Trehan, “3-D reconstruction of curved objects from 2-D images: recovery of breast shape,” Computational Electromagnetics Res. Lab., McMaster University, CEM-R-33, August 2006.
- [15] Vesna Kozelj. (August 2008). How to hold the camera with your hands for best support. knol<sup>TM</sup>. [Online]. Available: <http://knol.google.com/k/vesna-kozelj/how-to-hold-the-camera-with-your-hands/3k0expg5xjecw/2#>.
- [16] M. Georgiev, “Photogrammetry-based reconstruction of an object,” Computational Electromagnetics Res. Lab., McMaster University, CEM-R-43, June 2007.
- [17] Flea 2, Point grey Research, 12051 Riverside Way, Richmond, BC, Canada, 2007. [Online]. Available: <http://www.ptgrey.com/products/flea2/index.asp>.
- [18] Ansoft HFSS ver. 11, Ansoft Corporation, 225 West Station Square Drive, Suite 200, Pittsburgh, PA 15219, USA, 2008. [Online]. Available: <http://www.ansoft.com>.
- [19] XFDTD ver. 6.3, Remcom Inc., 300 Chesterfield Center, Suite 260 Chesterfield, MO 63017, USA, 2003. [Online]. Available: [www.remcom.com](http://www.remcom.com).
- [20] CST Microwave Studio, CST of Americal, Inc., Headquarters at 492 Old Connecticut Path, Suite 505 Framingham, MA 01701, USA, 2009. [Online]. Available: <http://www.cst.com/>.
- [21] Agilent ADS, Agilent Technologies, 1400 Fountaingrove Parkway, Santa Rosa, CA 954031799, USA. [Online]. Available: <http://www.home.agilent.com/agilent/home.jsp?cc=US&lc=eng>.
- [22] H. M. Jafari, M. J. Deen, S. Hranilovic, and N. K. Nikolova, “A study of ultrawideband antennas for near-field imaging,” *IEEE Trans. Antennas Propagat.*, vol. 55, no. 4, pp. 1184 – 1188, 2007.
- [23] A. Trehan, R. K. Amineh, M. S. Georgiev, and N. K. Nikolova, “Photogrammetry-based surface reconstruction for improving microwave breast tumor detection,” *Proc. of 24th Int. Review of Progress in Applied Computational Electromagnetics (ACES)*, March 2008.

- [24] A. Trehan, R. K. Amineh, M. S. Georgiev, and N. K. Nikolova, “Accuracy assessment of photogrammetry surface reconstruction for improving microwave imaging,” *IEEE International Symposium on Antennas and Propagation (APS)*, July 2008.
- [25] REVscan, Creaform Inc., 5825 rue St-Georges Lévis, Québec, Canada, 2009. [Online]. Available: [www.creaform3D.com](http://www.creaform3D.com).

## **CHAPTER 5**

# **PATIENT SPECIFIC NUMERICAL BREAST PHANTOMS**

### **INTRODUCTION**

Numerical simulations are an essential part of many design processes. Electromagnetic (EM) simulations are widely prevalent both in research and industry prior to any prototyping. This is required for optimizing the system to achieve best performance before proceeding toward fabrication. In active microwave imaging (AMWI), most of the proposed techniques are in simulations and there are very few clinical trials [1]. This brings the need to realistic numerical models of the breast in EM simulations.

The simple models of dielectric parameters for various breast tissues have been outlined in section 3 of chapter 2. These models were also used as a target

for the physical breast phantoms described in chapter 3. For physical breast phantoms, the goal is to match the dielectric parameters ( $\epsilon_r$  and  $\sigma$ ) as well as possible to the measured tissue parameters. For the numerical phantoms, these parameters are easily set up in the CAD files of the simulators. The EM simulators we use are either based on finite-element method (FEM) or on finite-difference time-domain (FDTD) methods. They have the capability to represent dielectric models both as simple Debye models (FDTD simulators) and user-defined frequency-dependent property data (FEM simulators).

The difficult part in preparing a numerical breast phantom is the 3-D CAD model. This is due to the extreme tissue heterogeneity and the variations in size generally found in breasts. In fact, a patient's breast might undergo many changes with age and lifestyle patterns. Most EM simulators have CAD capabilities just to represent simple 3-D canonical shapes to construct antennas and 2- or 2.5-D surfaces for planar circuit designs. This brings in the challenge of 3-D modeling in EM simulators, which struggles in accurately representing the interior structure of the breast and its surface that can be somewhat arbitrary. The surface acquisition for randomly shaped objects was discussed in chapter 4. The 3-D models for the reconstructed exterior surfaces acquired through this method are compatible with most EM simulators.

The sources for constructing the interior representation of the numerical breast models are usually Magnetic Resonance Images (MRI). Good initial numerical models can facilitate inversion in the tomographic microwave

approaches. This is essential in making microwave imaging a standalone cancer detection system.

Building high-fidelity numerical breast phantoms in EM simulations is the core of this chapter. This work is relevant even to general biomedical projects that might require EM or any other analysis software to simulate complex biological objects. In the remainder of this chapter, we refer to the numerical breast phantoms as phantoms. Section 1 discusses the phantom requirements from the point of view of classification. This includes the choice of patient categories for phantoms and the 3-D modeling features compatible with the CAD interfaces of the EM simulators. Section 2 discusses the MRI and the associated image processing methods. Section 3 details the algorithm to convert 2-D MR slice images into 3-D CAD models using an FEM-based solver. Section 4 discusses possible improvements.

## 1) PHANTOM REQUIREMENTS

### 1.1. *Patient Specificity*

From adolescence to menopause, breast tissue is subject to many hormone changes associated with the menstrual cycle, pregnancy, lactation, and age. The glandular breast tissue even changes throughout the menstrual cycle [2]. The fibro-connective and glandular tissue is measured in terms of density of breast tissue; where high density implies more fibro-glandular tissue as compared to adipose fat. It is known, that the density can be quite different from woman to



woman. Variations in the mammographic density of breast tissue are referred to as the parenchymal pattern of the breast [3]. As discussed in chapter 1, there is a classification based on the breast composition with regard to density by the American College of Radiology (ACR) under BI-RADS [4]. It is also referred to as the radiographic breast density classification and it pertains to mammography. It is again given here for convenience:

- The breast is almost entirely fat (< 25 % glandular). Such a breast is usually termed as ‘fatty’.
- There are scattered fibro-glandular densities (approximately 25% to 50% glandular).
- The breast tissue is heterogeneously dense, which could obscure detection of small masses (approximately 51% to 75% glandular).
- The breast tissue is extremely dense. This may lower the sensitivity of mammography (>75% glandular).

A study with 708 medical cases from a large cohort of 45,000 women assigned to mammography in the Canadian National Breast Cancer Screening Study (NBSS) concluded that increases in the level of breast tissue density as assessed by mammography are associated with increases in risk for breast cancer [3]. The study reported that there was a 43% increase in relative risk between the lower and the next higher category of density, as determined by the radiologist; and there was a 32% increase as determined by the computer assisted method. Also, similar large gradients in risk were found in women aged 40-49 years to

those aged 50-59 years. Another problem with radiographic dense breasts is that it is more difficult to detect cancers on screening mammography with high density breasts, which leads to lower rate of early detection and higher stage of cancer at disease presentation [5].

Age is another important factor when it comes to monitoring breast cancer risk. A woman's chance of being diagnosed with breast cancer depending on age is given by the National Cancer Institute (NCI) and has been shown in Table 1.1 of chapter 1. Also, age seems to influence the breast changes during lifetime. Women in their thirties and early forties, that is the pre-menopausal years, have mostly dense breasts. In the post-menopausal years, the glandular tissue of the breast (mainly epithelial cells) is largely replaced by fatty tissue, especially in parous women (*women who have given at least one birth*). The connective part of the stromal cells (*blood vessels, lymphatic, and subcutaneous fat tissue*) also shrinks [6]. This aspect is reflected in typical mammograms shown in Figure 5.1.

Other risk factors influencing breast changes are: (i) body mass index (BMI) where higher BMI loosely implies more adipose fat content in body and breast – but some studies show that adult weight gain is a bigger risk factor [7], (ii) menopause status which ties in with age related differences, and (iii) exogenous hormone use, which is highly inconclusive for assessing both risks and changes [7].

The study on the effects of all these factors on the electromagnetic diagnostic techniques was done by Poplack *et al.* [8]. They took subjects in four

age groups i.e., 40-49 years; 50-59 years; 60-69 years and 70-79 years. They used three techniques – near-infrared (NIR) spectroscopy, electrical impedance (EI) spectroscopy and microwave imaging (MI) spectroscopy, to measure the conductivity, permittivity and other electrical as well as pathological properties with respect to factors mentioned so far. According to the observations with MI spectroscopy, in agreement with other methods, there was statistically a 34% to 40% decrease in the conductivity and the permittivity with decreasing breast density (hence increasing age). The effect was more pronounced at 600 MHz with increasing fat content.

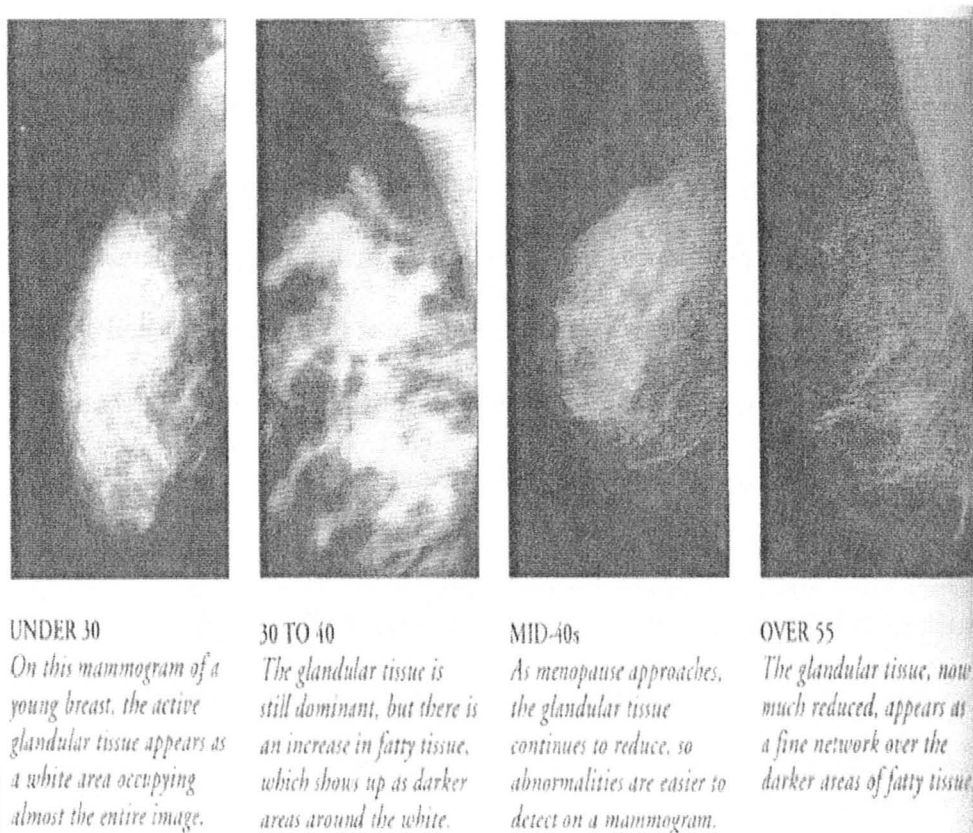


Figure 5.1: Mammograms showing age related variability (from [6]).

Races such as Caucasian, African American, and Asian are also sometimes predicted to play a role in incidence of breast cancer, where Asian women are said to be in low risk category and women in Western countries are said to be in high risk category. For instance, Chaudhary *et al.* [9] tried to explore the reasons for low incidence of cancer among Japanese women compared to their counterparts in Great Britain. It is assumed that genetic, environmental and lifestyle patterns affect breast density, which in turn affects the relative cancer risk. A study [5] with a review of 15,292 women aimed to compare breast density among white, African American, and Asian women. It correlated breast density and race with age, BMI, and breast or cup size. The investigation found no evidence that mammographic breast density differences exist across racial groups. In fact, differences in BMI, age and cup size seem to influence the density of breast among racial groups. The study argues that one might predict that racial groups with lower breast cancer risk should have lower mammographic density. But this study had 435 Asian women in their cohort (one of the largest) and found that density is highest among Asian women but still their risk is lower compared to Caucasians. This does not mean that density and risk are not related, but only that racial differences in risk do not seem to correlate with racial differences (or the lack thereof) in breast density. This warrants that studies relating mammographic density to cancer risk are usually with subjects from North America or Western countries and hence density might be a good predictor within racial groups. But its establishment as a generic predictor across racial groups requires further

studies. Also, more study is needed in relating race to the risk of developing breast cancer before it can be taken as a viable factor [5].

Based on the discussion and analysis so far, it seems that for North American women (target USA and Canada); the patient-specific breast models for EM techniques must include age and density (based on BI-RADS) as factors for establishing categories. BMI (subject to many changes both for a woman and within women) and breast size has been mostly assessed as a subset of density classification for their effects in breast tissue distribution. However, future studies may elevate them to main factors. Two categories are prominent with age: (a) pre-menopausal or women with age less than 50 years; and (b) post-menopausal or women of age more than 50 years. Four categories are based on density as per BI-RADS. Based on these classifications, eight patient-specific categories can be used to set up a data base for patient-specific models. This is done by selecting the suitable sets of MR images as discussed in section 2 of this chapter. The eight categories are listed as: (i) post-menopausal fatty, (ii) post-menopausal scattered density, (iii) post-menopausal heterogeneous density, (iv) post-menopausal extreme density, (v) pre-menopausal fatty, (vi) pre-menopausal scattered density, (vii) pre-menopausal heterogeneous density and, (viii) pre-menopausal extreme density.

### **1.2. 3-D Model Specificity**

The input necessary to construct appropriate 3-D CAD models of the breast for EM simulators is presented under the following three items:

### 1.2.1. 3-D modeling norms

Most of the physical geometry that is visible is in the form of solids. There are multiple ways that these solids can be represented in CAD applications for the purpose of design and development [10]. Some applications such as in gaming industry convert these solids into polygon meshes by the process of surface tessellation. However, the engineering and non-visual simulations require objects to be represented as solid volumes.

An important classification with modeling is the concept of manifold structures. The mathematical description can be quite complex and comprehensive as given in [11], [12]. A simplified mathematical result for 3-D modelers is given in [13] as the following definition:

*A manifold geometry is one that satisfies the following Euler-Poincare equation:*

$$E + 2 = V + F \quad (1)$$

*where  $E$  is the number of edges,  $V$  is the number of vertices, and  $F$  is the number of faces.*

A non-manifold geometry is the one that violates the above equation. In geometrical modeling context, the concept of manifold topology is often referred to as 2-manifold boundaries of solid objects [15]. It means that each point on the 2-dimensional boundary is completely surrounded by other points on the 2-dimensional boundary. Each point on the boundary of a manifold solid divides the modeling space into two regions – the region inside the solid and the region outside the solid. If at any point on the boundary, the modeling space is not

explicitly divided into two regions, then the object is non-manifold at that point. An example of a non-manifold vertex is shown in Figure 5.2 (a) and it can be seen that there are two "inside" regions associated with the point. One can go in any of two directions from this vertex to go "into" an object. The region can also extend along a curve and a typical example of this would be two solid blocks that share an edge. This is depicted in Figure 5.2 (b) where space is not divided into an "inside" and "outside" region at any given point along the edge. Similarly, a face can have a non-2-manifold region in its interior such as that shown in Figure 5.2 (c). In this example a face is non-manifold at the point where the two circular holes touch and at this point there are two directions "into" the interior of the face.

Non-manifold structures are usually not accepted as valid objects in most CAD packages and simulators. The special modeling operations such as union, subtraction etc., which are part of Boolean operations in 3-D modeling, have to be performed carefully between manifold structures to maintain the manifold characteristics in the result. Non-manifold structures need special algorithms to deal with and correct the invalid regions.

Some complicated scenarios of non-manifold topology construction due to various union operations are shown in Figure 5.3 (a)-(d) [16]. In each of these cases, the non-manifold edges are used more than two times by faces. These examples of non-manifold edges can be:

- Two solid regions meeting along an edge as shown in Figure 5.3 (a) and (d).

This may be a result of simple Union among cylinders or cubes.

- A single solid region that contains a non-manifold edge (locally, there are two solid regions that meet along the edge) as shown in Figure 5.3 (b).
- An external sheet face that is connected to a solid region along a non-manifold edge as shown in Figure 5.3 (c).

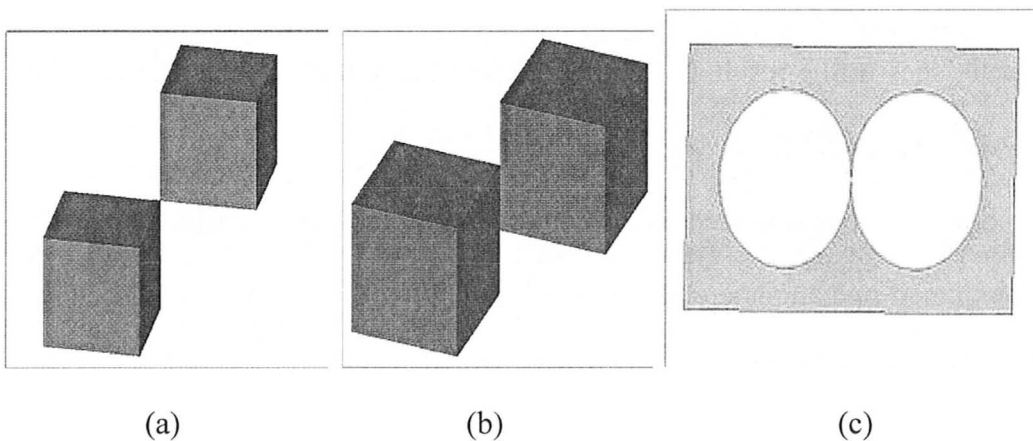


Figure 5.2: Examples of non-manifold topology: (a) a non-manifold vertex, (b) a non-manifold edge, and (c) a non-manifold vertex in a face. All examples are from [15].



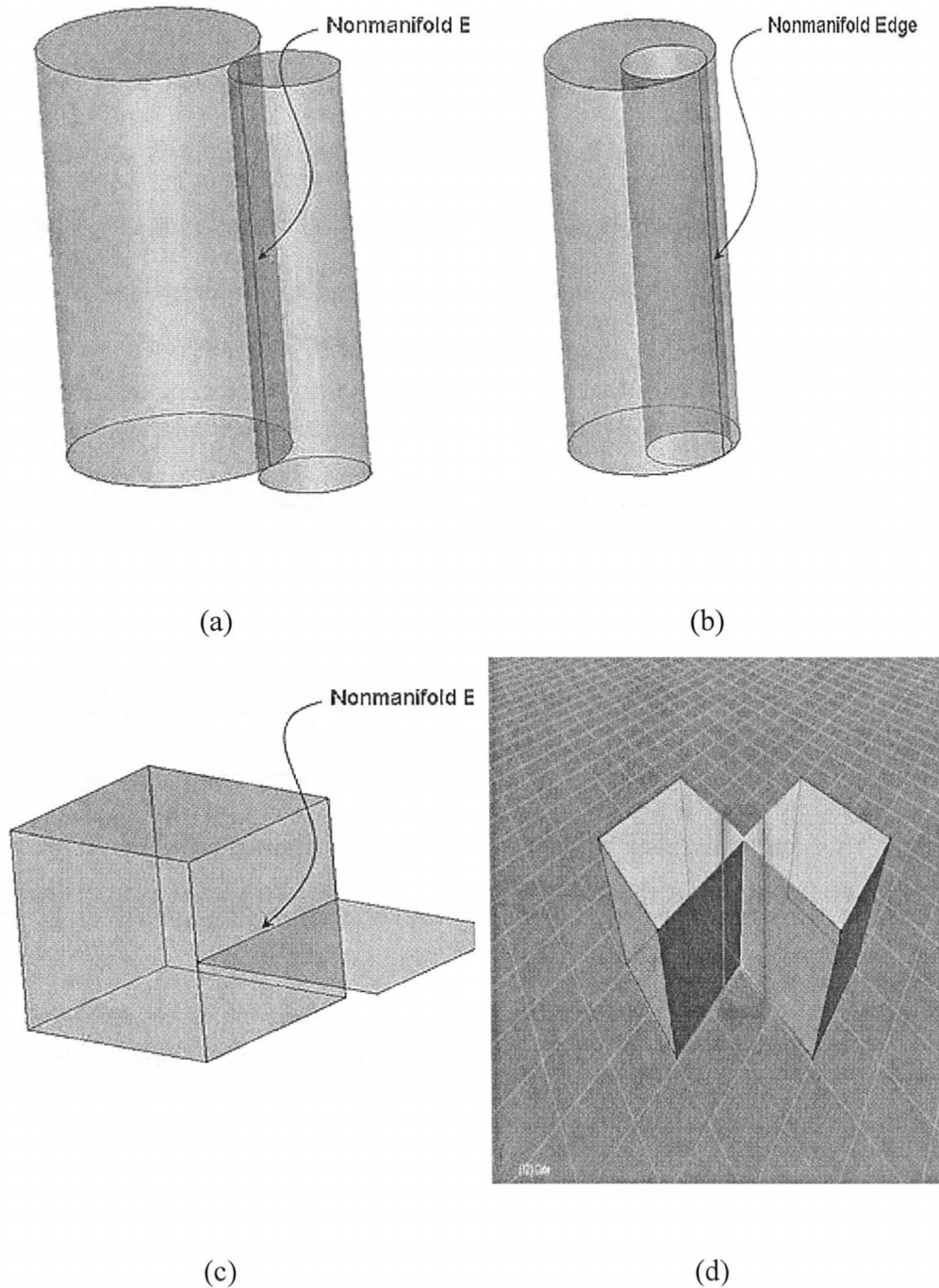


Figure 5.3: Common examples of non-manifold edge creation in solid modeling: (a) two solid regions touching along a non-manifold edge; (b) a single solid region with a non-manifold edge; (c) a solid region touches a sheet region along a non-manifold edge; and (d) two solid cubes united at a non-manifold edge. Examples (a), (b), and (c) are from [16] and (d), is from [17].

### 1.2.2. *Compatibility issues*

One of the difficulties in electromagnetic modeling has been the lack of standard CAD data to enable direct import of data into analysis software. Many solid modeling standards have been proposed over the years, but due to the many separate interests involved and differing geometrical requirements, a definitive standard has yet to be reached.

Recently a CAD format called SAT has gained favor and can be produced by many proprietary CAD mechanical drawing packages [18]. The SAT file is a format developed by Spatial Corporation [14] for the data storage from the ACIS geometric modeling kernel and has become a de-facto standard [18]. Products such as AutoCAD 2000, CADKEY, Turbo CAD, Solidworks and COSMOS all use the ACIS kernel for producing SAT data or allowing input and output of SAT files. This kernel is also being adopted for EM simulation. The ACIS kernel supports many advanced solid modeling capabilities, including analytic geometry representation.

A broad selection of third party mechanical CAD translation products are being constantly developed for the SAT format (e.g., the bi-directional ACIS Data Exchange Translators, which support geometry transfer to and from SAT using IGES, VDAFS and STEP formats) [19]. This format was also used in chapter 4 for simple models from photogrammetry-acquired 3-D models.

The SAT format is closely tied to ACIS's internal topological data structure, allowing the kernel to quickly rebuild the data structure from saved files. For



### 1.2.3. *Level of affordable complexity*

The objective here is to be able to run simulations with 3-D models both in frequency and time domain simulators. The Ansoft High-Frequency Structure Simulator (HFSS) [29] is a frequency-domain finite-element-based simulator used frequently in our research. Depending upon the complexity of the structure, this simulator may require thousands of megabytes (MB) of RAM. Computer-resource requirements are always an important consideration for users of this type of products [19].

The 3-D EM simulators based on finite-element methods require 3-D solid model representations that can be meshed with tetrahedral meshes. Analytic surface representations must be faceted prior to applying boundary conditions, assigning material properties and performing solution processes [19]. If the solid model is too discrete with many entities, it might pose memory restrictions considering that the simulator will mesh each entity into at least two tetrahedrons to solve inside the structure. Also, the computational resources increase manifold with complicated boundaries in a 3-D model. At the same time, care has to be taken not to perform operations that might make 3-D models contain non-manifold edges or intersection bodies. This is why we have to build algorithms that can simplify the 3-D modeling process, while the 3-D models of complex biological structures are acceptable in EM simulations.

It is important to state that the 3-D models we prepare to represent the patient-specific beasts are just initial models for the reconstruction algorithms.

There is no need to model exactly the breast complexity as seen in the detailed images from MRI. The AMWI techniques are not intended for use after an MRI is done. The AMWI techniques have to work as standalone methods. Hence, it is necessary to simplify the images (sub-section 2.3 of this chapter) to create simpler models that can be computationally efficient. In fact, the model simplification still needs improvement and this will be discussed in section 4 of this chapter.

Time-domain solvers based on the FDTD method may be more flexible with 3-D detailed models from MRI due to their implicit voxel-based meshing grid. However, model simplification can also help with their memory resources in this case because the voxel size depends on the smallest geometrical detail.

## **2) USING PATIENT SPECIFIC MAGNETIC RESONANCE IMAGES (MRI)**

Magnetic Resonance Imaging is a tomographic technique based on principles of nuclear magnetic resonance (NMR) [21]. This medical modality can provide a combination of high resolution, excellent soft tissue contrast, and a high signal-to-noise ratio. The process through which excited nuclei return to equilibrium after a radio frequency excitation (by giving up their energy to the environment) is known as relaxation. Some key pulse sequences for contrast in MR images are named as T1, T2, T2\*, FLAIR, STIR and PD weighted, which depend on the time constants of the relaxation processes. More details about this modality and the mechanisms involved can be easily found from many books on

the basic principles of MRI and in numerous publications such as [22].

T1 is also known as longitudinal relaxation or spin-lattice relaxation. The value of T1 is dependent upon the physical and chemical nature of the environment surrounding the excited nuclei. In general, smaller molecules, including water, relax much more slowly than medium sized molecules such as lipids [22]. The T1 value of protein-bound water is considerably shorter than that of free water. Accordingly, release of bound water in tumors or other lesions could increase the T1 value. For example, the T1 value of pure water is approximately 3 s, whereas that of fat is generally a few hundred milliseconds [22]. When a tissue with a short T1 is imaged using a sequence with a relatively longer time of repetition (TR), the signal from the tissue is intense. In T1 weighted MR images of the breast, fat gives a very bright (whitish) appearance and the high water content tissue appear darker, where muscle and ducts appear almost black. As confirmed by a radiologist, Dr. Boylan [23], T1 weighted images are best for distinguishing between tissues in breast.

### **2.1. *Image Formats***

The Digital Imaging and Communications in Medicine (DICOM) standard was created by the National Electrical Manufacturers Association (NEMA) [24] to aid the distribution and viewing of medical images, such as CT scans, MRIs, and ultrasound. All specifications about DICOM format are available in [24].

A single DICOM file contains both: (i) a header, which stores information about the patient's name, the type of scan, image dimensions, etc., and (ii) the

image data, which can contain information in three dimensions [25]. The information included in the headers of the DICOM images is also called metadata. In order to extract all this information from a typical DICOM image, MATLAB Image Processing toolbox [31] can be used. The *dicominfo* and *dicomread* functions can process almost all the metadata fields, returning a structure where every field is a specific item of image information. DICOM images may be ‘anonymized’ to remove any sensitive patient information. However, some of the basic pixel and plane attributes of the image are also given in the DICOM metadata. A few key ones are shown in Table 5.1. The pixel is the smallest element of the digital image and the signal in the voxel of the object being imaged is mapped to an intensity of the pixel as shown in Figure 5.5. DICOM image data can be compressed to reduce the image size. Files can be compressed using lossy or lossless variants of the JPEG format [25].

TABLE 5.1: SOME OF THE VARIOUS ATTRIBUTES STORED IN DICOM METADATA.

Metadata attributes	Description
PixelSpacing	The physical length and breadth of pixel as in the plane of 3-D space occupied by the patient, (in mm).
SliceThickness or SpacingBetweenSlices	The height of an image slice (in mm).
ImagePositionPatient	The $x$ , $y$ , and $z$ coordinate of the center of first voxel transmitted (in mm).
BitDepth	Number of bits used to describe each color of the pixel.
ColorType	Type of the image such as grayscale, indexed, RGB etc.

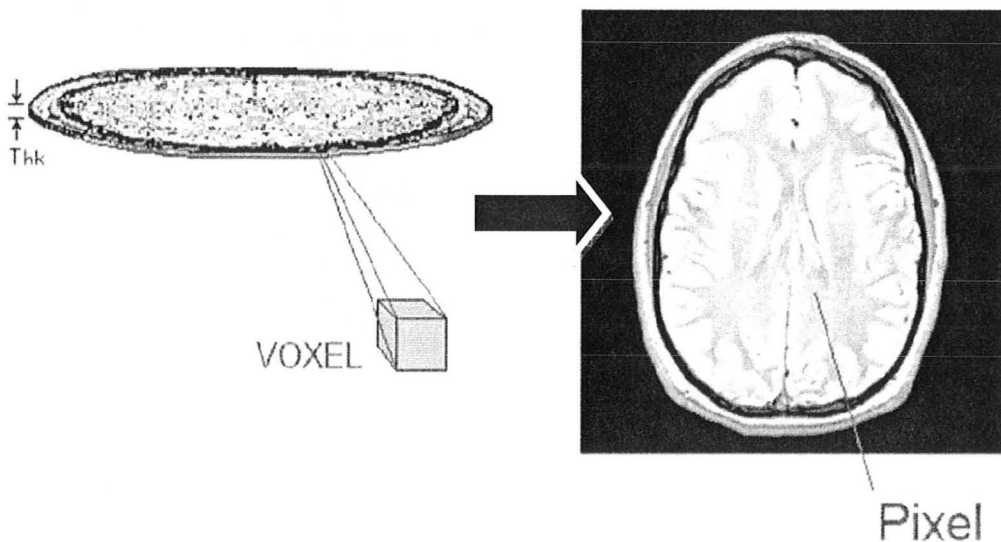


Figure 5.5: A voxel of tomographic slice through brain mapped to a pixel in MRI (from [21]).



## **2.2. Patient Database**

The MR images have been obtained from the Imaging Research Centre of St. Joseph's Healthcare Hamilton [23]. This has been courtesy of Dr. Mike Noseworthy and Dr. Colm Boylan who have helped extensively with consultation, data collection, and recommendations. We acquired 16 MRI sets such that each of the eight patient categories can have two allotted sets. This was done after we (me and Dr. Nikolova) obtained research ethics board approval (REB). It has been a long process to acquire these images and a lot of help and guidance was given by Dr. Noseworthy and Dr. Boylan.

## **2.3. Image Processing**

A typical MRI set has 90 to 120 images. A few of them at the start and end have to be discarded for our purposes as they are images of the chest wall and are usually too noisy to be used in models. This on an average leaves 75 to 85 slice images that are relevant and show the imaged breasts.

The DICOM image files for each set were converted into lossless JPEG with the help of a freeware application called XnView [32]. This conversion decreases the size of the images and makes it easier to use for image processing algorithms in MATLAB [31]. Also, information regarding the image is extracted from the DICOM metadata and is stored for each set. The information of PixelSpacing and SliceThickness (see Table 5.1) are important to get the resolution to convert a pixel to a voxel in 3-D space.

To use the T1 weighted MR images for making 3-D models, the important

step is the identification of the breast tissues in the images. As discussed in chapters 2 and 3, the important tissues to identify inside a breast are: fat, transitional tissue, fibro-glandular tissue, and muscle. A few functions for image processing have been written in MATLAB for this purpose. The first code to run is *initialize\_breast.m* before all the images in an MRI set can be segmented. This program is user-interactive and asks the user to select a cropping rectangle over the image showing the largest breast visually. This is because we intend to model just one breast, either left or right for all the images in the MRI set. Also, we need a constant image-array size (determined by the image showing the largest breast) for all the images to be coherent when modeling in 3-D space. The user has to draw a rectangle over the vital part of the image (the breast) that has to be modeled. This can also be interpreted as the region of interest (ROI). A properly selected ROI aids the algorithm later. Once the user is satisfied with the crop image shown interactively, *initialize\_breast.m* fine-tunes this crop rectangle and stores the information about the rectangle size and whether the left or right breast was selected. After this is done for each set, the same rectangle is used for all the images of the specific set to crop a breast and carry out the algorithm.

The first code of the image processing algorithm for all the images is then *crop\_clean\_image.m* that uses the stored rectangle information to crop the images. It also performs some morphological and edge detection steps to extract the applicable image and the outline of the breast. This flow is shown in Figure 5.6. Please note that initialization is performed once for each MRI set of 70 to 90

images.

Figure 5.7 shows the second step in the image processing algorithm. It is the essential step of identifying tissues in the breast volume by the intensity of the pixel. As said before, T1 weighted images have fat as a bright appearance and high-water content tissues as darker appearance. Tissue identification can be done numerically by looking at the image histograms in MATLAB. A range of pixel intensities can be mapped to a particular tissue identification number. These are termed material numbers. This makes it easier to use images later in the modeling. Also, it removes the noise, which is a part of most images. Thus, it gives clean arrays or maps to work with. The knowledge of the breast anatomy can be used since it is known that in the top image part we correlate dark pixel intensities with muscle while in the middle part, the dark intensities correspond to the dense glandular tissue. The extracted outline gives the limits of the region where the intensities are mapped and the location of the skin pixels is assigned. The intermediate intensity pixels are allotted “transitional-tissue” material number and the very bright pixels (mostly subcutaneous) are assigned the “fat” material number. This is done using a function called *assign\_material\_numbers.m*.

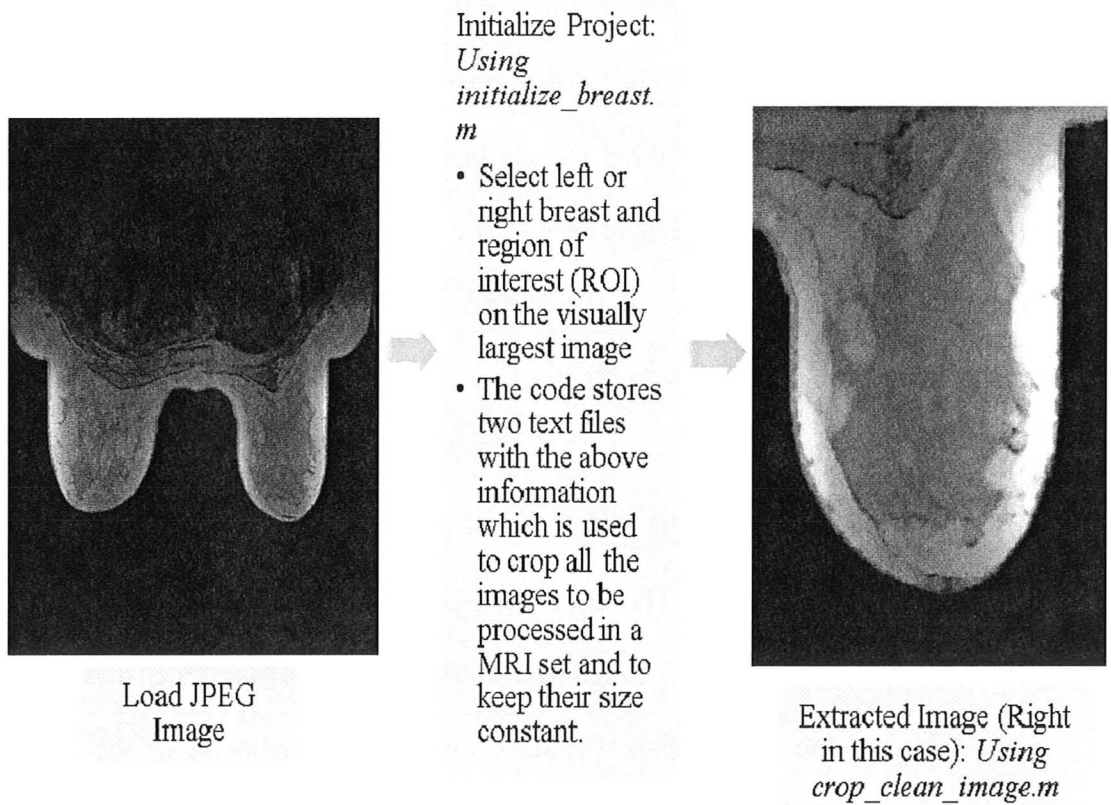


Figure 5.6: Flow chart showing the first three steps in the image processing of the MR images.

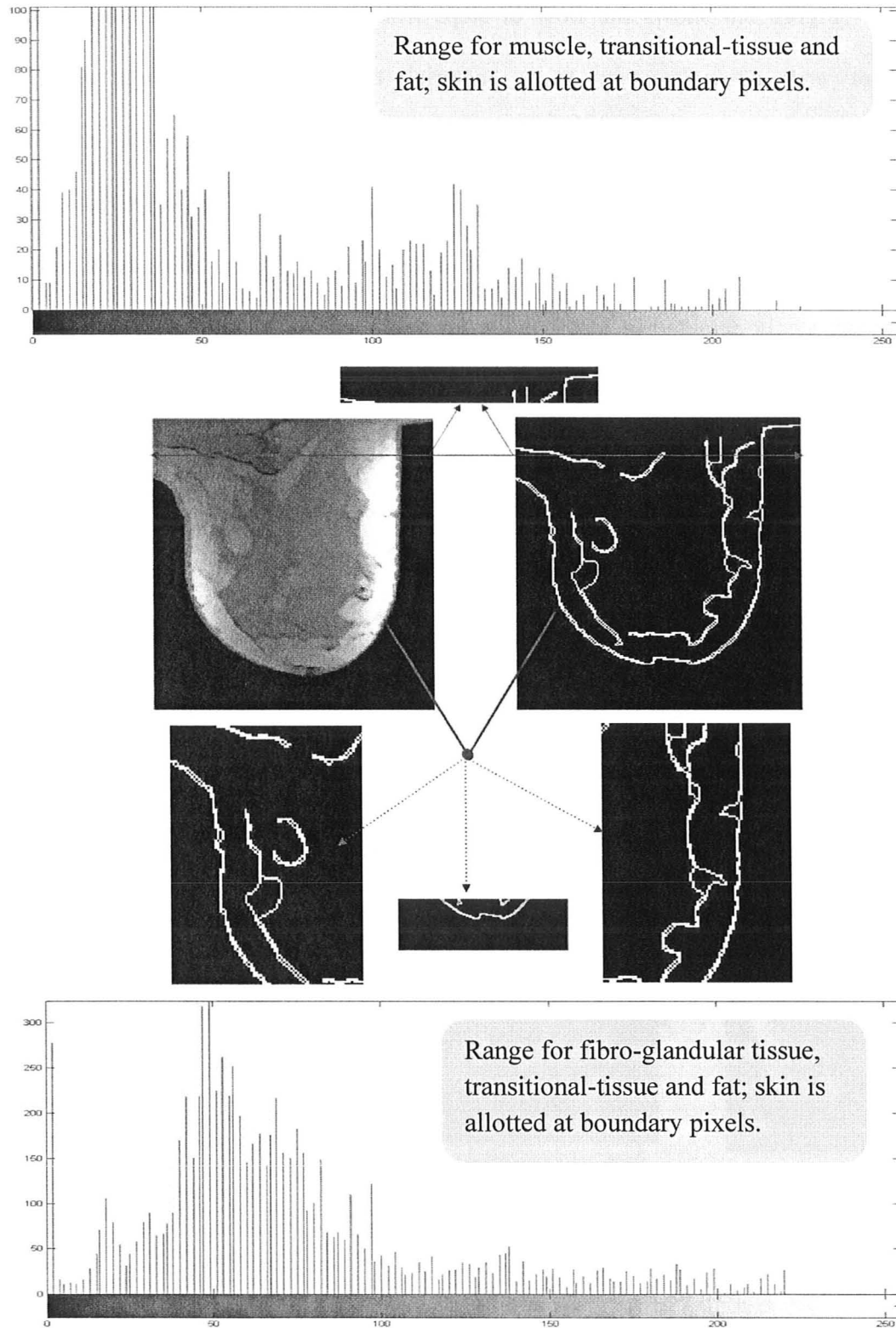


Figure 5.7: The segmentation process in *assign\_material\_numbers.m*.

Figure 5.8 shows the flow of steps from converting the extracted image from *crop\_clean\_image.m* to a material map by using *assign\_material\_numbers.m*, followed by the use of *process\_material\_map.m* to create smoother boundaries between different tissue regions. The smoothing is important for the 3-D simulation as will be described in the next section. Also, the skin pixels, which are not easily detected in MR images, are removed totally, and a smooth 2 mm thick layer (approximately 3 pixels) is introduced. Furthermore, the MR image is used only to determine the interior tissue distribution. The surface (or skin location) will be a result of the automatic surface reconstruction discussed in chapter 4. The final material maps can be easily converted to dielectric property maps (permittivity and conductivity) by the corresponding material numbers using the simple target dielectric models from section 3 of chapter 2. A typical example is shown in Figure 5.9.

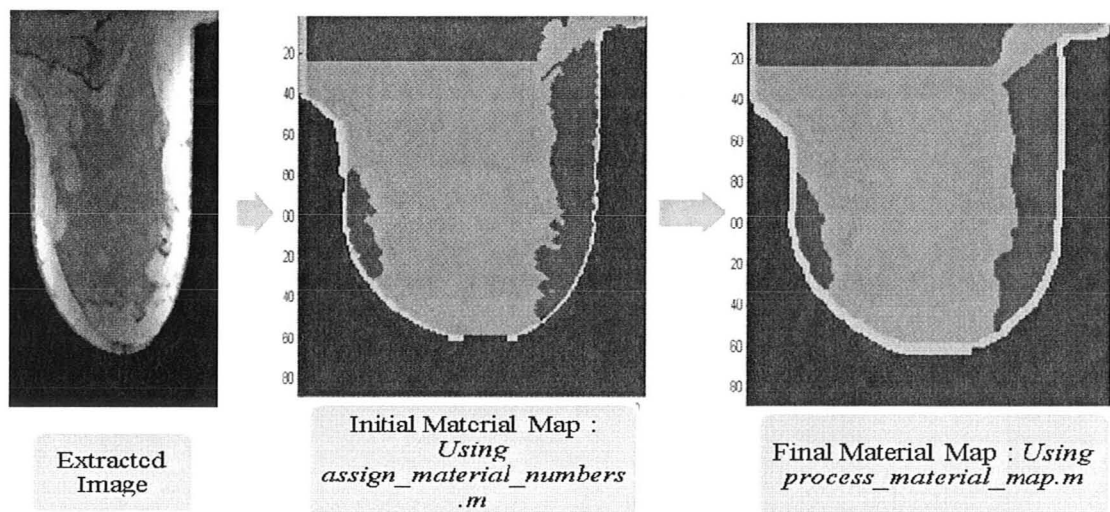


Figure 5.8: Flowchart showing the results of MATLAB codes in deriving a material map.

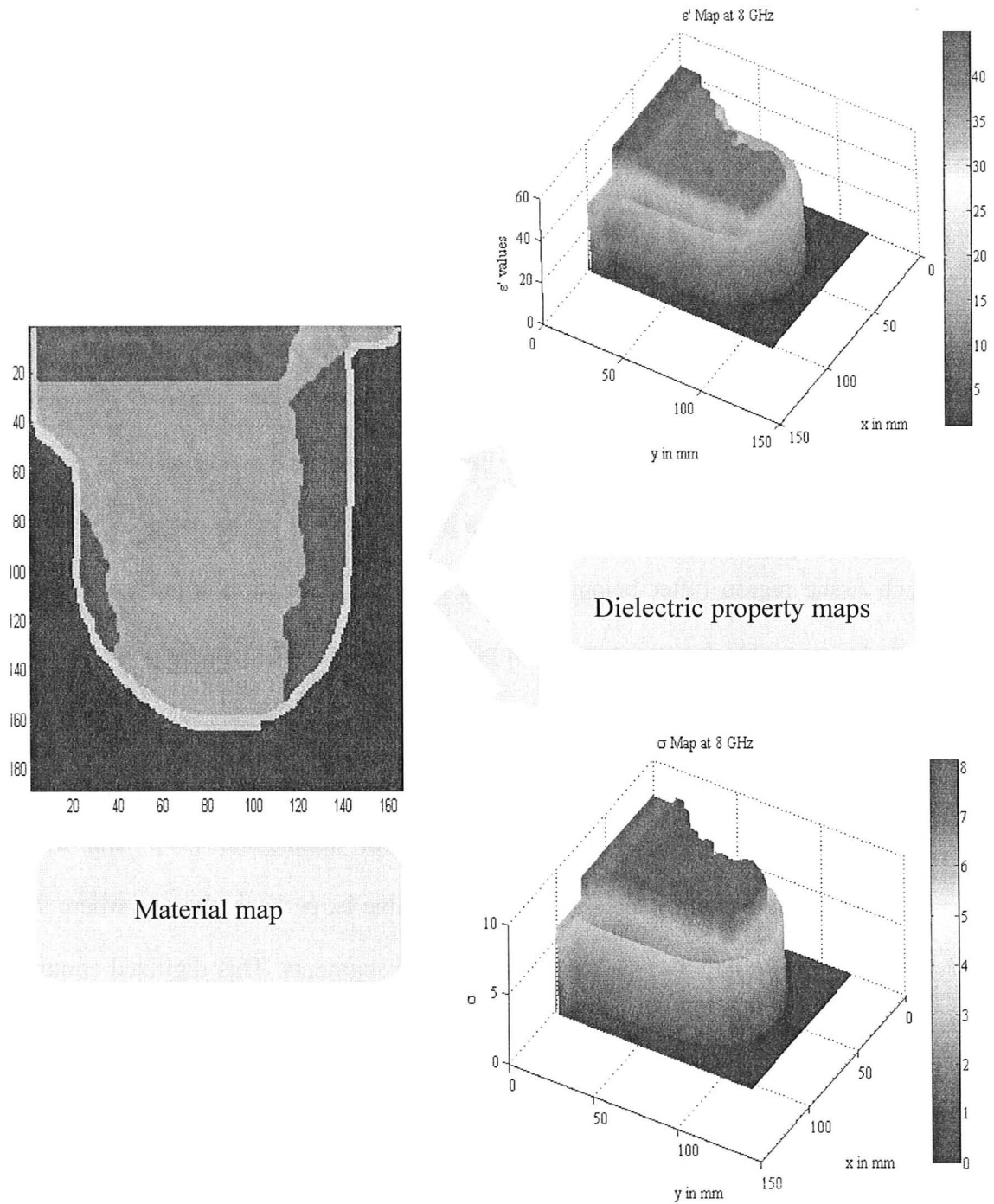


Figure 5.9: Material map conversion to dielectric property maps at 8 GHz.

### 3) 3-D MODELING WITH HFSS

The next objective is to construct the 3-D structure from a sequence of two-dimensional MR images in an EM simulator. HFSS is selected as it is the most commonly used simulator. A solution that can work with HFSS is definitely going to be acceptable for most analysis software packages.

#### 3.1. *Contour Construction in MATLAB*

The method we intend to use to construct each slice image is based on contour construction [27]. A contour line can be viewed mathematically as the intersection of an arbitrary surface and a plane. As seen in the previous section, each tissue region (after being smoothed out) can be seen as a polygon in the material map, which corresponds to a plane going through the surface in a breast slice.

Contour lines of an irregular surface do not lend themselves to curve fitting or any other attempts at precise mathematical description [27]. The most convenient numerical description of a contour line is, perhaps, the one where the line is approximated as a string of straight line segments. This digitized contour line requires two pieces of information – nodal coordinates and connectivity of nodes. The connectivity is defined by the sequence in which the nodes are listed. If the contour line traced between these sequential nodes is closed (*implies initial and final nodes are the same*), then it defines a polygon.

In the material map, each tissue region is a polygon. If the boundary nodes of these tissue regions are simply determined from the material map array as the



outmost pixels of the region, the tissue polygons drawn in 3-D space will be disconnected. Hence, the boundary edges drawn for the group of tissue polygons are not contiguous. An example is shown in Figure 5.10 where the disconnected polygons have a narrow gap, whose extent is one pixel resolution. To better understand this non-contiguity problem and a possible solution to fix it, a simple scenario is shown in Figure 5.11. There are two rectangular polygons in an image, where one polygon has been assigned a material number 40 and the other is assigned a material number 80. The polygons are traced by the connectivity lists using the boundary nodes of the polygons. The minimum distance between the nodes is the  $\Delta$  gap, which is the resolution coming from MRI. It can be clearly seen from the illustration on the left of Figure 5.11 that the transition between two polygons is not included in the connectivity lists. This leaves a  $\Delta$  gap between the polygons. The boundary nodes for the adjacent tissue polygon have to be overlapping, but not create an intersection region. One possible way to solve this is by successively fixing boundary nodes for each tissue polygon in a hierarchy. Here in the given example, a higher priority is given to material polygon numbered 40 and its boundary nodes are extended towards the polygon numbered 80. The gap between the two polygons is filled up with material number 40.

The above solution is implemented in an algorithm in *edging.m*, where the boundary nodes are fixed for each of the five tissues in succession. For instance, this is done by first defining the boundary nodes for muscle such that the region of the muscle polygon is non-intersecting with any other tissue polygon (fat,

transitional tissue, fibro-glandular tissue, and skin) and retains the contiguity. Then the boundary nodes for the transitional tissue are defined so that the region is non-intersecting with fat, fibro-glandular tissue, and skin (muscle is already taken care of). The process then follows with fat. The nodes for fibro-glandular tissue are determined at the end.

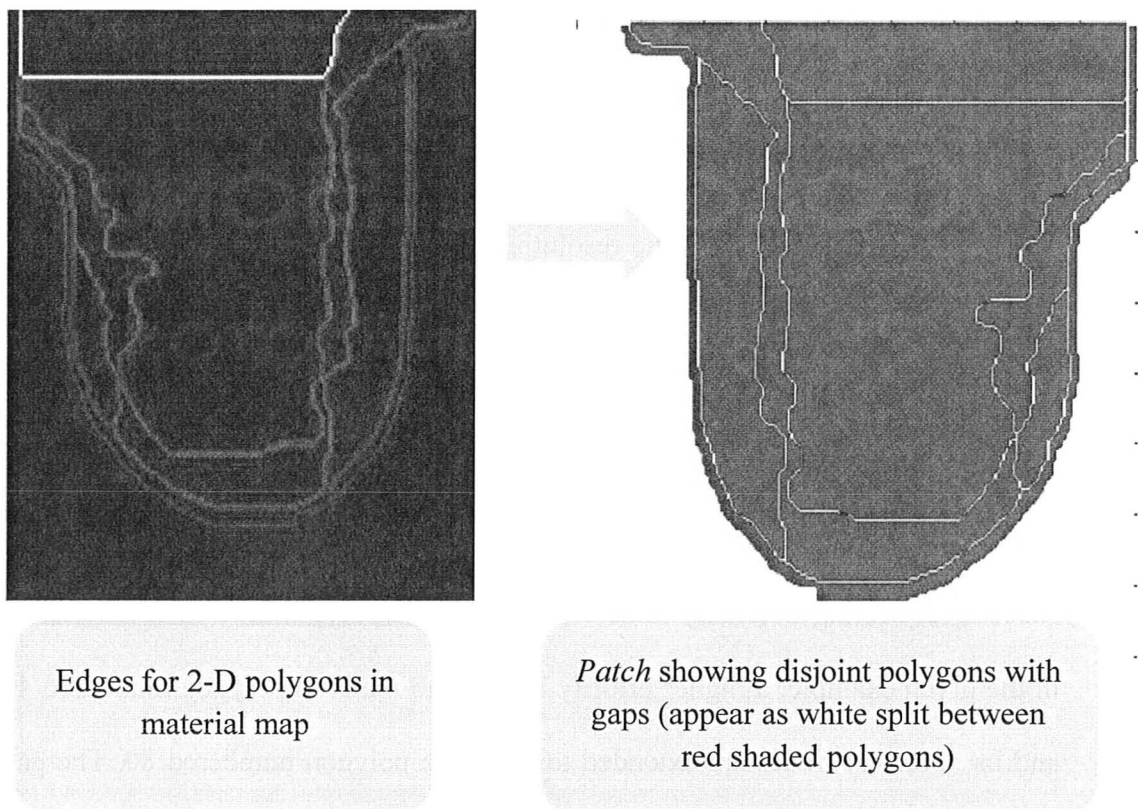


Figure 5.10: The boundary traced for polygons from material map in coordinate space.

Next, we need to find a path in a directed graph to get the connectivity list. There are certain heuristics for choosing an appropriate path with the requirement that the path is Hamiltonian (*a unique path that visits every node once*) [26] and

non-intersecting (for a valid non-manifold polygon). It is not advisable to use the connectivity algorithms in MATLAB. From our experience, in many cases, the connectivity list obtained with such algorithms draw intersecting polygons. An example is shown in the top image of Figure 5.12, where connectivity-based algorithms can lead to the wrong traced path.

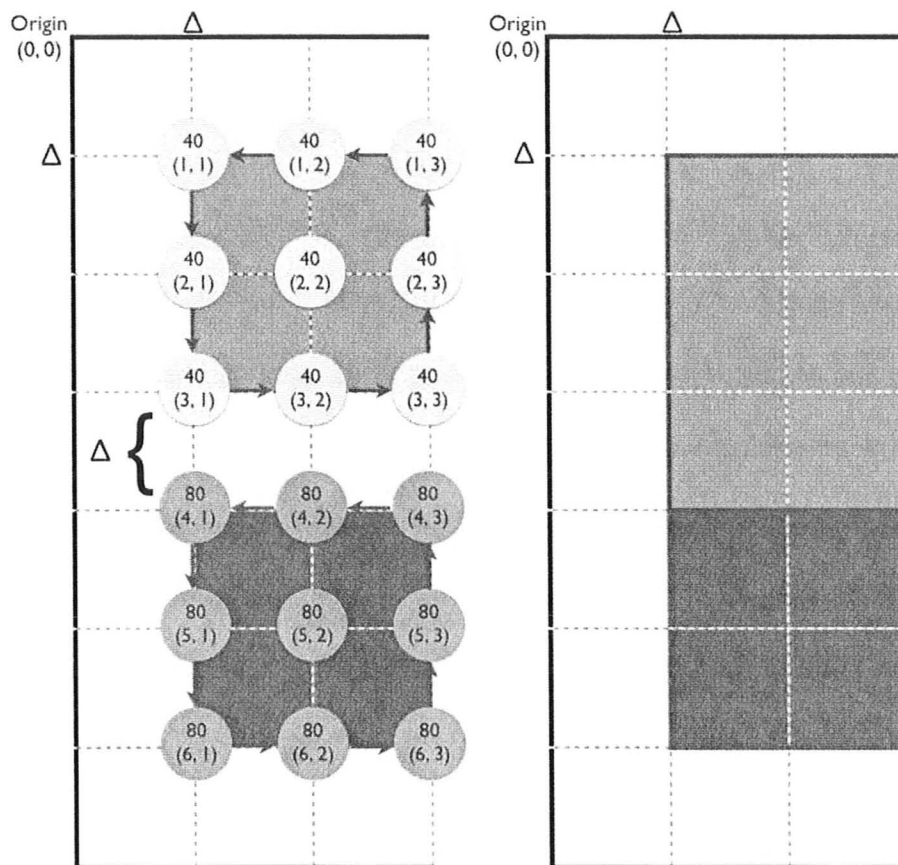


Figure 5.11: Example of two polygons with materials numbered 40 and 80. They are traced with connectivity nodes as shown on the left. A gap  $\Delta$  as coming from MRI, is left between the polygons due to no transition between 3<sup>rd</sup> and 4<sup>th</sup> row. One possible solution is to give higher priority to the material polygon number 40 (top) and to extend it towards the material polygon number 80 (bottom), as shown on the right.

Hence, a function called *boundary\_trace.m* was written to get good connectivity lists. The idea is to trace the correct path as shown in the bottom image of Figure 5.12. It uses a minimum-difference Hamiltonian-contour construction algorithm where each successive node is selected based on two proper criteria. Firstly, the change in next node’s array-index should be minimum, which can be evaluated with the sum-of-differences (SD) of row and column (col) indices of the array:

$$SD = \left| row\_index_{current\ node} - row\_index_{next\ node} \right| + \left| col\_index_{current\ node} - col\_index_{next\ node} \right| \quad (2)$$

Secondly, priority assessment in direction is done to select the next node. This is shown in Figure 5.13. The arrow ends at the node to be selected in the image-array for the connectivity list. The traversing of the path can be either clockwise (CW) or counter-clockwise (CCW). For HFSS this does not matter as long as the constructed polygon is closed and valid. The priority (P#) consideration is shown for SD evaluated up to 2. Above an SD of 2, the algorithm selects the first contender node in the list of unique nodes arranged in an ascending order. This seldom happens as nodes are usually close to each other. The connectivity lists starts with the uppermost node present in the edge map (obtained with *edging.m*) for each tissue polygon.

There are some error checks to make sure that there are no intersections or invalid list formations. The trickiest part is the node where three tissue materials meet. This makes *boundary\_trace.m* a non-trivial implementation. The problem is significant with forming a connectivity list for skin as it is very difficult to control

the crossed patterns formed at regions where there are just 2-pixel neighborhood. Hence, the construction of skin has been left out as a manual CAD manipulation process on the 3-D object imported after surface acquisition. The examples of results from *boundary\_trace.m* are shown in Figure 5.14. The figures show contiguous blocks traced from the connectivity lists.

There can be another occurrence that should be mentioned. There might be tissue polygons that do not share any boundaries with others but appear as holes within bigger polygons (that are of different tissue material than holes). It is very easy to detect these smaller polygons and make the path for them. However, there can be various sizes and shapes of these polygons and in modeling they stand out alone and cannot be united with the main body of their tissue type (and of course to the different tissue volume they are embedded in). In modeling, if one desires to ignore the small holes, one has to delete them. Some examples are shown in Figure 5.15.

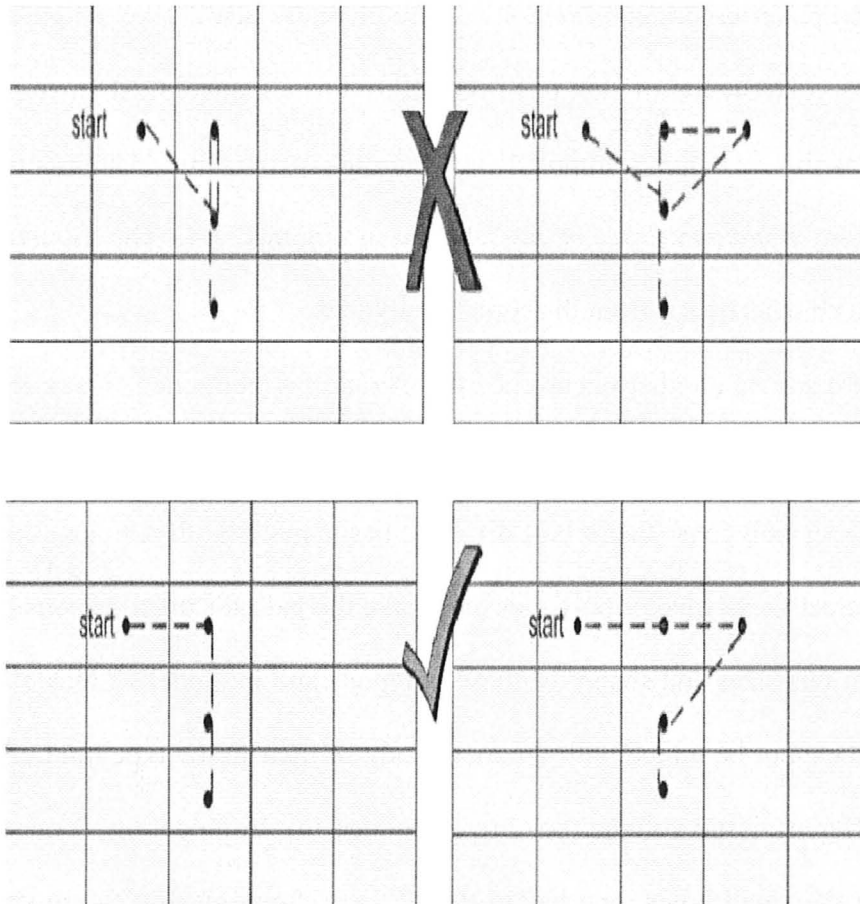


Figure 5.12: The top example shows the wrong path that can be formed if proper criteria are not taken in tracing the boundary (usually happens in connectivity-based algorithms). The bottom example shows the correct path that must be traced for a valid polygon formation.

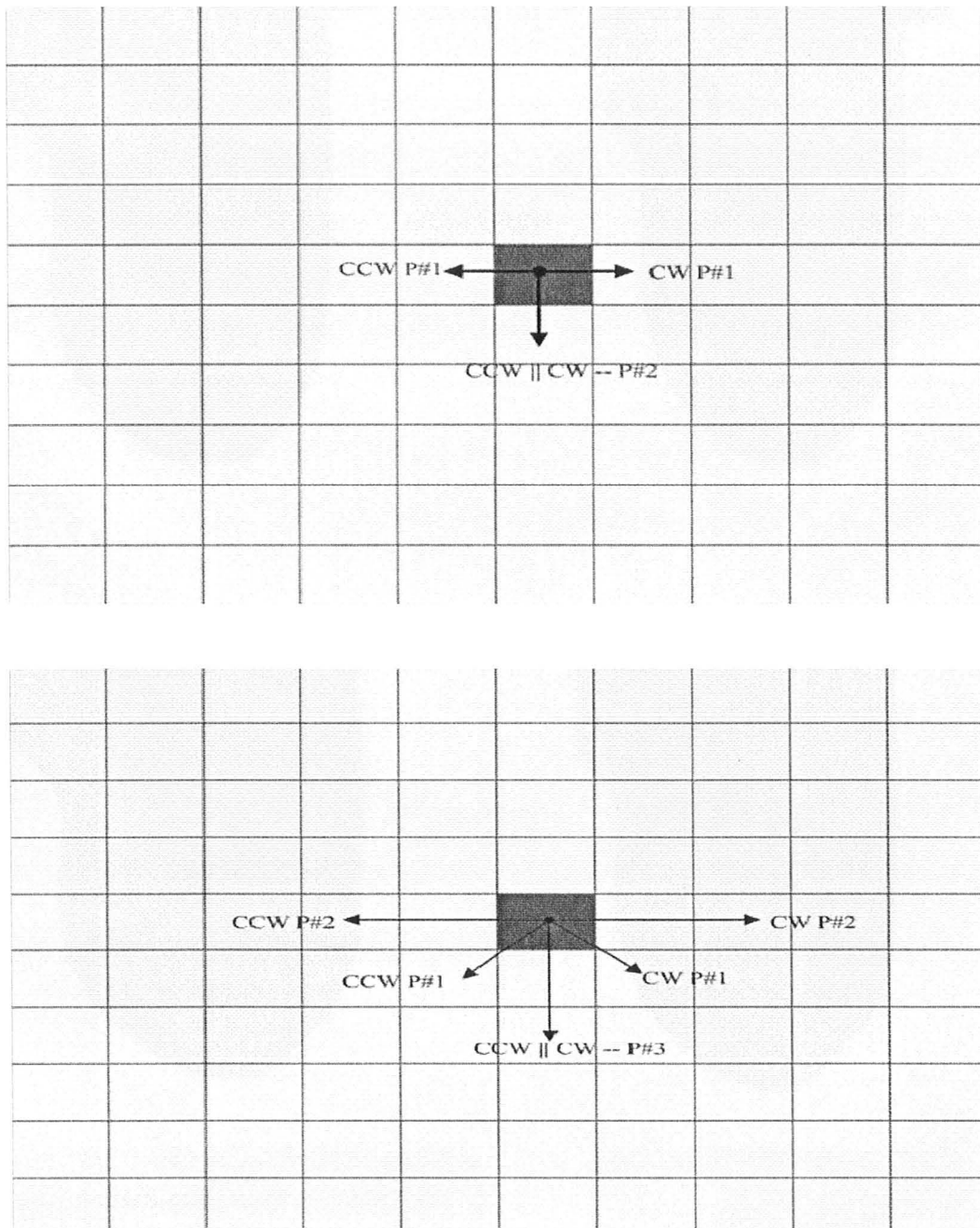


Figure 5.13: Minimum-difference algorithm to trace Hamiltonian-contour between nodes of a tissue polygon (CW: counterclockwise; CCW: counterclockwise; P#: priority to select node based on direction). The above plot is for a sum-of-differences (SD) of 1 and the plot below is for SD 2.

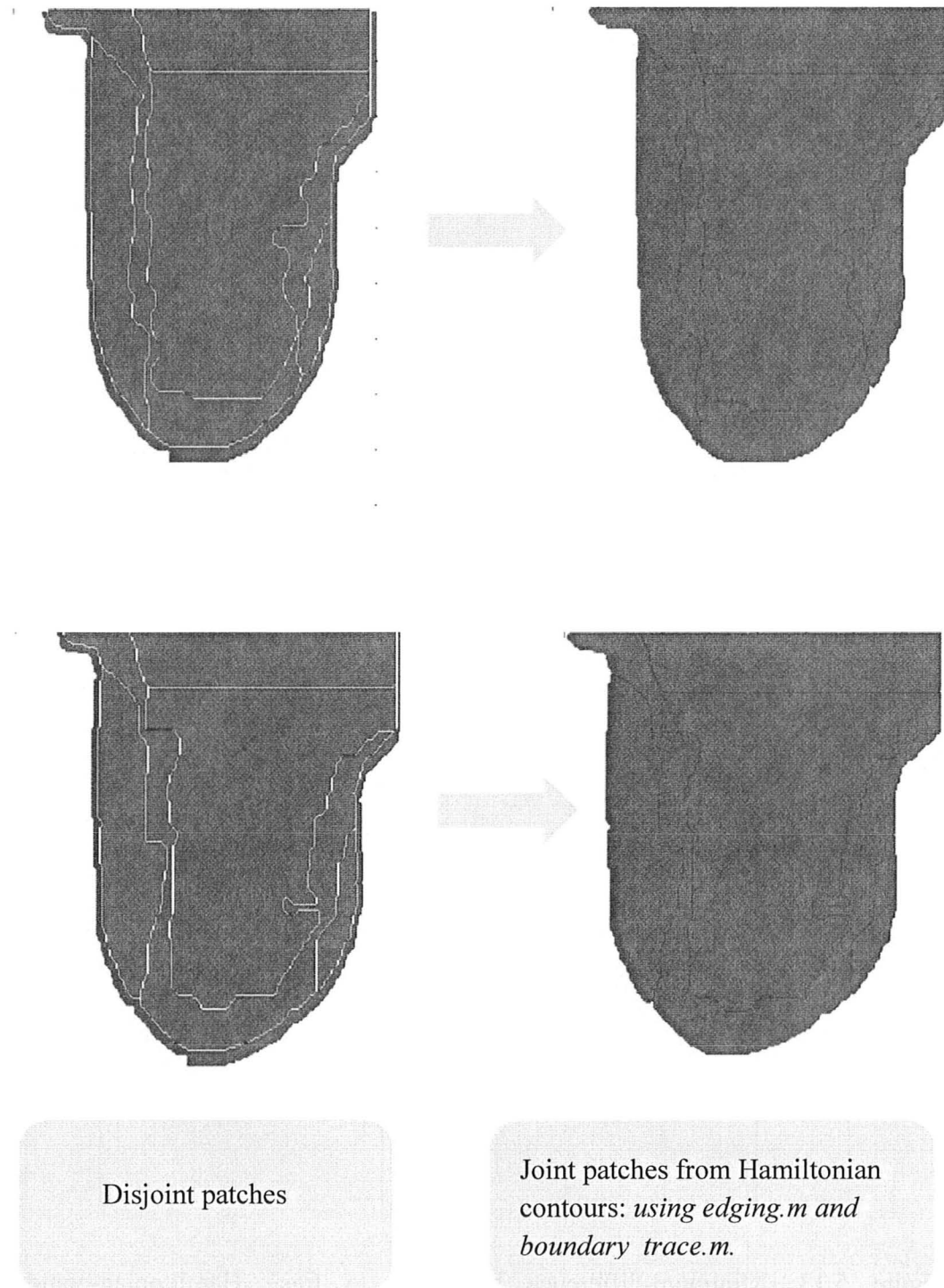


Figure 5.14: Examples showing the results of *edging.m* and *boundary\_trace.m* after the lists of nodes making a Hamiltonian Contour is obtained.



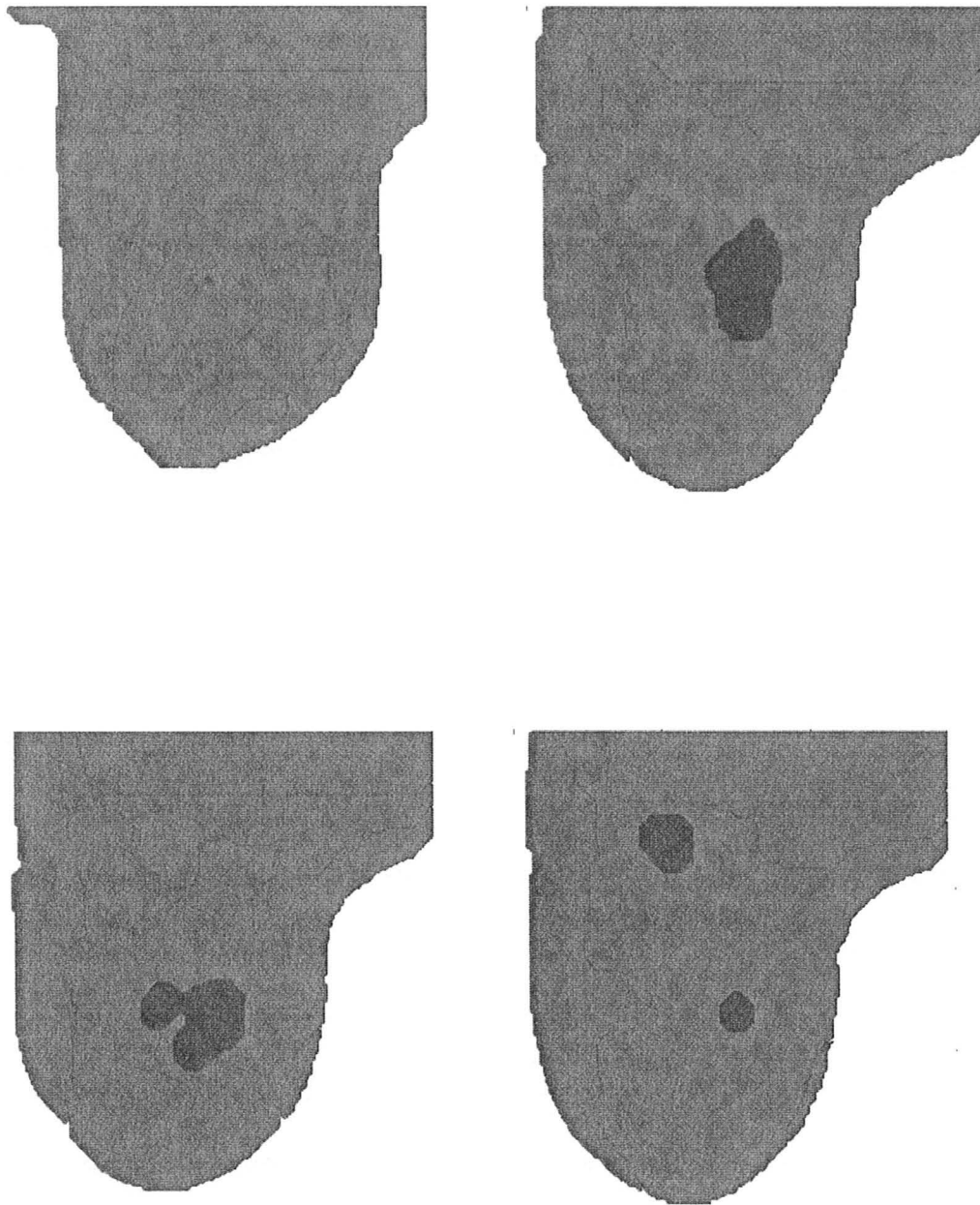


Figure 5.15: Examples showing various detected holes that are basically a small polygon within a bigger polygon (the bigger polygon's material is different from that of the smaller).

### **3.2. Polygon Formation in HFSS**

Once the lists are obtained in MATLAB, they can be converted to polygon formations in HFSS by using Visual Basic script file [30]. Scripting can be used to execute in HFSS any steps from model construction, simulation, and field export without using the graphical user interface (GUI) of HFSS. This script is generated using MATLAB where the connectivity list gives the node information and the resolution of the image gives the dimensions. Hence, a typical image is converted into contiguous polygons in 2-D plane in HFSS. The snapshot of these polygons being formed by an executed script is shown in Figure 5.16. The amount of time it takes to make one such 2-D slice varies from 15 minutes for a very big slice to 2 minutes for the small ones. The time depends on the number of nodes and hence the number of line segments to be drawn.

The memory and time in 3-D modeling is generally dependant on the number of entities used. If a data base has too fine a resolution, it is desirable to eliminate the less essential nodes to save memory and time. This may be done by rejecting nodes where the line segment to the next node has no direction change. For instance, the line segment going to a node in successive column but in the same row and vice versa can be determined in MATLAB by scanning through the lists. This results in longer segments in some polygons. This is shown in Figure 5.17. It has been found that this does cut back on the time and memory, by a factor proportional to the number of the deleted unnecessary nodes.

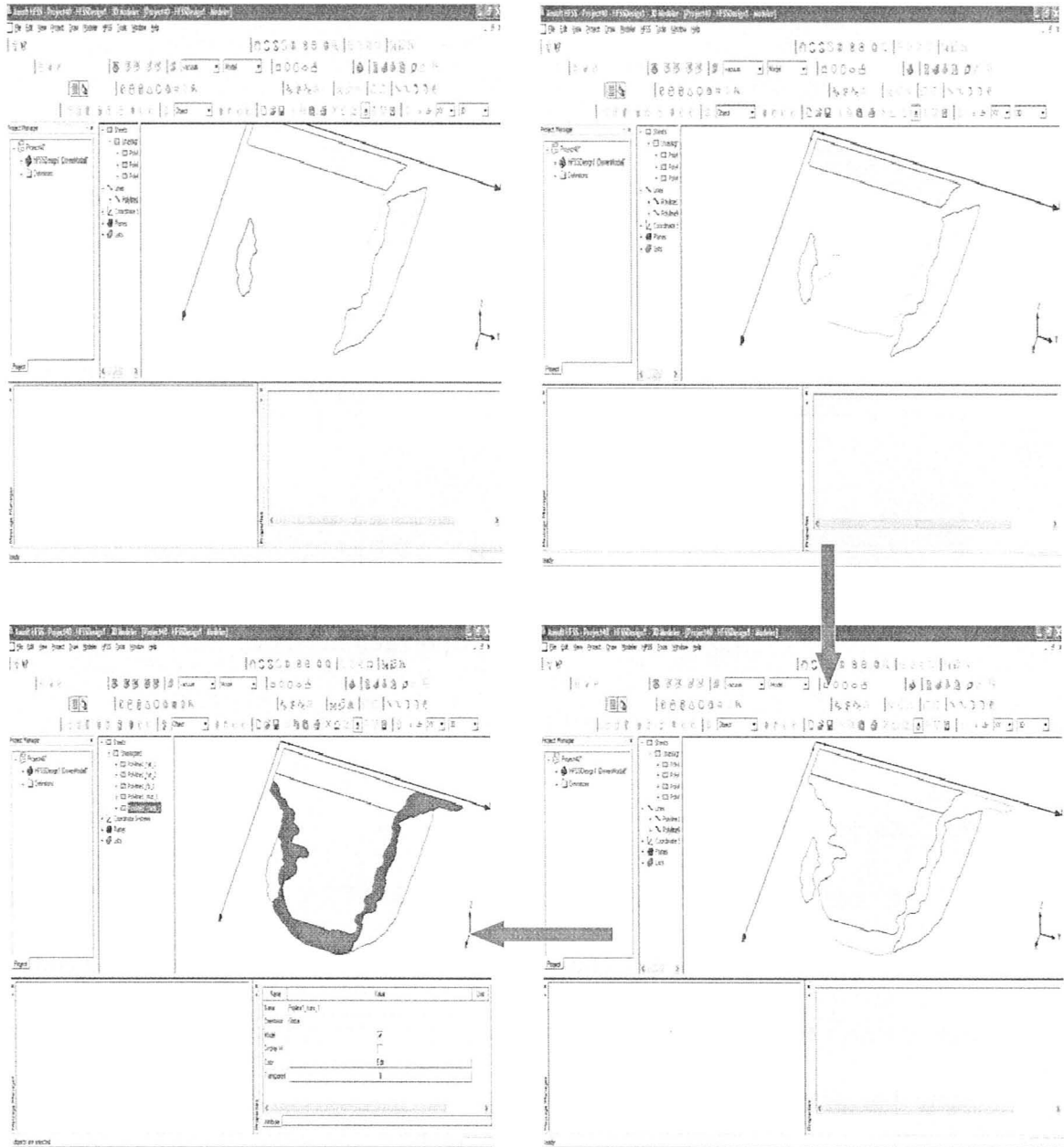


Figure 5.16: The screen shots showing the polygon formation in the HFSS interface using a Visual Basic script. The first and second images in the flow show the muscle and fat polygon constructed while the polygon for fibroglandular tissue is being traced. The third image shows the transitional-tissue polygon being traced next. The fourth image shows all contiguous tissue polygons constructed.

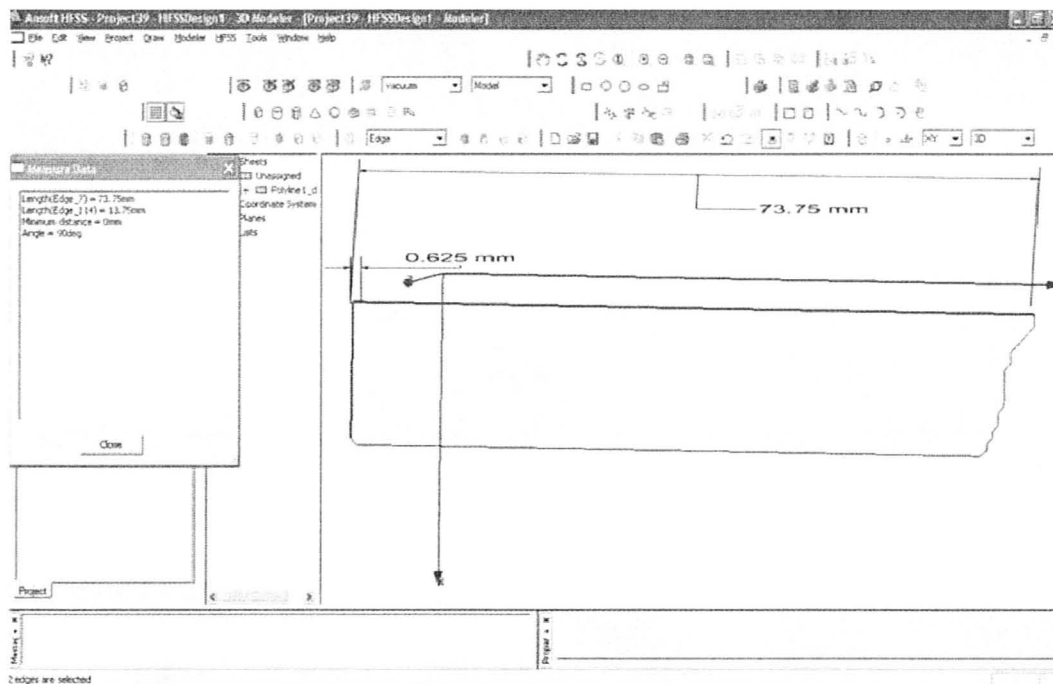


Figure 5.17: The muscle polygon in HFSS.

### 3.3. Simple GUI

A very simple GUI has been designed in MATLAB and named = “Patient Specific Numerical Breast Phantom Modeller” (PSNBPM), to execute the codes discussed so far. The last result from the GUI is an HFSS script file saved in the same file path where the images are loaded. The screenshots of the GUI are shown in Figure 5.18. This is just a starting phase in implementing a GUI. Due to time constraints, a lot remains to be done to make it more sophisticated. It is desirable to add more control options for image processing to the GUI and to enhance its interface.

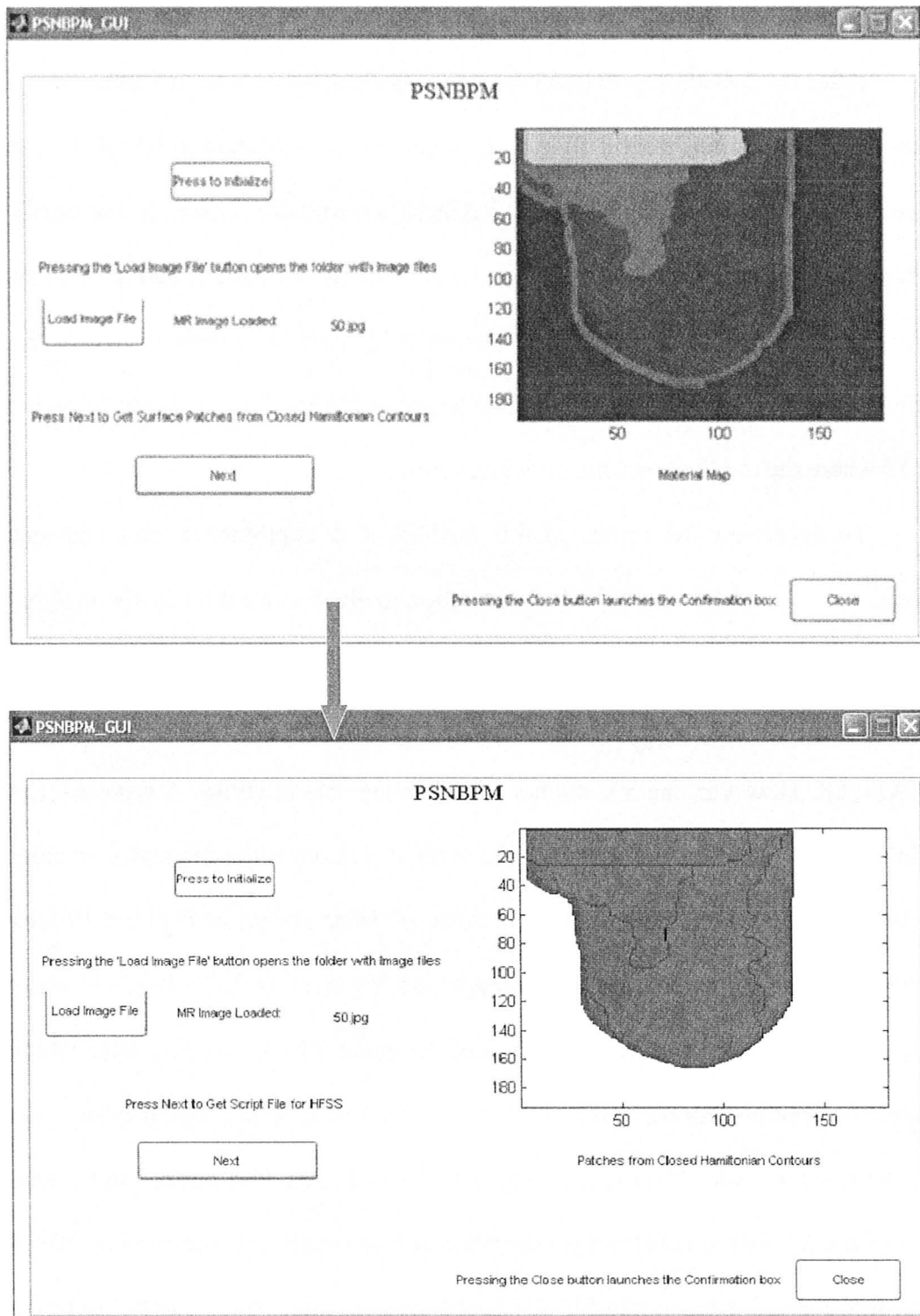


Figure 5.18: The simple GUI layout for PSNBPM.

### 3.4. *Slice-by-Slice Solid Construction in HFSS*

After the 2-D slice with tissue polygons is obtained as seen in Figure 5.16, it can be converted into a solid slice by a simple sweep operation in HFSS. This is usually incorporated in the script but has been shown here separately for clarity. The solid slice can then be assigned material properties, which is also done in the same script. To confirm that the created 3-D slice is errorless and fit for simulation, a validation check should be issued in HFSS. This is shown in Figure 5.19 where the check shows no modeling errors.

To appreciate the results of this method, it is important to state that one could use a voxel-by-voxel (VV) construction method using directly the material map generated from an MRI and its pixel resolution. This would save all the pre-processing in simplifying the material maps and making the connectivity lists in MATLAB. However, the VV method is not achievable in HFSS. A typical script file size for a Hamiltonian-contour (HC) method is 550 KB for a big slice whereas it is about 15 MB for the VV method. Also, the slice shown in Figure 5.19 took about 11 minutes for construction whereas the VV slice took 7.5 hours to make just 3363 voxels (where it was supposed to make 23,545 voxels) after which HFSS became unresponsive (after 9 hours). This is due to the high memory cost of the huge amount of entities in the MR slice of high resolution. Figure 5.20 shows the VV-based construction snapshot. It is expected that meshing by HFSS will make things even worse for VV-based method. Also, there can be no union performed to make bigger blocks as non-manifold edges are created as shown in

Figures 5.2 (b) and 5.3 (d).

The FDTD based time-domain solvers are suited to the VV-based method as the voxel structure is closer to their intrinsic meshing style. However, the HC method works better for them, too, to reduce the memory requirements. Figure 5.21 and Figure 5.22 show comparisons with comments on the file sizes. These examples are with QWED [33]. The important requirement is to have CCW orientation for the contour construction in QWED. It is needed for material assignment.

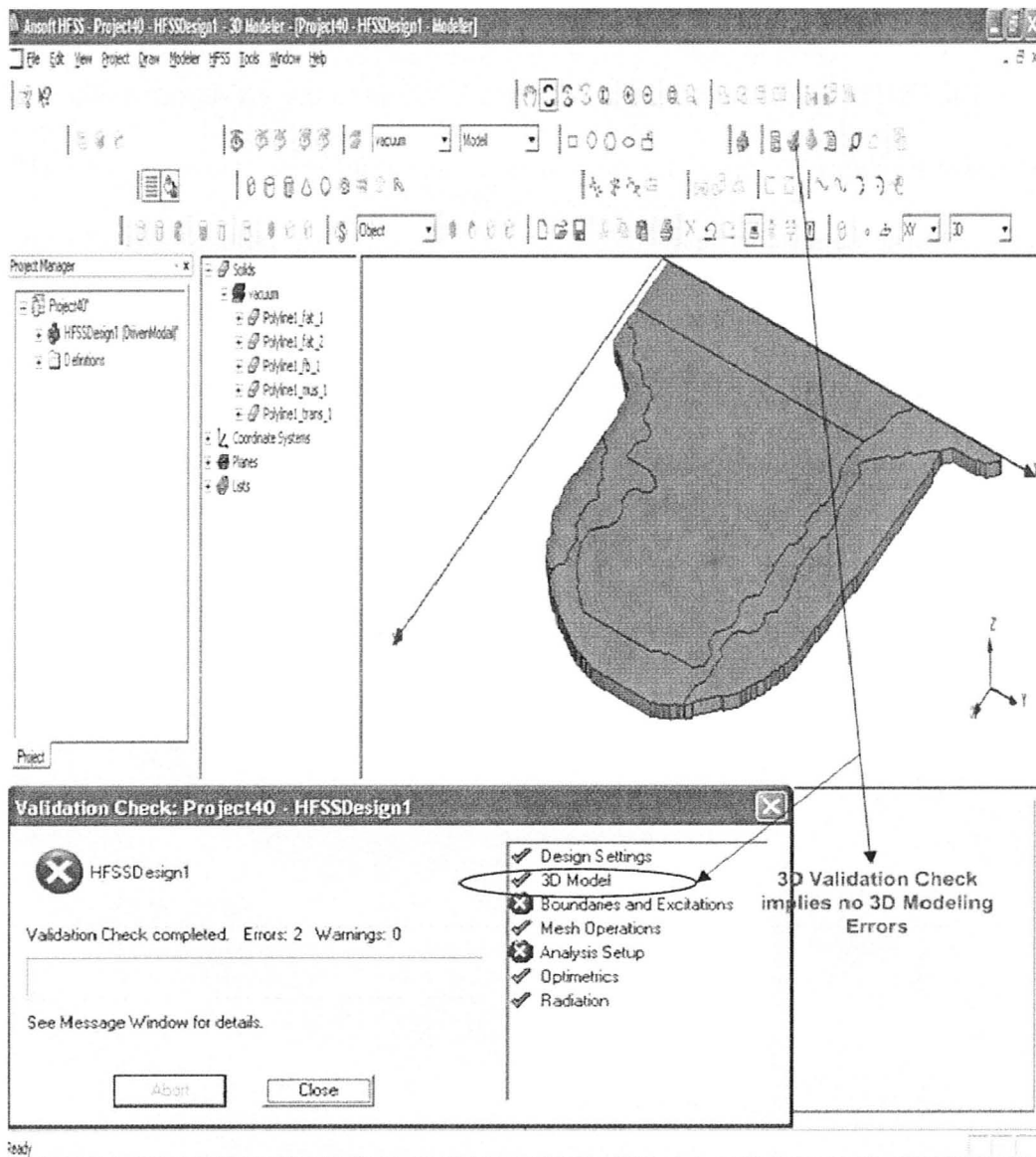


Figure 5.19: Screen shot showing HFSS slice for the MR image and the 3D validation check.



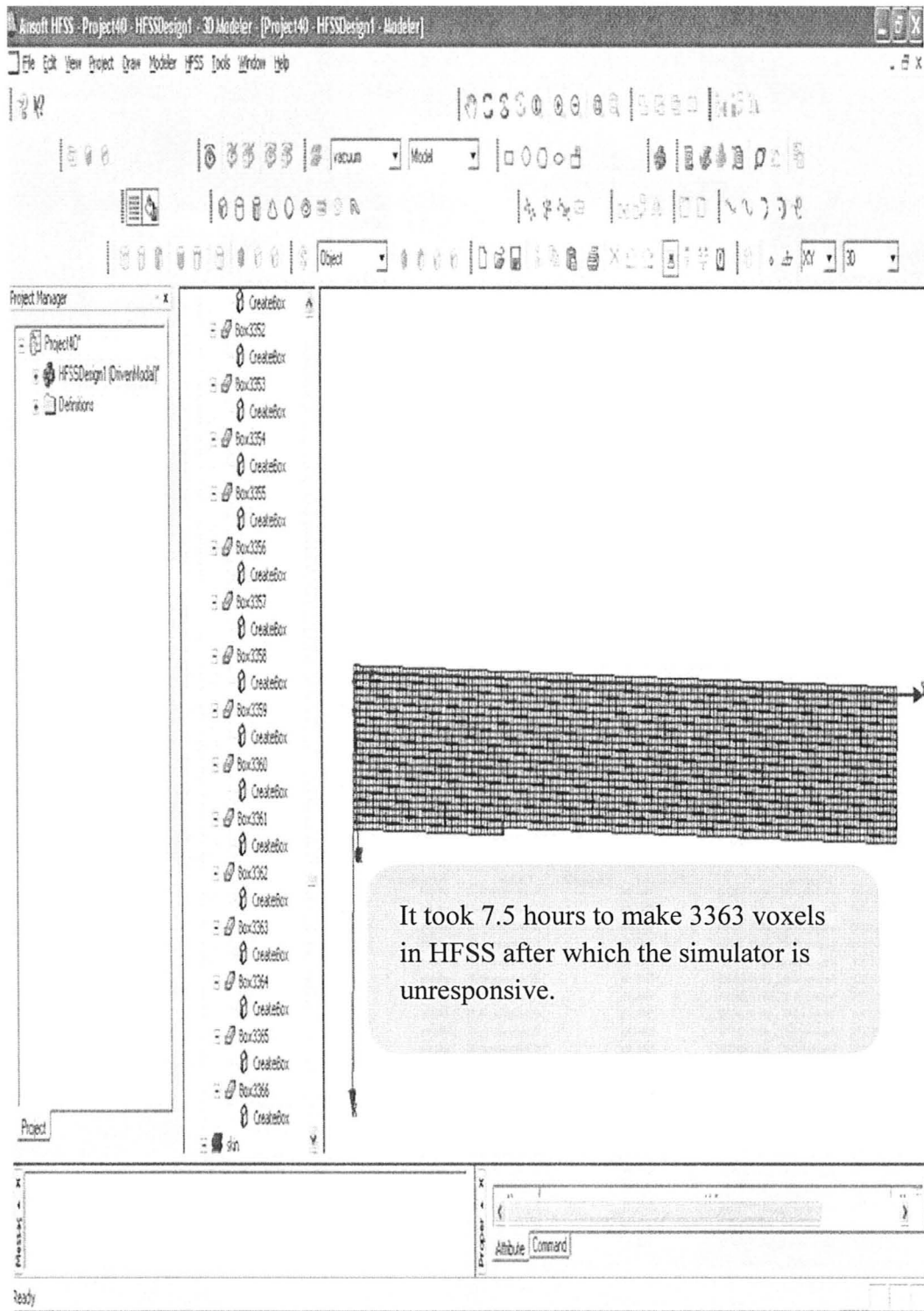


Figure 5.20: The voxel-by-voxel construction process in HFSS.

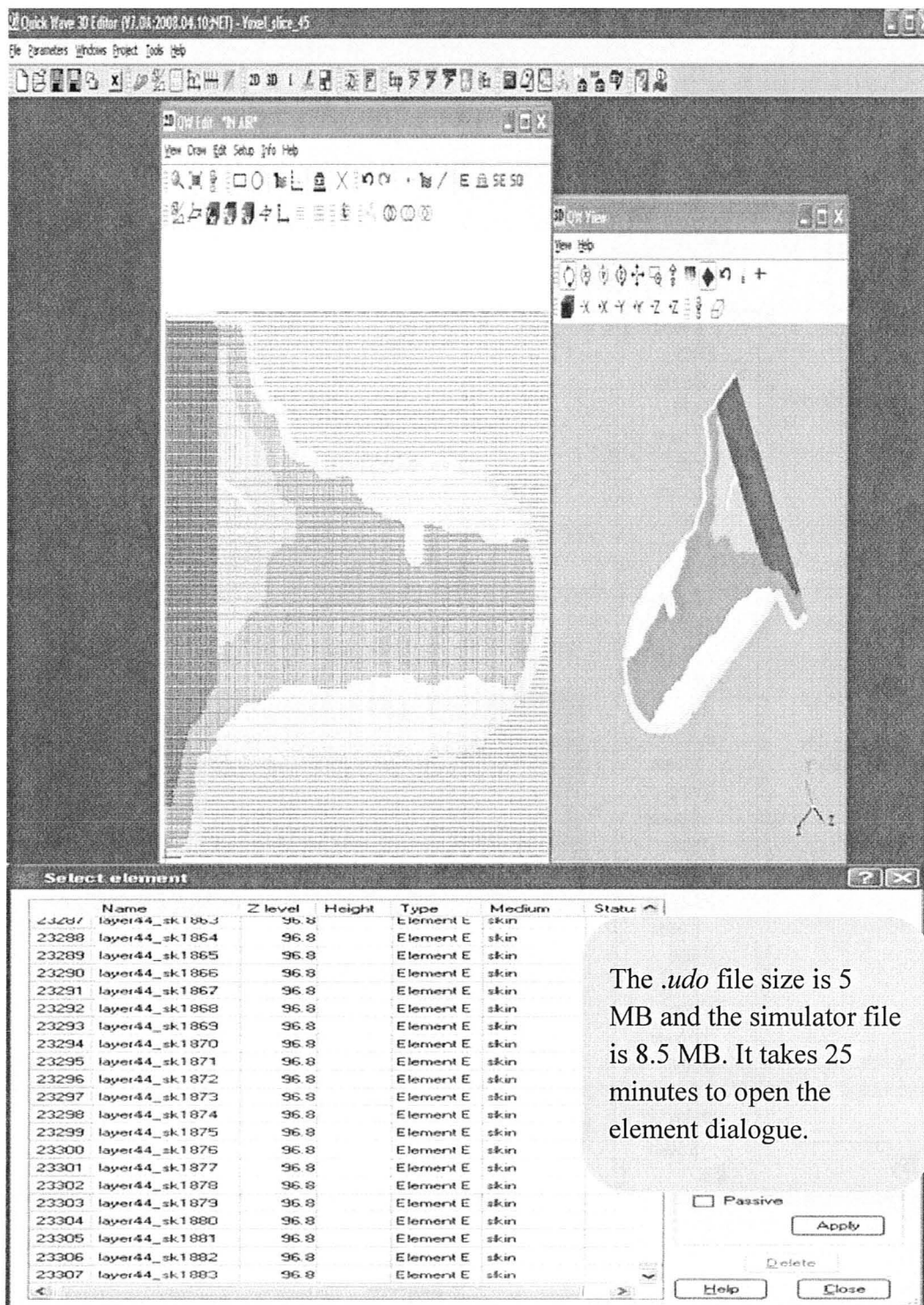


Figure 5.21: The screen shot showing the slice in the time-domain solver QWED with information on file sizes. The slice is made by the voxel-by-voxel method.

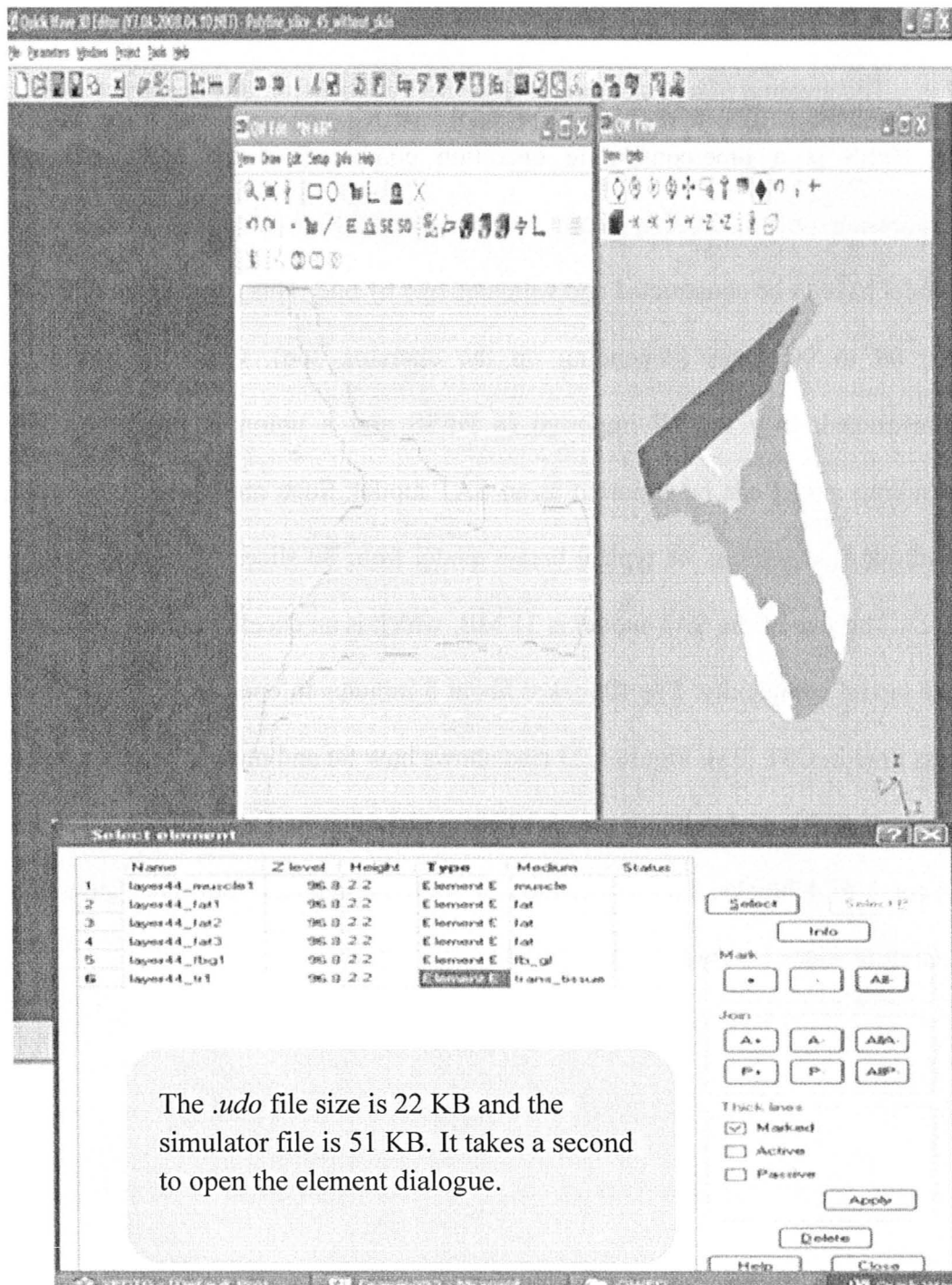


Figure 5.22: The screen shot showing the slice in the time-domain solver QWED with information on file sizes. The slice is made by the CCW Hamiltonian-contour construction method as required in QWED.

### **3.5. *SAT Models and Compatibility with Other EM Simulators***

The creation of a breast model as an SAT model from the constructed slices in HFSS is a time-consuming operation compared to the MATLAB pre-processing (which takes typically a few seconds). All the slices in the HFSS model have to be constructed and validated one by one. This can take up to 2 days for 80 to 90 slices (depending on the operator, too). Once the slices are constructed, they are all imported in HFSS and a union is performed. The resulting model can be exported as an SAT model. Such models are compatible with other simulators. A typical breast model from 80 slices is shown in Figure 5.23. The size of the SAT model is 31 MB, which is an excellent result in view of the model complexity. The file takes about 5 minutes to open in HFSS and even less time in CST [33]. Figure 5.23 also shows how fat and muscle could be united into one block each without errors whereas glandular and transitional tissue had about 3 to 4 blocks. This is because, at some boundaries, the union gave non-manifold edges for the latter two tissue types.

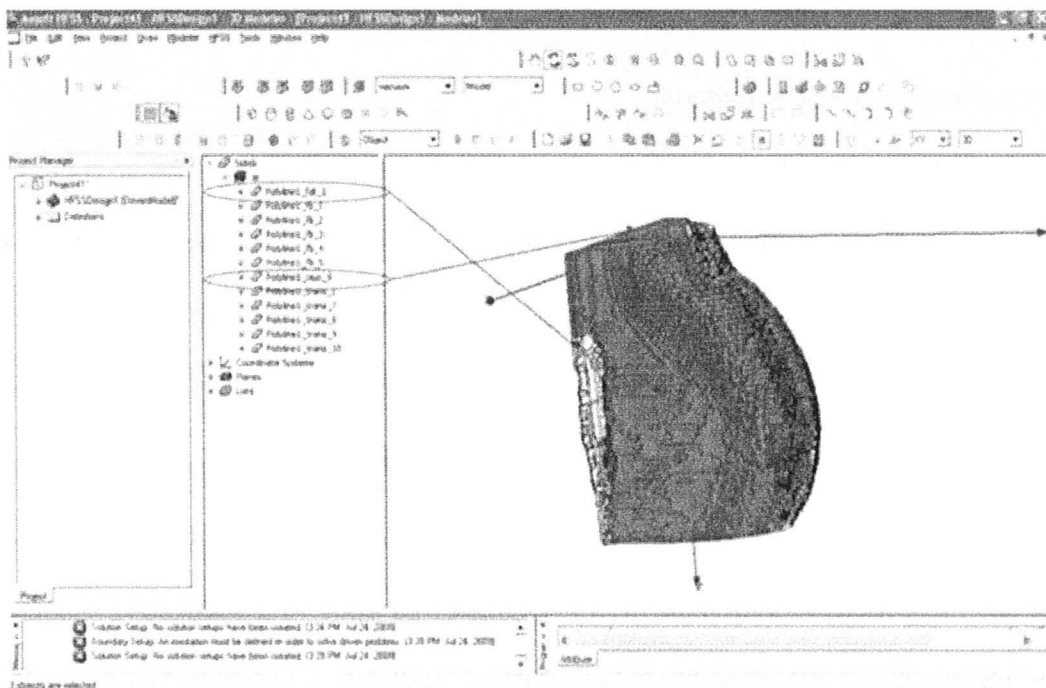
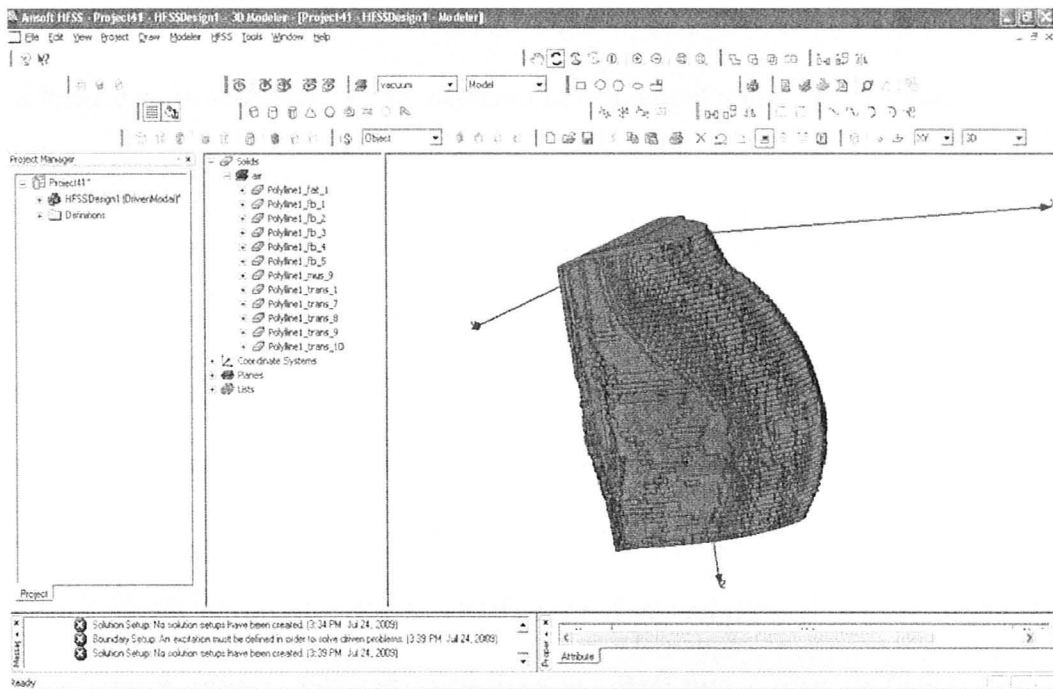


Figure 5.23: Screen shots showing the SAT file made by unifying 80 slices in HFSS. Muscle and fat for all the slices are unified without modeling error as shown in the bottom screen shot.

#### 4) SCOPE FOR MODEL SIMPLIFICATION

To reduce the computational requirements of the simulations, we need to reduce the memory requirements of the 3-D models. So far, we have described these aspects and presented a Hamiltonian-contour method that greatly improves upon the voxel-by-voxel method. Model simplification can be carried further if necessary. Both, FEM-based simulators and FDTD-based simulators, can work faster if the 3-D models are piecewise inhomogeneous models of low complexity. The meshing becomes more robust and the mesh edge length does not have to be too short. Hence, if a region-of-interest (ROI) of a tissue on an image can be approximated by only a few nodes or segments, then this greatly decreases the number of geometrical elements. This is shown in a crude example in Figure 5.24 for a transitional tissue polygon.

The algorithm to do the reduction in nodes can be used to further enhance the discussed HC method. The idea is that the structure of the tissue polygon is roughly rendered by connecting a few selected nodes. Hence, each polygon is redrawn by longer segments over the region-of-interest as seen in the material maps, instead of segment length that comes from the MRI resolution. The number of segments to be used can be flexible depending on the resolution desired and based on some threshold. This definitely has to be done in a successive manner for all the tissue polygons in an image slice; similar to what was done to make contiguous polygons (see sub-section 3.1 of this chapter). It is a situation analogous to fitting a puzzle with polygons. In summary, the scope of

improvement is both in the algorithm as well as in the GUI in order to give the user better control over the image processing and the connectivity lists.

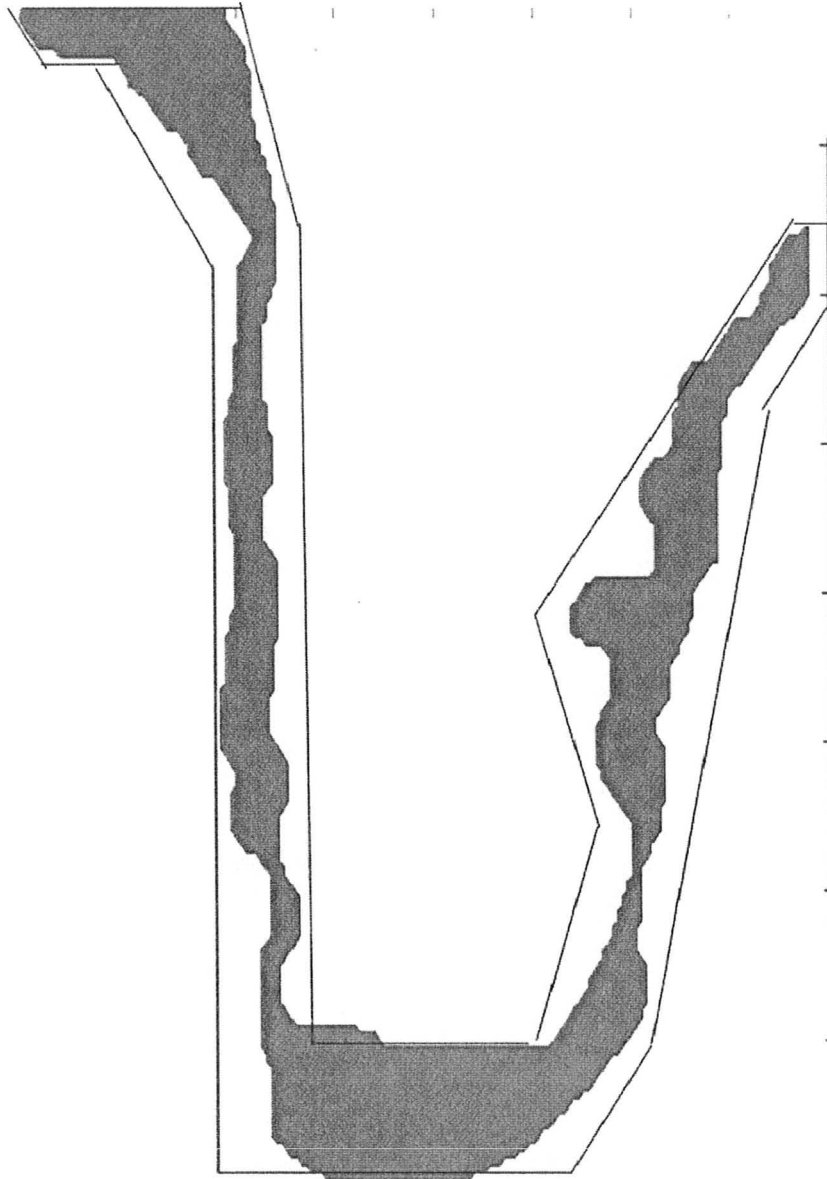


Figure 5.24: The diagram shows illustrates how fewer segments and nodes (see solid-line contour) can approximate a complex region-of-interest (see red shaded area).

---

**REFERENCES**

- [1] P. M. Meaney, M. W. Fanning, D. Li, S.P. Poplack, and K. D. Paulsen, “A clinical prototype for active microwave imaging of the breast,” *IEEE Trans. Microw. Theory Tech.*, vol. 48, pp. 1841 – 1853, 2000.
- [2] (May 2009). Managing Menopause. The Jean Hailes Foundation for Women’s Health, Victoria, Australia. [Online]. Available: <http://www.managingmenopause.org.au/content/view/37/62/>.
- [3] N. F. Boyd *et al.*, “Quantitative classification of mammographic densities and breast cancer risk: results from the Canadian National Breast screening study,” *Journal of National Cancer Institute*, vol. 87, no. 9, May 1995.
- [4] (November 2008). The American College of Radiology BI-RADS® ATLAS and MQSA: Frequently Asked Questions. American College of Radiology (ACR). [Online]. Available: [http://www.acr.org/SecondaryMainMenuCategories/quality\\_safety/BIRAD\\_SAtlas/BIRADSFAQs.aspx](http://www.acr.org/SecondaryMainMenuCategories/quality_safety/BIRAD_SAtlas/BIRADSFAQs.aspx).
- [5] M. G. del Carmen *et al.*, “Mammographic breast density and race,” *American Journal of Roentgenology: Women’s Imaging*, vol. 188, pp. 1147 – 1150, April 2007.
- [6] Dr. Miriam Stoppard, *The Breast Book*. DK ADULT Co., 1996, pp. 48.
- [7] H. S. Fiegelson, C. R. Jonas, L. R. Teras, M. J. Thun, and E. E. Calle, “Weight gain, body mass index, hormone replacement therapy, and postmenopausal breast cancer in a large prospective study,” *Cancer Epidemiology, Biomarkers & Prevention*, vol. 13, pp. 220 – 224, February 2004.
- [8] S. P. Poplack *et al.*, “Electromagnetic breast imaging: average tissue properties values in women with negative clinical findings,” *Radiology*, vol. 281, pp. 571 – 580, 2004.
- [9] M. A. Chaudary *et al.*, “A comparison of epidemiological characteristics in breast cancer patients and normal women in Great Britain and Japan: Results of a prospective study,” *Breast Cancer Research and Treatment*, vol. 18, pp. 19 – 22, 1991.
- [10] I. Stroud, *Boundary Representation Modelling Techniques*. Springer-Verlag Publishers: London: 2006.



- 
- [11] R. Bishop, and R. Crittenden, *Geometry of manifolds*. Academic Press, New York: 1964, pp. 1 – 22; 122 – 132.
- [12] Todd Rowland (July 2009). Manifold. MathWorld: A Wolfram Web Source. [Online]. Available: <http://mathworld.wolfram.com/Manifold.html>.
- [13] (December 2008). What is Non-manifold Geometry? KFourMetrics, Hyderabad, India. [Online]. Available: <http://www.kfourmetrics.com/wordpress/?p=93>.
- [14] The 3D ACIS Modeler, Spatial Corp. Headquarters, 310 Interlocken Parkway, Suite 200, Broomfield, CO 80021-3468, USA. [Online]. Available: <http://www.spatial.com/>.
- [15] (May 2009). Manifold and Non-manifold Objects. Spatial Docs, Spatial Corporation. [Online]. Available: [http://doc.spatial.com/index.php/Manifold\\_and\\_Non-manifold\\_Objects](http://doc.spatial.com/index.php/Manifold_and_Non-manifold_Objects).
- [16] (May 2009). Edge. Spatial Docs, Spatial Corporation. [Online]. Available: <http://doc.spatial.com/index.php/EDGE>.
- [17] [Online]. Available: <http://www.shapeways.com/tutorials/things-to-keep-in-mind>.
- [18] J. Oakley, C. P. Riley, S. Taylor, and C. W. Trowbridge, “Achieving the holy grail of seamless CAD data import into analysis software,” *COMPEL: The International Journal for Computation and Mathematics in Electrical and Electronic Engineering*, vol. 21, no. 4, pp. 512 – 518, 2002.
- [19] D. Wilson, “Data exchange and software integration: interdisciplinary design challenges,” *Artificial Intelligence for Engineering Design, Analysis and Manufacturing*, vol. 12, pp. 73 – 76, 1998.
- [20] S. McMains, J. Smith, and C. Sequin, “The evolution of a layered manufacturing interchange format,” *Proceedings of DETC02 2002 ASME Design Engineering Technical Conferences*, September 2002.
- [21] J. Hornak (2000). Magnetic Resonance Imaging. [Online Chapter]. Available: <http://www.cis.rit.edu/class/schp730/lect/lect-2.htm>.
- [22] C. E. Thomson *et al.*, “Magnetic resonance imaging – a general overview of principles and examples in veterinary neurodiagnosis,” *MRI-Principles and Neurodiagnosis*, vol. 34, no. 1, March 1992.

- [23] *Imaging Research Centre (IRC)*. Brain Body Institute, St. Joseph Healthcare Hospital, 50 Charlton Ave. East, Hamilton, Ontario.
- [24] *DICOM, Digital Imaging and Communications in Medicine*. National Electrical Manufacturers Association (NEMA), Suite 1752, 1300 North 17<sup>th</sup> Street, Rosslyn, VA 22209, USA. [Online]. Available: <http://medical.nema.org/dicom>.
- [25] David Clunie. An introduction to the DICOM single-file format. [Online Chapter]. Available: <http://www.sph.sc.edu/comd/rorden/dicom.html>.
- [26] T. H. Cormen, C. E. Leiserson, R. L. Rivest, C. Stein, *Introduction to Algorithms*, 2<sup>nd</sup> ed. MIT Press, 2004, pp. 527 – 549.
- [27] H. N. Christiansen, and T. W. Sederberg, “Conversion of complex contour line definitions into polygonal element mosaic,” *ACM (Association for Computing Machinery) SIGGRAPH Computer Graphics*, vol. 12, pp. 187 – 192, 1978.
- [28] H. K. Fuchs, and S. P. Uselton, “Optimal surface reconstruction from planar contours,” *Communications of the ACM (Association for Computing Machinery)*, vol. 20, no. 10, pp. 693 – 702, October 1977.
- [29] Ansoft HFSS ver. 11, Ansoft Corporation, 225 West Station Square Drive, Suite 200, Pittsburgh, PA 15219, USA, 2008. [Online]. Available: <http://www.ansoft.com>.
- [30] (June 2003). *Introduction to Scripting in HFSS*. Ansoft Corporation, 225 West Station Square Drive, Suite 200, Pittsburgh, PA 15219, USA, 2008.
- [31] MATLAB<sup>™</sup> 7.1, The MathWorks Inc., 3 Apple Hill Drive, Natick, MA, 2005. [Online]. Available: <http://www.mathworks.com/>.
- [32] XnView for Windows (June 2007). [Online]. Available: <http://www.xnview.com>.
- [33] CST Microwave Studio, CST of Americal, Inc., Headquarters at 492 Old Connecticut Path, Suite 505 Framingham, MA 01701, USA, 2009. [Online]. Available: <http://www.cst.com/>.
- [34] QW-3D v. 7.0, QWED Sp. z o.o., ul. Nowowiejska 28 lok. 32, 02-010 Warsaw, Poland, 2009. [Online]. Available: <http://www.qwed.com.pl/>.

# CHAPTER 6

## CONTRIBUTIONS TO NUMERICAL MODELING

### INTRODUCTION

So far, the chapters in this thesis have presented the work related to creating and representing the patient's breast in both experiments and simulations. In experiments, the imaging apparatus with the antennas is a key component in addition to the physical phantoms. Also, numerical modeling is an essential part of the reconstruction algorithms.

A novel TEM horn antenna has been proposed for microwave imaging of the breast by Reza K. Amineh of our group. The major design requirement achieved by the antenna is that it couples the microwave energy into the tissue

without being immersed itself in a coupling medium. This ensures that the imaging system including the antennas is convenient to use in a clinical environment, i.e., it is easy to maintain and sanitize after a patient is examined. The antenna has been designed to operate in the UWB range from 3.1 GHz to 10.6 GHz. The antenna has shown good results with wide impedance match and efficient power coupling capability. The antenna is a good contender for both microwave tomography (frequency-domain) and radar-based (time-domain) imaging systems. To confirm this, the fidelity of the antenna is computed numerically using EM simulators. The related work and results are presented in section 1 of this chapter. This material can be found in expanded form in a technical report [1].

Biomedical imaging applications with microwaves [2]-[5] have gained significant attention in recent years. However, clinical or commercial implementations are not yet within reach. Among the many challenges, the development of efficient and reliable reconstruction algorithms is a key. The reconstruction algorithm relies on the gradient (or Jacobian) computation with an electromagnetic (EM) forward model. Microwave tomography is based on such high-frequency forward models. The optimization problem associated with microwave tomography is solved by minimizing an objective function. The construction of appropriate objective functions is hence essential. The work and results related with this component is discussed in section 2 of this chapter. This

material can be found in expanded form in a technical report on sensitivity analysis for detection algorithms [6].

## 1) FIDELITY OF THE ANTENNA

### 1.1. Antenna Structure and Impedance Results

The TEM horn antenna is a traveling-wave structure that consists of two conducting plates. To radiate efficiently, its flare angle, plate width and length are properly chosen. The designed antenna is a linearly tapered structure, as shown in Figure 6.1. It features fabrication simplicity. TEM horn antennas are usually fed by a coaxial line. A balun is needed to match the impedance of a TEM horn, which is a balanced structure, to that of an unbalanced coaxial line [1], [7], [8].

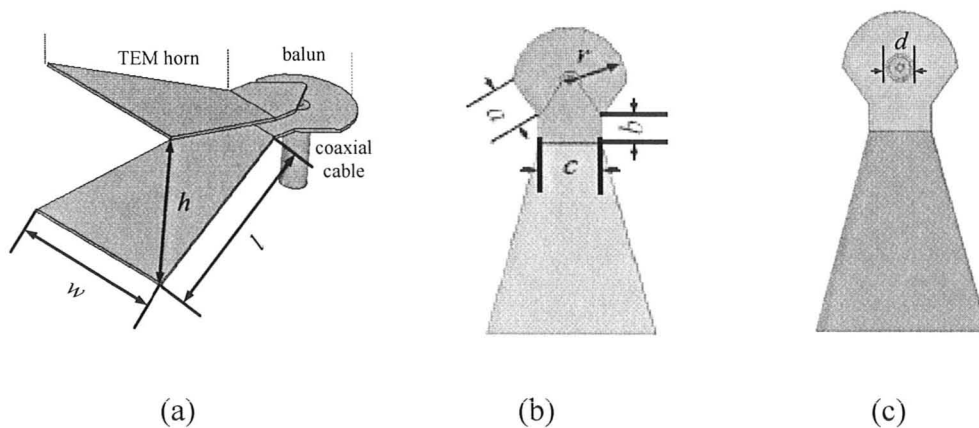
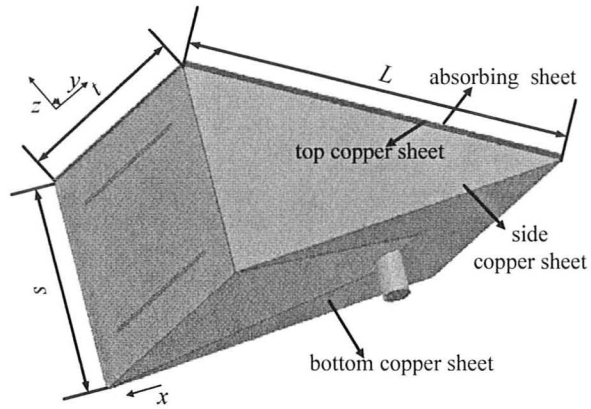
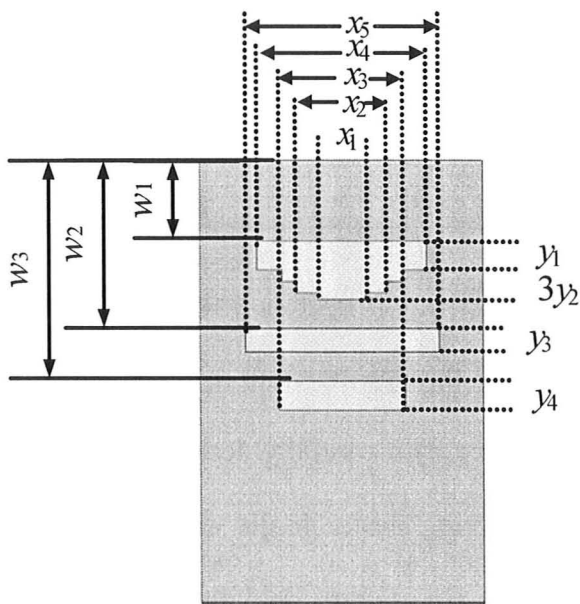


Figure 6.1: Antenna structure: (a) the TEM horn with a coaxial feed and the balun; (b) top view of the TEM horn; (c) bottom view of the TEM horn.

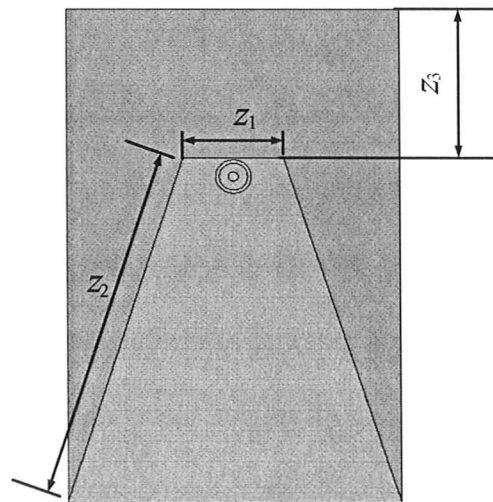
This TEM horn is placed in a solid dielectric medium, as shown in Figure 6.2, with  $\epsilon'_r = 10$  and  $\tan\theta = 0.01$  (ECCOSTOCK HiK Cement [9]) so that it can be used for direct measurement of the breast tissue without coupling liquid. In order to decouple the antenna from the surrounding medium, the outer surface of the dielectric enclosure is covered with copper sheets on the top, bottom, and side surfaces. These copper sheets are bonded together. The top and bottom copper sheets have patterned apertures in order to tune the impedance in the UWB range. The areas that are not covered by copper sheets are shown in pink (lighter gray in gray scale) in Figure 6.2. The shape parameters of the dielectric enclosure also influence the impedance of the antenna and the optimized values of the design are given in Table 6.1. The antenna length is 75 mm and the aperture size is 38 mm  $\times$  47 mm. A microwave absorbing sheet with  $\epsilon'_r \approx 30$ ,  $\epsilon''_r \approx 2$ ,  $\mu'_r \approx 1.7$ , and  $\mu''_r \approx 2.7$  (ECCOSORB FGM-40 [9]) is glued to the top surface to prevent undesired radiation and interference [7].



(a)



(b)



(c)

Figure 6.2: Antenna structure: (a) the TEM horn placed in a dielectric medium with relative permittivity of 10 with copper sheets on all outer surfaces except the front aperture and a microwave absorbing sheet on the top surface; (b) the copper sheet pattern on the top surface; (c) the copper sheet pattern on the bottom surface.

TABLE 6.1: DESIGN PARAMETERS OF ANTENNA.

Parameter	Value (mm)	Parameter	Value (mm)
$l$	39.6	$w_3$	38.0
$w$	31.2	$x_1$	8.0
$h$	22.6	$x_2$	21.0
$a$	8.3	$x_3$	28.0
$b$	5.0	$x_4$	32.0
$c$	11.4	$x_5$	15.0
$r$	10.5	$y_1$	5.0
$d$	5.0	$y_2$	2.0
$L$	75.9	$y_3$	4.0
$s$	38.0	$y_4$	5.0
$t$	47.0	$z_1$	14.0
$w_1$	14.0	$z_2$	55.3
$w_2$	29.0	$z_3$	23.0

The antenna achieves the design requirement of operation without coupling medium by: (i) directing all radiated power through its front aperture, and (ii) blocking external electromagnetic interference by a carefully designed enclosure consisting of copper sheets and power absorbing sheets. In the whole UWB, the antenna features: (a) good impedance match, (b) uniform field distribution at the antenna aperture, and (c) good coupling efficiency. These features are crucial in the detection and characterization of tumors. The measured results are also in fairly good agreement. Figure 6.3 shows that the measured and simulated (carried out with HFSS ver. 11 [12]) magnitude of reflection coefficient,  $|S_{11}|$ , is below -10 dB. Figure 6.4 shows that the antenna is well isolated from the environment.



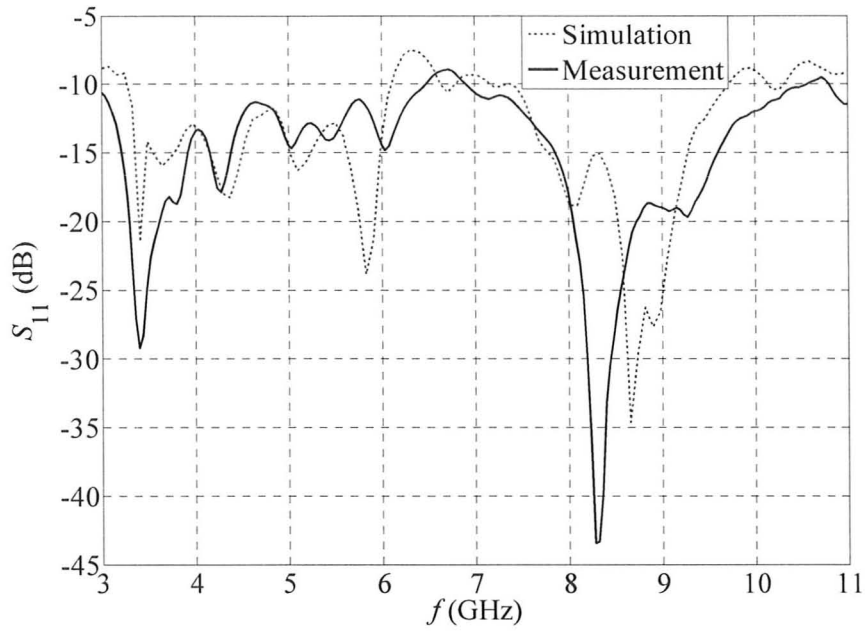


Figure 6.3: Simulated and measured insertion loss.

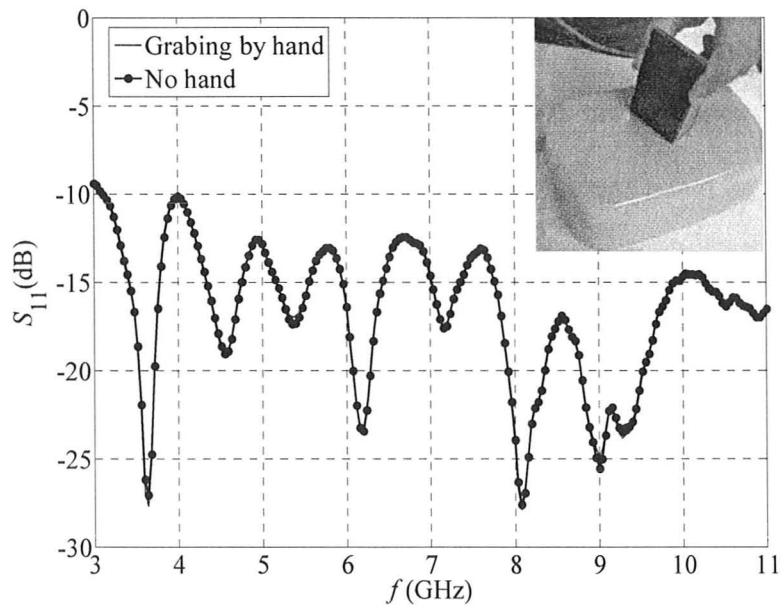


Figure 6.4: Measuring the breast phantom when grabbing the antenna directly.

## 1.2. Fidelity Evaluation

### 1.2.1. Theory and formulas

To gauge the level of distortion in the transient radiated pulse as it propagates through the tissue layers, we require a measure of its distortions in comparison with the input signal at the feed terminals of the antenna. Such a measure between two signals,  $r(t)$  and  $f(t)$ , which uses amplitude weighting and time shifting of the signal, is [10]:

$$d = \min_{\tau} \int_{-\infty}^{\infty} \left| \hat{r}(t - \tau) - \hat{f}(t) \right|^2 dt \quad (1)$$

where

$$\hat{r}(t) = \frac{r(t)}{\left[ \int_{-\infty}^{\infty} |r(t)|^2 \right]^{1/2}} \quad \text{and} \quad \hat{f}(t) = \frac{f(t)}{\left[ \int_{-\infty}^{\infty} |f(t)|^2 \right]^{1/2}} \quad (2)$$

The input  $f(t)$  and the output  $r(t)$  are normalized to have unit energy, and the delay  $\tau$  is varied to make the integral in (1) reach a minimum. Expanding (1), the distortion parameter  $d$  can be written as [10]:

$$\begin{aligned} d &= \min_{\tau} \left[ \int_{-\infty}^{\infty} |\hat{r}(t + \tau)|^2 dt + \int_{-\infty}^{\infty} |\hat{f}(t)|^2 dt - 2 \int_{-\infty}^{\infty} |\hat{f}(t) \hat{r}(t + \tau)| dt \right] \\ &\Rightarrow \min_{\tau} 2 \left[ 1 - \int_{-\infty}^{\infty} |\hat{f}(t) \hat{r}(t + \tau)| dt \right] = \min_{\tau} 2[1 - F] \end{aligned} \quad (3)$$

Here,  $F$  is defined as the fidelity, given by the formula:

$$F = \int_{-\infty}^{\infty} \left| \hat{f}(t) \hat{r}(t + \tau) \right| dt \quad (4)$$

The minimum distortion is obtained when  $\tau$  is chosen appropriately to maximize the integral term, which is the cross-correlation of  $\hat{r}(t)$ , the normalized transmitted E field magnitude [see (2)]; and  $\hat{f}(t)$ , the normalized input E field magnitude at or near the antenna terminals. Thus, the fidelity parameter  $F$  is determined by the peak of the cross-correlation function. Since a change in sign is usually not regarded as a distortion, the absolute value of  $F$  is used in measurements and calculations [10].

The use of  $F$  from (4) is particularly meaningful when the output is expected to be similar to the input. For instance, during this investigation, the tissue is in the near zone of the antenna (as there is direct contact); hence the fidelity  $F$  is examined as the deviation of the output radiated signal in the antenna bore sight direction, from the input signal in the coaxial feed.

### 1.2.2. Simulations and results

Two electromagnetic (EM) simulators based on FDTD were used. At first simulations were done with XFDTD ver. 6.3 [13]. Due to unsatisfactory impedance results with XFDTD, later CST Microwave Studio Suite [14] was employed. For details on simulations with both, refer to [1]. A summary is given below:

- (a) Simulation with XFDTD: The antenna structure modeled with the coaxial

cable simulated in XFDTD is shown in Figure 6.4. The available source types are lumped elements that can be either current sources or voltage sources (with and without a resistor). The antenna structure in Figure 6.5 uses resistive voltage source (RVS) element with a  $50 \Omega$  resistor. A zoom on the source (a RVS) is shown in Figure 6.6. The cable has to be truncated with absorbing wall at the cable's circular aperture to minimize reflections and numerical errors [11]. XFDTD does not allow defining the absorbing condition within the computation domain. This leads to the need to model a long cable from the feed to the top wall of the air box where it connects to Liao's absorbing boundary. Also, the material should be the same within 20 cells of the boundary condition in XFDTD and hence a PEC stub is used at the truncation. It is important to mention that XFDTD does not allow the modeling of absorbing sheets which have both electric and magnetic properties (i.e.,  $\epsilon_r' \neq 1$  and  $\mu_r' \neq 1$ ).

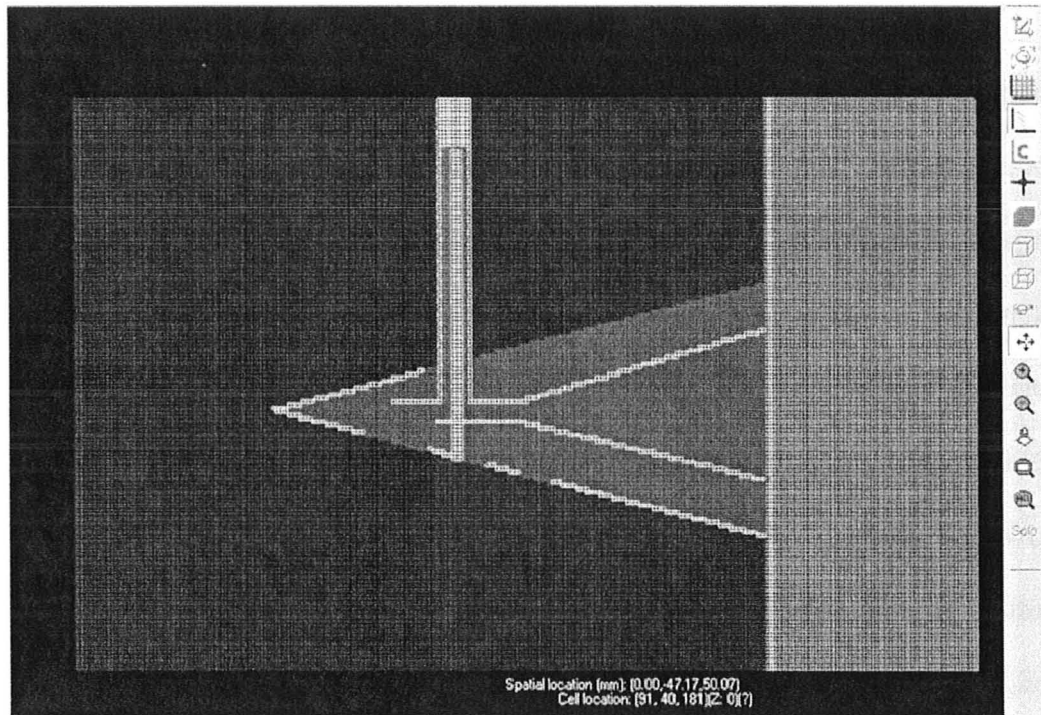


Figure 6.5: Antenna structure with meshed coaxial cable with a PEC stub at end.

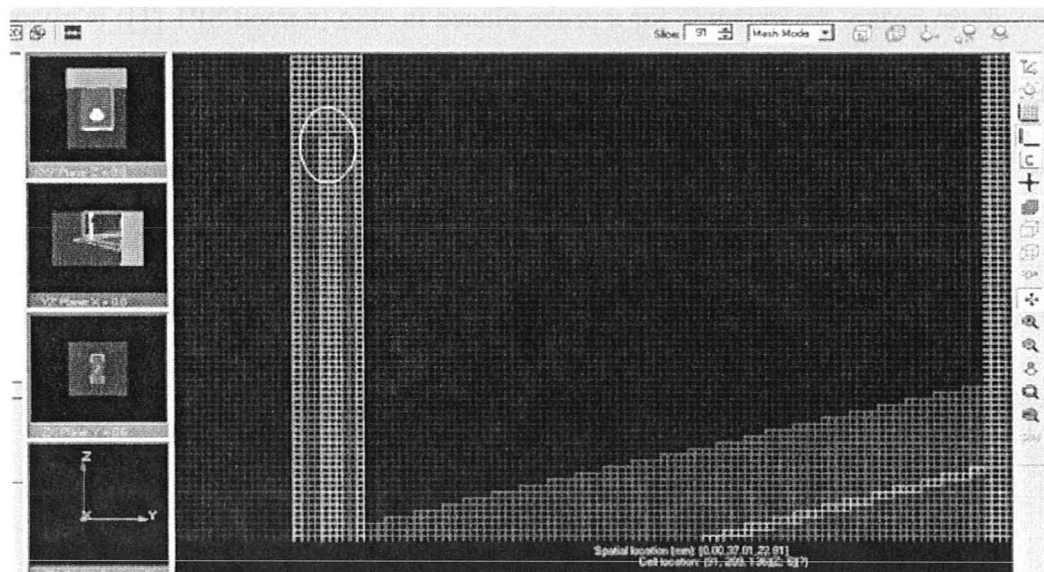


Figure 6.6: Resistive voltage source connected at the end of the inner cylinder. The source is at the centre of the white oval between the inner wire and the coax termination.

One of the fidelity results obtained with XFDTD is shown here. It is computed with respect to the incident field recorded in the feed region between parallel plates. The recorded field waveform is shown in Figure 6.7. The corresponding fidelity is shown in Figure 6.8. It is to be noted that although the attenuation in the fidelity graph should be decreasing monotonically, the result obtained here does not achieve this. Firstly, it might be due to the inaccuracies of fields given by the simulator. Secondly, there might be errors in shifting each waveform precisely by  $\tau$  time steps through a generic MATLAB [15] code. This shift is applied to all transmitted waveforms which are delayed compared to incident field at the feed. This is because to perform cross-correlation operation, the waveforms have to be matched. This is done by pattern matching with waveform peaks. An example for a probe placed in skin (named SP1 [1]) is given in Figure 6.9, where the top graph shows original waveform recorded at SP1 and the bottom graph shows the shifted waveform to match with the incident field.

The time shift  $\tau$  is chosen so as to achieve maximum fidelity. This is done iteratively after a suitable time step  $\tau_{est}$  is estimated by pattern matching. This iterative method is applied over a range of  $\tau$ :

$$\tau_{est} - \frac{\tau_{est}}{f} \leq \tau \leq \tau_{est} + \frac{\tau_{est}}{f} \quad (5)$$

where  $f = 5, 10$ , etc. is any factor. Here, a factor of 10 was used for optimum correlation.

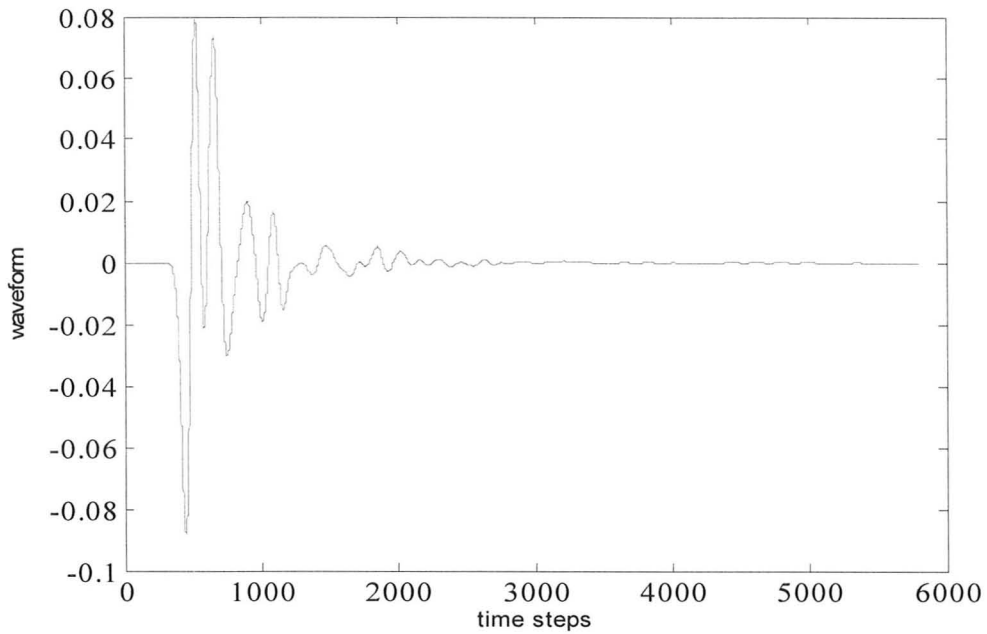


Figure 6.7: Time waveform ( $E_z$  field) recorded between the horn plates inside the antenna.

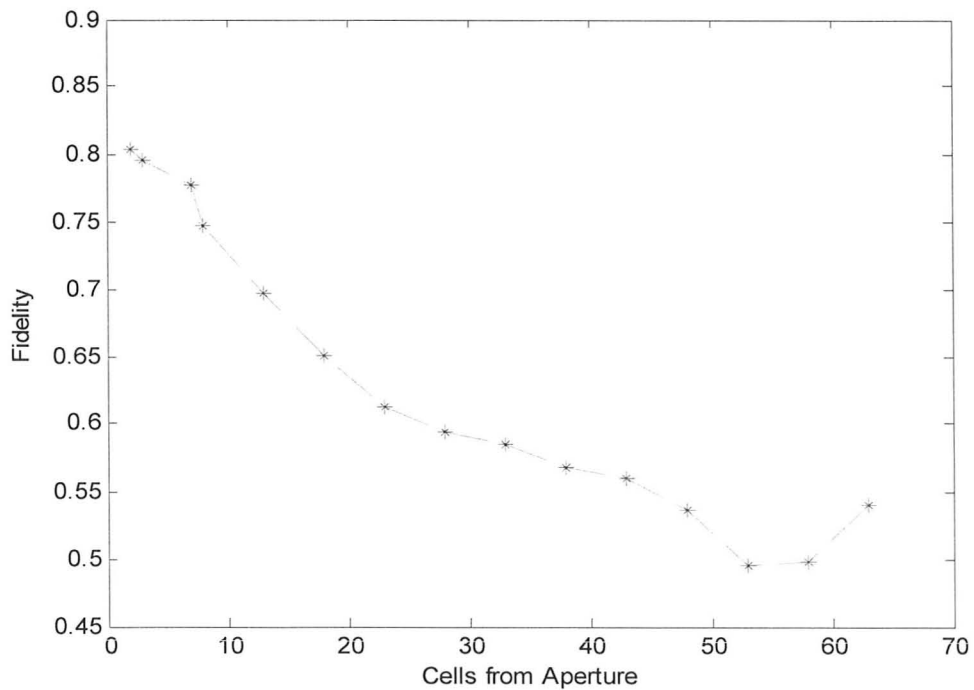


Figure 6.8: Fidelity along the boresight direction of the antenna as a function of the distance from the aperture.

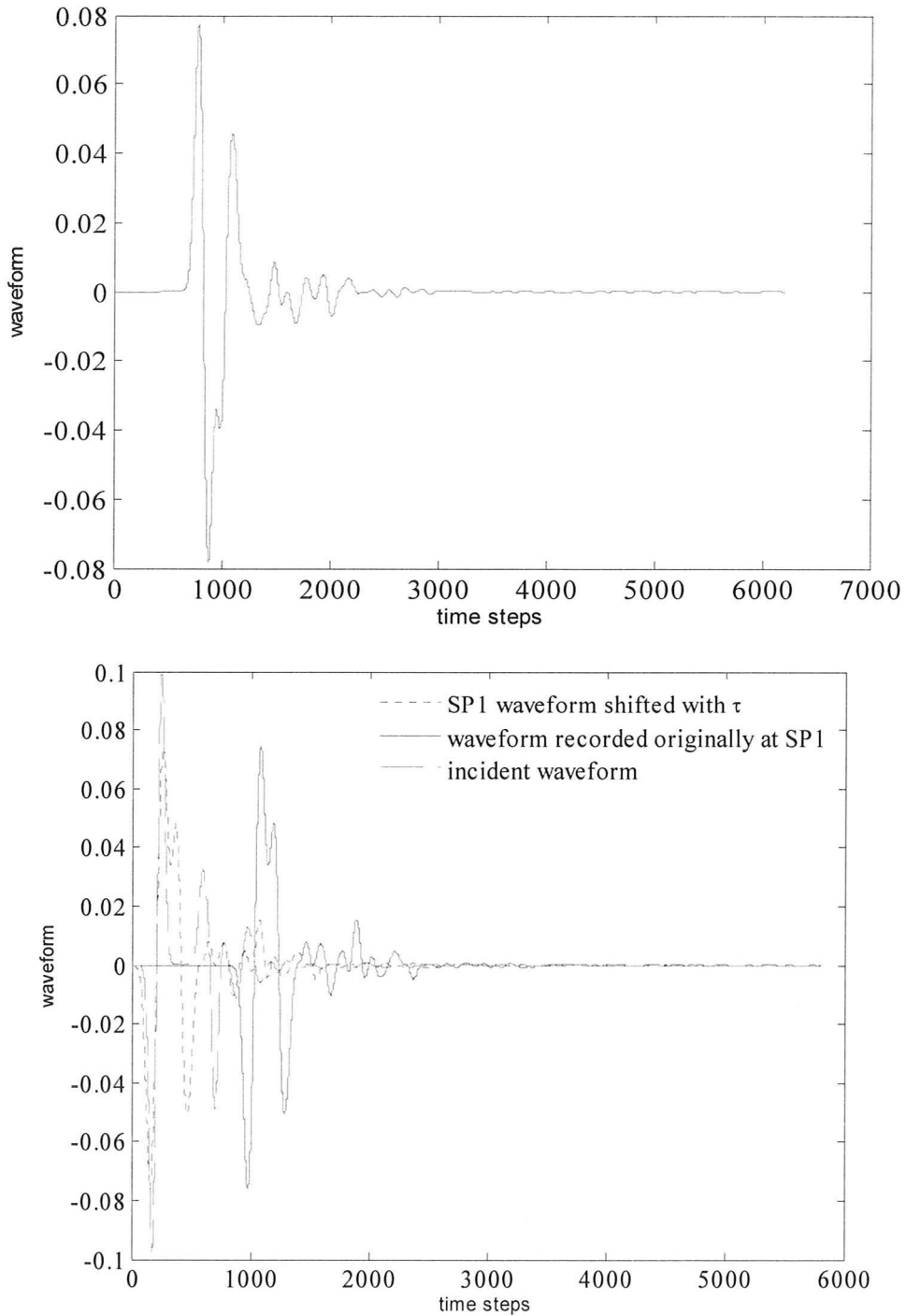


Figure 6.9: The top graph shows the time waveform recorded at probe SP1 and the bottom graph shows the same waveform shifted to coincide with the incident waveform to obtain maximum fidelity.



(b) Simulation with CST: CST features an excellent GUI and a reliable time-domain solver. The antenna model was imported directly from HFSS and is shown in Figure 6.10. The material definition could be made same as in HFSS. For accurate coaxial cable modeling, CST gives an option for automatic template that can be applied to coaxial cable excitation with the dominant TEM mode as shown in Figure 6.11. CST ensures that the waveguide mode is confined within the cable and there will be no radiation from the aperture as in XFDTD. The excitation is set up automatically in the desired frequency range. The boundary is set up as PML with the default space. The simulation takes more time than in XFDTD. The result for the reflection coefficient is better with CST compared to XFDTD (refer to [1]). It is shown in Figure 6.12.

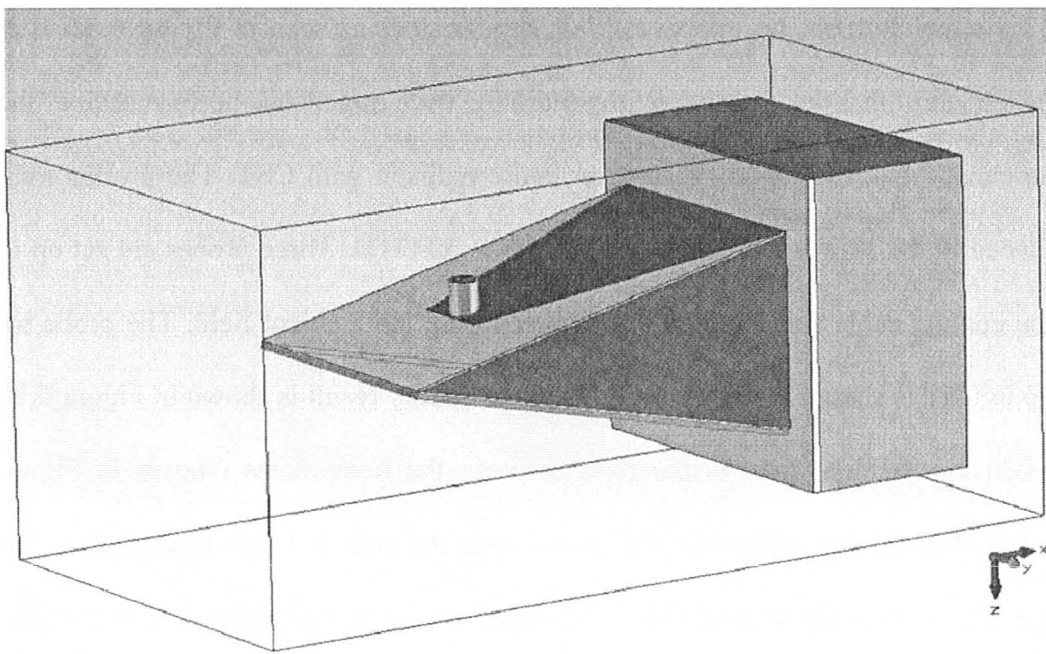


Figure 6.10: Antenna structure in CST which is imported from HFSS.

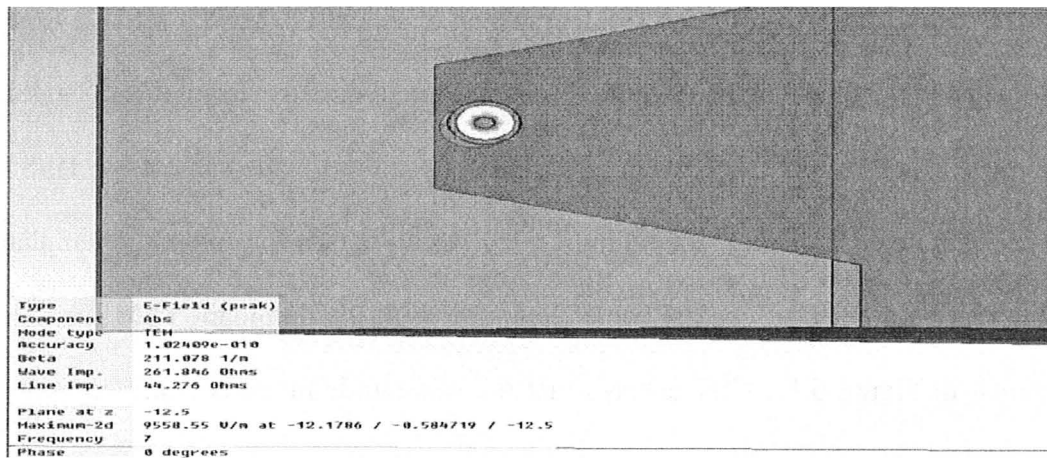


Figure 6.11: Coaxial cable excited with automatic waveguide port template in CST.

The absorbing sheet was introduced in CST, same as in HFSS. The user defined material measurements for skin and tissue were also incorporated [1], [7]. This simulation set up improves  $|S_{11}|$  significantly as seen in Figure 6.12. It is hence learnt that the absorber is important for wide impedance performance of the antenna. Also, the fidelity results are more realistic with CST. The probes were placed in the skin and tissue layers similar to XFDTD. Three probes are set up in the coaxial cable and the feed line for recording the incident field. The probe set up in CST is shown in Figure 6.13. The best fidelity result is shown in Figure 6.15 when the incident field is the field between the horn plates (shown in Figure 6.14). The fidelity values for the probes near the skin to tissue transition region are smaller than the other probes. This could be due to the higher loss in the skin as well as the near field nature of the field right next to the antenna aperture.

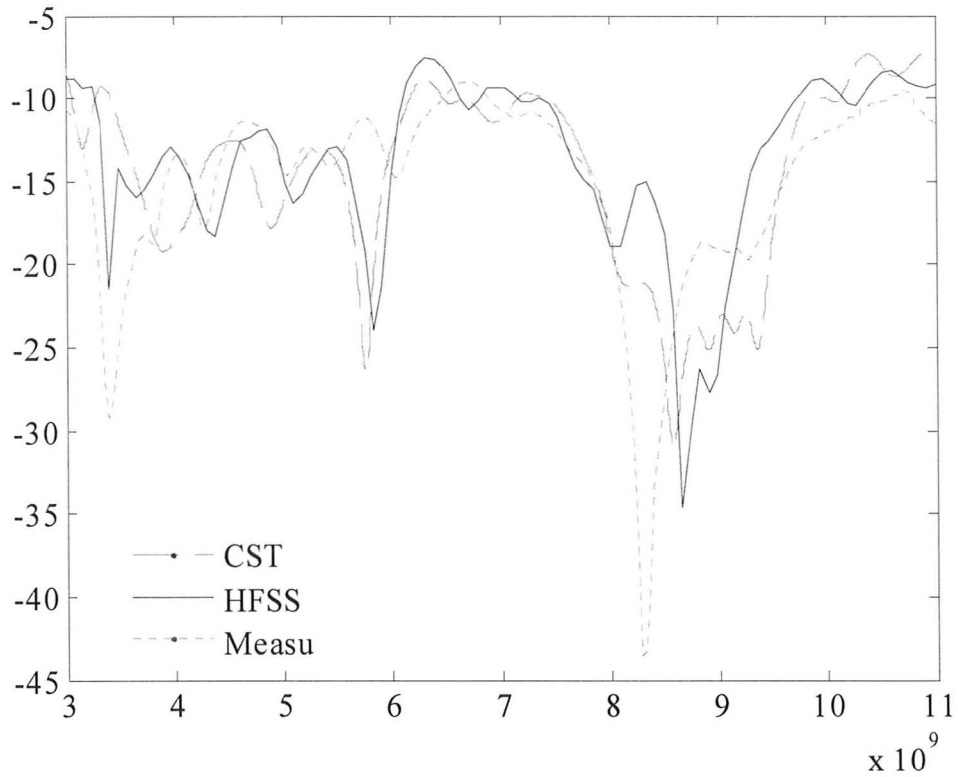


Figure 6.12:  $|S_{11}|$  simulated in CST compared to that simulated in HFSS and the measured one.

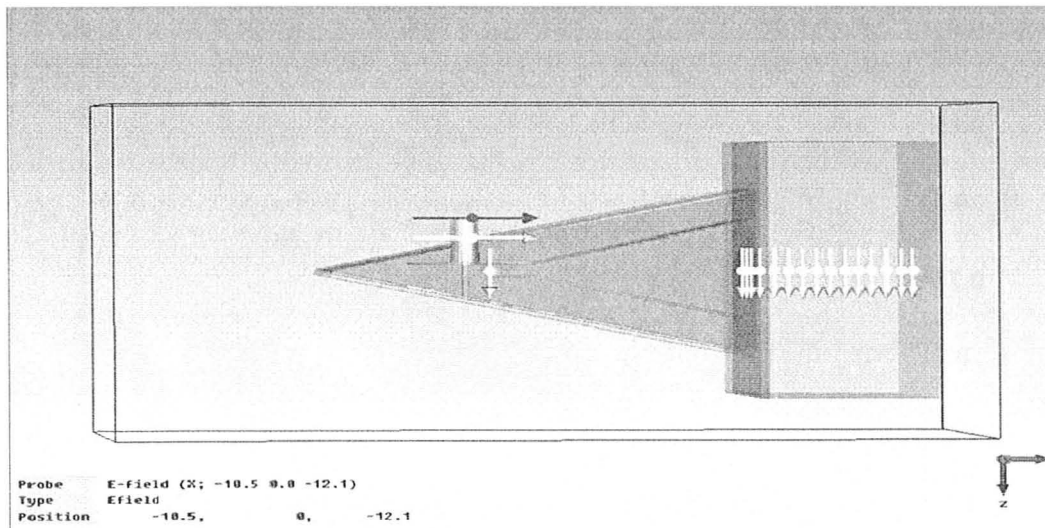


Figure 6.13: Probe set up in CST to record the  $E_z$  field time waveforms in the skin and tissue layers.

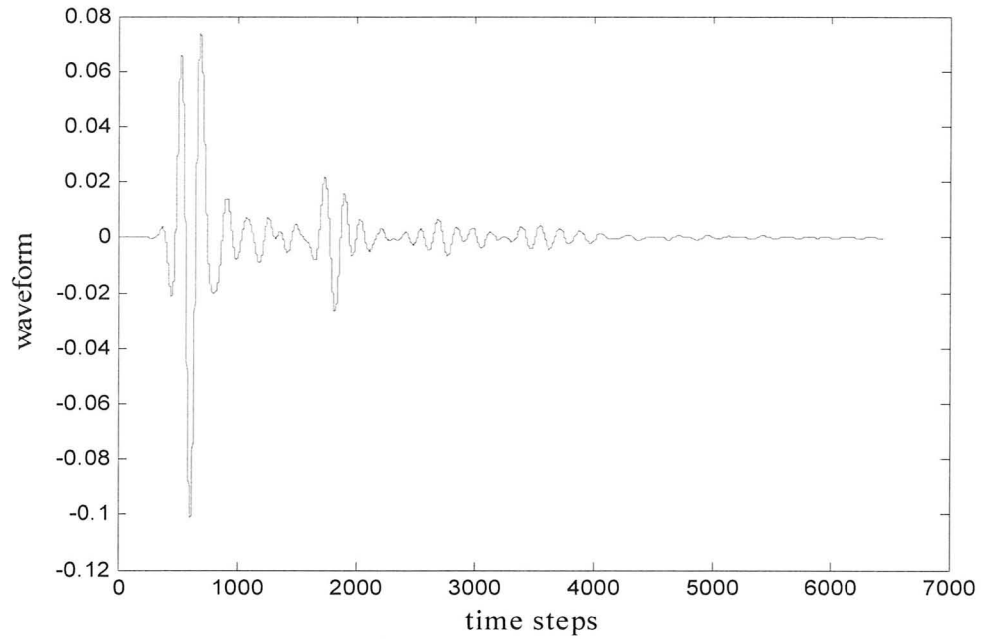


Figure 6.14: Time waveform ( $E_z$  field) recorded between the horn plates inside the antenna.

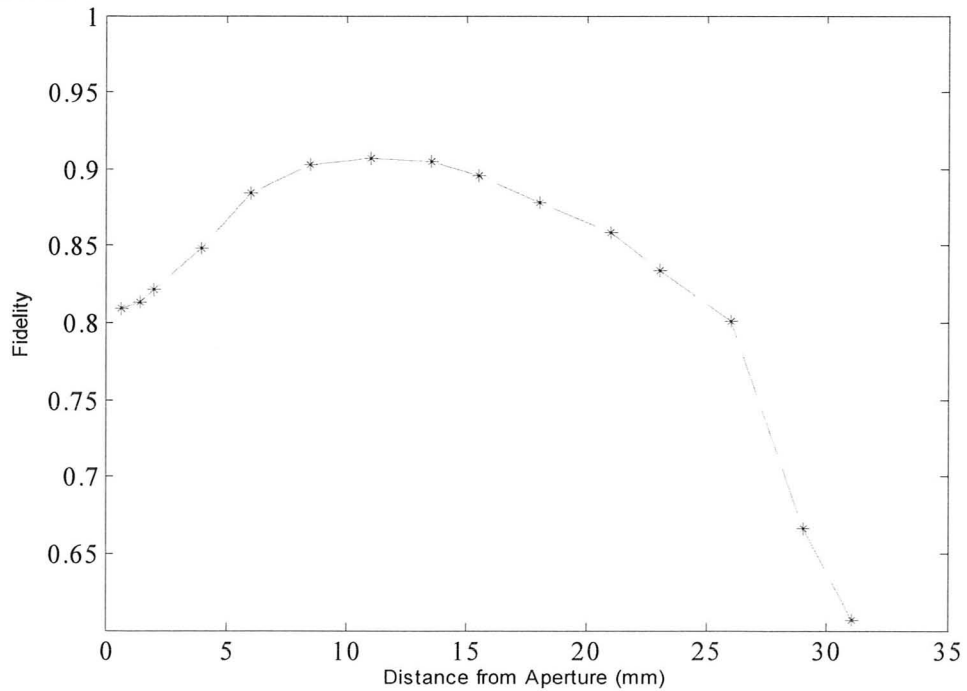


Figure 6.15: Fidelity in the boresight direction of the antenna as a function of the distance from the aperture.

These fidelity results were discussed in a presentation in this year's IEEE Antenna and Propagation Society (APS) symposium [8].

## 2) 3-D JACOBIAN MAPS FROM SELF-ADJOINT SENSITIVITY ANALYSIS

### 2.1. *Objective Functions for Jacobian Maps*

The objective function is a measure of the difference between the measured (or target) responses and the responses produced by the forward model for the current estimate of the permittivity distribution. The forward model is typically a high-frequency electromagnetic (EM) simulation. The optimization problem is solved iteratively by properly updating the complex permittivity. Gradient-based optimization techniques are preferred due to their fast convergence. However, gradient-based techniques require the Jacobian of the objective function. Our group's previous work has addressed the memory-efficient self-adjoint technique which can make the Jacobian computation possible and can be applied with commercial simulators [16]. The objective function has been defined before in [16] as:

$$F(\boldsymbol{\varepsilon}) = \|\boldsymbol{\Phi}(\boldsymbol{\varepsilon}) - \bar{\boldsymbol{\Phi}}\| + \delta \cdot \|\boldsymbol{\varepsilon} - \boldsymbol{\varepsilon}_b\| \quad (6)$$

where  $\bar{\boldsymbol{\Phi}}$  is the vector of target responses,  $\boldsymbol{\Phi}$  is the vector of responses obtained from the forward model, and  $\|\cdot\|$  represents a suitable, e.g.,  $l_2$  norm. The second term in (6) is the regularization term where the coefficient  $\delta$  is usually chosen

between 0 and 0.5. The vector  $\boldsymbol{\varepsilon}$  represents the unknown complex permittivity profile of the reconstructed scatterer in the assumed discrete space while  $\boldsymbol{\varepsilon}_b$  is the “background” permittivity profile which is assumed known. In previous work [16], the particular objective function and its Jacobian was considered:

$$F(\boldsymbol{\varepsilon}) = 0.5 \left( \sum_{i,j=1}^{N_e} |S_{ij} - \bar{S}_{ij}|^2 + \delta \sum_{n=1}^N |\varepsilon_n - \varepsilon_{bn}|^2 \right) \quad (7)$$

Here,  $N_e$  is the number of the excitation sources, and  $N$  is the number of the optimizable parameters. The objective function  $F$  contains the information of all  $S$ -parameters of interest in the forward model and the measurement. The complex permittivity of each voxel  $\varepsilon_n$  is expressed in terms of its real part  $\varepsilon'_n$  and its equivalent specific conductivity  $\sigma_n$  as:

$$\varepsilon_n = \varepsilon'_n \left( 1 - j \frac{\sigma_n}{\omega \varepsilon'_n} \right), \quad n = 1, \dots, N \quad (8)$$

The respective derivatives of the objective function in (7) are:

$$\frac{\partial F}{\partial \varepsilon'_n} = \sum_{i,j=1}^{N_e} \left[ (S_{ij} - \bar{S}_{ij})_R \cdot \left( \frac{\partial S_{ij}}{\partial \varepsilon'_n} \right)_R + (S_{ij} - \bar{S}_{ij})_I \cdot \left( \frac{\partial S_{ij}}{\partial \varepsilon'_n} \right)_I \right] + \delta \cdot (\varepsilon_n - \varepsilon_{bn})_R \quad (9)$$

$$\frac{\partial F}{\partial \sigma_n} = \sum_{i,j=1}^{N_e} \left[ (S_{ij} - \bar{S}_{ij})_R \cdot \left( \frac{\partial S_{ij}}{\partial \sigma_n} \right)_R + (S_{ij} - \bar{S}_{ij})_I \cdot \left( \frac{\partial S_{ij}}{\partial \sigma_n} \right)_I \right] - (\delta / \omega) \cdot (\varepsilon_n - \varepsilon_{bn})_I \quad (10)$$

In (9)-(10), each complex response derivative: (i)  $\partial S_{ij} / \partial \varepsilon'_n$  and (ii)  $\partial S_{ij} / \partial \sigma_n$ ; ( $i, j = 1, \dots, N_e, n = 1, \dots, N$ ), is computed using the sensitivity formula

in [16]. These derivatives, which constitute the Jacobian matrix, have been plotted as functions of the position of the voxel whose complex permittivity is an optimizable parameter. Such plots are referred to as Jacobian maps. This study exemplifies how the minima and maxima of a Jacobian distribution are indicative of the location at which the model constitutive parameters are the most different from those of the object under test. However, in microwave imaging experiments, exact knowledge of the vector responses may not be available. Often, the magnitude of the responses can only be measured without the phase information. Hence, there is the need for new objective function formulations where separate terms are defined for the magnitude and the phase of the responses.

### 2.1.1. Objective functions based on magnitudes of responses

We consider the objective function based on the magnitude of the responses:

$$F_M(\boldsymbol{\epsilon}) = 0.5 \sum_{i,j=1}^{N_e} (|S_{ij}| - |\bar{S}_{ij}|)^2 \quad (11)$$

Its respective derivatives are:

$$\left. \frac{\partial F_M}{\partial p} \right|_{p=\epsilon'_n, \sigma_n} = \sum_{i,j=1}^{N_e} (|S_{ij}| - |\bar{S}_{ij}|) \frac{\partial |S_{ij}|}{\partial p}, \quad n = 1, \dots, N \quad (12)$$

In (12), each response derivative  $\partial |S_{ij}| / \partial p$  ( $p = \epsilon'_n, \sigma_n, i, j = 1, \dots, N_e, n = 1, \dots, N$ )

is computed using (A1) in the Appendix A.

### 2.1.2. Objective functions based on phases of responses

We consider the objective function based on the phase of the responses:

$$F_p(\boldsymbol{\varepsilon}) = 0.5 \sum_{i,j=1}^{N_e} |e^{j\angle S_{ij}} - e^{j\angle \bar{S}_{ij}}|^2 \quad (13)$$

The above is equivalent to:

$$F_p(\boldsymbol{\varepsilon}) = 0.5 \sum_{i,j=1}^{N_e} [(\cos \angle S_{ij} - \cos \angle \bar{S}_{ij})^2 + (\sin \angle S_{ij} - \sin \angle \bar{S}_{ij})^2] \quad (14)$$

Its respective derivatives are (see Appendix A):

$$\left. \frac{\partial F_p}{\partial p} \right|_{p=\varepsilon'_n, \sigma_n} = \sum_{i,j=1}^{N_e} \sin(\angle S_{ij} - \angle \bar{S}_{ij}) \frac{\partial \angle S_{ij}}{\partial p}, \quad n = 1, \dots, N \quad (14)$$

In (14), each response derivative  $\partial \angle S_{ij} / \partial p$  ( $p = \varepsilon'_n, \sigma_n, i, j = 1, \dots, N_e, n = 1, \dots, N$ ) is computed using (A9) in Appendix A.

### 2.1.3. The sign of the Jacobian maps

In general, the derivative of an objective function  $F = 0.5(R - \bar{R})^2$  with respect to a parameter  $p$ , can be expressed as  $\partial F / \partial p = (R - \bar{R}) \partial R / \partial p$ , where  $R$  and  $\bar{R}$  are the real-valued model and target responses, respectively. There are 4 types of scenarios that arise as presented in Figure 6.16 [6]:

- (a) CASE 1:  $\partial F / \partial p < 0$  is fulfilled when: (i)  $\partial R / \partial p > 0$  and  $R < \bar{R}$ , case 1 in Figure 6.16; (ii)  $\partial R / \partial p < 0$  and  $R > \bar{R}$ , case 2 in Figure 6.16. When  $\partial F / \partial p < 0$ , the parameter  $p$  has to be increased in order to match  $R$  and  $\bar{R}$ .
- (b) CASE 2:  $\partial F / \partial p > 0$  is fulfilled when: (i)  $\partial R / \partial p > 0$  and  $R > \bar{R}$ , case 3 in Figure 6.16; (ii)  $\partial R / \partial p < 0$  and  $R < \bar{R}$ , case 4 in Figure 6.16. When  $\partial F / \partial p > 0$ , the parameter  $p$  has to be decreased in order to match  $R$  and  $\bar{R}$ .



The case of interest to us is Case 1 as will be discussed in section 2.2 of this chapter.

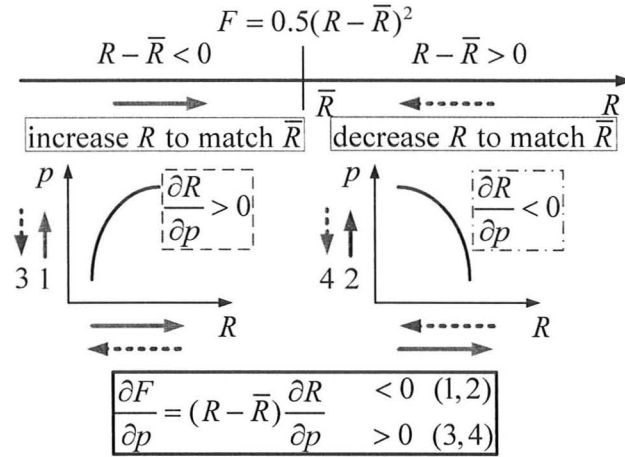


Figure 6.16: Four types of scenarios for the derivatives of the objective function  $F = 0.5(R - \bar{R})^2$  with respect to a parameter  $p$ , which can be expressed as  $\partial F / \partial p = (R - \bar{R}) \partial R / \partial p$ , where  $R$  and  $\bar{R}$  are the responses from the forward model and the measured (target) model.

### 2.2. Simple Numerical Models and Results

In order to test the Jacobians of the objective functions, the target model and the corresponding forward model were set up in an FDTD based solver QWED [17]. Figure 6.17 (a) shows a 2-D cut of the target model, which serves to obtain the “measured” field data. It consists of a homogeneous background and a lossy homogeneous spherical scatterer. The spherical scatterer has its center at (20, 20, 20) mm and its diameter is 2 mm. Its constitutive parameters are  $\epsilon_{rs} = 30$  and

$\sigma_s = 3$  S/m. The homogeneous background constitutive parameters are  $\epsilon_{rb} = 6$  and  $\sigma_b = 0.2$  S/m. The diameter of the cylindrical region of interest is 14 mm and its height is 40 mm. Figure 6.17 (b) shows the 2-D cut of the forward model. It represents a typical starting point for imaging reconstruction, which assumes a “scatterer-free” model. This model is identical with the target model except for the absence of the scatterer. A uniform mesh with  $\Delta h = 0.5$  mm is used with six symmetrically distributed point-wise excitations [see points  $P_{1,2,\dots,6}$  in Figure 6.17 (a)-(b)]. The excitation used is a modulated Gaussian pulse, which covers the frequency band from 3.0 GHz to 10.0 GHz. For further details on the simulation set-up, refer to [6].

The response from the simulations is a vector of the point-wise transmission coefficient  $S_{ij}$  ( $i, j = 1, 2, \dots, 6, i \neq j$ ) which are used in (12) and (14). Note that both of the objective functions  $F_M$  and  $F_P$  contain all the transmission coefficients. We compute the Jacobian at different frequencies for the forward model in the cubic region. Its 2-D cut at  $z = 20$  mm is shown in Figure 6.17 (b) with red dash line. We refer to this region as the Jacobian computational domain. The complex permittivities of all voxels inside the Jacobian computational domain are optimizable parameters.

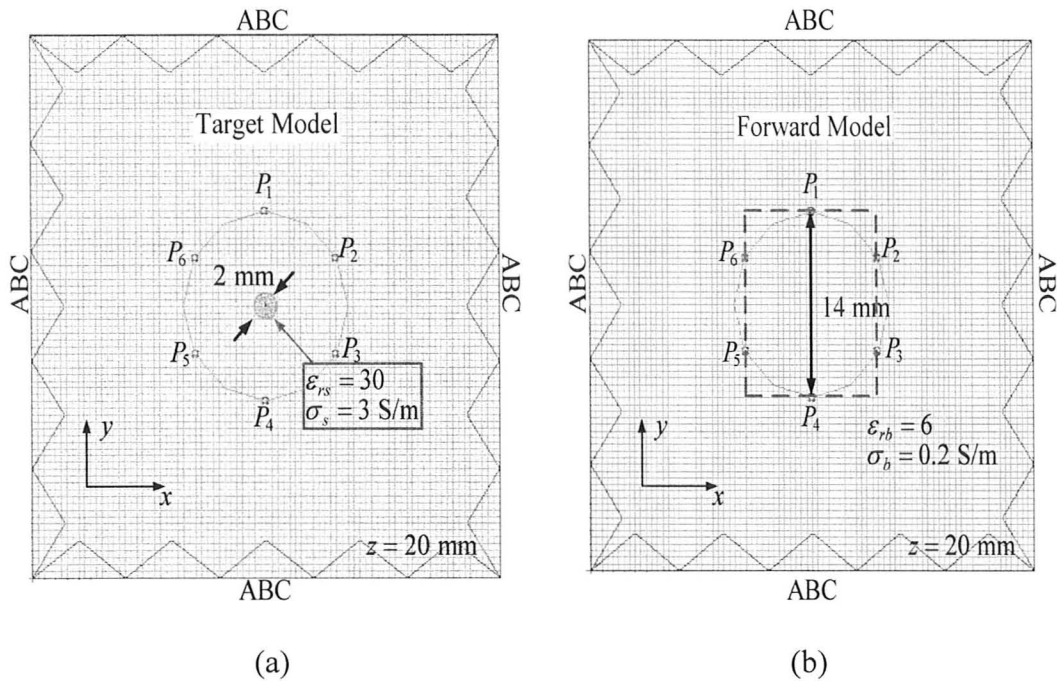


Figure 6.17: Cross-section in the  $xy$  plane of the: (a) target model and, (b) the corresponding forward model where the red-dash rectangle is the Jacobian computational domain.

The plots of the Jacobian maps in the Jacobian computational domain are then acquired in the plane  $z = 20$  mm, which contains the scatterer's center in the target model. Figure 6.18 shows the Jacobian maps at 10 GHz.

Note that in this example, it is already known that the dielectric parameters of the scatterer are higher than those of the background. Therefore, the derivative of the objective function with respect to the parameter should be negative as seen in the analysis illustrated in Figure 6.16. All positive derivatives are ignored (case 3 and case 4 in Figure 6.16). Note that, minima might appear on the fringes of the

imaged domain. We take into account only minima which are smaller than the derivatives of all surrounding voxels. These are referred to as *true minima*. This is relevant to the case of breast imaging as the tumor is supposed to have higher permittivity and conductivity compared than the background healthy tissue.

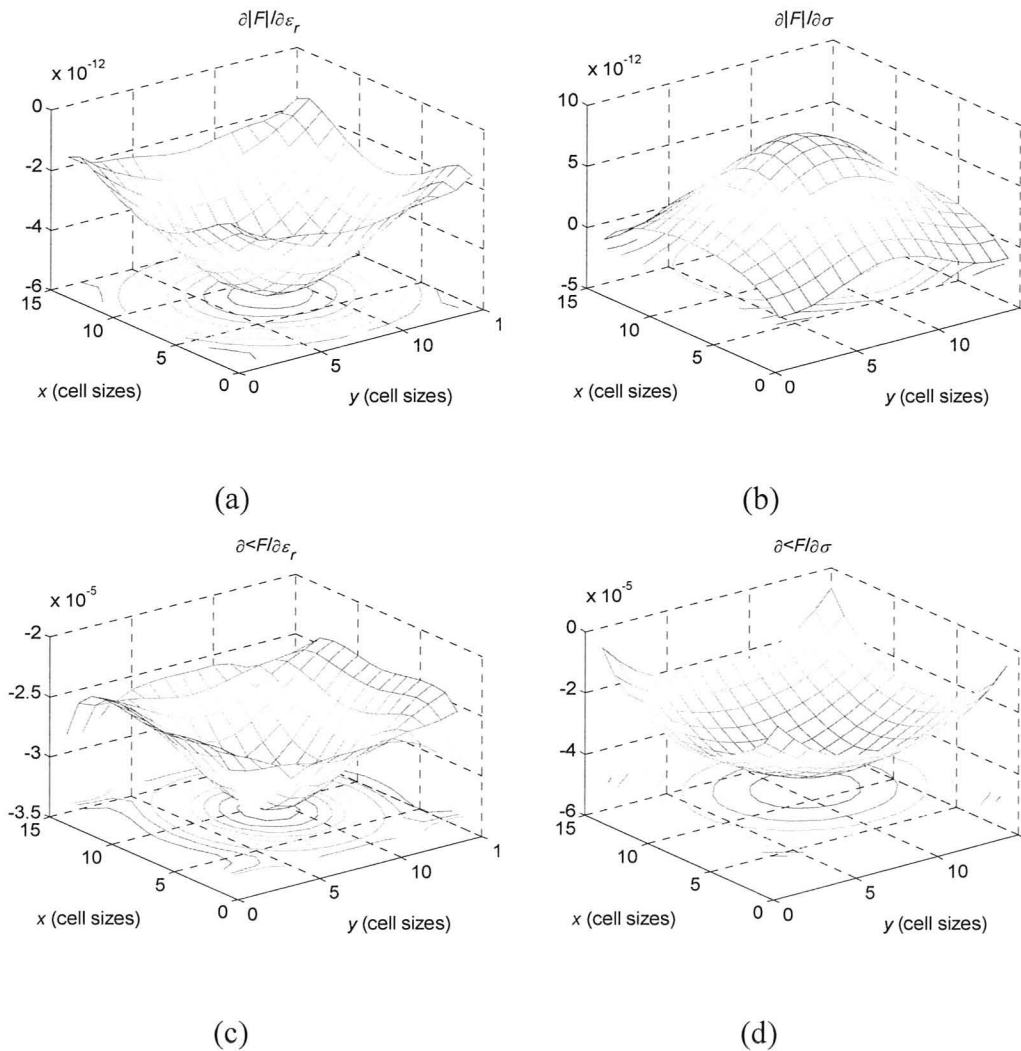


Figure 6.18: Jacobian maps in the plane  $z=20$  mm at 10 GHz: (a)  $\frac{\partial |F|}{\partial \epsilon_r}$ ; (b)  $\frac{\partial |F|}{\partial \sigma}$ ; (c)  $\frac{\partial \angle F}{\partial \epsilon_r}$ ; (d)  $\frac{\partial \angle F}{\partial \sigma}$ .

It is observed that in the Jacobian maps for this example, all true minima appear at the point (20, 20, 20) mm, which coincides with the center of the scatterer in the target model. It is the same with other frequencies. On an average, a wide-band set of Jacobian maps indicates fairly accurately the location of the scatterer. The locations of the true minima of all Jacobian maps for frequency range from 3 GHz to 10 GHz at 1 GHz intervals are listed in Table 6.2. Here, the derivatives of the two objective functions  $F_M (|F|)$  and  $F_P (\angle F)$  with respect to the relative permittivity and the conductivity are considered.

Further, all the Jacobian maps are properly selected and averaged at different frequencies in order to strengthen the effects of parameter perturbations. Firstly, we select all the valid Jacobian maps in the frequency range of 3 to 10 GHz with 0.1 GHz frequency step. A map is considered valid if it contains a true minimum smaller than zero (negative derivative). Then, we average the locations of all the true minima for all valid maps. The averaged true minimum for different Jacobian maps is listed in Table 6.3.

This example illustrates nicely the benefits that high-quality Jacobian maps can bring to image reconstruction. In particular, the true minima (or maxima) of a Jacobian distribution are indicative of the location at which the model constitutive parameters differ the most from those of the object under test.

TABLE 6.2: TRUE MINIMA FOR TWO OBJECTIVE FUNCTIONS W.R.T.  $\varepsilon_r$  OR  $\sigma$  IN THE FREQUENCY RANGE FROM 3 GHz TO 10 GHz.

Derivative w.r.t. Parameter	Frequency (GHz)	$ F $ Location $(x, y)$ (in mm)	$\angle F$ Location $(x, y)$ (in mm)
$\frac{\partial}{\partial \varepsilon_r}$	3	None	(20.0, 20.0)
	4	None	(19.0, 21.5)
	5	None	(22.0, 22.5)
	6	(20.0, 20.0)	(23.0, 22.5)
	7	(20.0, 20.0)	None
	8	(20.0, 20.0)	(20.0, 20.0)
	9	(20.0, 20.0)	(20.0, 20.0)
	10	(20.0, 20.0)	(20.0, 20.0)
$\frac{\partial}{\partial \sigma}$	3	(20, 20)	None
	4	(20, 20)	None
	5	(18.5, 20.5)	(20.0, 20.0)
	6	(22.0, 23.0)	(20.0, 20.0)
	7	None	(20.0, 20.0)
	8	None	(20.0, 20.0)
	9	None	(20.0, 20.0)
	10	None	(20.0, 20.0)

TABLE 6.3: AVERAGE TRUE MINIMUM FOR TWO OBJECTIVE FUNCTIONS W.R.T.  $\epsilon_r$  OR  $\sigma$ .

Derivative w.r.t Parameter	$ F $ Location $(x, y)$ (in mm)	$\angle F$ Location $(x, y)$ (in mm)
$\frac{\partial}{\partial \epsilon_r}$	(20.0, 20.0)	(20.362, 21.1293)
$\frac{\partial}{\partial \sigma}$	(19.9697, 20.6212)	(20.0, 20.0)

Our next goal is to verify the capability of our self-adjoint sensitivity analysis (SASA) [16] in detection. The same models were used, except that the scatterer in Figure 6.15 (a) is moved to various locations in the background medium. Consider the case when its center is moved to the right along the  $x$  axis to the point (23.5, 20, 20) mm. This case is referred to as the Right Case. We also consider the case when its center is moved to the left along the  $x$  axis to the point (16.5, 20, 20) mm. This is called the Left Case. Finally, its center is moved up and down along the  $y$  axis to the points (20, 23.5, 20) mm (Up Case) and (20, 16.5, 20) mm (Down Case).

The same investigation as in the Center Case was then applied to these 4 different cases. Table 6.4 gives the locations obtained for the true minima of the Jacobian maps in the frequency range from 3 GHz to 10 GHz at 1 GHz intervals for the Right Case. The actual center of the scatterer is at the point (23.5, 20, 20) mm for this case. The averaged true minimum for the whole frequency range of

interest from different valid Jacobian maps is also listed in Table 6.5. Similar results were obtained for the remaining three cases.

The objective of microwave tomography is to reconstruct the complex permittivity profile in an imaged 3-D volume. Jacobian maps at different frequencies and based on different parameters ( $p = \epsilon'_n, \sigma_n$ ) facilitated by the objective functions  $F_M$  and  $F_P$ , carry useful and unique information. For robust reconstruction and study, these various maps have to be combined so as to give a single coherent image. For any sort of combination, the Jacobian maps have to be comparable in magnitudes, which greatly differ based on the objective functions  $F_M$  and  $F_P$ . This is because the amplitude value of the Jacobian maps from  $F_M$  is smaller than the Jacobian maps from  $F_P$  by an approximate factor of 107. Therefore, all valid Jacobian maps in the frequency range from 3 GHz to 10 GHz (evaluated with 0.1 GHz frequency step) are normalized through the modified root sum square (RSS) formula:

$$\left. \frac{\partial F}{\partial p} \right|_{\text{RMS}} = \frac{1}{N_x N_y} \frac{\frac{\partial F}{\partial p}(x_i, y_j)}{\sqrt{\sum_{i=1}^{N_x} \sum_{j=1}^{N_y} \left( \frac{\partial F}{\partial p} \right)^2(x_i, y_j)}}. \quad (15)$$

Here,  $F$  is any objective function either based on the magnitudes or the phases of the responses,  $\partial F / \partial p$  is the Jacobian (derivative) of the objective function,  $N_x$  and  $N_y$  are the number of probes along the  $x$  and  $y$  axis in the computational domain,  $x_i$  and  $y_i$  are the  $x$ - and  $y$ -coordinate for each probe, respectively.



TABLE 6.4: TRUE MINIMA FOR TWO OBJECTIVE FUNCTIONS W.R.T.  $\varepsilon_r$  OR  $\sigma$  IN THE FREQUENCY RANGE FROM 3 GHz TO 10 GHz FOR THE RIGHT CASE.

Derivative w.r.t. Parameter	Frequency (GHz)	$ F $ Location $(x, y)$ (in mm)	$\angle F$ Location $(x, y)$ (in mm)	
$\frac{\partial}{\partial \varepsilon_r}$	3	None	(20.0, 20.0)	
	4	None	(22.5, 20.0)	
	5	None	(23.5, 20.0)	
	6	None	(24.0, 19.0)	
	7	None	None	
	8	(23.5, 20.0)	None	
	9	(23.0, 20.0)	None	
	10	(23.0, 20.0)	(16.5, 20.0)	
	$\frac{\partial}{\partial \sigma}$	3	(21.0, 20.0)	None
		4	(22.0, 20.0)	None
5		(23.0, 20.0)	(20.5, 20.0)	
6		(24.0, 20.0)	(21.0, 20.0)	
7		None	(21.5, 20.0)	
8		None	(22.0, 20.0)	
9		None	(22.5, 20.0)	
10		None	(22.5, 20.0)	

*Actual Location is (23.5, 20.0) mm*

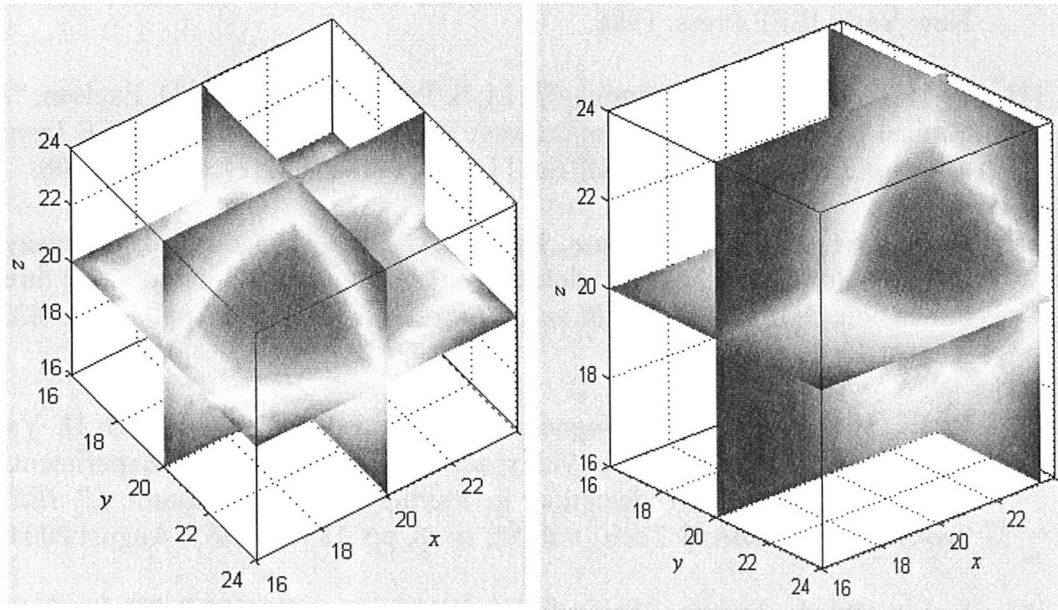
TABLE 6.5: AVERAGE TRUE MINIMUM FOR TWO OBJECTIVE FUNCTIONS W.R.T.  $\varepsilon_r$  OR  $\sigma$ .

Derivative w.r.t Parameter	$ F $ Location $(x, y)$ (in mm)	$\angle F$ Location $(x, y)$ (in mm)
$\frac{\partial}{\partial \varepsilon_r}$	(23.1250, 20.0)	(22.4857, 19.8571)
$\frac{\partial}{\partial \sigma}$	(22.8684, 20.1053)	(21.508, 20.0)

To obtain 3-D Jacobian maps, we performed two more steps after the RMS normalization. Firstly, we reversed the sign of the normalized Jacobian maps in order to obtain the maxima instead of the minima (to get the red color for the scatterer). Secondly, we normalized the obtained Jacobian maps by their own maxima in order to make the values within all maps between 0 and 1. To combine, we simply added all these valid normalized maps together. We refer to the obtained maps as the combination maps. The 3-D sliced combination maps for the Center Case and the Right Case are shown in Figure 6.19 (a)-(b). It is stated again that the scatterer's center is at point (20, 20, 20) mm for the Center Case and it is at (23.5, 20, 20) mm for the Right Case. The corresponding true minimum of each combination map is listed in Table 6.6.

TABLE 6.6: TRUE MINIMUM IN THE COMBINATION MAPS.

	True Center Location $(x, y)$ (in mm)	Map Minimum Location $(x, y)$ (in mm)
Center Case	(20.00, 20.00)	(20.00, 20.00)
Right Case	(23.50, 20.00)	(23.00, 20.00)



(a)

(b)

Figure 6.19: 3-D Jacobian maps: (a) Center Case with the scatterer's center at (20, 20, 20) mm; (b) Right Case with the scatterer's center at (23.5, 20, 20) mm.

These results for 3-D imaging were a part of the workshop presentation in 2009 International Microwave Symposium [19]. Currently, work is underway on testing the objective functions and algorithms with various scenarios and assessing the limitations of the technique. Also, resolution studies and complicated numerical models are being investigated.

## REFERENCES

- [1] A. Trehan, “Fidelity evaluation of a novel UWB TEM horn antenna,” Computational Electromagnetics Res. Lab., McMaster University, CEM-R-54, May 2009.
- [2] L. E. Larsen and J. H. Jacobi, *Medical Applications of Microwave Imaging*. New York: IEEE Press, 1986.
- [3] P. M. Meaney, M. W. Fanning, D. Li, S. P. Poplack, and K. D. Paulsen, “A clinical prototype for active microwave imaging of the breast,” *IEEE Trans. Microw. Theory Tech.*, vol. 48, no. 11, pp. 1841 – 1853, November 2000.
- [4] E. Fear, X. Li, S. C. Hagness, and M. A. Stuchly, “Confocal microwave imaging for breast cancer detection: Localization of tumors in three dimensions,” *IEEE Trans. Biomed. Eng.*, vol. 49, no. 8, pp. 812 – 822, August 2001.
- [5] X. Li, S. K. Davis, S. C. Hagness, D. W. van der Weide, and B. D. Van Veen, “Microwave imaging via space-time beamforming: Experimental investigation of tumor detection in multilayer breast phantoms,” *IEEE Trans. Microw. Theory Tech.*, vol. 52, no. 8, pp. 1856 – 1865, August 2004.
- [6] L. Liu and A. Trehan, “Self-adjoint sensitivity analysis for 3D Jacobians maps in imaging and detection,” Computational Electromagnetics Res. Lab., McMaster University, CEM-R-50, May 2009.
- [7] R. Khalaj Amineh, A. Trehan, and N. K. Nikolova, “TEM horn antenna for ultra-wide band microwave breast imaging,” *Progress In Electromagnetics Research B*, vol. 13, pp. 59 – 74, 2009.

- [8] R. K. Amineh, A. Trehan, and N. K. Nikolova, “Ultra-wide band TEM horn antenna for microwave imaging of the breast,” *IEEE International Symposium on Antennas and Propagation (APS)* (Charleston SC), June 2009.
- [9] Emerson & Cuming Microwave Products, Inc., 28 York Avenue, Randolph, MA 02368 USA. [Online]. Available: <http://www.eccosorb.com/main/RegionalHome.html>.
- [10] D. Lamensdorf, L. Susman, “Baseband-Pulse-Antenna Techniques,” *IEEE Antennas and Propagation Magazine*, vol. 36(1), pp. 20 – 29, February 1994.
- [11] A. Hajiaboli and M. Popovic, “FDTD subcell modeling of the inner conductor of the coaxial feed: accuracy and convergence analysis,” *IEEE Trans. on Magnetics*, vol. 43, no. 4, April 2007.
- [12] Ansoft HFSS ver. 11, Ansoft Corporation, 225 West Station Square Drive, Suite 200, Pittsburgh, PA 15219, USA, 2008. [Online]. Available: <http://www.ansoft.com>.
- [13] XFDTD ver. 6.3, Remcom Inc., 300 Chesterfield Center, Suite 260 Chesterfield, MO 63017, USA, 2003. [Online]. Available: [www.remcom.com](http://www.remcom.com).
- [14] CST Microwave Studio, CST of Americal, Inc., Headquarters at 492 Old Connecticut Path, Suite 505 Framingham, MA 01701, USA, 2009. [Online]. Available: <http://www.cst.com/>.
- [15] MATLAB™ 7.1, The MathWorks Inc., 3 Apple Hill Drive, Natick, MA, 2005. [Online]. Available: <http://www.mathworks.com/>.
- [16] Y. P. Song and N. K. Nikolova, “Memory efficient method for wideband self-adjoint sensitivity analysis,” *IEEE Trans. Microw. Theory Tech.*, vol. 56, no. 8, pp. 1917 – 1927, August 2008.
- [17] QW-3D v. 7.0, QWED Sp. z o.o., ul. Nowowiejska 28 lok. 32, 02-010 Warsaw, Poland, 2009. [Online]. Available: <http://www.qwed.com.pl/>.
- [18] W. C. Chew and J. H. Lin, “A frequency-hopping approach for microwave imaging of large inhomogeneous bodies,” *IEEE Microwave Guided Wave*

*Lett.*, vol. 5, pp. 439 – 441, December 1995.

- [19] N. K. Nikolova, L. Liu, and A. Trehan, “Adjoint sensitivities in microwave imaging and design tuning,” Workshop on EM-Based Microwave Optimization Technology: State of the Art and Applications, *IEEE MTT-S Int. Symposium* (Boston, MA), June 2009.

# CHAPTER 7

## CONCLUSIONS AND SUGGESTIONS

### 1) RESULTS CONCLUDED

This thesis describes contributions, which can aid research in developing active microwave imaging (AMWI) techniques for breast cancer detection. This endeavor resulted in the following achievements:

- The dielectric properties of the breast tissues have been studied and summarized from both old and recent *ex vivo* studies. The dielectric-property data from the recent studies have been chosen to be the target for creating physical and numerical phantoms. For this, simple Debye models have been proposed that can be used in electromagnetic simulations.
- Methodologies to fabricate physical phantoms that can mimic an electromagnetic medium comparable to the tissues in the breast have been laid

down. This is required for experimental work such as: (i) to test the designed sensors for AMWI, (ii) to optimize the scanning arrangements of the sensors, and (iii) to conduct scatterer detection studies with tumor simulants immersed in healthy-tissue simulants. The physical phantoms developed through our work are easy to make, they are replaceable, they resemble the dielectric properties of the breast tissues, and they reproduce well the contrast from high-water content tissues (HWCT) to intermediate-water content tissues (IWCT) to low-water content tissues (LWCT). Another convenient attribute is that they can retain their shape without being too stiff, which eases the experimental protocol.

➤ The surface acquisition system based on photogrammetry developed by our group [1]-[2] has been a significant result. It solves the skin detection problem in microwave imaging of the breast. The methods proposed prior to our methodology were based on complex antenna scanning arrangements and only proven in simulations.

➤ The memory efficient 3-D CAD models created from MRI images that can be used in EM simulators is also a useful achievement. This is an initial step towards work with realistic and good initial models required for microwave tomography. Also, to establish direct approaches such as with microwave holography, realistic numerical models in simulations are necessary.

➤ The sensor to be used in the imaging array has been designed for frequency-sweep measurements. However, its fidelity evaluated in chapter 6, shows that the antenna is a good candidate for time-domain pulsed measurements as well.



➤ The formulation of appropriate objective functions for reconstruction algorithms based on self-adjoint sensitivity analysis (SASA) and their prospective use in plotting Jacobian maps for breast imaging has been discussed in chapter 6. The results are encouraging so far.

## 2) SUGESSTIONS FOR FUTURE WORK

### 2.1. *Future Enhancements of The Work Presented in Thesis*

The enhancement in all above mentioned contributions is essential to further make experiments and simulations easier to conduct. Some of the ideas for future work are listed below:

➤ The scope of making more realistic physical phantoms with different shapes for designing arrays was discussed at the end of chapter 3. This must be carried forward. Also, more contrast studies with different phantoms must be performed. The loss is also an important factor to study. For instance, the loss of the phantoms, which is similar to that of human tissues, can be quite high. This may make signals too weak to measure with the network analyzers. Hence, low-noise microwave amplifiers might be required to be integrated in an imaging system for high-frequency measurements.

➤ The surface acquisition system based on photogrammetry was a prototype to prove to the microwave research community the efficacy of optical methods to reconstruct random surfaces rather than using the microwave methods. The system has now been upgraded to a laser scanner. Studies must be carried out to

see how to best integrate the reconstructed surface shapes within the EM forward models.

➤ For numerical phantoms, the simplification of the models as discussed in section 4 of chapter 5 can make the simulations faster. This is necessary during the development stage of the reconstruction algorithms. Waiting for weeks for the simulations to be completed, in order to know whether an approach has potential or not, is not feasible.

The main contribution toward the creation of numerical phantoms is the pre-processing with the Hamiltonian-contour (HC) method which allows for the 2-D union over an image slice. This method is much more memory efficient than the voxel-by-voxel construction method. It decreases the number of geometrical entities (few polygons instead of thousands of voxels) in representing the same information from the image. After getting the connectivity lists, it is not necessary to always use the HFSS interface to create the 3-D slice of swept polygons. Other CAD packages such as the Geomagic Studio [4] can also be used. This needs further investigation. Also, it was observed in QWED [5] that the slice construction with HC method took just a few seconds unlike HFSS [6] (that can take several minutes).

➤ The work with Jacobian maps for detection of scatterers, discussed in chapter 6, has shown promise in examples with simple numerical models. The investigation of the sensitivity algorithm must be carried forward with more complex numerical models.

## **2.2. *Future Directions for AMWI***

Microwave imaging research has suffered from inadequate and simplistic assumptions in many prior studies. There is a need to develop more rigorous algorithms. For this, verification with both experiments and simulations is required with each new phase in the algorithm development. Also, the new directions in research can be established only with thorough experimental confirmations. This is where the use of easy to use and realistic phantoms plays a key role.

The electrical property contrast between tissues in the microwave region is mainly characterized by their water content. The earlier belief that malignant tissues have high contrast with healthy tissues is valid only for “fat” as healthy tissue. The characterization of heterogeneous breast tissue has shown that the contrast is low between the fibro-glandular healthy tissue and the malignant tissues. Unfortunately, most cancers develop in the glandular tissue. To augment the contrast between malignant tissue and glandular tissue, some exogenous agents can be investigated. The use of contrast agents is not new to conventional imaging modalities. Malignant tumors are known to get the maximum concentration of exogenous agents due to high blood supply. The concept of contrast agents is being investigated in microwave imaging, too. However, the author would recommend that experimental and simulation studies are carried out to determine the minimum contrast that is detectable with microwave techniques before deciding on the kind and quantity of contrast agents.

In relation to the tissue dielectric properties discussed in sub-section 2.2.8, of chapter 2, the recent studies of *ex vivo* tissue dielectric properties is not the final word on the electrical contrast between tissues. More elaborate *in vivo* studies must be employed to know the real contrast during measurements with patients. Also, more statistical analysis must be done to determine the difference in dielectric properties between malignant and benign breast tissues, if any.

The goal of microwave imaging is to become a wide screening tool to detect malignancy in its early stages. The images to be produced with AMWI are in effect dielectric-property maps that show elevated permittivity and conductivity for the malignant regions. MRI is an excellent modality for acquiring detailed images of internal tissues, but as discussed in chapter 1, it is used judiciously due to its very high cost. AMWI is not expected to replace the existing modalities but is hoped to help early cancer detection and to help prioritize MRI testing.

Multi-modality is another direction of study which must include AMWI. The time is right for combining imaging modalities to improve the best and curb the worst. Combinations which can be studied include “microwave-only” approaches combining tomographic and direct approaches within AMWI, or “across-modalities” approaches combining microwaves with electrical impedance tomography or elastography. The objective is to develop a multi-modal imaging system that can detect early malignancy, overcome the usage of non-ionizing radiation, cut-back on false positive rate, and still be cost effective for wide screening.

**REFERENCES**

- [1] A. Trehan, R. K. Amineh, M. S. Georgiev, and N. K. Nikolova, “Photogrammetry-based surface reconstruction for improving microwave breast tumor detection,” *Proc. of 24th Int. Review of Progress in Applied Computational Electromagnetics (ACES)*, March 2008.
- [2] A. Trehan, R. K. Amineh, M. S. Georgiev, and N. K. Nikolova, “Accuracy assessment of photogrammetry surface reconstruction for improving microwave imaging,” *IEEE International Symposium on Antennas and Propagation (APS)*, July 2008.
- [3] MATLAB™ 7.1, The MathWorks Inc., 3 Apple Hill Drive, Natick, MA, 2005. [Online]. Available: <http://www.mathworks.com/>.
- [4] Geomagic Studio, Geomagic U.S. Corporate Headquarters, 3200 East Hwy 54, Cape Fear Building, Suite 300, Research Triangle Park, NC, 27709 USA. [Online]. Available: <http://www.geomagic.com/en/>.
- [5] QW-3D v. 7.0, QWED Sp. z o.o., ul. Nowowiejska 28 lok. 32, 02-010 Warsaw, Poland, 2009. [Online]. Available: <http://www.qwed.com.pl/>.
- [6] Ansoft HFSS ver. 11, Ansoft Corporation, 225 West Station Square Drive, Suite 200, Pittsburgh, PA 15219 USA, 2008. [Online]. Available: <http://www.ansoft.com>.

## APPENDIX A

### A.I. The Derivative of the Magnitude of a Function

Let  $f = f_R + jf_I$ . Find  $\partial |f| / \partial x$  if  $\partial f_R / \partial x$  and  $\partial f_I / \partial x$  are known.

$$\begin{aligned}
 \frac{\partial |f|}{\partial x} &= \frac{\partial}{\partial x} \sqrt{f \cdot f^*} \\
 &= \frac{1}{2|f|} \left[ f^* \cdot \frac{\partial f}{\partial x} + f \cdot \frac{\partial f^*}{\partial x} \right] \\
 &= \frac{1}{2|f|} \left[ f^* \cdot \frac{\partial f}{\partial x} + (f^* \cdot \frac{\partial f}{\partial x})^* \right] \quad (A1) \\
 &= \frac{1}{|f|} \cdot \text{Re} \left[ f^* \cdot \frac{\partial f}{\partial x} \right] \\
 &= \frac{1}{|f|} \cdot \left[ f_R \frac{\partial f_R}{\partial x} + f_I \frac{\partial f_I}{\partial x} \right]
 \end{aligned}$$

In general, if  $F = \frac{1}{n} |f|^n$ , then

$$\frac{\partial F}{\partial x} = |f|^{n-2} \cdot \text{Re} \left[ f^* \cdot \frac{\partial f}{\partial x} \right] \quad (A2)$$

In (A1)-(A2), the complex response derivative  $\partial f / \partial x$  is computed using the sensitivity formula in [1].

### A.II. The Derivative of the Phase of a Function

Let  $f = |f| e^{j\phi}$ . Find  $\partial \phi / \partial x$  if  $\partial f_R / \partial x$  and  $\partial f_I / \partial x$  are known.

$$\frac{\partial f}{\partial x} = \frac{\partial |f|}{\partial x} e^{j\phi} + |f| \cdot j e^{j\phi} \frac{\partial \phi}{\partial x} \quad (A3)$$

Multiply both sides of (A3) with  $e^{-j\phi}$  and move the  $\partial \phi / \partial x$  term to the left of the equation, we obtain:

$$j|f| \frac{\partial \phi}{\partial x} = \frac{\partial f}{\partial x} e^{-j\phi} - \frac{\partial |f|}{\partial x} \quad (\text{A4})$$

Divide both sides of (A4) by  $j|f|$  to obtain:

$$\begin{aligned} \frac{\partial \phi}{\partial x} &= \frac{1}{j|f|} \left[ \frac{\partial f}{\partial x} e^{-j\phi} - \frac{\partial |f|}{\partial x} \right] \\ &= \frac{1}{j|f|} \left[ \frac{\partial f |f|}{\partial x |f|} e^{-j\phi} - \frac{\partial |f|}{\partial x} \right] \\ &= \frac{1}{j|f|} \left\{ \frac{1}{|f|} \frac{\partial f}{\partial x} f^* - \frac{1}{|f|} \operatorname{Re} \left[ f^* \frac{\partial f}{\partial x} \right] \right\} \quad (\text{A5}) \\ &= \frac{1}{j|f|^2} \operatorname{Im} \left[ f^* \frac{\partial f}{\partial x} \right] \cdot j \\ &= \frac{1}{|f|^2} \left[ f_R \frac{\partial f_I}{\partial x} - f_I \frac{\partial f_R}{\partial x} \right] \end{aligned}$$

In (A5), the complex response derivative  $\partial f / \partial x$  is computed using the sensitivity formula in [1].

### A.III The Derivative of the Objective Function Based on Phase

The objective function based on phase is formulated as (see sub-section 2.1.2.):

$$F_p(\boldsymbol{\epsilon}) = 0.5 \sum_{i,j=1}^{N_e} |e^{j\angle S_{ij}} - e^{j\angle \bar{S}_{ij}}|^2 \quad (\text{A6})$$

Using (A6), the derivatives of  $F_p$  with respect to any parameter  $p = \epsilon'_n, \sigma_n$  is obtained as:

$$\left. \frac{\partial F_p}{\partial p} \right|_{p=\epsilon'_n, \sigma_n} = (e^{j\angle S_{ij}} - e^{j\angle \bar{S}_{ij}})_R \cdot \operatorname{Re} \frac{\partial e^{j\angle S_{ij}}}{\partial p} + (e^{j\angle S_{ij}} - e^{j\angle \bar{S}_{ij}})_I \cdot \operatorname{Im} \frac{\partial e^{j\angle S_{ij}}}{\partial p} \quad (\text{A7})$$

Each term in (A7) is expanded as:

$$(e^{j\angle S_{ij}} - e^{j\angle \bar{S}_{ij}})_R = \cos \angle S_{ij} - \cos \angle \bar{S}_{ij} \quad (1)$$

$$(e^{j\angle S_{ij}} - e^{j\angle \bar{S}_{ij}})_I = \sin \angle S_{ij} - \sin \angle \bar{S}_{ij} \quad (2)$$

$$\operatorname{Re} \frac{\partial e^{j\angle S_{ij}}}{\partial p} = -\sin \angle S_{ij} \frac{\partial \angle S_{ij}}{\partial p} \quad (3) \quad (\text{A8})$$

$$\operatorname{Im} \frac{\partial e^{j\angle S_{ij}}}{\partial p} = \cos \angle S_{ij} \frac{\partial \angle S_{ij}}{\partial p} \quad (4)$$

Substituting (A8) in (A7), we derive the final expression as:

$$\begin{aligned} \left. \frac{\partial F_p}{\partial p} \right|_{p=\varepsilon'_n, \sigma_n} &= (\cos \angle S_{ij} - \cos \angle \bar{S}_{ij}) \cdot \left( -\sin \angle S_{ij} \frac{\partial \angle S_{ij}}{\partial p} \right) \\ &\quad + (\sin \angle S_{ij} - \sin \angle \bar{S}_{ij}) \cdot \cos \angle S_{ij} \frac{\partial \angle S_{ij}}{\partial p} \quad (\text{A9}) \\ &= \sin(\angle S_{ij} - \angle \bar{S}_{ij}) \cdot \frac{\partial \angle S_{ij}}{\partial p} \end{aligned}$$

## REFERENCE

- [1] Y. P. Song and N. K. Nikolova, "Memory efficient method for wideband self-adjoint sensitivity analysis", *IEEE Trans. Microw. Theory Tech.*, vol. 56, no. 8, pp. 1917 – 1927, August 2008.



## BIBLIOGRAPHY

Agilent ADS, Agilent Technologies, 1400 Fountaingrove Parkway, Santa Rosa, CA 95403-1799, USA. [Online]. Available: <http://www.home.agilent.com/agilent/home.jsp?cc=US&lc=eng>.

R. K. Amineh, A. Trehan, and N. K. Nikolova, "TEM horn antenna for ultra-wide band microwave breast imaging," *Progress In Electromagnetics Research B*, vol. 13, 59 – 74, 2009.

R. K. Amineh, A. Trehan, and N. K. Nikolova, "Ultra-wide band TEM horn antenna for microwave imaging of the breast," *IEEE International Symposium on Antennas and Propagation (APS)* (Charleston SC), June 2009.

Ansoft HFSS ver. 11, Ansoft Corporation, 225 West Station Square Drive, Suite 200, Pittsburgh, PA 15219 USA, 2008. [Online]. Available: <http://www.ansoft.com>.

ASTM International, 100 Barr Harbor Drive, West Conshohocken, PA, 19428-2959 USA. [Online]. Available: <http://www.astm.org/>.

M.G. Bini, A. Ignesti, L. Millanta, Olmi R, N. Rubino, R. Vanni, "The polyacrylamide as a phantom material for electromagnetic hyperthermia studies," *IEEE Trans Biomed. Eng.*, vol. 31, no. 3, pp. 317 – 322, March 1984.

R. Bishop, and R. Crittenden, *Geometry of manifolds*. Academic Press, New York: 1964, pp. 1 – 22; 122 – 132.

E. J. Bond, X. Li, S. C. Hagness, and B. D. Van Veen, "Microwave imaging via space-time beamforming for early detection of breast cancer," *IEEE Trans. Antennas Propagat.*, vol. 51, no. 8, pp. 1690 – 1705, 2003.

N. F. Boyd *et al.*, “Quantitative classification of mammographic densities and breast cancer risk: results from the Canadian National Breast screening study,” *Journal of National Cancer Institute*, vol. 87, no. 9, May 1995.

S. Boyles. (August 2007). MRI detects early breast cancer cells. WebMD Health News. [Online]. Available: <http://www.medicinenet.com/script/main/art.asp?articlekey=83133>.

(April 2009). Breast Cancer Statistics 2009. Canadian Cancer Society, Toronto, ON. [Online]. Available: [http://www.cancer.ca/canada-wide/about%20cancer/cancer%20statistics/stats%20at%20a%20glance/breast%20cancer.aspx?sc\\_lang=en](http://www.cancer.ca/canada-wide/about%20cancer/cancer%20statistics/stats%20at%20a%20glance/breast%20cancer.aspx?sc_lang=en)

(November 2008). Breast Cancer Statistics. Breastcancer.org (BCO). [Online]. Available: [http://www.breastcancer.org/symptoms/understand\\_bc/statistics.jsp](http://www.breastcancer.org/symptoms/understand_bc/statistics.jsp).

A. E. Bulyshev, S. Y. Semenov, A. E. Souvorov, R. H. Svenson, A. G. Nazarov, Y.E. Sizov and G. P. Tatsis, “Computational modeling of three-dimensional microwave tomography of breast cancer,” *IEEE Trans. Biomed. Eng.*, vol. 48, no. 9, pp. 1053 – 1056, September 2001.

A. M. Campbell, and D. V. Land, “Dielectric properties of female human breast tissue measured in vitro at 3.2 GHz,” *Phys. Med. Biol.*, vol. 37, pp. 193 – 210, 1992.

S. S. Chaudhary, R. K. Mishra, A. Swarup, and J. M. Thomas, “Dielectric properties of normal and malignant human breast tissues at radiowave and microwave frequencies,” *Indian J. Biochem. Biophys.*, vol. 21, pp. 76 – 79, February 1984.

M. A. Chaudary *et al.*, “A comparison of epidemiological characteristics in breast cancer patients and normal women in Great Britain and Japan: Results of a prospective study,” *Breast Cancer Research and Treatment*, vol. 18, pp. 19 – 22, 1991.

W. C. Chew and J. H. Lin, “A frequency-hopping approach for microwave imaging of large inhomogeneous bodies,” *IEEE Microwave Guided Wave Lett.*,

vol. 5, pp. 439 – 441, December 1995.

J. W. Choi *et al.*, “Microwave detection of metastasized breast cancer cells in the lymph node; potential applications or sentinel lymphadenectomy,” *Breast Cancer Res. Treat.*, vol. 86, pp. 107 – 115, 2004.

H. N. Christiansen, and T. W. Sederberg, “Conversion of complex contour line definitions into polygonal element mosaic,” *ACM (Association for Computing Machinery) SIGGRAPH Computer Graphics*, vol. 12, pp. 187 – 192, 1978.

D. Clunie. An introduction to the DICOM single-file format. [Online Chapter]. Available: <http://www.sph.sc.edu/comd/rorden/dicom.html>.

T. H. Cormen, C. E. Leiserson, R. L. Rivest, C. Stein, *Introduction to Algorithms*, 2<sup>nd</sup> ed. MIT Press, 2004, pp. 527 – 549.

CST Microwave Studio, CST of Americal, Inc., Headquarters at 492 Old Connecticut Path, Suite 505 Framingham, MA 01701, USA, 2009. [Online]. Available: <http://www.est.com/>.

M. G. del Carmen *et al.*, “Mammographic breast density and race,” *American Journal of Roentgenology: Women’s Imaging*, vol. 188, pp. 1147 – 1150, April 2007.

*DICOM, Digital Imaging and Communications in Medicine*. National Electrical Manufacturers Association (NEMA), Suite 1752, 1300 North 17<sup>th</sup> Street, Rosslyn, VA 22209, USA. [Online]. Available: <http://medical.nema.org/dicom>.

(May 2009). Edge. Spatial Docs, Spatial Corporation. [Online]. Available: <http://doc.spatial.com/index.php/EDGE>.

T. S. England and N. A. Sharples, “Dielectric properties of the human body in the microwave region of the spectrum,” *Nature*, vol. 163, pp. 487 – 488, 1949.

Emerson & Cuming Microwave Products, Inc., 28 York Avenue, Randolph, MA 02368 USA. [Online]. Available:

<http://www.eccosorb.com/main/RegionalHome.html>.

Flea 2, Point grey Research, 12051 Riverside Way, Richmond, BC, Canada, 2007. [Online]. Available: <http://www.ptgrey.com/products/flea2/index.asp>.

E. C. Fear, P. Meaney, and M. Stuchly, “Microwaves for breast cancer detection,” *IEEE Potentials*, vol. 22, no. 1, pp. 12 – 18, 2003.

E. C. Fear and M. A. Stuchly, “Microwave detection of breast cancer,” *IEEE Trans. Microwave Theory Tech.*, vol. 48, no. 11, pp. 1854 – 1863, 2000.

E. Fear, X. Li, S. C. Hagness, and M. A. Stuchly, “Confocal microwave imaging for breast cancer detection: Localization of tumors in three dimensions,” *IEEE Trans. Biomed. Eng.*, vol. 49, no. 8, pp. 812 – 822, August 2001.

H. S. Fiegelson, C. R. Jonas, L. R. Teras, M. J. Thun, and E. E. Calle, “Weight gain, body mass index, hormone replacement therapy, and postmenopausal breast cancer in a large prospective study,” *Cancer Epidemiology, Biomarkers & Prevention*, vol. 13, pp. 220 – 224, February 2004.

H. K. Fuchs, and S. P. Uselton, “Optimal surface reconstruction from planar contours,” *Communications of the ACM (Association for Computing Machinery)*, vol. 20, no. 10, pp. 693 – 702, October 1977.

S. Gabriel, R. W. Lau, and C. Gabriel, “The dielectric properties of biological tissues: II. Measurements on the frequency range 10 Hz to 20 GHz,” *Phys. Med. Biol.*, vol. 41, no. 11, pp. 2251 – 2269, November 1996.

S. Gabriel, R. W. Lau, and C. Gabriel, “The dielectric properties of biological tissues: III. Parametric models for the dielectric spectrum of tissues,” *Phys. Med. Biol.*, vol. 41, pp. 2271 – 2293, April 1996.

M. Georgiev, “Photogrammetry-based reconstruction of an object,” Computational Electromagnetics Res. Lab., McMaster University, CEM-R-43, June 2007.

Geomagic Studio, Geomagic U.S. Corporate Headquarters, 3200 East Hwy 54, Cape Fear Building, Suite 300, Research Triangle Park, NC, 27709 USA. [Online]. Available: <http://www.geomagic.com/en/>.

A. Hajiaboli and M. Popovic, "FDTD subcell modeling of the inner conductor of the coaxial feed: accuracy and convergence analysis," *IEEE Trans. on Magnetics*, vol. 43, no. 4, April 2007.

R. J. Halter *et al.*, "The correlation of in vivo and ex vivo tissue dielectric properties to validate electromagnetic breast imaging: initial clinical experience," *Phys. Med. Biol.*, vol. 30, pp. 121 – 136, June 2009.

Jay R. Harris, Marc E. Lippman, Monica Morrow, C. Kent Osborne, *Diseases of the Breast*, 2nd edition. Lippincott Williams and Wilkins, pp. 130, pp. 400 – 455, 1999.

G. Hartsgrove, A. Kraszewski, and A. Surowiec, "Simulated biological materials for electromagnetic radiation absorption studies," *Bioelectromagnetics*, vol. 8, pp. 29 – 36, 1987.

M. K. Hoevel, "Contoured mammography phantom with skin," U.S. Patent 4 655 716, April 7, 1987.

J. Hornak (2000). Magnetic Resonance Imaging. [Online Chapter]. Available: <http://www.cis.rit.edu/class/schp730/lect/lect-2.htm>.

*Imaging Research Centre (IRC)*. Brain Body Institute, St. Joseph Healthcare Hospital, 50 Charlton Ave. East, Hamilton, Ontario.

(June 2003). *Introduction to Scripting in HFSS*. Ansoft Corporation, 225 West Station Square Drive, Suite 200, Pittsburgh, PA 15219, USA, 2008.

K. Ito, "Numerical and experimental human body phantoms," *2007 IET Seminar on Antennas and Propagation for Body-Centric Wireless Communications*, April

2007.

H. M. Jafari, M. J. Deen, S. Hranilovic, and N. K. Nikolova, “A study of ultrawideband antennas for near-field imaging,” *IEEE Trans. Antennas Propagat.*, vol. 55, no. 4, pp. 1184 – 1188, April 2007.

W. T. Joines, Y. Zhang, C. Li, and R. L. Jirtle , “The measured electrical properties of normal and malignant human tissues from 50 to 900 MHz,” *Med. Phys.*, vol. 21, pp. 547 – 550, January 1994.

M. Kerr. (November 2007). 3-D mammography cuts false-positive rates by half. Reuter Health, Chicago. [Online]. Available:

<http://www.reuters.com/article/healthNews/idUSCOL97439820071129>.

M. Klemm, I. J. Craddock, J. Leendertz, A. W. Preece, R. Benjamin, “Breast cancer detection using symmetrical antenna array,” *IEEE International Symposium on Antennas and Propagation (APS)*, July 2008.

Vesna Kozelj. (August 2008). How to hold the camera with your hands for best support. knol™. [Online]. Available: <http://knol.google.com/k/vesna-kozelj/how-to-hold-the-camera-with-your-hands/3k0expg5xjecw/2#>.

J. W. Lagendijkt, P. Nilssoni, “Hyperthermia dough: a fat and bone equivalent phantom to test microwave/radiofrequency hyperthermia heating systems,” *Phys. Med. Biol.*, vol. 30, no. 7, pp. 709 – 712, February 1985.

B. Lambert. (April 2008). Dr. K. A. Mauritz Research Group - Dielectric spectroscopy. [Online]. Available: <http://www.psrm.usm.edu/mauritz/dilect.html>.

D. Lamensdorf, L. Susman, “Baseband-Pulse-Antenna Techniques,” *IEEE Antennas and Propagation Magazine*, vol. 36(1), pp. 20 – 29, February 1994.

L. E. Larsen and J. H. Jacobi, *Medical Applications of Microwave Imaging*. New York: IEEE Press, 1986.

M. Lazebnik, L. McCartney, D. Popovic, C. B. Watkins, M. J. Lindstorm, J. Harter, S. Sewall, A. Magliocco, J. H. Brooske, M. Okoniewski and S. C. Hagness, “ A large – scale study of the ultra wideband microwave dielectric

properties of normal breast tissue obtained from reduction surgeries,” *Phys. Med. Biol.*, vol. 52, pp. 2637 – 2656, April 2007.

M. Lazebnik, L. McCartney, D. Popovic, C. B. Watkins, M. J. Lindstorm, J. Harter, S. Sewall, A. Magliocco, J. H. Brooske, M. Okoniewski and S. C. Hagness, “A large-scale study of the ultrawideband microwave dielectric properties of normal, benign and malignant breast tissues obtained from cancer surgeries,” *Phys. Med. Biol.*, vol. 52, pp. 6093 – 6115, October 2007.

M. Lazebnik, M. Okoniewski, J. H. Brooske, S. C. Hagness, “Highly accurate Debye models for normal and malignant breast tissue dielectric properties at microwave frequencies,” *IEEE Microwave and Wireless Components Letters*, vol. 17, no. 12, pp. 822 – 824, December 2007.

X. Li, E. J. Bond, B. D. Van Veen and S. C. Hagness, “An overview of ultrawideband microwave imaging via space-time beamforming for early-stage breast-cancer detection,” *IEEE Antennas Propagat. Mag.*, vol. 47, pp. 19 – 34, February 2005.

X. Li, S. K. Davis, S. C. Hagness, D. W. V. Weide, and B. D. Van Veen, “Microwave imaging via space-time beamforming: experimental investigation of tumor detection in multilayer breast phantoms,” *IEEE Trans. Microwave Theory Tech.*, vol. 52 no. 8, pp. 1856 – 1865, August 2004.

X. Li and S. C. Hagness, “A confocal microwave imaging algorithm for breast cancer detection,” *IEEE Microwave Wireless Compon. Lett.*, vol. 11, no. 3, pp. 130 – 132, 2001.

Q. H. Liu, Z. Q. Zhang, T. T. Wang, J. A. Bryan, G. A. Ybarra, L. W. Nolte, and W. T. Joines, “Active microwave imaging I — 2-D forward and inverse scattering methods,” *IEEE Trans. Microwave Theory Tech.*, vol. 50, no. 1, pp. 123 – 133, January 2002.

L. Liu and A. Trehan, “Self-adjoint sensitivity analysis for 3D Jacobians maps in imaging and detection,” Computational Electromagnetics Res. Lab., McMaster University, CEM-R-50, May 2009.

Y. Machii, H. Aoki, K. Koshiii, “Fat thickness estimation method using bio electrical property examination by gel phantom model test,” *2006 International Symposium on Micro-NanoMechatronics and Human Science*, November 2006.

(September 2008). Mammograms and other Breast Imaging Procedures. American Cancer Society (ACS). [Online]. Available: [http://www.cancer.org/docroot/PED/content/PED\\_2\\_3X\\_Mammography\\_and\\_Other\\_Breast\\_Imaging\\_Procedures.asp](http://www.cancer.org/docroot/PED/content/PED_2_3X_Mammography_and_Other_Breast_Imaging_Procedures.asp).

(May 2009). Managing Menopause. The Jean Hailes Foundation for Women’s Health, Victoria, Australia. [Online]. Available: <http://www.managingmenopause.org.au/content/view/37/62/>.

(May 2009). Manifold and Non-manifold Objects. Spatial Docs, Spatial Corporation. [Online]. Available: [http://doc.spatial.com/index.php/Manifold\\_and\\_Non-manifold\\_Objects](http://doc.spatial.com/index.php/Manifold_and_Non-manifold_Objects).

MATLAB™ 7.1, The MathWorks Inc., 3 Apple Hill Drive, Natick, MA, 2005. [Online]. Available: <http://www.mathworks.com/>.

S. McMains, J. Smith, and C. Sequin, “The evolution of a layered manufacturing interchange format,” *Proceedings of DETC02 2002 ASME Design Engineering Technical Conferences*, September 2002.

P. M. Meaney, M. W. Fanning, D. Li, S. P. Poplack, and K. D. Paulsen, “A clinical prototype for active microwave imaging for the breast,” *IEEE Trans. Microwave Theory Tech.*, vol. 48, no. 11, pp. 1841 – 1853, November 2000.

(October 2003). MRI vs. Mammography: Which is better for screening women at high risk of breast cancer? National Cancer Institute (NCI). [Online]. Available: <http://www.cancer.gov/clinicaltrials/results/mri-vs-mammography0603>.

National Academy Press. (2001). *Mammography and Beyond: Developing Techniques for the Early Detection of Breast Cancer*. Institutes of Medicine, Washington, DC. [Online]. Available: [http://books.nap.edu/openbook.php?record\\_id=10107&page=9](http://books.nap.edu/openbook.php?record_id=10107&page=9).



(February 2008). National Breast and Ovary Cancer Center, Australia. [Online]. Available: <http://www.breasthealth.com.au/types/preinvasive.html>.

R. Nilavalan, J. Leendertz, I. Craddock, A. Preece, and R. Benjamin, “Numerical analysis of microwave detection of breast tumours using synthetic focussing techniques,” *In Proc. IEEE Antennas and Propagation Society Symp.*, pp. 2440–2443, vol. 3, 2004.

N. K. Nikolova, L. Liu, and A. Trehan, “Adjoint sensitivities in microwave imaging and design tuning,” Workshop on EM-Based Microwave Optimization Technology: State of the Art and Applications, *IEEE MTT-S Int. Symposium* (Boston, MA), June 2009.

J. Oakley, C. P. Riley, S. Taylor, and C. W. Trowbridge, “Achieving the holy grail of seamless CAD data import into analysis software,” *COMPEL: The International Journal for Computation and Mathematics in Electrical and Electronic Engineering*, vol. 21, no. 4, pp. 512 – 518, 2002.

Y. Okano, K. Ito, I. Ida, M. Takahashi, “The SAR evaluation method by a combination of Thermographic Experiments and Biological Tissue-Equivalent Phantoms,” *IEEE Trans. Microwave Theory Tech.*, vol. 48, no. 11, pp. 2094 – 2103, November 2000.

Y. Okano, K. Ito, and H. Kawai, “Solid phantom composed of glycerin and its application to SAR estimation,” *IEICE Trans. Commun. (Japanese Edition)*, Vol. J83-B, no. 4, pp. 534 – 543, 2000.

T. Onishi, R. Ishido, T. Takimoto, K. Saito, S. Uebayashi, M. Takahashi and K. Ito, “Biological tissue-equivalent agar-based solid phantoms and SAR estimation using the thermo graphic method in the range of 3-6 GHz,” *IEICE Trans Commun.*, vol. E88-B, no. 9, pp. 3733 – 3741, September 2005.

PhotoModeler Pro 5.2.3., Eos Systems Inc., 210 - 1847 West Broadway, Vancouver, BC, Canada, 2007. [Online]. Available: <http://www.photomodeler.com/index.htm>.

T. L. Pope, M. E. Read, T. Medsker, A. J. Buschi, and A. N. Brenbridge, “Breast skin thickness: normal range and causes of thickening shown on film-screen mammography,” *J. The Canadian Assoc. Radiologists*, vol. 35, pp. 365 – 368, 1984.

S. P. Poplack *et al.*, “Electromagnetic breast imaging: average tissue properties values in women with negative clinical findings,” *Radiology*, vol. 281, pp. 571 – 580, 2004.

(May 2006). Probability of Breast Cancer in American Women. National Cancer Institute (NCI). [Online]. Available: <http://www.cancer.gov/cancertopics/factsheet/Detection/probability-breast-cancer>.

Product Selector – Laboratory Water Types. Millipore Corporate Headquarters, Billerica, MA 01821, USA. [Online]. Available: <http://www.millipore.com/labwater/lw3/productselector>.

QW-3D v. 7.0, QWED Sp. z o.o., ul. Nowowiejska 28 lok. 32, 02-010 Warsaw, Poland, 2009. [Online]. Available: <http://www.qwed.com.pl/>.

Radiology Support Devices Inc., 1904 East Dominguez Street Long Beach, CA 90810 USA. [Online]. Available: <http://www.rsdphantoms.com/index.html>.

REVscan, Creaform Inc., 5825 rue St-Georges Lévis, Québec, Canada, 2009. [Online]. Available: [www.creaform3D.com](http://www.creaform3D.com).

T. Rowland (July 2009). Manifold. MathWorld: A Wolfram Web Source. [Online]. Available: <http://mathworld.wolfram.com/Manifold.html>.

T. Rubæk, P. M. Meaney, P. Meincke, and K. D. Paulsen, “Nonlinear microwave imaging for breast-cancer screening using gauss–newton’s method and the CGLS inversion algorithm,” *IEEE Trans. Antennas Propagat.*, vol. 55, no. 8, pp. 2320 – 2331, 2007.

A. Samani, J. Zubovits, D. Plewes, “Elastic moduli of normal and pathological human breast tissues: an inversion-technique-based investigation of 169 samples,”

*Phys. Med. Biol.*, vol. 52, pp. 1565 – 1576, February 2007.

M. N. O. Sadiku, *Elements of Electromagnetics*, 4<sup>th</sup> ed. Oxford University Press: New York, 2007, pp. 435 – 445.

(April 2007). Screening Mammograms: Questions and Answers. National Cancer Institute (NCI). [Online]. Available: <http://www.cancer.gov/cancertopics/factsheet/Detection/screening-mammograms>.

L. Sha, E. R. Ward, B. Story, “A review of dielectric properties of normal and malignant breast tissue,” *Proc. IEEE Southeast Conf.*, pp.457 – 462, 2002.

J. M. Sill and E. C. Fear, “Tissue sensing adaptive radar for breast cancer detection—experimental investigation of simple tumor models,” *IEEE Trans. Microwave Theory Tech.*, vol. 53, no. 11, pp. 3312 – 3319, November 2005.

Y. P. Song and N. K. Nikolova, “Memory efficient method for wideband self-adjoint sensitivity analysis”, *IEEE Trans. Microw. Theory Tech.*, vol. 56, no. 8, pp. 1917 – 1927, August 2008.

J. P. Stang, W. T. Joines, Q. H. Liu, G. A. Ybarra, R. T. George, M. Yuan, and I. Leonhardt, “A tapered microstrip patch antenna array for use in breast,” *IEEE International Symposium on Antennas and Propagation (APS)*, June 2009.

Dr. M. Stoppard, *The Breast Book*. DK ADULT Co., 1996, pp. 48.

I. Stroud, *Boundary Representation Modelling Techniques*. Springer-Verlag Publishers: London: 2006.

A. J. Surowiec, S. S. Stuchly, J. R. Barr, and A. Swarup, “Dielectric properties of breast carcinoma and the surrounding tissues,” *IEEE Trans. Biomed. Eng.*, vol. 35, pp. 257 – 263, April 1988.

(November 2008). The American College of Radiology BI-RADS® ATLAS and MQSA: Frequently Asked Questions. American College of Radiology (ACR). [Online]. Available: [http://www.acr.org/SecondaryMainMenuCategories/quality\\_safety/BIRADSAtlas/BIRADSFAQs.aspx](http://www.acr.org/SecondaryMainMenuCategories/quality_safety/BIRADSAtlas/BIRADSFAQs.aspx).

The 3D ACIS Modeler, Spatial Corp. Headquarters, 310 Interlocken Parkway, Suite 200, Broomfield, CO 80021-3468, USA. [Online]. Available: <http://www.spatial.com/>.

C. E. Thomson *et al.*, “Magnetic resonance imaging – a general overview of principles and examples in veterinary neurodiagnosis,” *MRI-Principles and Neurodiagnosis*, vol. 34, no. 1, March 1992.

A. Trehan, “3-D reconstruction of curved objects from 2-D images: recovery of breast shape,” Computational Electromagnetics Res. Lab., McMaster University, CEM-R-33, August 2006.

A. Trehan, “Summary of materials and recipes available in the literature to fabricate biological phantoms for RF and microwave experiments,” Computational Electromagnetics Res. Lab., McMaster University, CEM-R-45, August 2008.

A. Trehan, R. K. Amineh, M. S. Georgiev, and N. K. Nikolova, “Photogrammetry-based surface reconstruction for improving microwave breast tumor detection,” *Proc. of 24th Int. Review of Progress in Applied Computational Electromagnetics (ACES)*, March 2008.

A. Trehan, R. K. Amineh, M. S. Georgiev, and N. K. Nikolova, “Accuracy assessment of photogrammetry surface reconstruction for improving microwave imaging,” *IEEE International Symposium on Antennas and Propagation (APS)*, July 2008.

A. Trehan, “Fidelity evaluation of a novel UWB TEM horn antenna,” Computational Electromagnetics Res. Lab., McMaster University, May. 2009.

A. V. Vorst, A. Rosen, Y. Kotsuka, *RF/Microwave Interaction with Biological Tissues*. John Wiley & Sons Inc., 2006, pp. 14 – 78. (December 2008). What is Non-manifold Geometry? KFourMetrics, Hyderabad, India. [Online]. Available: <http://www.kfourmetrics.com/wordpress/?p=93>.

T. C. Williams, E.C. Fear, David T. Westwick, “Tissue sensing adaptive radar for

breast cancer detection: investigations of an improved skin sensing method,” *IEEE Trans. Microwave Theory Tech.*, vol. 54, no. 4, pp. 1308 – 1314, 2006.

D. Wilson, “Data exchange and software integration: interdisciplinary design challenges,” *Artificial Intelligence for Engineering Design, Analysis and Manufacturing*, vol. 12, pp. 73 – 76, 1998.

D. W. Winters, E. J. Bond, B. D. Van Veen, S. C. Hagness, “Estimation of the frequency-dependent average dielectric properties of breast tissue using a time-domain inverse scattering technique,” *IEEE Trans. Antennas Propag.*, vol. 54, pp. 3517 – 3528, November 2006.

D. W. Winters, B. D. V. Veen, and S. C. Hagness, “Dimensionality reduction in inverse scattering: applications to microwave imaging for breast cancer detection,” *1<sup>st</sup> Int. Conf. on Applied Inverse Problems 2007: Theoretical and Computational Aspects (AIP 2007)*, 2007.

D. A. Woten, S. Pandaraju, and M. El-Shenawee, “Breast skin effect on scattered electromagnetic fields,” *Proc. of 24th Int. Review of Progress in Applied Computational Electromagnetics (ACES)*, March 2008.

T. Wuren, T. Takai, M. Fujii, and I. Sakagami, “Effective 2-Debye-pole FDTD model of electromagnetic interaction between whole human body and UWB radiation,” *IEEE Microw. Wireless Comp. Lett.*, vol. 17, no. 7, pp. 483 – 485, July 2007.

XFDTD ver. 6.3, Remcom Inc., 300 Chesterfield Center, Suite 260 Chesterfield, MO 63017, USA, 2003. [Online]. Available: [www.remcom.com](http://www.remcom.com).

XnView for Windows (June 2007). [Online]. Available: <http://www.xnview.com>.  
W. L. Young, N. Y. Hoffman, *Breast Cancer: A Practical Guide to Diagnosis Volume 1 – Procedures*, 1<sup>st</sup> edition. Mt. Hope Publishing Co., pp. 23, 1994.

Z. Q. Zhang, Q. H. Liu, C. Xiao, E. Ward, G. Ybarra, and W. T. Joines, “Microwave breast imaging: 3-D forward scattering simulation,” *IEEE Trans. Biomed. Eng.*, vol. 50, no. 10, pp. 1180 – 1189, 2003.

